The Dissertation Committee for Haotian Wang Certifies that this is the approved version of the following dissertation:

A General Poro-Elasto-Plastic Model for Poorly Consolidated Sands

Committee:

Mukul M. Sharma, Supervisor

Kishore K. Mohanty

Loukas F. Kallivokas

John T. Foster

Nicolas D. Espinoza

A General Poro-Elasto-Plastic Model for Poorly Consolidated Sands

by

Haotian Wang

Dissertation

Presented to the Faculty of the Graduate School of

The University of Texas at Austin

in Partial Fulfillment

of the Requirements

for the Degree of

Doctor of Philosophy

The University of Texas at Austin

December 2018

Dedication

To my parents, Lijun Wang and Ping Li,

my wife, Xiqian Liu,

and my daughter, Zhifan Wang,

for their sacrifice, support and love.

Acknowledgements

I would like to express my deep gratitude to my advisor, Dr. Mukul M. Sharma, for his guidance and support throughout my PhD study at the University of Texas at Austin. He has always made himself available to clarify my doubts and provide insightful discussions despite his busy schedules. His valuable advice and comments from both scientific perspective and industrial view help me to better understand not only the fundamental work of my research, but also its potential application to the oil and gas industry. I would also like to thank my dissertation committee members: Dr. Kishore Mohanty, Dr. Loukas Kallivokas, Dr. John Foster and Dr. Nicolas Espinoza, for their helpful suggestions on my research and their time for reviewing my dissertation.

I am thankful to all department staffs for their assistance, and I would like to give a special thanks to Jin Lee, who provides invaluable support during my stay in the group.

I would like to thank my friends and colleagues in the department for their support and contributions. Specially, I would like to thank Dr. Philip Cardiff, Dr. Ripudaman Manchanda, Dr. Jongsoo Hwang and Deepen Gala for good advice and collaboration on my research.

I would also like to thank ExxonMobil and PetroChina Tarim Oilfield Company for financial support, providing experimental data and field data, and their permission to publish the work.

Finally, I would like to thank my parents, my wife, and my beloved daughter, for their endless support and unconditional love.

A General Poro-Elasto-Plastic Model for Poorly Consolidated Sands

Haotian Wang, Ph.D.

The University of Texas at Austin, 2018

Supervisor: Mukul M. Sharma

Sand failure and production are likely to occur during oil and gas production, especially in poorly consolidated formations. Most past research focuses on either experimental work to understand sanding mechanisms or simple sand production models to estimate the onset of sand production. Such models are usually not enough to capture sanding behavior in complex situations in the field. In this dissertation, a numerical 3D sand production prediction model is developed based on a general poro-elasto-plastic model for multi-phase fluid flow, which can predict both the onset of sanding and the volume of sand produced. The model is thoroughly validated with multiple analytical solutions. It is also validated with experiment data for the onset of sanding, sand production volume, and cavity shape caused by sand production. The model results are shown to agree well with all these experimentally measured quantities and for the first time predict sanding behavior in complex geometries over a wide range of conditions.

From extensive sand production experiments, four distinct cavity shapes have been frequently observed: spiral shear band cavity, V-shape cavity, dog-ear cavity, and slit mode cavity. However, the reasons and the sanding mechanisms responsible for this behavior have not been fully articulated. Results presented here show that the model is capable of capturing all the complicated cavity shapes, and provide qualitative guidelines to define the conditions under which each type of cavity will be formed.

The effect of different well completions on sand failure and production have been investigated with the model. Results show the potential advantage of using frac-packs for reducing the fluid pressure gradients and redistributing stresses. In addition, the impact of rock and fluid properties on sanding behavior has been studied to show the importance of mechanical failure and fluid erosion on sanding. Wells with multiple oriented perforations are analyzed to study the effect of perforation design on sand production.

The application of the model has been further extended to quantitatively explain some field observations, including: delayed sanding in gas wells, sanding caused by water breakthrough, and water hammer effects. Simulation results suggest that rock strengthening by water evaporation and non-Darcy effects in gas flow can delay sand production. On the other hand, sanding after water breakthrough can be explained by accelerating sand failure and fluid erosion due to an increase in the water saturation. The impact of water hammer on sand failure has been investigated to optimize subsurface valve location and shut-in procedure.

Finally, the sand production model is applied to a field case for HPHT wells to study sanding mechanisms for different sanding behavior observed in two wells in similar locations in the field. Simulation results show that rock heterogeneity and natural fractures are the most likely reasons for sand production in this field. The difference in onset of sanding from the two wells can be explained by different in-situ stresses, while the difference in severity of sanding can be explained by differences in pressure drawdown and the orientation of perforations. The critical drawdown during reservoir depletion are determined under different conditions from the model to guide drawdown management so as to prevent sanding issues.

Table of Contents

List of Tables

List of Figures

Chapter 1: Introduction

Sand production is a common concern throughout the life of oil and gas wells and is more likely to occur in poorly consolidated sands (Bianco and Halleck, 2001) and deep reservoirs (Vaziri, 1986; Vaziri et al, 2002). Sand production may adversely affect the well completion due to plugging of perforations or production liners, wellbore instability, failure of sand control completions (Willson et al., 2002), or collapse of some sections of a horizontal well. In addition, sand-related problems always increase production costs considerably by causing erosion of pipelines and surface facilities, reduction in productivity, intervention costs and complexities, and other environmental effects (Rahmati et al., 2012). On the other hand, a controllable amount of sand production can avoid redundant and complex sand control completions, such as gravel packs, which have been extensively used to prevent sand production in unconsolidated formations (Saucier, 1974). Thus, before making a decision on which method of sand control to use, if any, it is crucial to estimate the onset of sand production and the volume of sand produced (Mondal et al., 2016; Wu et al., 2016; Wu at al., 2018).

The physics of sand production is very complex, as it includes the dynamic interaction between formation rock and fluid flow (Liang et al., 2015; Liang et al., 2017; Liang et al., 2018). During oil and gas production, the rock around the well/perforation may lose its integrity and suffer mechanical instability. Some portion of the rock may degrade to single sand grains or flakes. The degraded sands will stay in the formation until the hydrodynamic forces induced by fluid flow are large enough to bring them into the well and further to the surface, resulting in sand production. Due to its nature, sand production can be affected by several important factors, such as in-situ stresses, rock properties, fluid properties, well completions, production design, etc.

1.1 OBJECTIVES OF THE RESEARCH

In this research, the main goals are to develop a 3D numerical model for a poro-elasto-plastic medium, and to use it to predict both the onset of sand production and the volume of produced sand under different stress and fluid flow conditions. The model will also be used to better understand the mechanisms of sand production from distinct failure patterns and fluid erosion behaviors. The detailed objectives for the development and application of the model are summarized as follows:

1. To develop a 3D poro-elasto-plastic model with both single phase and multi-phase fluid flow;
2. To apply a modified Mohr-Coulomb-with-Cap model with strain hardening/softening for shear/tensile/compressive yield and stress return algorithm;
3. To implement a sanding criterion that includes both mechanical failure and fluid erosion for sand production prediction;
4. To benchmark distinct cavity shapes due to sand production in experiments and fields and better understand the mechanism of sanding;
5. To evaluate different well completions and their impact on sand failure during production;
6. To study the effect of rock and fluid properties on the onset of sanding and the sand production volume in open-hole wells;
7. To study the effect of perforation parameters on sand production in cased and perforated wells. These parameters include perforation orientation, perforation diameter, and perforation length;
8. To study the effect of fluid flow on sand failure and production in open-hole wells;

9. To apply the sand production model to field studies and to predict the severity of sanding based on drilling, cementing, completion and production practices.

1.2 Outline of The Dissertation

The dissertation is presented in nine chapters. Chapter 1 introduces the background and the objectives of the research.

Chapter 2 shows the field evidence of sand production and reviews the mechanisms behind sanding issues. In addition, recent studies on sand production, both experimental and from simulations, have been reviewed and compared.

Chapter 3 develops the governing equations for the poro-elasto-plastic model in single phase and multi-phase fluid flow, and describes the modified Mohr-Coulomb-with-Cap model implemented in the solver. In this chapter, the numerical model is validated with analytical solutions for various cases.

Chapter 4 describes the development of the sand production model, including sanding criteria and a cell removal algorithm. Some novel features, such as dynamic mesh refinement, are introduced and tested. The sand production model is benchmarked with experiments.

Chapter 5 reviews different cavity shapes due to sand production from both experiments and field data, and benchmarks the model under the same conditions. Distinct failure patterns and sanding mechanisms are discussed, to provide recommendations for field operations.

Chapter 6 presents the impact of different well completions on sand failure using the sand production model. In addition, a systematic study of the effect of rock and fluid properties on sand production has been conducted. For perforated wells, the importance of

completion parameters such as perforation orientation, diameter, and length on sand production are highlighted.

In Chapter 7, the effect of fluid flow on sand failure and production has been studied. Firstly, the difference of sanding behavior in oil and gas flow are compared and investigated, showing the importance of non-Darcy effects and rock weakening by water contact. Secondly, the mechanisms of sand production in multi-phase fluid flow are studied, including the effect of capillary cohesion and water saturation. Thirdly, the impact of water hammer events on sand failure and injectivity loss in injection wells are explored.

Chapter 8 presents a predictive field case sand production study using the sand production model developed in this dissertation. Two selected wells suffering sanding issues are evaluated using cementing, completion, and production data to estimate sanding severity. Based on the results, recommendations are proposed to avoid well productivity loss and sand fill-up.

Finally, Chapter 9 summarizes the conclusions from this research and proposes recommendations for future work.

REFERENCES

Bianco, L. and P. Halleck. 2001. Mechanisms of arch instability and sand production in two-phase saturated poorly consolidated sandstones. *Paper presented at the SPE European Formation Damage Conference.*

Liang, Y., D. DiCarlo, and M. A. Hesse. 2015. Experiment and Simulation Study of Hydrodynamic Dispersion and Finger Dynamics for Convective Dissolution of Carbon Dioxide. *Presented at the AGU Fall Meeting Abstracts.*

Liang, Y., J. Sheng, J. Hildebrand. 2017. Dynamic permeability models in dual-porosity system for unconventional reservoirs: Case studies and sensitivity analysis. *Presented at the SPE Reservoir Characterisation and Simulation Conference and Exhibition, Society of Petroleum Engineers.*

Liang, Y., Y. Ning, L. Liao, B. Yuan. 2018. Special Focus on Produced Water in Oil and Gas Fields: Origin, Management, and Reinjection Practice, in: Formation Damage During Improved Oil Recovery. *Elsevier, pp. 515–586.*

Mondal, S., C. H. Wu, M. M. Sharma, R. A. Chanpura, M. Parlar, and J. A. Ayoub. 2016. Characterizing, Designing, and Selecting Metal Mesh Screens for Standalone-Screen Applications. *SPE Drilling & Completion,* 31(02), 85-94.

Rahmati, H., A. Nouri, H. Vaziri, and D. Chan. 2012. Validation of predicted cumulative sand and sand rate against physical-model test. *Journal of Canadian Petroleum Technology,* 51(5), 403-410.

Saucier, R. 1974. Considerations in gravel pack design. *Journal of Petroleum Technology, 26*(02), 205-212.

Vaziri, H. 1986. Mechanics of fluid and sand production from oil sand reservoirs. *Annual Technical Meeting. Petroleum Society of Canada.*

Vaziri, H., Y. Xiao, and I. Palmer. 2002. Assessment of several sand prediction models with particular reference to HPHT wells. *Paper presented at the SPE ISRM Rock Mechanics Conference, Irving, TX*.

Willson, S. M, Z. A. Moschovidis, J. R. Cameron, and I. D. Palmer. 2002. New model for predicting the rate of sand production. *Paper presented at the SPE/ISRM Rock Mechanics Conference, Irving, Texas, 20-23 October 2002.*

Wu, C.H., M. M. Sharma, M. J. Fuller and S. Mathis. 2018, February. Estimating Sand Production Through Gravel Packs. *In SPE International Conference and Exhibition on Formation Damage Control.*

Wu, C.H., M. M. Sharma, R. Chanpura, M. Parlar and J. Ayoub. 2016. Factors Governing the Performance of Multi-Layered Metal-Mesh Screens. *In SPE International Conference and Exhibition on Formation Damage Control. Society of Petroleum Engineers.*

Chapter 2: Background and Literature Review

2.1 Field Evidence of Sand Production

Sand failure and production have been observed frequently during field operations, especially in poorly consolidated sands with low rock strength and in deep reservoirs where high stresses and high pressure are expected. It can be triggered during drilling, completion, injection, or production operations. During drilling, formation damage such as fluid/solids invasion may occur, which will result in a higher drawdown being required for production and can potentially lead to sanding. Completion induced sanding issues may occur under various conditions of stresses. While injecting into a well, rock weakening and fatigue failure caused by unplanned water hammer events are commonly seen. For production wells, rock near the well experiences increasing effective stresses and becomes more prone to failure. In addition, in many depleted reservoirs, sand production becomes a serious issue when water breakthrough occurs.

Rock damage, induced by drilling and completion operations, can have a significant impact on sand production. For example, sanding problems are reported in VLG 3676, Block VII, one of the most important fields in Ceuta, which is located in the deep and layered Eocene reservoirs of southern Lake Maracaibo, Western Venezuela (Tovar et al., 1999). As observed in the field, most of the wells produced sand from the very beginning. Sand production became worse when depletion effects started to add to the in-situ effective stresses. Finally, throughout the field, some wells suffered catastrophic failure (casing collapse), while others consistently produced sand at higher levels than the specified limit of 10lbs/1000bbls (Fig. 2.1), which was initially set as the manageable limit. A comprehensive review of drilling and completion practices indicated that formation damage mainly contributed to the sanding problem, revealing that skin values > 80 were often associated with sand production. Initially, damage in these wells occurred during

drilling, as a result of fluid and solids invasion into the formation matrix. Due to rock damage, high drawdown was required to produce through the damage zone beyond the perforation, which induced sand production.

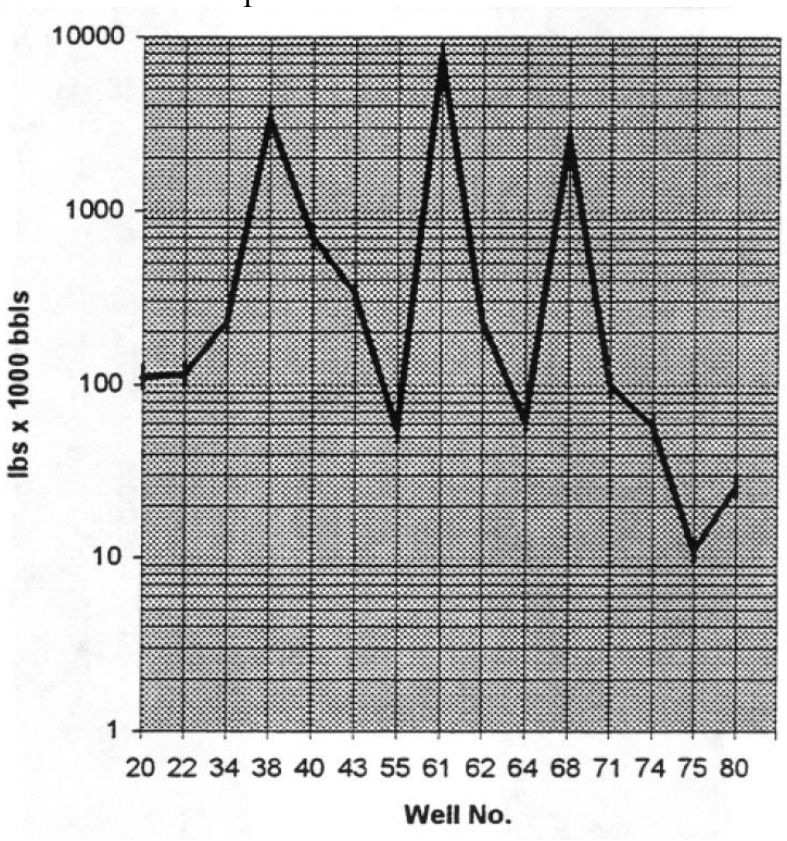

Fig. 2.1: Sand production history – Ceuta (Tovar et al., 1999)

High stresses and high initial pore pressure can be another culprit for sand failure and sand production. Vaziri (1986) stated that creation of wellbores in deep reservoirs leads to significant changes in the stress and pore pressure profile around the well cavity. The shear stresses developed and the pressure gradients established are sufficient to cause instability over a long distance beyond the stress relieved zone, giving rise to sand production. Later, Allen and Waters (1999) analyzed the early operating experience in Erskine field, and concluded that due to very high initial pressures, there would be a

tremendous decline in pore pressure over the field life. The combination of initial high stresses induced some localized formation collapse, giving rise to the production of sand. Another sand production case due to high stresses happened around the San Andreas fault in California (Morita and Boyd, 1991). Although the rock is strong and well compacted, bore-hole breakout, casing collapse, and sand problems frequently occurred in the reservoir. A wellbore stability analysis suggested that high horizontal tectonic force and high stress difference were the main reasons.

Sand failure and further production are also common in reservoirs with low rock strength and weak inter-grain cementation. Field observations in a poorly consolidated sand in Alaska shows that the amount of produced sand is significant in such reservoirs due to shear failure, while sand production due to tensile failure is sporadic and generally small in magnitude (Morita and Boyd, 1991). On the other hand, in the Marnock field, the rock is identified with an unconfined compressive strength in the range 1250 – 4500 psi, with the presence of weak chlorite cement in places (Law et al., 2000). These lead to rock failure and sand production during the early years of field life.

Fluid flow is also important in controlling sanding behavior. In contrast to traditional reservoirs where rock failure is a relatively good indicator of the onset of sanding, sand production can be delayed in some reservoirs, even if the rock is in failure mode. As seen in Table 2.1, sanding is delayed in four typical HPHT fields, and the explanation falls into two categories (Palmer et al., 2006): 1. The failed sand is held back by capillary cohesion in multi-phase flow (gas and water); 2. The failed sands are held back due to stress reduction by the arching effect. Similarly, experience in Louisiana has shown that initially sand production will occur in small and controllable bursts, which has been explained on the basis of the grain-to-grain frictional resistance and the capillary cohesion, binding the individual sand grains (Glass, 2005). This has also been confirmed in a North

Sea reservoir, which frequently shows sand production following water breakthrough, due to the loss of capillary forces (Morita and Boyd, 1991). Fig. 2.2 shows a typical set of field data for the onset of sanding with water breakthrough. However, sand production may not occur immediately with water breakthrough, as implied in Fig. 2.3.

Table 2.1 Delayed sanding in HPHT gas wells (Palmer et al., 2006)

Field	Water influx	Explanation
Tuscaloosa, onshore GOM	Sand came in with water	Sand held back by capillary cohesion
Picaroon, Shelf GOM	Sand came in with water	Sand held back by capillary cohesion
Alex, Shelf GOM	Sand came in without water	Arching above perfs reduces stress, delays sanding
Shearwater, central North Sea	Sand came in without water	Arching above perfs reduces stress, delays sanding

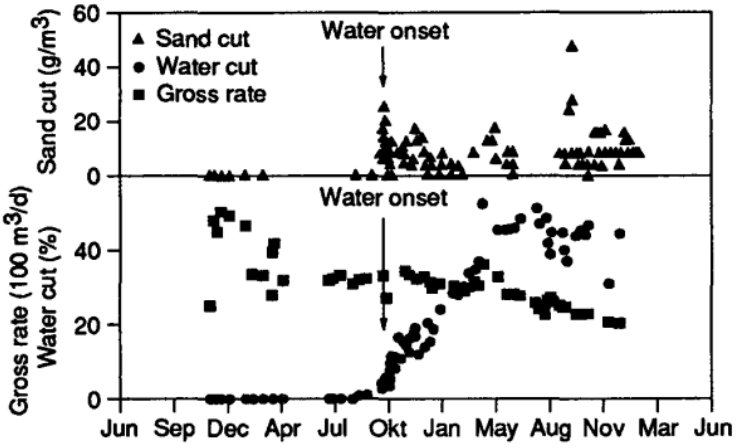

Fig. 2.2: Field record of onset of sanding with water breakthrough (Veeken et al., 1991)

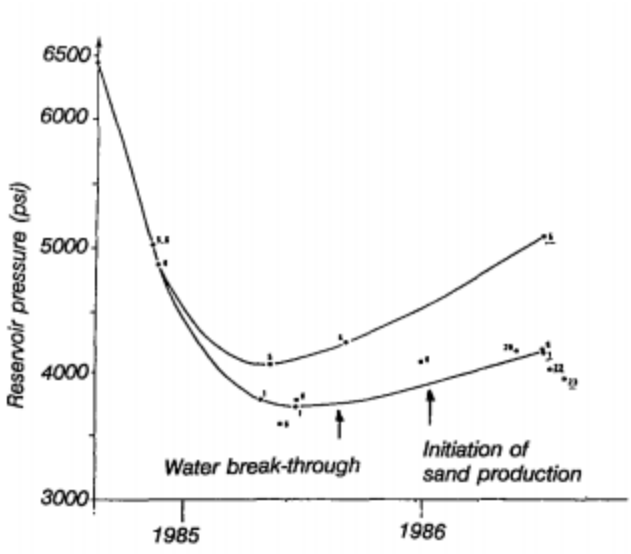

Fig. 2.3: Field record of onset of sanding after water breakthrough (Morita and Boyd, 1991)

2.2 REVIEW OF SAND PRODUCTION MECHANISMS

Sand production is identified as the result of both mechanical and fluid flow effects. The mechanical effect involves mechanical instability and degradation around the wellbore/perforation (Rahmati et al., 2013), caused by shear failure, tensile failure, or compressive failure (Wang and Sharma, 2017). This is related to stresses, rock strength (Yue et al., 2016; Yue et al., 2018), and pore pressure change. Once the rock fails, fluid erosion is applied to the degraded sands, where the hydrodynamic force, induced by fluid pressure gradients competes with gravity and any residual resistance force. The erosion process is influenced by various mechanisms (Gravanis et al., 2015), including drawdown, drawdown rate (ramp-up strategy), depletion, flow rate, water-cut, completion strategy (size, phasing, and orientation of perforations), and frequency of shut-downs and start-ups.

2.2.1 Mechanical Failure

An essential prerequisite for sand production is rock failure and degradation, which can be triggered by three types of failure: 1. Shear failure; 2. Tensile failure; 3. Compressive failure.

2.2.1.1 Shear Failure

Shear failure occurs when the shear stress exceeds the shear strength of the rock. The excessive shear stress can be generated by a large in-situ stress contrast or a large drawdown or depletion, and can result in a catastrophic quantity of produced sand (Acock et al., 2004). On the other hand, small shear strength may be caused by poor cementation in the rock, or the presence of weak planes and natural fractures.

Fig. 2.4 shows the Mohr Coulomb yield criterion for shear failure. The red line, determined by the rock cohesion and internal friction angle, represents the critical stress conditions where rock may fall in shear. Initially, when the rock is intact, the blue circle calculated by maximum and minimum stresses stays under the red line, representing the stable state. With the pore pressure decreasing due to production the Mohr circle grows larger until it reaches the red line (e.g. green circle), then the rock goes into a shear yield state. The rock will fail immediately if the post-yield period is small i.e. the rock is brittle. However, for most ductile rocks, after reaching the shear yield state, they can still sustain the stress while continuing to deform (in a plastic manner instead of elastic). In this case, shear failure will be delayed until a critical strain is reached. Fig. 2.5 illustrates the general process in a stress-strain relation for the rock. Once the rock deforms plastically, cohesion will decrease gradually, and the Mohr Coulomb yield surface will change correspondingly (right in Fig. 2.5).

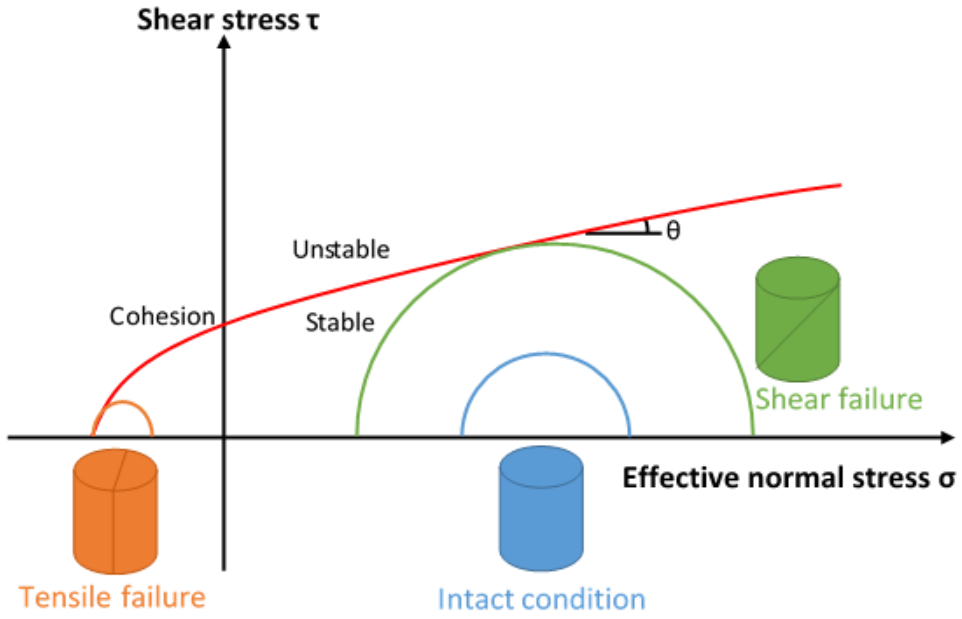

Fig. 2.4: Shear failure and tensile failure

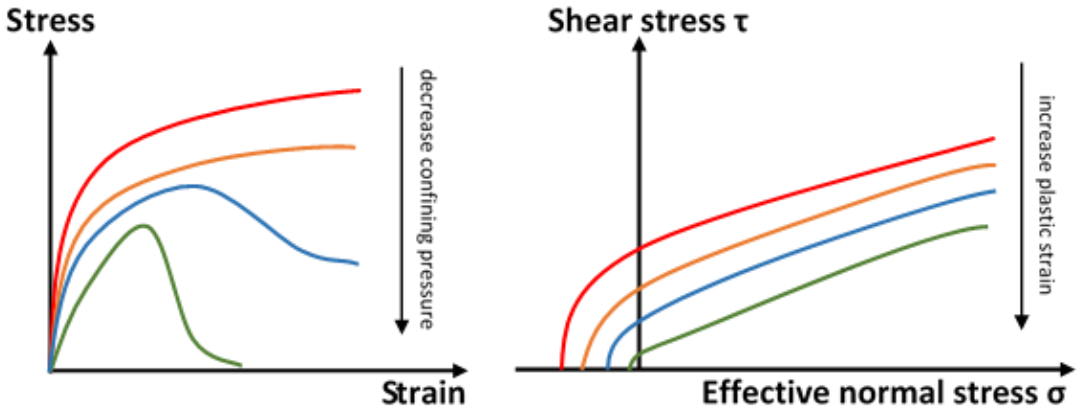

Fig. 2.5: Rock stress strain curve (left) and transient Mohr Coulomb yield surface (right)

2.2.1.2 Tensile Failure

Tensile failure is also an important reason for sand production. It typically occurs in weak sandstones, and is primarily driven by a high fluid flow rate (Acock et al., 2004). At the surface of the wellbore or perforations, the radial stress and the pore pressure are both equal to the well pressure, implying that the effective normal stress is zero. If the pore

pressure gradient is larger than the radial stress gradient at the cavity wall, the effective radial stress will become tensile, and the condition for tensile failure can be fulfilled at some point on/inside the wall (Fjar et al., 2008). However, this type of failure is usually sporadic (Acock et al., 2004), with relatively low volumes of sand, and often stabilizes with time.

2.2.1.3 Volumetric Failure

Another failure type frequently observed in both experiments and in the field is volumetric failure (Papamichos et al., 2008; Haimson and Kovacich, 2003). This is also known as pore collapse. It is associated with both drawdown and depletion, and usually occurs in high-porosity, low-strength reservoirs (Fjar et al., 2008). This failure pattern leads to the formation of a slit mode failure zone that grows from the tip of the initial shear failure zone (Fig. 2.6). As fluid flow induced erosion washes away the failed sands, the slit can grow rapidly resulting in significant sand production. Haimson and Kovacich (2003) studied this phenomenon through laboratory experiments, and concluded that the formation of such failure zones is associated with compaction bands, which are zones of localized compaction failure. Furthermore, they proposed that the length of such a slit is proportional to the stress contrast, as seen in Fig. 2.7.

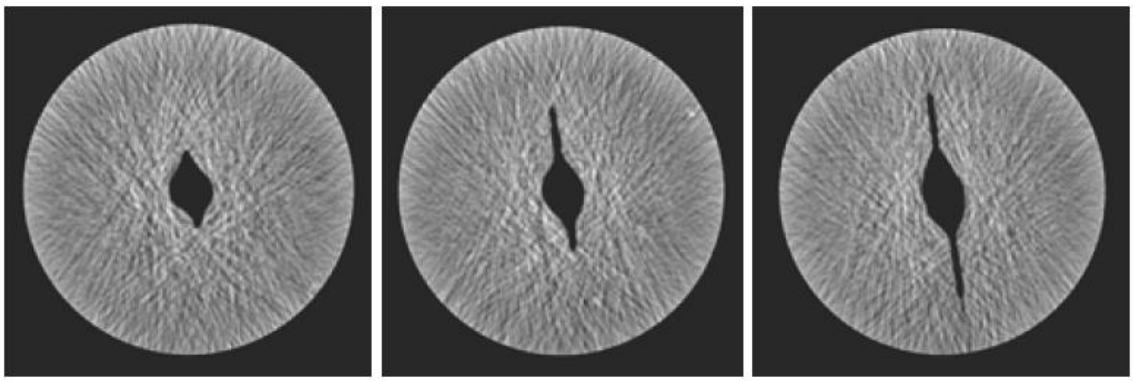

Fig. 2.6: Slit mode cavity due to volumetric failure (Papamichos et al., 2008)

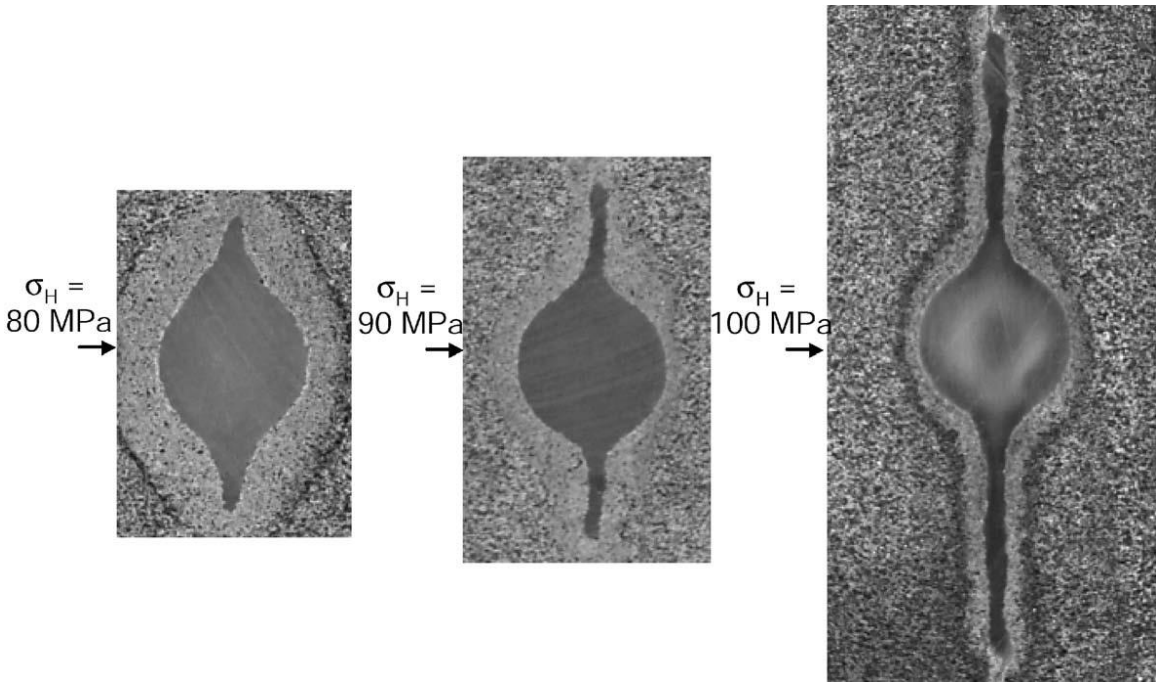

Fig. 2.7: Effect of stress contrast on slit mode cavity (Haimson and Kovacich, 2003)

2.2.2 Fluid Erosion

Besides mechanical instabilities, hydro-mechanical instabilities, due to internal and surface erosion, which are responsible for releasing and transferring particles into the wellbore and to the surface, are also important (Vardoulakis et al., 1996). Skjaerstein et al. (1997) introduced the idea that internal erosion may be related to micromechanical impacts imposed on the solid skeleton as a result of viscous shear through mobile solids in the pore network, while surface erosion may be due to the combined effect of parallel flow of a free surface and normal flow over the surface. Since hydrodynamic force in fluid flow is the primary reason for sand transport, fluid erosion and, therefore, sand production rate is related to fluid velocity, fluid viscosity, fluid density, sand shape and sand size.

2.3 RESEARCH ON SAND PRODUCTION

Sanding related researchers have been mainly focused on two aspects of the problem: experimental tests and sand production modeling. Experimental studies are usually designed to reveal the mechanisms of sanding, and provide insights into the physics that needs to be captured for modeling and operations. In addition, some researchers conducted tests to study the relation between sanding and external conditions, such as stresses, drawdown, and flow rate. On the other hand, many sand production models have been developed, from analytical solutions to empirical correlations, to complex numerical solutions. The objectives of these models are to capture the physics of sand production, and ultimately accurately predict both the onset of sanding and sand production. However, as reported, most models are only valid for certain fields and can hardly be applied to the general conditions, due to the complexity of sand production process (Rahmati et al., 2013).

2.3.1 Sand Production Experiments

Most sand production experiments are conducted using the hollow cylinder test to mimic the wellbore or perforation conditions. Fig. 2.8 shows the classic schematic of the setup for a hollow cylinder sand production test. In this test, the fluid flow rate and external stress are increased stepwise to estimate the sand production rate vs time, fluid flow rate and external stress. Results have shown that in weak sandstones, the material around a production cavity must fail mechanically by the applied stresses before it can be eroded away by fluid flow (Papamichos et al., 2001). Once the material around the cavity is removed, the sand production process may replicate with failure and erosion of newly exposed material. In addition, Papamichos et al. (2001) concluded that the sand production rate increases with both external stress and fluid flow rate.

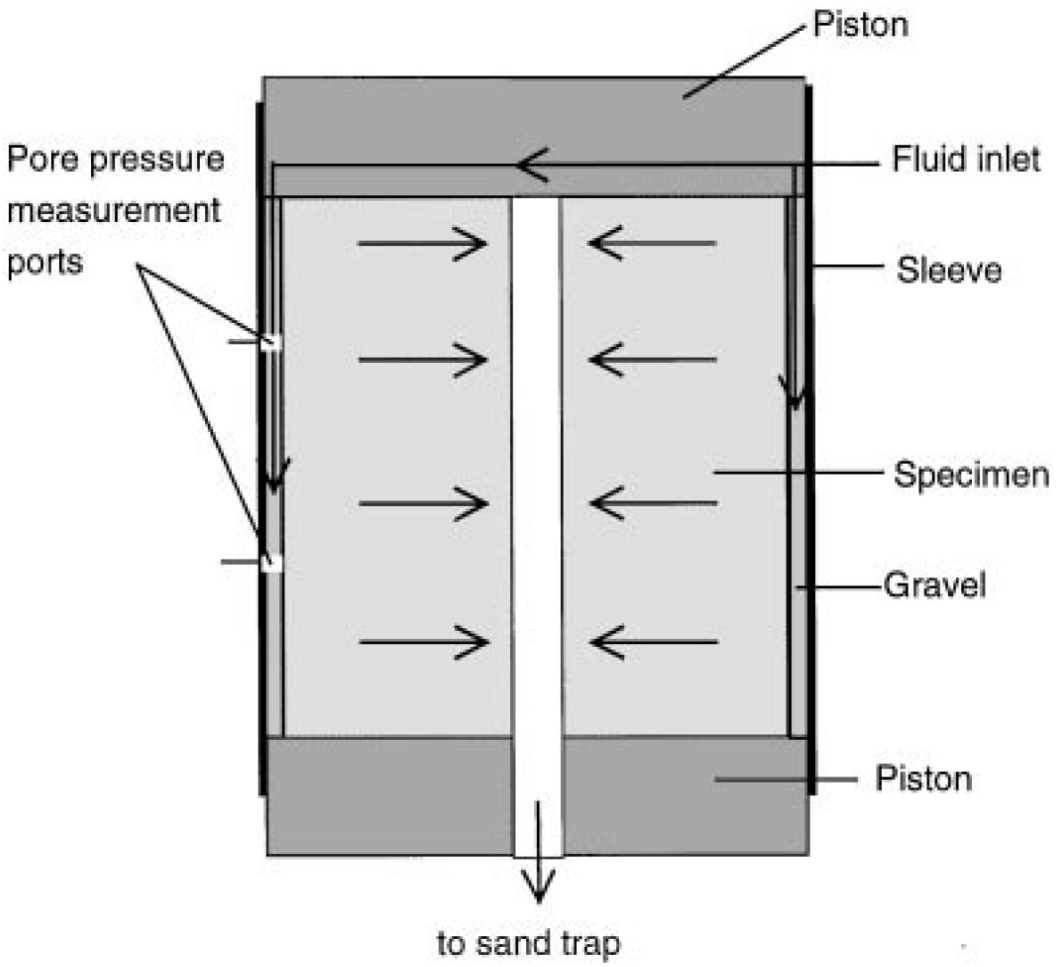

Fig. 2.8: Schematic of test setup for radial fluid flow in the sand production test with hollow cylinder specimen (Papamichos et al., 2001)

Besides the classic sand production tests to study the relation between sand production and external conditions, there are some experiments set up to qualify the distinct cavity patterns developed during sand production. Papamichos et al. (2000) quantitatively studied sand production under various flow and stress conditions. Results for isotropic stress conditions show a failure pattern that is dominated by shear failure bands with sand being produced from a localized region (left in Fig. 2.9). This failure pattern (right in Fig.

2.9) has also been observed in other experiments (Meier et al., 2013). V-Shape (Fig. 2.10) and dog-ear breakouts (Fig. 2.11) are other common cavity shapes frequently observed from experiments conducted under anisotropic stress conditions (Papamichos et al., 2008; Sinaki, 2012; Haimson, 2007; Addis et al., 1990). On the other hand, in sandstones with high porosity, a distinctive cavity shape, known as slit mode breakout (Fig. 2.6), is found in several experiments under either isotropic (Papamichos et al., 2008) or anisotropic stress conditions (Haimson and Kovacich, 2003). Haimson and Kovacich (2003) further concluded that with a higher stress contrast, a longer slit length can be obtained. These cavity shapes are induced by different failure mechanisms, and these failure mechanisms have a significant effect on both the onset of sanding and the sand production rate. Later, Wang and Sharma (2017) systematically studied these cavity patterns and illustrated the mechanisms and conditions for each distinct cavity shape.

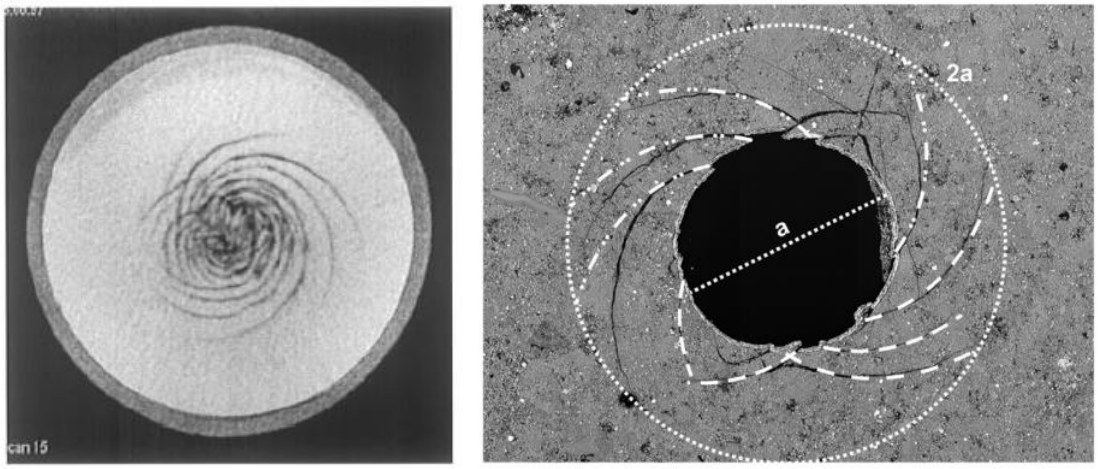

Fig. 2.9: Shear band cavity in experiments: Papamichos et al., 2000 (left) and Meier et al., 2013 (right)

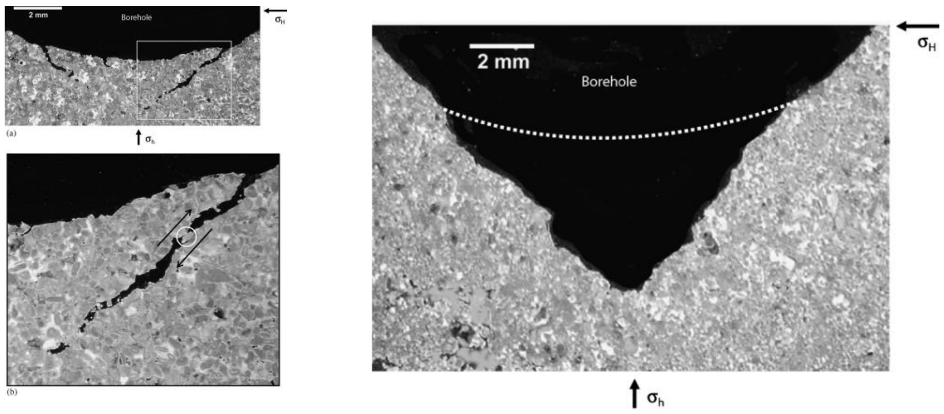

Fig. 2.10: The development of a V-shape cavity for Austin Chalk (Haimson, 2007)

Fig. 2.11: Dog-ear cavity around hole after sand production (Papamichos et al., 2008)

With more and more attention paid to the effect of fluid erosion on sand production, there are some experiments to investigate the effect of fluid flow mechanisms from the observations. Ray et al. (2014) recently tested sand production characteristics in three different sandstone outcrops under varying fluid flow conditions, and observed different sanding behavior for brine, oil and gas flow. Later, Cerasi et al. (2015) conducted a systematic series of experiments, showing higher compressive stresses are required for the

onset of sand production with compressed air flow when compared with liquid flow, as shown in Fig. 2.12. Wang et al. (2017) studied this phenomenon and concluded that in the experiment, water evaporation induced rock strengthening is the main reason for the delay of sand initiation.

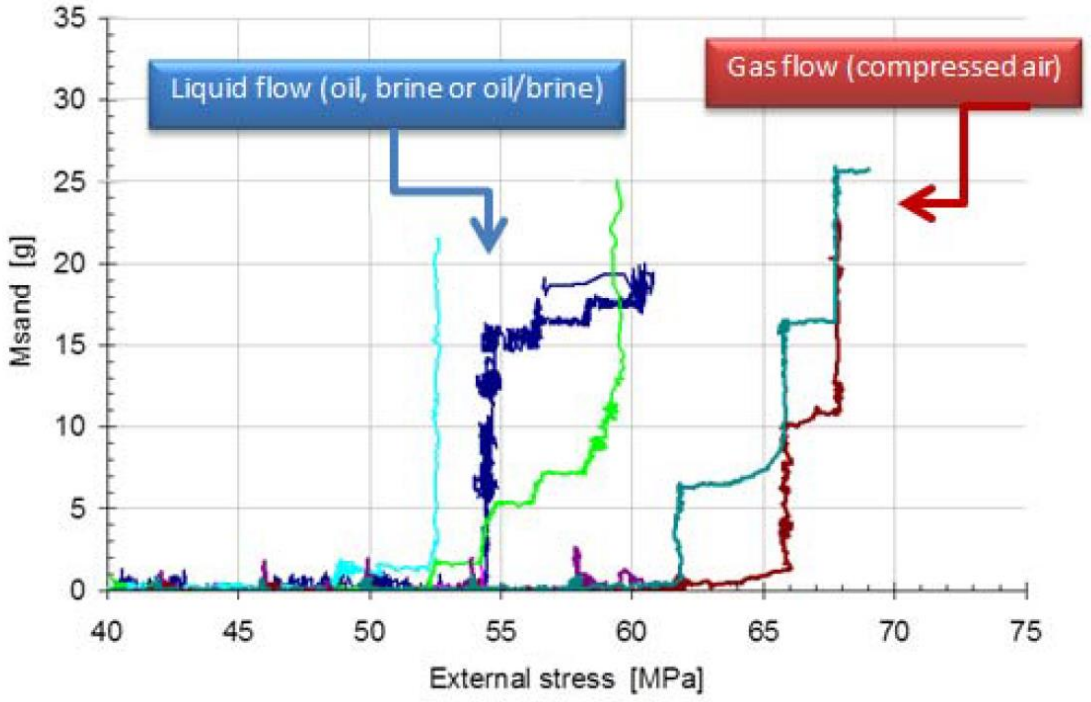

Fig. 2.12: Sand production delayed in gas flow (Cerasi et al. 2015)

2.3.2 Sand Production Models

Due to the complexity and limitation of experiments, a few sand production models have been developed to efficiently study the sanding problems and estimate sand production. These models vary from analytical solutions to empirical relationships and numerical models.

Almost all the analytical models for sand production prediction are only based on the mechanical failure of the rock. They are fast and easy to use, but only suitable to predict

the onset of sand production and have many limitations (Rahmati et al., 2013). Most of these models are only valid for capturing a single mechanism of sanding and under simplified geometrical and boundary conditions, which may not be practical and representative. Similarly, empirical relationships for sand production are valid under many assumptions and may not be applicable for different rock types and different conditions. So far, numerical models are regarded as the most powerful tools for sand production prediction, as they can overcome the above limitations.

There are two approaches in numerical models to simulate sand production. The first one is the continuum approach, where governing differential equations are derived to treat the behavior of solid and fluid continuously. This approach relies on the assumption that material properties are continuous and uniform. The second approach is the discrete element method (DEM), which is useful for helping understand sanding mechanisms, but cannot be applied to large-scale problems because of the unacceptably large computational time. Most often, the continuum approach is used for dealing with large-scale problems and predicting the onset and rate of sand production, while DEM is preferred when we want to analyze the grain scale mechanisms of sand production.

Continuum elastic models were mainly used for predicting the onset of sand production or the initiation of mechanical failure around the wellbore in the early research until Vardoulakis et al. (1996) studied the hydro-mechanical aspect of sand production based on a three-phase mixture theory. Papamichos and Stavropoulou (1998) later combined the evolution of localized deformation with hydrodynamic erosion. “Deformation localization” is a phenomenon that describes the formation of shear bands which are narrow zones of concentrated plastic deformation, and is one of the key parameters in sanding prediction models (Rahmati et al., 2013). Since then, many researchers have implemented strength hardening/softening of the sand in their models to

capture the realistic post-failure plastic behavior of rock (Papamichos et al., 2001; Vaziri et al., 2002; Nouri et al., 2006; Nouri et al., 2007; Vaziri et al., 2008; Detournay, 2009; Nouri et al., 2009; Kim and Sharma, 2011).

It is commonly accepted that sand production continuum models have two essential parts: rock failure and/or degradation and a sanding criterion. In early models the elastic brittle failure model had been implemented in sand production simulation (Nordgren, 1977; Coates and Denno, 1981; Risnes et al., 1982; Edwards et al., 1983), but elastic brittle failure rock behavior leads to excessive stress concentrations at the borehole wall, resulting in an overestimation of initial sand production. Therefore, more research was focused on elasto-plastic material models (Morita et al., 1989; Antheunis et al., 1976; Peden et al., 1986; Papamichos and Vardoulakis, 2001; Wan and Wang, 2004; Servant et al., 2006; Wang et al., 2005; Wang et al., 2006; Detournay, 2009; Wan and Wang, 2004; Vaziri et al., 2008; Nouri et al., 2003; Rahmati et al. 2012; Azadbakht et al., 2012; Wang et al., 2016; Wang and Sharma, 2016). The yield function, Mohr-Coulomb model is the most popular model used in this past work. Vaziri et al. (2002) improved the Mohr-Coulomb model with a bilinear yield function to differentiate sand behavior under low and high confining stresses. This theory was later used and described thoroughly by Nouri et al. (2009) and Jafarpour et al. (2012). Detournay (2009), on the other hand, studied the slit (or fracture-like) cavity-evolution pattern, and implemented the compaction-type failure by using a double yield cap constitutive law to capture compaction bands. This model showed that the slit mechanism developed as a combination of volumetric collapse (compaction band formation) and transport of failed material by hydrodynamic forces, and it was able to reproduce qualitatively the slit mode of cavity evolution observed in laboratory settings.

Sanding criteria are normally based on shear failure, tensile failure, compressional failure, critical pressure gradient, critical drawdown pressure, critical plastic strain or

erosion criteria (Rahmati et al., 2013). Tensile failure is recognized as the primary mechanism for rock degradation, and is proposed as the criterion for sand production. Shear failure, on the other hand, is the dominant mechanism in cemented sands, and can be combined with tensile failure as the sanding criteria (Crook et al., 2003; Morita et al., 1989). Compressional failure may happen during large reservoir pressure depletion and pore collapse, where plastic volumetric compression forms and sand may produce. It is more dominant in highly porous weak materials where void spaces are easy to collapse under high loading. Weingarten and Perkins (1995) also took pressure gradient into account for sanding criteria. Burton et al. (1998) further involved maximum plastic strain in their model.

Application of conventional, shear-failure based models is shown to be overly conservative in capturing the onset of sanding (Vaziri et al., 2002), as can be seen in Fig. 2.13. This is because for a given rock strength, failure is hastened in high stress and pressure systems. The early failure of rock makes the difference between sand failure and sand production more pronounced relative to normally-pressured systems, where more experience has been available and apparently better correspondence between field and predictions have been observed.

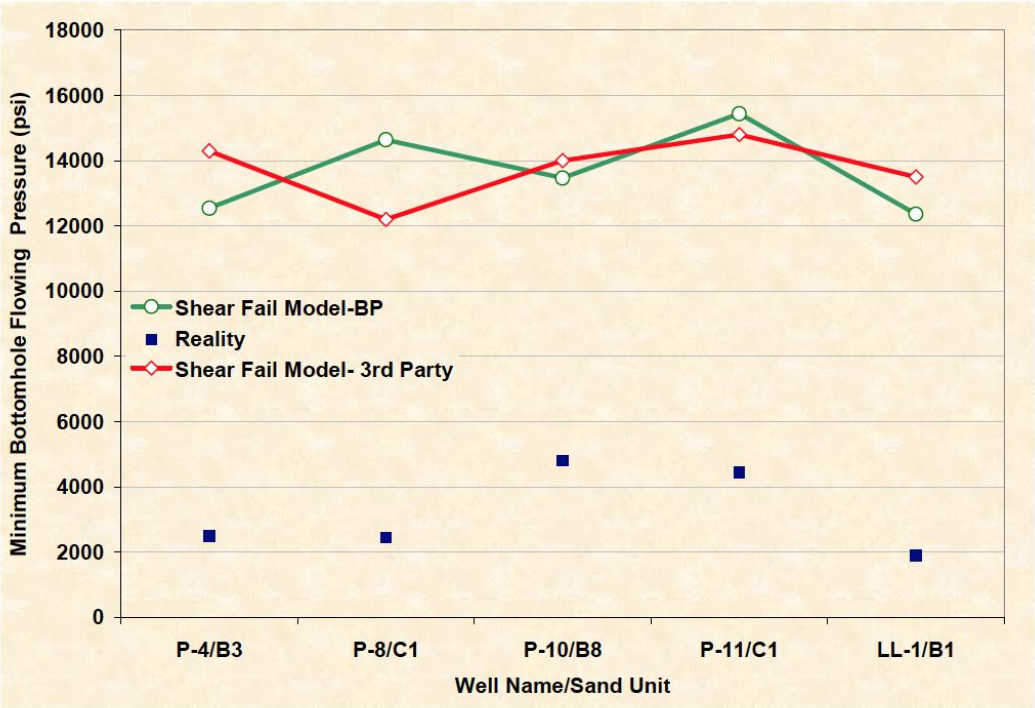

Fig. 2.13: Overestimation of the onset of sanding using shear-failure based model (Vaziri et al., 2002)

Thus, sand internal and surface erosion due to dynamic seepage drag forces are also important in sand production because they may release and transport sand particles. Most models are concentrated on surface erosion criterion. Radial flow (Vadoulakis et al., 1996) and axial flow (Vadoulakis et al., 2001) were tested as erosion progresses could be observed with time. Papamichos et al. (2001) developed a hydro-mechanical model by coupling the poro-mechanical behavior of the solid-fluid system with the erosion behavior of the solids due to fluid flow, and extended their work (2005) with a porosity diffusion law to show that the sand rate decreases with time until process of erosion zone enlargement takes place, which is in consistent with experimental and field data.

REFERENCES

Acock, A., T. ORourke, D. Shirmboh, J. Alexander, G. Andersen, T. Kaneko, A. Venkitaraman, J. López-de Cárdenas, M. Nishi, M. Numasawa. and K. Yoshioka. 2004. Practical approaches to sand management. *Oilfield Rev, 16(1),* pp.10-27.

Addis, M. A., N. R. Barton, S. C. Bandis, and J. P. Henry. 1990. Laboratory studies on the stability of vertical and deviated boreholes. *In SPE Annual Technical Conference and Exhibition.*

Allen, R. F. and M. Walters. 1999. Erskine Field: Early Operating Experience. *Offshore Europe Oil and Gas Exhibition and Conference.*

Antheunis, D., P. Vriezen, B. Schipper, and A. Van der Vlis. 1976. Perforation collapse: failure of perforated friable sandstones. *Paper presented at the SPE European Spring Meeting.*

Azadbakht, S., M. Jafarpour, H. Rahmati, A. Nouri, H. Vaziri, and D. Chan. 2012. A numerical model for predicting the rate of sand production in injector wells. *Paper presented at the SPE Deepwater Drilling and Completions Conference.*

Burton, R. C., E. R. Davis, and N. Morita. 1998. Application of Reservoir Strength Characterization and Formation Failure Modeling to Analyze Sand Production Potential and Formulate Sand Control Strategies for a Series of North Sea Gas Reservoirs. *Society of Petroleum Engineers*. doi:10.2118/48979-MS .

Cerasi, P., A. Berntsen, L. E. Walle, and E. Papamichos. 2015. Sand production delay in gas flow experiments. *Paper presented at the 49th US Rock Mechanics Symposium, San Francisco, CA, USA, June 2015.*

Coates, G. R. and S. A. Denoo. 1981. Mechanical properties program using borehole analysis and mohr's circle. *In Proceedings of the 22nd Annual Logging Symposium.*

Crook, T., S. Willson, J. G. Yu, and R. Owen. 2003. Computational modelling of the localized deformation associated with borehole breakout in quasi-brittle materials. *Journal of Petroleum Science and Engineering, 38*(3-4), 177-186. doi: 10.1016/s0920-4105(03)00031-7.

Detournay, C. 2009. Numerical modeling of the slit mode of cavity evolution associated with sand production. *SPE Journal,* 14(04), 797-804.

Edwards, D. P., Y. Sharma, and A. Charron. 1983. Zones of sand production identified by log-derived mechanical properties: a case study. *In Proceedings of the 8th European Formation Evaluation Symposium*.

Elliott, G. S., R. A. Brockman, and R. M. Shivers. 1995. HPHT drilling and completion design for the Erskine field. *Offshore Europe Conference.*

Fjar, E., R. M. Holt, A. M. Raaen, R. Risnes, and P. Horsrud. 2008. *Petroleum related rock mechanics*. Vol. 53. Elsevier, 2008.

Glass, A. W. 2005. High pressure, high temperature developments in the United Kingdom Continental Shelf. *Research report 409.*

Gravanis, E., E. Sarris, and P. Papanastasiou. 2015. Hydro-mechanical erosion models for sand production. *International Journal for Numerical and Analytical Methods in Geomechanics* 39.18 (2015): 2017-2036.

Haimson, B. 2007. Micromechanisms of borehole instability leading to breakouts in rocks. *International Journal of Rock Mechanics and Mining Sciences,* 44(2), 157-173.

Haimson, B. and J. Kovacich. 2003. Borehole instability in high-porosity Berea sandstone and factors affecting dimensions and shape of fracture-like breakouts. *Engineering Geology,* 69(3), 219-231.

Jafarpour, M., H. Rahmati, S. Azadbakht, A. Nouri, D. Chan, and H. Vaziri. 2012. Determination of mobilized strength properties of degrading sandstone. *Soils and Foundations, 52*(4), 658-667. doi: 10.1016/j.sandf.2012.07.007.

Kim, S. H., M. M. Sharma, and H. J. Fitzpatrick. 2011. A Predictive model for sand production in poorly consolidated sands. *Paper presented at the International Petroleum Technology Conference.*

Law, D., A. S. Dundas, and D.J. Reid. 2000. HPHT Horizontal Sand Control Completion. In *SPE/CIM International Conference on Horizontal Well Technology*.

Meier, T., E. Rybacki, A. Reinicke, and G. Dresen. 2013. Influence of borehole diameter on the formation of borehole breakouts in black shale. *International Journal of Rock Mechanics and Mining Sciences, 62,* 74-85.

Morita, N. and P. A. Boyd. 1991. Typical sand production problems case studies and strategies for sand control. *SPE Annual Technical Conference and Exhibition.*

Morita, N., D. Whitfill, I. Massie, and T. Knudsen. 1989. Realistic sand-production prediction: numerical approach. *SPE production engineering,* 4(01), 15-24.

Nordgren, R. P. 1977. Strength of well completions. *In Proceedings of the 18th US Symposium on Rock Mechanics*.

Nouri, A., E. Kuru, and H. Vaziri. 2007. Enhanced modelling of sand production through improved deformation and stress analysis. *Paper presented at the Canadian International Petroleum Conference.*

Nouri, A., E. Kuru, and H. Vaziri. 2009. Elastoplastic modelling of sand production using fracture energy regularization method. *Journal of Canadian Petroleum Technology*, 48(4), 64-71.

Nouri, A., H. Vaziri, H. A. Belhaj, and M. R. Islam. 2006. Sand-production prediction: a new set of criteria for modeling based on large-scale transient experiments and numerical investigation. *SPE Journal, 11*(02), 227-237.

Palmer, I. D., N. Higgs, I. Ispas, K. Baksh, and K.O. Krieger. 2006. Prediction of sanding using oriented perforations in a deviated well, and validation in the field. *In SPE International Symposium and Exhibition on Formation Damage Control.*

Papamichos, E. and M. Stavropoulou. 1998. An erosion-mechanical model for sand production rate prediction. *International Journal of Rock Mechanics and Mining Sciences, 35*(4), 531-532.

Papamichos, E., A. Skjærstein, and J. Tronvoll. 2000. A volumetric sand production experiment. *Paper presented at the 4th North American Rock Mechanics Symposium. American Rock Mechanics Association, 2000.*

Papamichos, E., I. Vardoulakis, J. Tronvoll, and A. Skjaerstein. 2001. Volumetric sand production model and experiment. *International Journal for Numerical and Analytical Methods in Geomechanics*, 25(8), 789-808. doi: 10.1002/nag.154

Papamichos, E., J. Stenebraten, P. Cerasi, A. Lavrov, I. Vardoulakis, G.F. Fuh, M. Brignoli, Goncalves CJ de Castro, and O. Havmoller. 2008. Rock type and hole failure pattern effects on sand production. *Paper presented at the 42th US Rock Mechanics Symposium and 2th US-Canada Rock Mechanics Symposium, San Francisco, CA, USA, June 2008.*

Peden, J., and A. Yassin. 1986. The determination of optimum completion and production conditions for sand-free oil production. *Paper presented at the SPE Annual Technical Conference and Exhibition.*

Rahmati, H., A. Nouri, H. Vaziri, and D. Chan. 2012. Validation of predicted cumulative sand and sand rate against physical-model test. *Journal of Canadian Petroleum Technology,* 51(5), 403-410.

Rahmati, H., M. Jafarpour, S. Azadbakht, A. Nouri, H. Vaziri, D. Chan, and Y. Xiao. 2013. Review of Sand Production Prediction Models. *Journal of Petroleum Engineering*, 2013, 1-16. doi: 10.1155/2013/864981.

Ray, P., M. Rijken, J. Cameron, C. Jones, and A. EI-Fayoumi. 2014. Estimating sand production volume in Oil and Gas Reservoir. *Paper presented at the SPE Annual Technical Conference and Exhibition, Amsterdam, The Netherlands, October 2014.*

Risnes, R., R. K. Bratili, and P. Horsrud. 1982. Sand stresses around a wellbore. *SPE Journal*, vol. 22, no. 6, pp. 883–898, 1982.

Servant, G., P. Marchina, Y. Peysson, E. Bemer, and J. F. Nauroy. 2006. Sand erosion in weakly consolidated reservoirs: experiments and numerical modeling. *Paper presented at the SPE/DOE Symposium on Improved Oil Recovery.*

Sinaki, A. R. Y. 2012. Sand production simulation under true-triaxial stress conditions.

Skjaerstein, A., M. Stavropoulou, I. Vardoulakis, and J. Tronvoll. 1997. Hydrodynamic erosion: A potential mechanism of sand production in weak sandstones.

International journal of Rock Mechanics and Mining Sciences, vol. 34, no. 3-4, pp 292.el-292.e18.

Tovar, J. J., L. Zerpa, and E. Guerra. 1999. Impact of formation damage on sand production in Deep Eocene Reservoirs, Lake Maracaibo, Venezuela: A case history. *European formation damage conference.*

Vardoulakis, I., M. Stavropoulou, and P. Papanastasiou. 1996. Hydro-mechanical aspects of the sand production problem. *Transport in porous media*, *22*(2), 225-244.

Vaziri, H., A. Nouri, K. A. Hovem, and X. Wang. 2008. Computation of sand production in water injectors. *SPE Production & Operations, 23*(04), 518-524.

Vaziri, H., B. Barree, Y. Xiao, I. Palmer, and M. Kutas. 2002. What is the magic of water in producing sand? *Paper presented at the SPE Annual Technical Conference and Exhibition.*

Vaziri, H., Y. Xiao, and I. Palmer. 2002. Assessment of several sand prediction models with particular reference to HPHT wells. *Paper presented at the SPE ISRM Rock Mechanics Conference, Irving, TX*.

Vaziri, H. 1986. Mechanics of fluid and sand production from oil sand reservoirs. *Annual Technical Meeting. Petroleum Society of Canada.*

Veeken, C. A. M., D. R. Davies, C. J. Kenter, and A. P. Kooijman. 1991. Sand production prediction review: developing an integrated approach. *In SPE annual technical conference and exhibition.*

Wan, R. and J. Wang. 2004a. Analysis of sand production in unconsolidated oil sand using a coupled erosional-stress-deformation model. *Journal of Canadian Petroleum Technology,* 43(2), 47-53.

Wan, R. and J. Wang. 2004b. Modelling of sand production and wormhole propagation in an oil saturated sand pack using stabilized finite element methods. *Journal of Canadian Petroleum Technology,* 43(4), 45-52.

Wang, H. and M. M. Sharma. 2016. A fully 3-D, multi-phase, poro-elasto-plastic model for sand production. *In SPE Annual Technical Conference and Exhibition. Society of Petroleum Engineers, 2016.*

Wang, H. and M. M. Sharma. 2017. The Role of Elasto-Plasticity in Cavity Shape and Sand Production in Oil and Gas Wells. *In SPE Annual Technical Conference and Exhibition. Society of Petroleum Engineers, 2017.*

Wang, H., D. P. Gala, and M. M. Sharma. 2017. Effect of Fluid Type and Multi-Phase Flow on Sand Production in Oil and Gas Wells. *In SPE Annual Technical Conference and Exhibition. Society of Petroleum Engineers, 2017.*

Wang, H., P. Cardiff, and M. M. Sharma. 2016. A 3-D poro-elasto-plastic model for sand production around open-hole and cased & perforated wellbores. *Paper presented at 50th US Rock Mechanics Symposium, Houston, Texas, USA, June 2016.*

Wang, J., D. Walters, A. Settari, and R. Wan. 2006. An integrated modular approach to modeling sand production and cavity growth with emphasis on the multiphase flow and 3D effects. *Paper presented at the Proceedings of the 41st US Symposium on Rock Mechanics Symposium.*

Wang, J., R. Wan, A. Settari, and D. Walters. 2005. Prediction of volumetric sand production and wellbore stability analysis of a well at different completion schemes. *Paper presented at the Alaska Rocks 2005 Proceedings of the 40th US Symposium on Rock Mechanics.*

Weingarten, J. and T. Perkins. 1995. Prediction of sand production in gas wells: methods and Gulf of Mexico case studies. *Journal of Petroleum Technology,* 47(07), 596-600.

Yue, K., J. E. Olson, and R. A. Schultz. 2016. Calibration of stiffness and strength for layered rocks. *Presented at the 50th US Rock Mechanics/Geomechanics Symposium, Houston, Texas, June 26–29, 2016.*

Yue, K., J. E. Olson, and R. A. Schultz. 2018. Layered modulus effect on fracture modeling and height containment. *Presented at the Unconventional Resources Technology Conference, Houston, Texas, July 23–25, 2018.*

Chapter 3: Development of A Poro-Elasto-Plastic Model for Single Phase and Multi-Phase Fluid Flow

3.1 INTRODUCTION

Sand production is a coupled problem in which both geomechanics and fluid flow play an important role. Effective stresses and rock properties determine the deformation and mechanical failure of rock, while the pressure gradient of the fluid is crucial for sand erosion. Therefore, a coupled geomechanical - fluid flow model is necessary for predicting effective stresses and pressure transients around the wellbore/perforations. Most poorly consolidated sands usually appear to be ductile, with large plastic deformation. Most current models assume linear elastic behavior. In this study, a Mohr-Coulomb based plastic model is implemented to account for plasticity after rock yielding. To sustain the validity of continuum mechanics a suitable stress return algorithm is applied once the stress state exceeds the Mohr-Coulomb yield envelop. Plastic strain is calculated based on these corrected stresses.

For continuum mechanics, the classic poro-elasto-plastic problem can be solved numerically using one of three related methods: Finite Difference Methods (FDM), Finite Element Methods (FEM) and Finite Volume Methods (FVM). In FDM, partial differential equations (PDEs) for displacement and fluid pressure are derived in differential forms, discretized by a topologically square grid and approximated by the application of a local Taylor expansion (Peiró and Sherwin, 2005). FDM demonstrates its reliability and accuracy when dealing with poro-elasto-plastic problems with simple geometries (FLAC3D®), however, this method is limited when handling complex geometries in multiple dimensions. This issue motivates the application of an integral form of the PDEs such as that used in FEM and FVM. FEM is widely used in engineering sciences, especially stress analysis, due to its flexibility in handling material inhomogeneity and anisotropy,

complex geometries and boundary conditions and dynamic problems (Jing, 2003). The disadvantage of FEM includes the increased complexity in the mathematics for the formulations and the handling of computationally expensive numerical integrations. FVM incorporates most of the advantages of FEM, while the implementation from both a mathematical and programing perspectives is relatively straightforward, and thus will be adopted in this work.

3.2 MATHEMATICAL MODEL

To derive the general poro-elasto-plastic equations, we start with Biot's poro-elastic theory (Detournay and Cheng, 1993) and couple it with the Mohr-Coulomb plasticity model (Vermeer and De Borst, 1984). A tension positive sign convention is used.

3.2.1 Coupled Single Phase Fluid Flow and Elasto-Plasticity Model

3.2.1.1 Poro-Elastic Formulation

The constituents in the reservoir include two parts: solid and fluid. We have different governing equations for these two constituents. For the solid constituent, a momentum balance in the form of Cauchy's equation yields

$$\frac{\partial^2(\rho u)}{\partial t^2} = \nabla \cdot \sigma + F \tag{3.1}$$

Total stress, σ, follows a constitutive law and can be expressed as

$$\sigma = 2G\varepsilon + \lambda tr(\varepsilon)I - \alpha pI \tag{3.2}$$

The strain tensor, ε, in Eq. (3.2) is defined in terms of the displacement vector as,

$$\varepsilon = \frac{1}{2}[\nabla u + (\nabla u)^T] \tag{3.3}$$

By incorporating Eqs. (3.2) and (3.3) to Eq. (3.1), we obtain the governing equation for the solid constituent:

$$\frac{\partial^2(\rho u)}{\partial t^2} = \nabla \cdot [G\nabla u + G(\nabla u)^T + \lambda I tr(\nabla u)] - \alpha \nabla p + F \tag{3.4}$$

Eq. (3.4) represents the rock deformation caused by either a mechanical boundary force or a fluid pressure change. The LHS of Eq. (3.4) is the time derivative of rock displacement, which is relatively small when compared with the pressure transient for a poro-elastic material. However, if plasticity is considered and the transient period of plastic deformation (such as strain localization) is of interest, this term may not be neglected. The governing equation shown above takes the poro-elastic effect into account, thus the effective stress can be affected by not only the magnitude of fluid pressure change but also the pressure gradient in the reservoir.

For the fluid constituent, the continuity equation is written as,

$$\frac{\partial(\phi \rho_f)}{\partial t} + \nabla \cdot (q \rho_f) = 0 \tag{3.5}$$

The relation between flow rate and fluid pressure obeys Eq. (3.6) if we assume Darcy's law for single phase fluid flow in the reservoir.

$$q = \frac{k}{\mu} \nabla (p - \rho_f g h) \tag{3.6}$$

Next, the constitutive equation for the fluid can be expressed as,

$$p = M(\phi - \alpha \varepsilon_b) \tag{3.7}$$

Where M is the Biot Modulus.

For an ideal porous medium,

$$M = \frac{K_f}{\phi + (\alpha - \phi)(1 - \alpha)\frac{K_f}{K}} \tag{3.8}$$

If the solid grains are assumed to be incompressible, M can be further simplified as

$$M = \frac{K_f}{\phi} \tag{3.9}$$

Where Kf is the inverse of the fluid compressibility,

$$K_f = \frac{\Delta p}{\frac{\Delta V_f}{V_f}} \tag{3.10}$$

For a compressible fluid (e.g. a non-ideal gas), we have the equation of state

$$pV = ZRT \tag{3.11}$$

By substituting Eqs. (3.6), (3.7), and (3.11) into Eq. (3.5), we obtain the governing equation for a non-ideal gas as,

$$\frac{\partial}{\partial t}\left[\left(\frac{p}{M} + \alpha\varepsilon_b\right)\frac{p}{Z}\right] - \frac{k}{\mu}\nabla \cdot \left[\frac{p}{Z}\nabla\left(p - \frac{p}{ZRT}gh\right)\right] = 0 \tag{3.12}$$

For an incompressible fluid, the fluid density is constant, then Eq. (3.12) can be simplified as,

$$\frac{\partial p}{\partial t} + \alpha M\frac{\partial \varepsilon_b}{\partial t} - \frac{k}{\mu}M\nabla^2 p + \frac{k}{\mu}M\nabla^2\left(\rho_f gh\right) = 0 \tag{3.13}$$

In the above two governing equations, the mechanical effect on fluid flow is incorporated into the volumetric strain change, which results from the rock deformation (from Eq. (3.4)). During oil/gas production, as effective stress increases around wellbore/perforations, the pore volume reduces the volumetric strain increases, leading to a competing effect on fluid pressure.

The two set of governing equations, Eq. (3.4) and Eq. (3.12)/(3.13), are coupled and solved to obtain displacement and fluid pressure for a single phase poro-elastic reservoir.

3.2.1.2 Poro-Elasto-Plastic Formulation

When plasticity is taken into account, the fluid flow governing equation remains the same as Eq. (3.12) or Eq. (3.13). However, the governing equation for the stress-strain constitutive law is different. For elasticity, the constitutive law is formed with the total

components of stress and strain. This has also been used in some plasticity theories, called deformation theories of plasticity (Khan and Huang, 1995). Nevertheless, this approach cannot be used once the stress-strain relation is non-unique, such as unloading or strain softening (Chen and Baladi, 1985). Since plastic deformation is dependent on the loading path, it is necessary to integrate the incremental stress-strain relation along the loading path to obtain the final state of deformation (Khan and Huang, 1995). Therefore, the incremental form of the stress-strain constitutive equation is implemented in this work. This relation is shown below:

$$d\sigma = 2Gd\varepsilon + \lambda tr(d\varepsilon)I - \alpha dpI \tag{3.14}$$

Where the incremental total strain is composed of incremental elastic strain and incremental plastic strain,

$$d\varepsilon = d\varepsilon_e + d\varepsilon_p \tag{3.15}$$

Substituting Eqs. (3.14) and (3.15) into Eq. (3.1) and rearranging, we obtain the governing equation for rock deformation for a poro-elasto-plastic medium,

$$\frac{\partial^2(\rho u)}{\partial t^2} = \nabla \cdot [G\nabla du + G(\nabla du)^T + \lambda Itr(\nabla du)] - \nabla \cdot \left[2G\left(d\varepsilon_p\right) + \lambda Itr\left(d\varepsilon_p\right)\right] + \nabla \cdot (\sigma^{old} - \alpha pI) + F \tag{3.16}$$

Eq. (3.16) and Eq. (3.12)/(3.13) are fully coupled and solved to obtain incremental displacement and fluid pressure for single phase, poro-elasto-plastic reservoir. Note that the incremental plastic strain is also an unknown in Eq. (3.16), and it will be solved separately using a stress return algorithm (discussed later).

3.2.2 Coupled Multi-Phase Fluid Flow and Elasto-Plastic Model

3.2.2.1 Black-Oil Model

In this section, a black-oil multi-phase fluid flow model is coupled with the elasto-plastic model. Multi-phase fluids, water, gas and oil, are assumed as immiscible and

slightly compressible fluids and flow in the reservoir (Wang and Sharma, 2016; Bhardwaj et al., 2016).

Starting with the mass balance for water coupled with rock deformation, we have

$$\frac{d(\phi S_w \rho_w)}{dt} + \nabla \cdot (\rho_w v_w) + S_w \rho_w \nabla \cdot (v_s) = 0 \tag{3.17}$$

For the first term on the LHS, we can write it as,

$$\frac{d(\phi S_w \rho_w)}{dt} = \phi S_w \frac{d\rho_w}{dt} + \phi \rho_w \frac{dS_w}{dt} + S_w \rho_w \frac{d\phi}{dt} \tag{3.18}$$

For slightly compressible fluid, the time derivative of density is represented in terms of pressure as,

$$\frac{d\rho_w}{dt} = \rho_w c_w \frac{dp_w}{dt} \tag{3.19}$$

Recall the definitions of rock compressibility and multi-phase fluid pressure (composed of both water and oil pressure)

$$c_R = \frac{1}{\phi}\frac{d\phi}{dp} \tag{3.20}$$

$$p = S_o p_o + S_w p_w \tag{3.21}$$

The time derivative of porosity then can be written as

$$\frac{d\phi}{dt} = \frac{d\phi}{dp}\frac{dp}{dt} = c_R \phi \frac{d(S_o p_o + S_w p_w)}{dt} \tag{3.22}$$

By taking Eqs. (3.18), (3.19) and (3.22) into Eq. (3.17), dividing water density, and neglecting the term $v_w \nabla \cdot (\rho_w)$ (since the square of the pressure gradient is very small), we arrive at the mass balance equation for water,

$$\phi S_w c_w \frac{dp_w}{dt} + \phi \frac{dS_w}{dt} + \phi S_w c_R \frac{d(S_o p_o + S_w p_w)}{dt} + \nabla \cdot (v_w) + S_w \nabla \cdot (v_s) = 0 \tag{3.23}$$

Similarly, the mass balance equation for oil can be expressed as

$$\phi S_o c_o \frac{dp_o}{dt} + \phi \frac{dS_o}{dt} + \phi S_o c_R \frac{d(S_o p_o + S_w p_w)}{dt} + \nabla \cdot (v_o) + S_o \nabla \cdot (v_s) = 0 \quad (3.24)$$

For two phase fluid flow, $S_w + S_o = 1$. Then the summation of Eqs. (3.23) and (3.24) becomes

$$\phi S_w c_w \frac{dp_w}{dt} + \phi S_o c_o \frac{dp_o}{dt} + \phi c_R \frac{d(S_o p_o + S_w p_w)}{dt} + \nabla \cdot (v_w) + \nabla \cdot (v_w) + \nabla \cdot (v_s) = 0 \quad (3.25)$$

Eq. (3.25) can be further rearranged by applying capillary pressure ($p_c = p_o - p_w$) and assuming that capillary pressure is a function of water saturation ($p_c = p_c^0 \left(1 - \frac{S_w - S_{wr}}{1 - S_{wr} - S_{or}}\right)^{Epc}$)

$$\phi(c_R + S_w c_w + S_o c_o) \frac{dp_o}{dt} - \phi \left[(c_R + c_w) S_w \frac{\partial p_c}{\partial S_w} + c_R p_c\right] \frac{dS_w}{dt} + \nabla \cdot (v_w) + \nabla \cdot (v_w) + \nabla \cdot (v_s) = 0 \quad (3.26)$$

In order to eliminate the time derivative of water saturation in Eq. (3.26), we recall Eq. (3.24) for water saturation

$$\begin{aligned} \phi \frac{dS_w}{dt} &= \phi S_o c_o \frac{dp_o}{dt} + \phi S_o c_R \frac{d(S_o p_o + S_w p_w)}{dt} + \nabla \cdot (v_o) + S_o \nabla \cdot (v_s) \\ &= \phi S_o (c_R + c_o) \frac{dp_o}{dt} - \phi S_o c_R \left(S_w \frac{\partial p_c}{\partial S_w} + p_c\right) \frac{dS_w}{dt} + \nabla \cdot (v_o) + S_o \nabla \cdot (v_s) \\ &= \frac{\phi S_o (c_R + c_o) \frac{dp_o}{dt} + \nabla \cdot (v_o) + S_o \nabla \cdot (v_s)}{1 + S_o c_R \left(S_w \frac{\partial p_c}{\partial S_w} + p_c\right)} \end{aligned} \quad (3.27)$$

Taking the above equation to Eq. (3.26), we obtain the oil pressure equation as

$$\phi c_t \frac{dp_o}{dt} - \left[(c_R + c_w) S_w \frac{\partial p_c}{\partial S_w} + c_R p_c\right] \left[\frac{\phi S_o (c_R + c_o) \frac{dp_o}{dt} + \nabla \cdot (v_o) + S_o \nabla \cdot (v_s)}{1 + S_o c_R \left(S_w \frac{\partial p_c}{\partial S_w} + p_c\right)}\right]$$

$$+ \nabla \cdot (v_w) + \nabla \cdot (v_w) + \nabla \cdot (v_s) = 0 \quad (3.28)$$

Where the total compressibility c_t is defined as

$$c_t = c_R + S_w c_w + S_o c_o \tag{3.29}$$

Next, we assume Darcy flow for oil/water in the reservoir

$$v_i = -\frac{kk_{ri}}{\mu_i}(\nabla p_i - \rho_i g) = -\lambda_i(\nabla p_i - \rho_i g) \tag{3.30}$$

Where i represents the oil or water phase. The relative permeability for each phase is calculated by a Brooks and Corey model (Brooks and Corey, 1964). The final saturation equation for water phase can be written as

$$\phi\frac{dS_w}{dt} = \frac{\phi(c_R + c_o)(1 - S_w)}{1 + A_{cap}}\frac{dp_o}{dt} - \frac{1}{1 + A_{cap}}\nabla \cdot [\lambda_o(\nabla p_o - \rho_o g)] + \frac{1 - S_w}{1 + A_{cap}}\frac{\partial(\nabla \cdot u)}{\partial t} \tag{3.31}$$

Where

$$A_{cap} = c_R(1 - S_w)\left(S_w B_{cap} + p_c\right) \tag{3.32}$$

$$B_{cap} = \frac{\partial p_c}{\partial S_w} \tag{3.33}$$

The final pressure equation for the oil phase can be expressed as,

$$\left[\phi c_t - \frac{\phi(c_R + c_o)(1 - S_w)C_{cap}}{1 + A_{cap}}\right]\frac{dp_o}{dt} - \left(1 - \frac{C_{cap}}{1 + A_{cap}}\right)\nabla \cdot [\lambda_o(\nabla p_o - \rho_o g)] - \nabla \cdot \left[\lambda_w\left(\nabla p_o - B_{cap}\nabla S_w - \rho_w g\right)\right] - \left[\frac{(1 - S_w)C_{cap}}{1 + A_{cap}} - 1\right]\frac{\partial(\nabla \cdot u)}{\partial t} = 0 \tag{3.34}$$

Where

$$C_{cap} = (c_R + c_w)S_w B_{cap} + c_R p_c \tag{3.35}$$

Eqs. (3.31) and (3.35) are the governing equations for oil and water flow in the reservoir. Two unknowns, water saturation and oil pressure, are solved using an IMPES method. In these two equations, capillary pressure and solid displacement are coupled explicitly, but will be solved during the iteration loops.

The governing equation for solid deformation is the same as Eq. (3.16) for an elasto-plastic domain coupled with fluid flow. For multiphase fluid flow, since fluid pressure can be defined as Eq. (3.21), together with the capillary pressure definition, we reach the final formulation for the solid deformation equation as,

$$\frac{\partial^2(\rho u)}{\partial t^2} = \nabla \cdot [G\nabla du + G(\nabla du)^T + \lambda Itr(\nabla du)] - \nabla \cdot \left[2G\left(d\varepsilon_p\right) + \lambda Itr\left(d\varepsilon_p\right)\right] + \nabla \cdot (\sigma^{old}) - \alpha\nabla p_o + \alpha\left(S_w B_{cap} + p_c\right)\nabla S_w + F \quad (3.36)$$

3.2.2.2 Compositional Model

A compositional multi-phase fluid flow model using an equation of state (EOS) which is fully coupled with reservoir geomechanics has been developed in our group and is used in this work. It is capable of handling any number of hydrocarbon components and three phases (oil, water and gas) and allows the density, compressibility and viscosity of reservoir fluids to change with pressure, temperature and fluid compositions (Liang et al., 2013; Liang et al., 2018). Multi-phase flow with non-Darcy effect, relative permeability and capillary pressure effects and water evaporation due to expanding gas are also considered (Wang et al., 2017).

The equations for multi-phase, multi-component fluid flow in a deforming porous media are presented in this section. The rock plastic deformation is calculated using the same set of equations as shown in Eq. (3.36). The primary variables are rock deformation, pressure, fluid velocity and component moles. Secondary variables such as stresses, strains and fluid saturations are obtained from the primary ones. Calculations of volume derivatives, phase stability, compositions, density, relative permeability and viscosity have been described in further detail elsewhere (Chang, 1990).

The combination of multi-phase non-Darcy law and mass conservation equation for component ‘i’ in terms of moles per unit time gives the component balance equations

$$\frac{1}{V}\frac{\partial N_i}{\partial t} - \nabla \cdot \sum_{j=1}^{N_p} \xi_j x_{ij} k \frac{k_{rj}}{\mu_j} \nabla\left(p + p_{cj}\right) - \nabla \cdot \sum_{j=1}^{N_p} \xi_j x_{ij} k \frac{k_{rj}}{\mu_j} \beta_j \rho_j |v_j| \cdot v_j = 0 \qquad (3.37)$$

Where i denotes for each component and j denotes for water, oil or gas phase.

The constraint that the pore volume of a deforming porous media should be filled with the total fluid volume results in the pressure equation

$$\frac{1}{M}\frac{\partial p}{\partial t} - \sum_{i=1}^{N_c+1} \frac{\partial V_t}{\partial N_i} \nabla \cdot \sum_{j=1}^{N_p} \xi_j x_{ij} k \frac{k_{rj}}{\mu_j} \nabla\left(p + p_{cj}\right) - \sum_{i=1}^{N_c+1} \frac{\partial V_t}{\partial N_i} \nabla \cdot \sum_{j=1}^{N_p} \xi_j x_{ij} k \frac{k_{rj}}{\mu_j} \beta_j \rho_j |v_j| \cdot v_j$$

$$+\alpha \frac{\partial (\nabla \cdot u)}{\partial t} = 0 \qquad (3.38)$$

3.2.3 The Mohr-Coulomb with Cap Model

3.2.3.1 Yield Surfaces

The original Mohr-Coulomb model is developed to determine the shear yielding of a rock under anisotropic stresses. The red line in Fig. 3.1 represents the shear yield surface in a shear stress – normal stress space (left in Fig. 3.1) and in deviatoric stress – mean stress space (right in Fig. 3.1). If the stress state falls within the surface, the rock is stable and can continue deforming with a linear elastic behavior. Otherwise, the rock is yielding and may either go into failure (brittle) or deform plastically (ductile). The equation for the shear yield surface can be expressed as

$$f^s = \sigma_1 - N_\varphi \sigma_3 + 2c\sqrt{N_\varphi} \qquad (3.41)$$

where N_φ is obtained from the internal friction angle as,

$$N_\varphi = \frac{1 + sin\varphi}{1 - sin\varphi} \qquad (3.42)$$

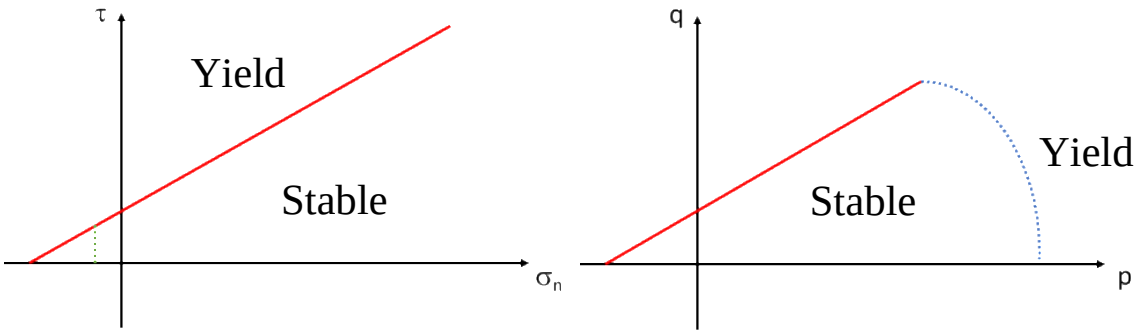

Fig. 3.1: The modified Mohr-Coulomb model with tensile cut-off (left) and Cap model (right)

The above shear yield surface is a good approximation for intact rock shear strength, however, it may overestimate the rock tensile strength during tensile loading. Instead, a tensile cut-off is necessary to be applied to estimate tensile yielding. The green dashed line in Fig. 3.1 shows the tensile yield surface for the rock, and the value is roughly around 0.1UCS. This surface can be expressed as

$$f^t = \sigma_3 - \sigma_t = \sigma_3 - t_{cutoff}\frac{c}{tan\varphi} \tag{3.43}$$

For most of the time, shear and tensile yield surfaces are enough to calibrate rock damage behavior. Nevertheless, if a rock exhibits strong compaction with high stresses and fails with pore collapse, neither shear nor tensile yield criteria are valid. For this circumstance, a compressive yield surface is proposed, which provides a cap under a high mean stress condition (blue dash line in Fig. 3.1). Eqn. (3.44) shows a vertical cap indicating a compressive yield when the mean stress exceeds a critical value.

$$f^c = \sigma_m + \sigma_c \tag{3.44}$$

These three yield surfaces do not have to be static (perfect plasticity). In fact, experiment analysis on rock properties shows that shear strength, tensile strength and compressive strength may change during plastic deformation and the rock behavior can be

strain softening or hardening. Thus, in the model, these strengths can be varied with equivalent plastic strain (defined in Eqn. (3.45)). This dependence is obtained from rock triaxial experiments or from empirical correlations given in Eqns (3.46) to (3.47) (Vermeer and De Borst, 1984).

$$\bar{e}^p = \bar{e}^p_{oldTime} + \sqrt{\frac{2}{3} d\varepsilon^p_{dev} d\varepsilon^p_{dev}} \tag{3.45}$$

$$c^* = cexp\left[-\left(\frac{\bar{e}^p}{\varepsilon^c}\right)^2\right] \tag{3.46}$$

$$sin\varphi^* = 2\frac{\sqrt{(\bar{e}^p \varepsilon^f)}}{\bar{e}^p + \varepsilon^f} \quad for\, \bar{e}^p \leq \varepsilon^f;\; sin\varphi^* = sin\varphi \quad for\, \bar{e}^p > \varepsilon^f \tag{3.47}$$

3.2.3.2 Stress Return Algorithm

In a continuum model for rock deformation, once the calculated stress state is beyond the yield surfaces, it should be returned on the yield surfaces and the plastic strain is calculated from the stress correction. The return mapping, called the elastic predictor plastic corrector algorithm, has been implemented in our model. Fig. 3.2 illustrates the principle of return mapping. The initial stress state (σ_n) in the rock is within the elastic domain. By applying a stress with the assumption of linear elasticity, a trial stress is first computed (σ^{trial}). If the trial stress state is beyond the yield surface, which implies that yield occurs, a plastic corrector is applied by adding a plastic cumulative stress increment ($-\Delta\sigma^p$) to the trial stress so that $f(\sigma_{n+1}) = 0$. The corrected stress (σ_{n+1}) is the final stress at the equilibrium condition. The expressions for the return boundaries, the conditions of the return type and the corrected stresses are given in detail in Appendix A.

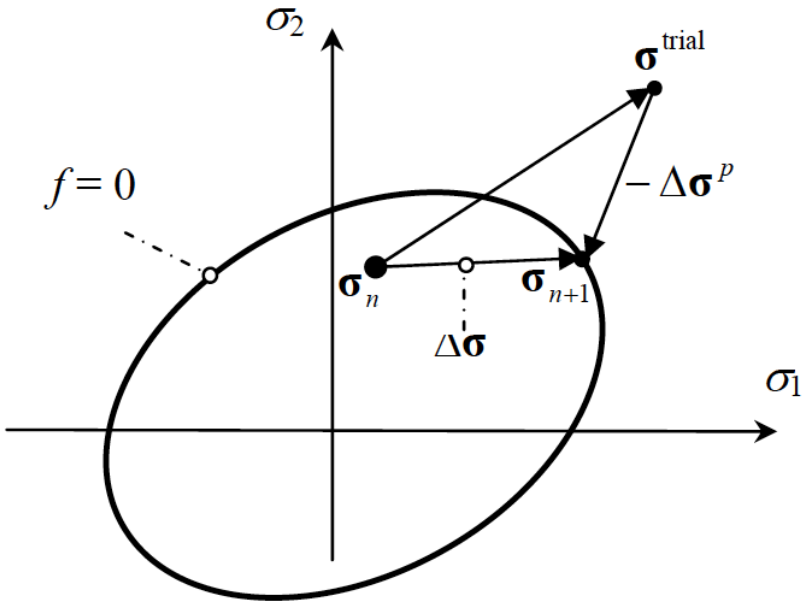

Fig. 3.2: Principle of return mapping (Saksala, 2009)

Furthermore, the incremental plastic strain is calculated as

$$d\varepsilon^p = \Delta\lambda \frac{\partial g}{\partial \sigma} \tag{3.48}$$

where g is the plastic potential, which determines the direction of incremental plastic strain, and can be written for shear yield, tensile yield and compressive yield respectively as

$$g^s = \sigma_1 - N_\psi \tag{3.49}$$

$$g^t = -\sigma_3 \tag{3.50}$$

$$g^c = \frac{1}{3}(\sigma_1 + \sigma_2 + \sigma_3) \tag{3.51}$$

In shear, the plastic potential, N_ψ is related to the dilation angle,

$$N_\psi = \frac{1 + sin\psi}{1 - sin\psi} \tag{3.52}$$

Dilation angle controls the plastic volumetric strain during shear plastic deformation. For associated plastic flow rule, dilation angle is equal to internal friction angle. For sands, dilation angle is usually smaller than internal friction, representing a non-associated plastic flow rule. If the dilation angle is 0, rock volume is preserved during shear deformation.

In Eqn. (3.48), $\Delta\lambda$ is the incremental plastic multiplier, and is defined as

$$\Delta\lambda = \frac{f(\sigma)}{\left(\frac{\partial g}{\partial \sigma}\right)^T E \left(\frac{\partial f}{\partial \sigma}\right)} \tag{3.53}$$

Since this algorithm provides analytical solutions, it's very fast to calculate the plastic strain and correct stresses. However, its limits are also obvious. Firstly, it's not applicable to compressive yield, which is important for rock failure. Secondly, the algorithm is only valid for linear yield surfaces. In reality, rock strength changes with confining stresses, indicating curved yield surfaces with different stress conditions. To model such rock properties, this return algorithm does not work. To resolve above two shortcomings, a more general stress return algorithm for multi-surface plasticity is developed in the model, and is shown in Appendix B.

3.3 MODEL VERIFICATION

3.3.1 Validation of Poro-Elastic Model

In this case, we have a porous medium subjected to a compressive load and a drained condition at the top plane (Fig. 3.3). The input data are present in Table 3.1, while pore pressure and displacement distributions are calculated numerically and validated with the analytical solutions (Detournay and Cheng, 1993) in Figs. 3.4 and 3.5. At a certain time, pore pressure is 0 at the top (due to the drained condition) and increases with depth (compression induced pore pressure). On the other hand, displacement is the largest at the

top (due to compression) and decreases with depth as zero displacement boundary is specified at the bottom. Furthermore, pore pressure decreases with time and causes an increase in the effective stress, thus displacement increases with time. Results show excellent agreement with the analytical solutions.

In addition, a mesh convergence study was conducted on this problem. Fig. 3.6 shows the results with a different number of meshes (from 20 to 200). It indicates that as the mesh is made finer, results for pore pressure and displacement converge to the analytical solution.

Table 3.1 Input data for validation of poro-elastic model

Parameters	Value
Porosity	0.2
Permeability (m^2)	1.5E-14
Biot coefficient	0.6
Young's modulus (GPa)	10
Poisson's ratio	0.2
Viscosity (Pa·s)	0.001
Fluid modulus (GPa)	2.3
Traction (Pa)	20000

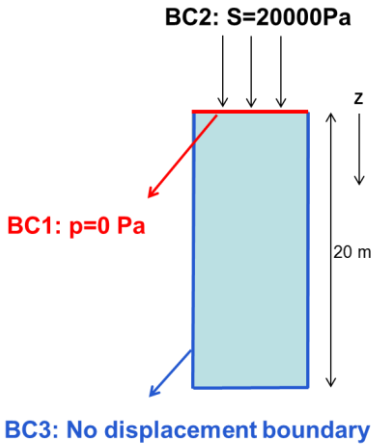

Fig. 3.3: Case setup for validation of poro-elastic model

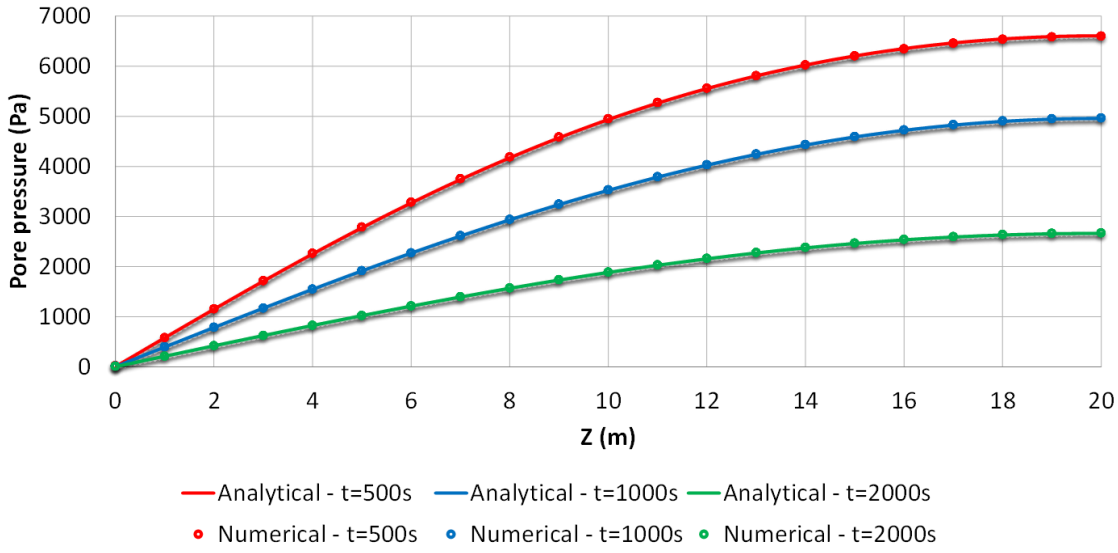

Fig. 3.4: Poro-Elastic validation: pore pressure distribution with time

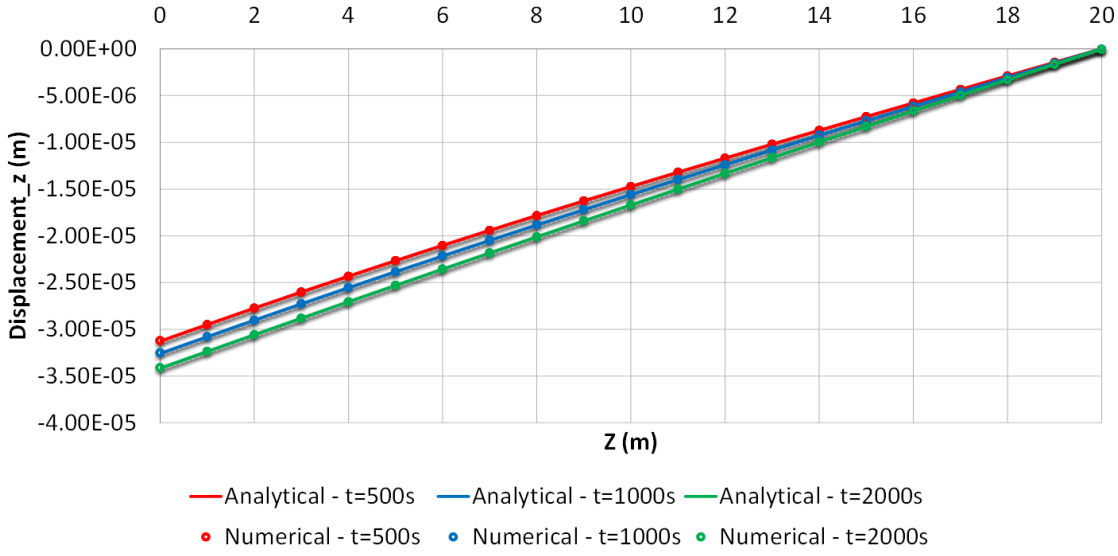

Fig. 3.5: Poro-Elastic validation: displacement distribution with time

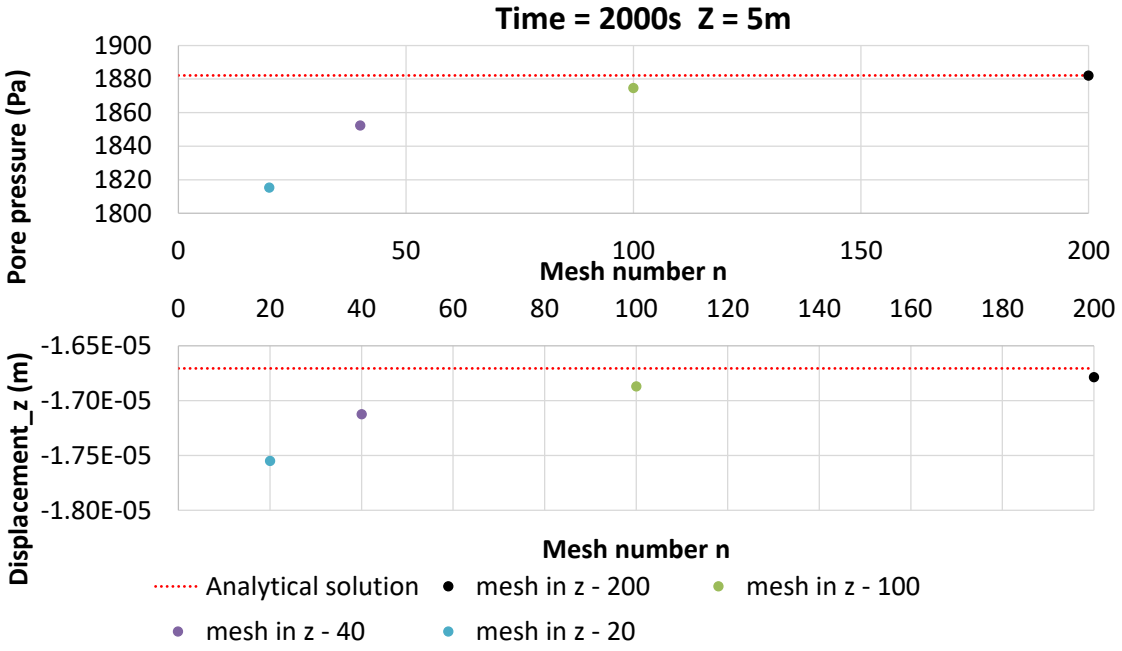

Fig. 3.6: Poro-Elastic validation: mesh convergence study with pore pressure (top) and displacement (bottom) at z=5m and time=2000s

3.3.2 Validation of Elasto-Plastic Model

In this case, an elasto-plastic plate with a hole at the center is compressed by an isotropic stress (Fig. 3.7). Rock properties are displayed in Table 3.2. The hole surface is exposed to the atmosphere, with zero effective normal stress. At equilibrium, the stresses and displacement calculated in the model are compared with analytical solutions (Salencon, 1969) in Figs. 3.8 and 3.9. We observe an excellent match between numerical and analytical results.

Table 3.2 Input data for validation of elasto-plastic model

Parameters	Value
Bulk modulus (GPa)	3.9
Shear modulus (GPa)	2.8
Cohesion (MPa)	3.45
Friction angle (deg)	30
Dilation angle (deg)	0
Far-field stress (MPa)	25

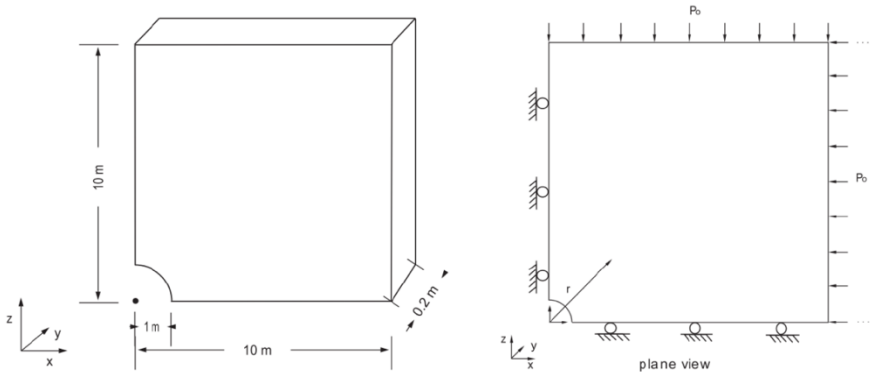

Fig. 3.7: Case setup for validation of elasto-plastic model

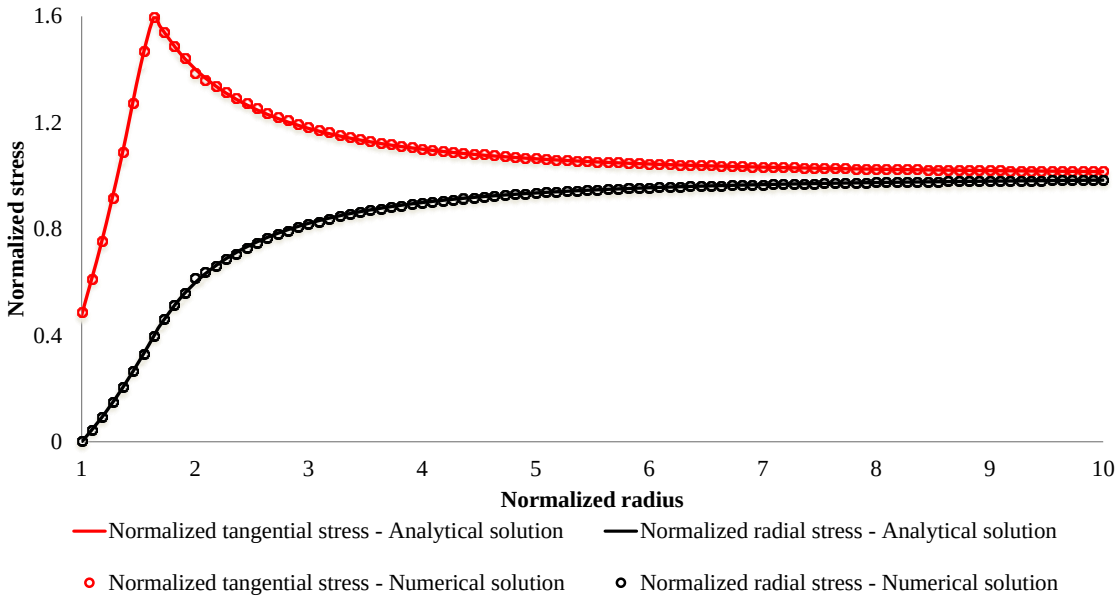

Fig. 3.8: Elasto-Plastic validation: normalized stresses with distance from hole

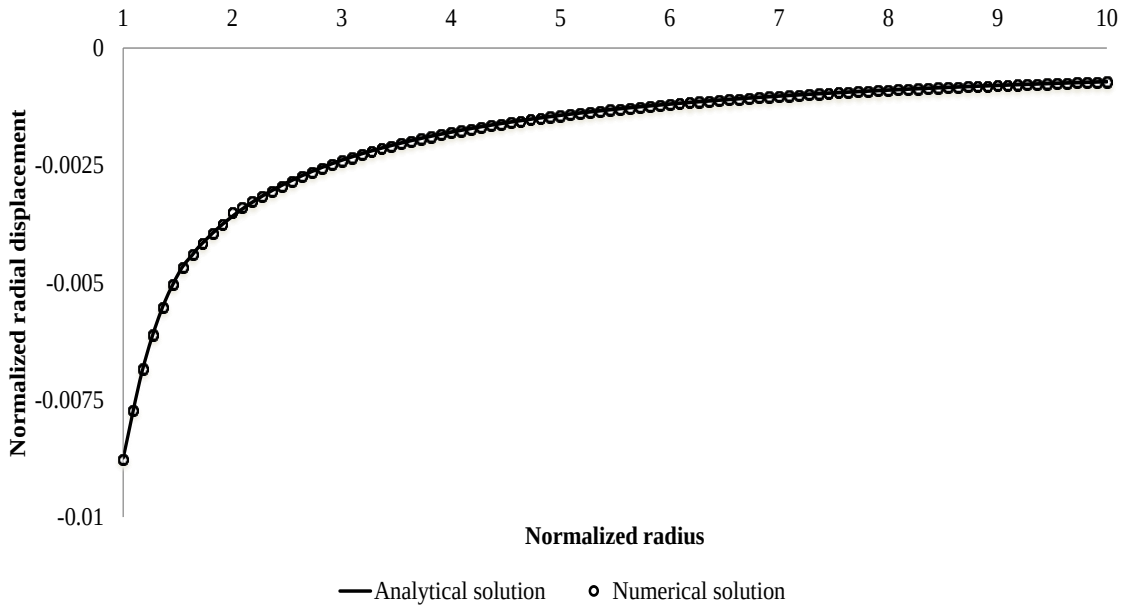

Fig. 3.9: Elasto-Plastic validation: normalized radial displacement with distance from hole

3.3.3 Validation of Uniaxial and Triaxial Test

In this case, both the uniaxial and triaxial tests are validated for the yield stresses. Figs. 3.10 and 3.11 show the setup of the uniaxial and triaxial tests respectively, while Tables 3.3 and 3.4 display the parameters for these tests. Perfect plasticity is assumed for the post yield behavior. As seen in Figs. 3.12 and 3.13, after yielding, yield stresses calculated from the numerical model are exactly the same as the analytical solutions for the uniaxial and triaxial tests.

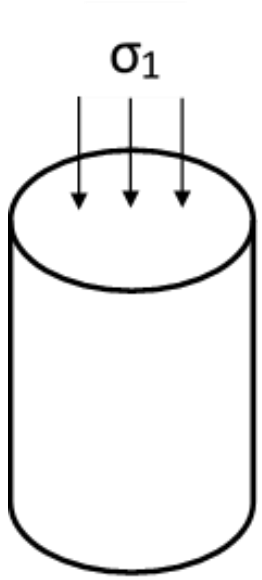

Fig. 3.10: Case setup for validation of uniaxial test

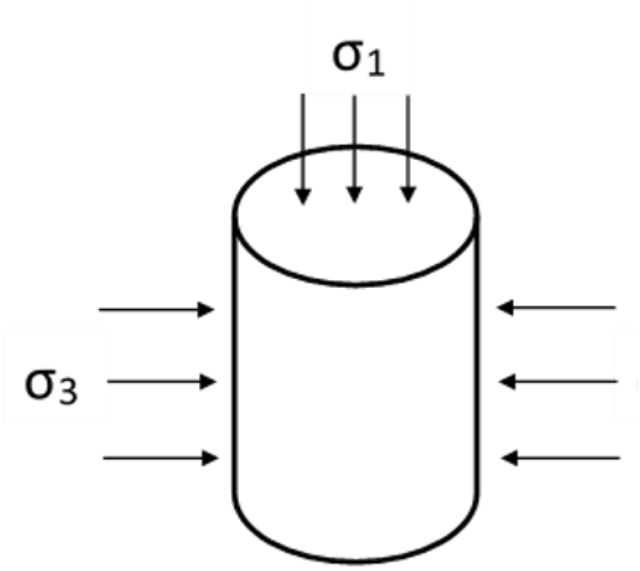

Fig. 3.11: Case setup for validation of triaxial test

Table 3.3 Input data for validation of uniaxial test

Parameters	Values
Radius (mm)	25.5
Height (mm)	105
Young's modulus (GPa)	0.3
Poisson's ratio	0.05
Internal friction angle	30
Cohesion (MPa)	0.5
Compression rate (mm/s)	0.0125

Table 3.4 Input data for validation of triaxial test

Parameters	Values
Radius (mm)	25.5
Height (mm)	105
Young's modulus (GPa)	0.3
Poisson's ratio	0.05
Internal friction angle	30
Cohesion (MPa)	0.5
Compression rate (mm/s)	0.0125
Confining pressure (MPa)	2

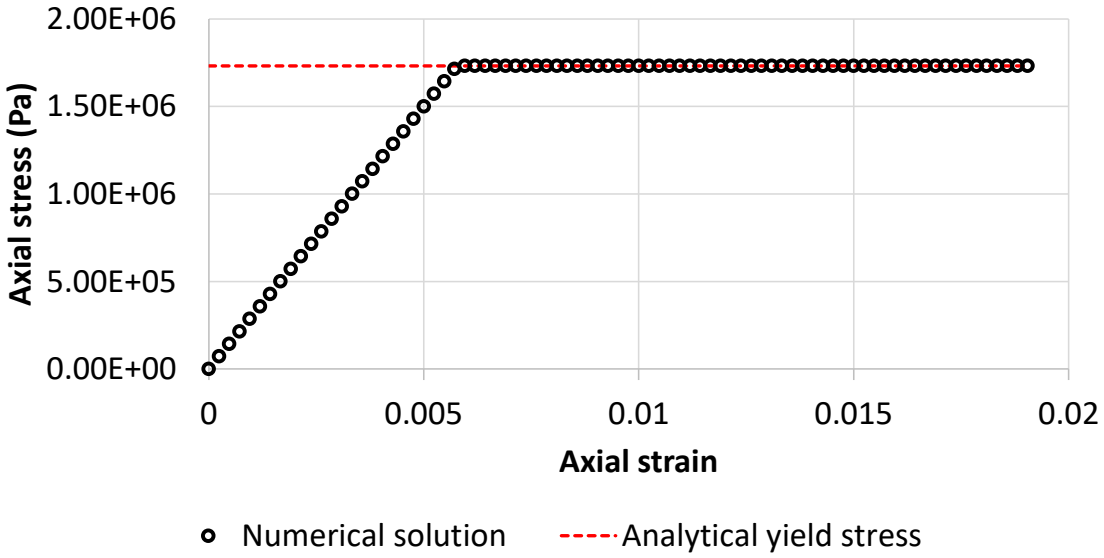

Fig. 3.12: Uniaxial test validation for yield stress

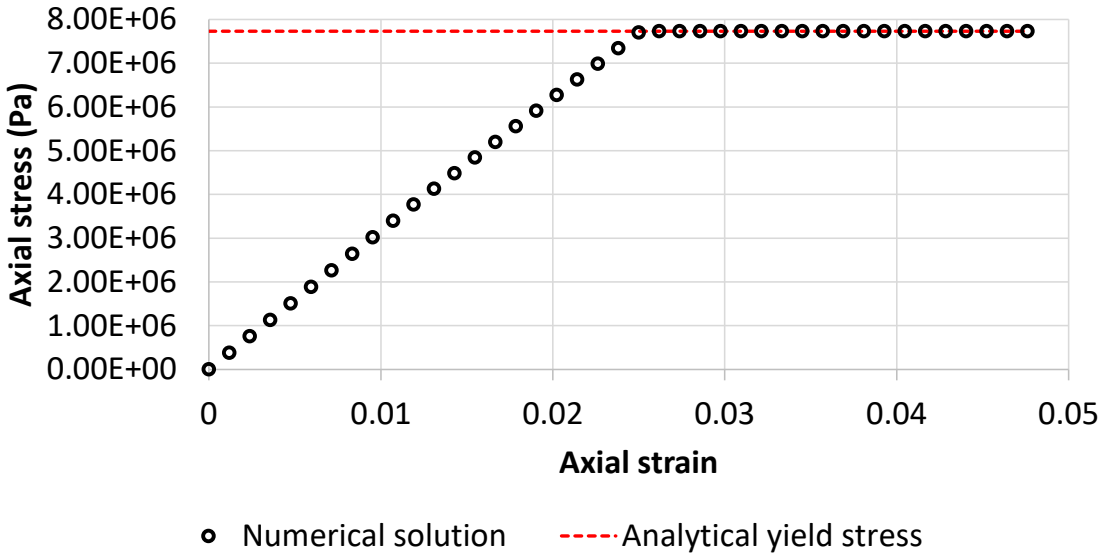

Fig. 3.13: Triaxial test validation for yield stress

3.3.4 Validation of Compressible Gas Flow

In the fourth case, a gas material balance validation case is set up. A compositional fluid flow model using an equation of state (EOS), coupled with reservoir geomechanics (GEORES-Comp) has been developed and used for this validation. The analytical expression for the material balance of a depletion from gas reservoir is written as (Dake, 1978)

$$\frac{P}{Z} = \left(\frac{P}{Z}\right)_{init}\left(1 - \frac{G_p}{G_{init}}\right)$$

Results of numerical solution and analytical solution are plotted in Fig. 3.14, showing a perfect match.

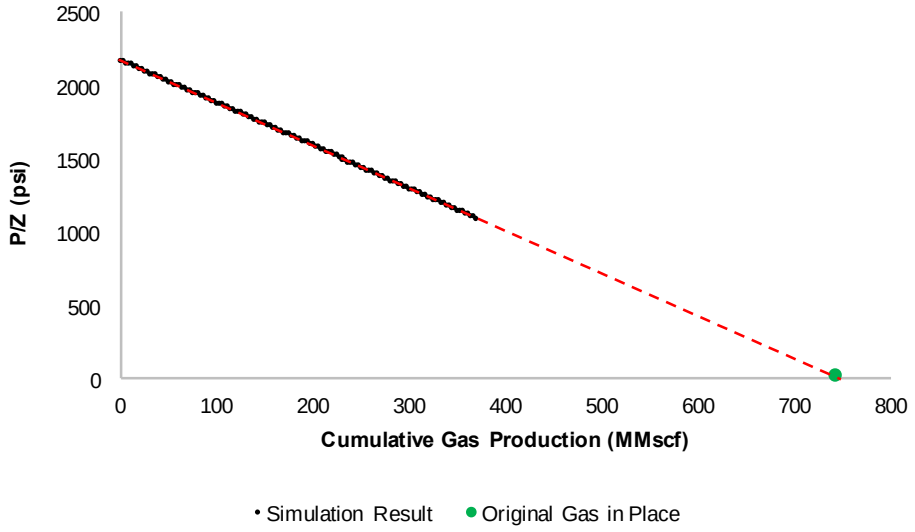

Fig. 3.14: Gas material balance validation (courtesy of Deepen Gala)

3.3.5 Validation of Multi-Phase Fluid Flow

The last validation case is for the multi-phase fluid flow model. A waterflooding problem that has an analytical Buckley-Leverett solution was chosen to compare with our numerical model. Without capillary pressure, numerical solutions perfectly match the analytical solution, as seen in Fig. 3.15. If the effect of capillary pressure is considered in

the numerical model, results are shown in Fig. 3.16. It demonstrates that with capillary pressure, the water saturation front is smoother than without capillary pressure, which is expected.

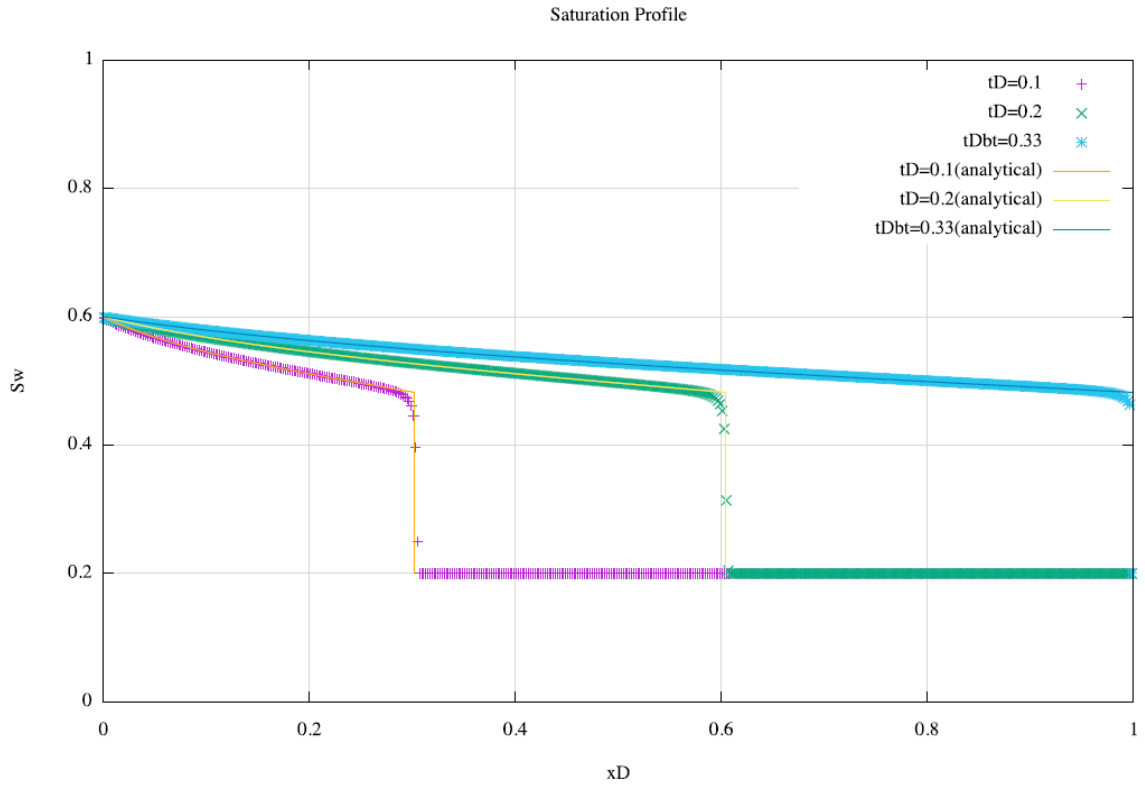

Fig. 3.15: Buckley-Leverett validation: no capillary pressure in numerical model

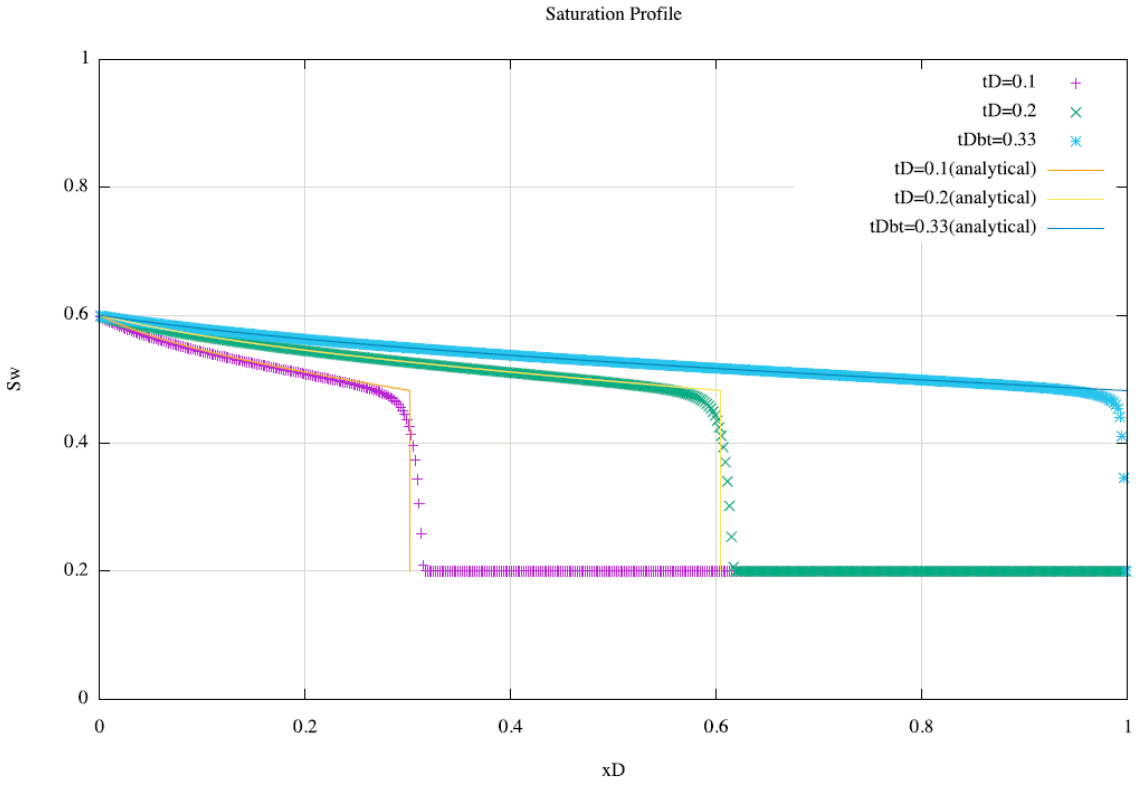

Fig. 3.16: Buckley-Leverett validation: with capillary pressure in numerical model

3.4 CONCLUSIONS

A 3-D poro-elasto-plastic model has been developed that predicts the pressure transient response and rock deformation. For single phase fluid flow, it is capable of simulating incompressible, slight compressible, or compressible fluid behavior. For multi-phase fluid flow, both a black-oil model and a complex compositional fluid flow model have been developed, and the capillary pressure is calculated at each location to estimate capillary cohesion (later used in the sand production model). For solid deformation, linear elasticity followed by the modified Mohr-Coulomb plastic model has been implemented to predict both elastic and plastic strain and determine the yield and failure state. Post-yield behavior of the rock can be modeled as either perfect plasticity or strain hardening/softening, based on an analysis of triaxial tests. Furthermore, cap model is

integrated with the plastic model (which can also be strain hardening or softening) to model compressive yield and failure.

The model has been comprehensively validated for different cases, for fluid flow and rock deformation, and further to coupled problems. Validations for a poro-elastic problem, an elasto-plastic problem, a uniaxial and triaxial test, a gas material balance, and the Buckley-Leverett problem have been conducted. These comparisons show excellent agreement between the numerical and analytical solutions.

NOMENCLATURE

c: Cohesion

c_R: Rock compressibility

c_t: Total compressibility

c_w: Water compressibility

du: Solid incremental displacement

$d\varepsilon$: Incremental strain tensor

$d\varepsilon_e$: Incremental elastic strain tensor

$d\varepsilon_p$: Incremental plastic strain tensor

$d\sigma$: Incremental stress tensor

Epc: capillary pressure coefficient

F: Body force

G: Shear modulus

K: Formation bulk modulus

k: Permeability

K_f: Fluid bulk modulus

M: Biot modulus

N: Phase component

N_c: The number of components (methane, ethane, propane etc.)

N_p: The number of phases (oil, water and gas)

p: Pore pressure

p_c: Capillary pressure

p_o: Oil pressure

p_w: Water pressure

q: Fluid flow rate

S_o: Oil saturation

S_{or}: Residual oil saturation

S_w: Water saturation

S_{wr}: Irreducible water saturation

t: Time

t_{cutoff}: Tensile cut-off coefficient

u: Solid displacement

V: Cell volume

v_o: Oil velocity

v_s: Solid velocity

Vt: Total fluid volume (oil + water+gas)

v_w: Water velocity

x_{ij}: The fraction of component i in phase j

α: Biot's coefficient

ε: Strain tensor

ε_b: Volumetric strain

ϕ: Porosity

φ: Internal friction angle

λ: Lame's first parameter

λ_o: Oil mobility ratio

λ_w: Water mobility ratio

μ: Fluid viscosity

ρ: Formation density

ρ_f: Fluid density

ρ_w: Water density

σ: Stress tensor

σ_c: Cap pressure

σ_m: Mean effective stress

σ^{old}: Stress tensor in old time

REFERENCES

Bhardwaj, P., R. Manchanda, J. Hwang, P. Cardiff, and M. M. Sharma. 2016. A New Reservoir Scale Model for Fracture Propagation and Stress Reorientation in Injection Wells. *Paper presented at 50th US Rock Mechanics Symposium, Houston, Texas, USA, June 2016.*

Brooks, R. and A. Corey. 1964. Hydraulic Properties of Porous Media. *Colorado State University, Hydro Paper*.

Chang, Y. -B. 1990. Development and Application of an Equation of State Compositional Simulator. *Ph.D. Dissertation, University of Texas at Austin, Austin, Texas.*

Chen, W. F. and G. Y., Baladi. 1985. Soil plasticity: theory and implementation. *Vol. 38. Elsevier.*

Detournay, E. and A. H. D. Cheng. 1993. Fundamentals of poroelasticity. In *Comprehensive Rock Engineering: Principles, Practice & Projects, Vol. II, Analysis and Design Method*: 113-171. Pergamon Press.

Jing, L. 2003. A review of techniques, advances and outstanding issues in numerical modelling for rock mechanics and rock engineering. *International Journal of Rock Mechanics and Mining Sciences, 40(3), 283-353.*

Khan, A. S. and S. Huang. 1995. Continuum theory of plasticity. *John Wiley & Sons.*

Liang, Y., B. Wen, M. A. Hesse, and D. DiCarlo. 2018. Effect of Dispersion on Solutal Convection in Porous Media. *Geophysical Research Letters.*

Liang, Y., D. DiCarlo, and M. A. Hesse. 2013. Experimental Study of Convective Dissolution of Carbon Dioxide in Heterogeneous Media. *Presented at the AGU Fall Meeting Abstracts.*

Peiró, J. and S. Sherwin. 2005. Finite difference, finite element and finite volume methods for partial differential equations. *Handbook of materials modeling: 2415-2446.*

Saksala, T. 2009. Geometric return algorithm for non-associated plasticity with multiple yield planes extended to linear softening/hardening models. *Rakenteiden Mekaniikka (Journal of Structural Mechanics)*, *42*(2), pp.83-98.

Salencon, J. 1969. Contraction quasi-statique d'une cavite a symetrie spherique ou cylindrique dans un milieu elastoplastique. *In Annales des ponts et chaussées*, 4: 231-236.

Vermeer, P. A. and R. De Borst. 1984. Non-associated plasticity for soils, concrete and rock. *Heron, 29(3): 3-64.*

Wang, H. and M. M. Sharma. 2016. A fully 3-D, multi-phase, poro-elasto-plastic model for sand production. *In SPE Annual Technical Conference and Exhibition. Society of Petroleum Engineers, 2016.*

Wang, H., D. P. Gala, and M. M. Sharma. 2017. Effect of Fluid Type and Multi-Phase Flow on Sand Production in Oil and Gas Wells. *In SPE Annual Technical Conference and Exhibition. Society of Petroleum Engineers, 2017.*

Wu, Y.-S., J. Li, D. Ding, C. Wang, and Y. Di. 2014. A Generalized Framework Model for the Simulation of Gas Production in Unconventional Gas Reservoirs. *SPE Journal, 19(05): 845-857.*

Chapter 4: Development of Sand Production Model

4.1 Introduction

Sand production involves two steps: 1. Rock mechanical instability and degradation; 2. Fluid erosion for sand transportation. The former mechanism has been taken into account by many models to predict the onset of sanding (Risnes et al., 1982; Morita et al., 1989; Weingarten and Perkins, 1992; Wang and Dusseault, 1996). These models are fast, however, they have some limitations (Rahmati et al., 2013). The first limitation being that they can only predict the onset of sanding, but not the sand production volume, which is also critical for designing sand management systems. Secondly, most of these models only consider one failure mechanism, which is insufficient in most cases and so cannot be applied to all fields. Thirdly, these models are limited to simple geometries and boundary conditions, which may not be applicable in real field cases (e.g. perforated wells, deviated wells, and fractured wells). Finally, these models do not consider plasticity which is essential to include in any model for sand failure and production. In order to accurately predict both the onset of sanding and the sand production rate, different mechanical failure mechanisms, plasticity, complex shapes of cavities and fluid erosion must be considered in the sand production model.

4.2 Model Description

With the development of the 3D poro-elasto-plastic model described in Chapter 3, we can calculate pore pressure transients and rock deformation in a coupled manner. In addition, with the modified Mohr-Coulomb with a cap model, different yield conditions may be applied to limit the stresses and obtain the accumulated plastic strain. Physically, the rock can sustain a certain amount of plastic strain before complete failure, and the magnitude of this strain depends on the rock properties (small critical plastic strain if the

rock is brittle and a large value if the rock is ductile). This value can be obtained from experiments such as triaxial tests. On the other hand, once the sand fails, a new erosion criterion for entrainment of the sand based on the calculation of hydrodynamic and resistant forces on sand grains, is implemented to predict sand erosion and will be discussed in the following section. If both failure and erosion criteria are met, sand will be produced and the cell elements are dynamically removed to model cavity propagation. Further, in order to efficiently capture the strain concentration regions before and after cavity expansion, a dynamic mesh refinement/un-refinement algorithm is implemented in the model.

4.2.1 Mechanical Failure

4.2.1.1 Tensile Failure

Tensile yield happens when the minimum principal stress exceeds the tensile strength. For sand production related issues, this can be triggered by either a mechanical or fluid flow effect. Mechanically, if the stress contrast is very large, a tensile stress may appear along the maximum stress direction around the well, leading to tensile yield. On the other hand, if the drawdown is large, the pressure induced radial stress may increase beyond the tensile strength of the rock. In this model, once tensile yielding occurs, a tensile plastic strain is calculated. If the accumulated tensile plastic strain is larger than the critical value, tensile failure is reached and the failed sands are ready for fluid erosion.

4.2.1.2 Shear Failure

Shear yield occurs when the shear stress exceeds the shear strength. With the Mohr-Coulomb model, the shear strength is controlled by the cohesion and the internal friction angle, while the shear stress is related to the maximum and minimum principal stresses. As with tensile yield, shear yield is also affected by both mechanical and fluid flow effects. In contrast with mechanical instability, shear yield is prompted by not only stress contrast,

but also the stress magnitude. The larger stress contrast and stress magnitude are, the more likely it is for the sand to yield in shear mode. From a fluid flow point of view, both injection and production can cause shear yield. During injection, with an increase in pore pressure, the effective stresses decrease and the Mohr circle moves towards the yield surface. During production, the reduction of pore pressure increases effective stresses, but with different amounts due to the poroelastic effect. This may cause the Mohr circle to move towards the yield surface. Once shear yielding occurs, shear plastic strain is calculated. Shear failure in the model is detected as soon as the accumulated shear plastic strain exceeds the critical value (obtained from experiments).

4.2.1.3 Volumetric Failure

Volumetric failure (compressive failure) is likely to occur during production in high porosity reservoirs, where compaction strength is low. As oil/gas is produced, the depletion of the reservoir results in an increase in the mean effective stress (near wellbore/perforation/fracture). Once it exceeds the compaction strength (represented by a cap in the model), volumetric yielding begins and a volumetric plastic strain is obtained. Volumetric failure takes place when the accumulated volumetric plastic strain is larger than the critical volumetric plastic strain.

4.2.2 Sand Erosion

As long as one type of failure is reached, the failed rock is assumed to be degraded into sand grains, and they will stay in the formation until the drag force acting on the sands exceeds the resistance force that holds the sands in place. In our model, the kinetic force of any phase (oil, water or gas) on the failed sands consists of form drag and friction drag, and is calculated as a general form by Eqn. (4.1).

$$F_{drag,j} = \pi r^2 \left(\frac{1}{2}\rho_j v_j^2\right) f \tag{4.1}$$

The friction factor (f) in this formula is a non-linear function of Reynolds number and is calculated based on Fig. 4.1. Mathematically, it is defined as

$$f = \frac{24}{Re} \qquad for\ Re < 0.1$$

$$f = \left(\sqrt{\frac{24}{Re}} + 0.5407\right)^2 \qquad for\ 0.1 < Re \leq 500 \tag{4.2}$$

$$f = 0.44 \qquad for\ Re \geq 500$$

The Reynolds number for any phase of fluid is expressed as

$$Re_j = \frac{2R_{sand} v_j \rho_j}{\mu_j} \tag{4.3}$$

From the above definitions, we can observe a non-unique relationship between drag force and fluid velocity: for creeping flow, drag force is linearly proportional to the velocity; however, as Reynolds number increases, the drag force is nonlinearly proportional to the velocity; ultimately, in turbulent flow, drag force on sand grains becomes proportional to the square of the fluid velocity.

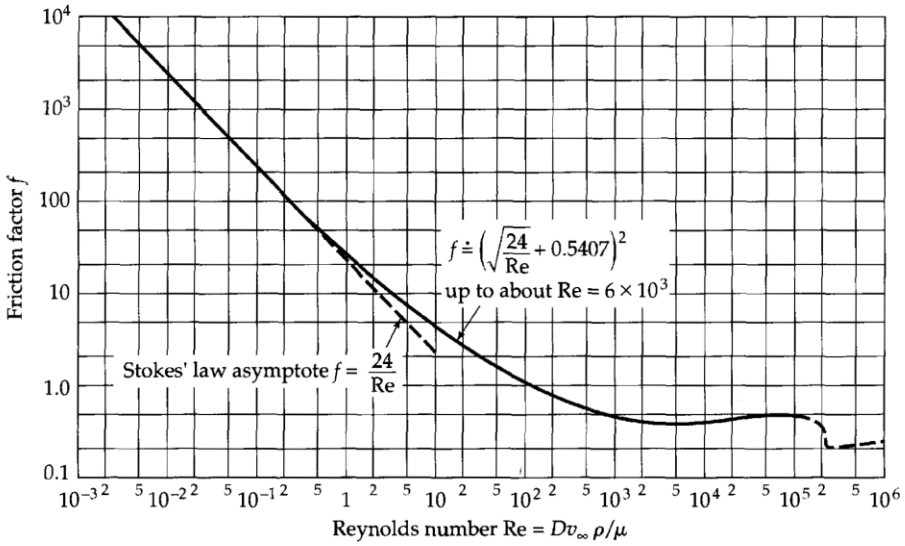

Fig. 4.1: Friction factor expression in different flow regimes (Bird et. al, 1989)

On the other hand, the resistance force consists of the gravitational and capillary cohesion force (only in multi-phase) on the sand grains. Since the magnitude of capillary cohesion is much smaller than rock cohesion, it is not incorporated into the failure calculations. However, capillary cohesion is important in fluid erosion as it adds comparable resistance to avoid failed sands being eroded. Thus, for multi-phase fluid flow cases, the resistance force for a sand particle in any fluid phase is calculated using the formula as shown in Eqn. (4.4), where c_{cap} is the capillary cohesion depending on the capillary pressure.

$$F_{resistance,j} = \frac{4}{3}\pi r^3\left(\rho_{sand} - \rho_j\right)g + 4\pi r^2 c_{cap} \tag{4.4}$$

Furthermore, the capillary pressure for a water-oil system with water as a wetting phase is calculated using the correlation shown below

$$p_c = p_c^0\left(1 - \frac{S_w - S_{wr}}{1 - S_{wr} - S_{or}}\right)^{Epc} \tag{4.5}$$

Capillary cohesion depends on the capillary pressure, water saturation and the internal friction angle and is calculated using Eqn. (4.6).

$$c_{cap} = S_w \times p_c \times tan\varphi \tag{4.6}$$

4.2.3 Dynamic Sand Removal

Sand production occurs only if both rock failure and fluid erosion criteria are met. In the model, once the two criteria are met, a novel dynamic cell removal algorithm is implemented to represent sand entrainment.

From previous experiments and field observations, sands are produced from the well/perforation. Thus, a surface-erosion based cell removal method is developed. We check the cells on the production surfaces for failure and fluid erosion, and they are deleted from the mesh system if the two criteria are met. This leads to a topology change of well/perforation boundary surfaces, which requires the current stress/pore pressure boundary conditions to be applied on the new exposed faces (now part of the well/perforation boundary surface). Since the geometry has changed, stress and pore pressure distributions are recalculated to obtain equilibrium before going into the next simulation step.

The volume of sand production is calculated based on the volume of removed cells and porosity,

$$V_{sand} = (1 - \phi)\Sigma V_{removed\,element} \tag{4.7}$$

4.2.4 Dynamic Mesh Refinement and Un-refinement

During rock deformation, if plasticity occurs, the plastic transient zone can affect both the failure location and conditions. In addition, localized plasticity such as thin shear and compaction bands can develop if the rock exhibits non-associative plasticity or strain

softening behavior. Therefore, it is necessary to apply fine grids to capture it. However, one issue when doing so is that the computational time can increase significantly when increasing the number of grids. One solution to this problem is the application of dynamic mesh refinement (Deb et al., 1996; Barry et al., 1998). The purpose is to reduce the computational time while keeping an accurate plasticity calculation.

In the model, we have developed a dynamic mesh refinement/un-refinement algorithm. Initially, a coarse mesh is used for rock deformation within the elastic region. Once plasticity occurs, the local mesh is refined to capture the plastic zone. With an increase in plastic strain, a higher level of mesh refinement can be used to capture the strain localization region (shear/compaction bands). When focusing on the unloading outside of the strain localization region, the mesh becomes coarse reducing the total mesh number and overall computational time.

Fig. 4.2 shows a case with a rectangular rock sample subjected to uniaxial loading. Dynamic mesh refinement is applied in this model for rock deformation with plasticity. The original coarse mesh size is 0.8m, with two levels of mesh refinement (0.4m and 0.2m) for low and high plastic strain. At the beginning, when the loading force is small, the rock deforms elasticity, without any localization phenomenon. As the loading force increases, at time = 4.88 min, plastic strain develops and dynamic mesh refinement initiates. At the center of the rock sample, high plastic strain (in dark green and red zone) is obtained and a higher refinement level (0.2m mesh size) is used. On the other hand, the low plastic strain zone (light green zone) has a lower mesh refinement level (0.4m) to account for the plasticity transient. When the loading is further increased (at time = 4.93 min), plastic strain tends to be localized to form an x-shape shear band, and mesh un-refinement starts to work in the unloading zone outside the shear bands. Fine meshes in the previous green zone become coarse and reverse back to the original coarse mesh (0.8m). After 5 minutes of

loading, the force remains constant and ultimate rock deformation is shown at time = 5.02 minutes with an x-shape shear band captured by fine meshes.

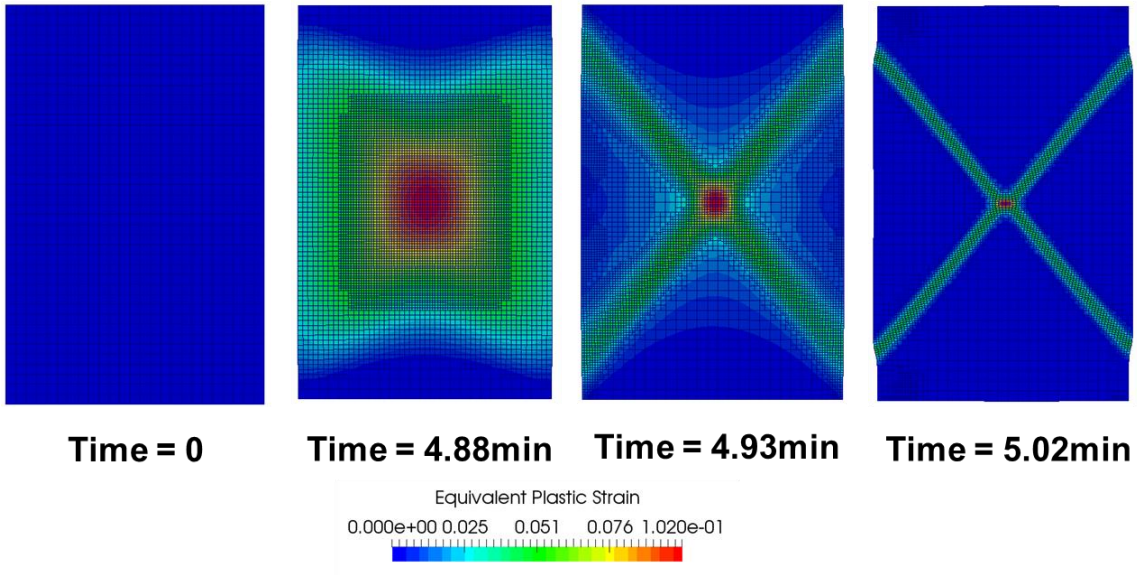

Fig. 4.2: The application of dynamic mesh refinement/un-refinement in elasto-plastic deformation

Next, we compared the accuracy and computational time needed for this problem when using a static and dynamic mesh for this scenario. In the first three cases, a static mesh with different mesh sizes (0.8m, 0.4m and 0.2m) is used to calculate rock deformation and the last case utilizes dynamic mesh refinement/un-refinement as discussed above. Fig. 4.3 shows the plastic contour for these four cases, suggesting a better accuracy for the last two. On the other hand, the computation time for each case is plotted in Fig. 4.4. With the same accuracy, the dynamic mesh refinement/un-refinement method can reduce the computational time by a factor of 5, compared to a static fine mesh (0.2m).

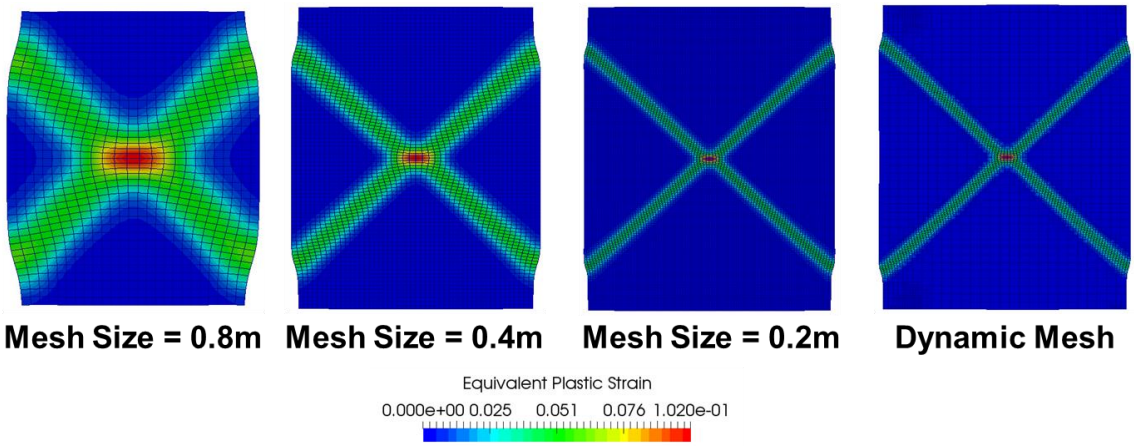

Fig. 4.3: Comparison of plastic contour between static mesh and dynamic mesh

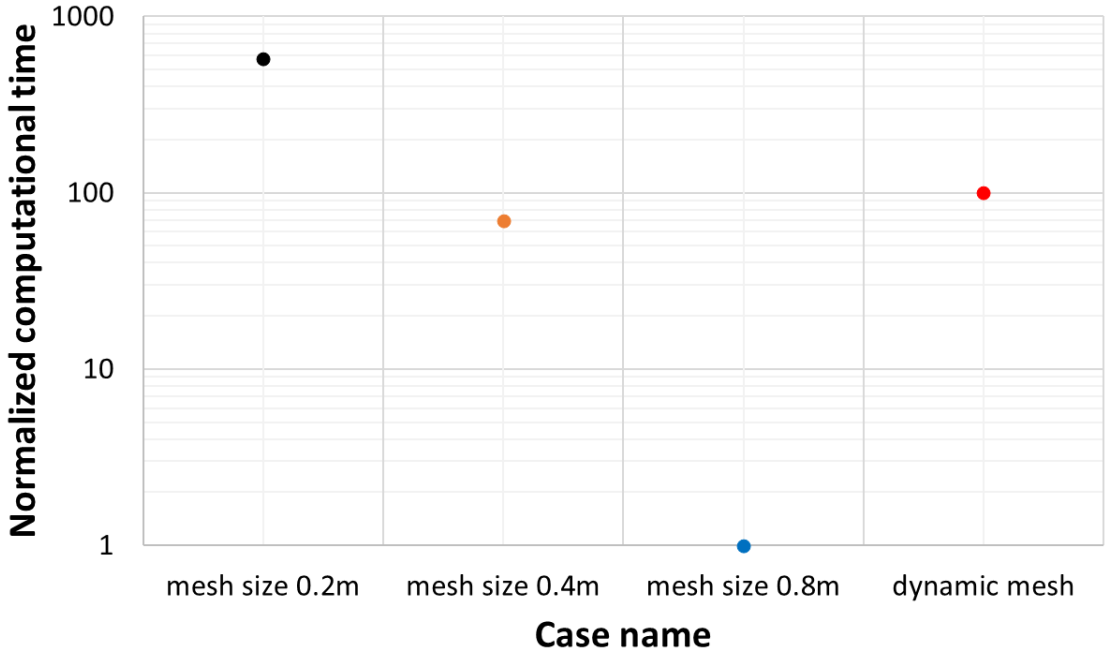

Fig. 4.4: Comparison of computational time between static mesh and dynamic mesh

4.3 SAND PRODUCTION MODEL VERIFICATION

Since there is no analytical solution for sand production prediction for both the onset of sanding and the sand production volume, the sand production model is validated against experimental data.

4.3.1 Sand Production Experiment

Experimental investigations were reported on Castlegate outcrops in PEA135 JIP Consortium conducted by FracTech LTD in 1998 for the measured sanding of thick-walled cylinders with different IDs and ODs. Three cases are presented and compared in the section: sample A with 4”×8”×0.63” (OD×Length×ID), sample B with 3”×6”×0.5” and sample C with 4”×8”×0.5”. Initially the rock sample is subjected to 250 psi hydrostatic loading (left figure in Fig. 4.5). The confining stress increases hydrostatically (right figure in Fig. 4.5) while the borehole discharge is collected in batches. Produced sand grains are detected at certain confining stresses. With a further increase in confining stresses, more sand is produced and collected. After sanding, the cavity shapes around the borehole for these samples are displayed in Figs. 4.6 to 4.8.

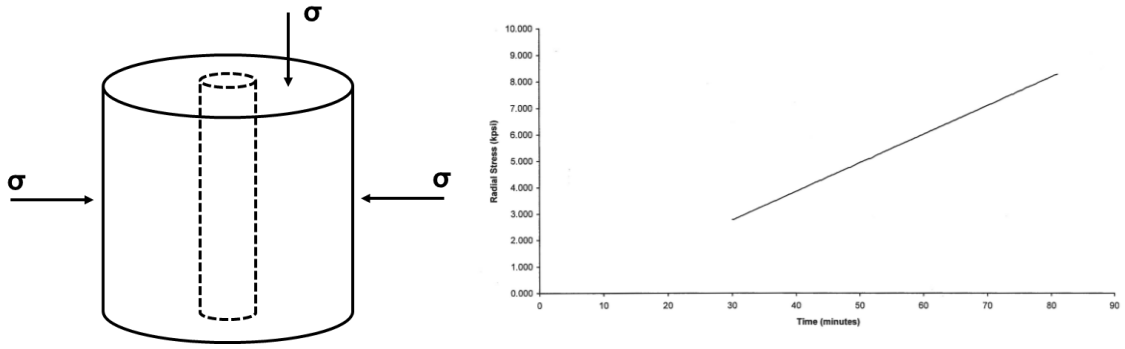

Fig. 4.5: Sand production experiment setup: loading setup (left) and loading history (right)

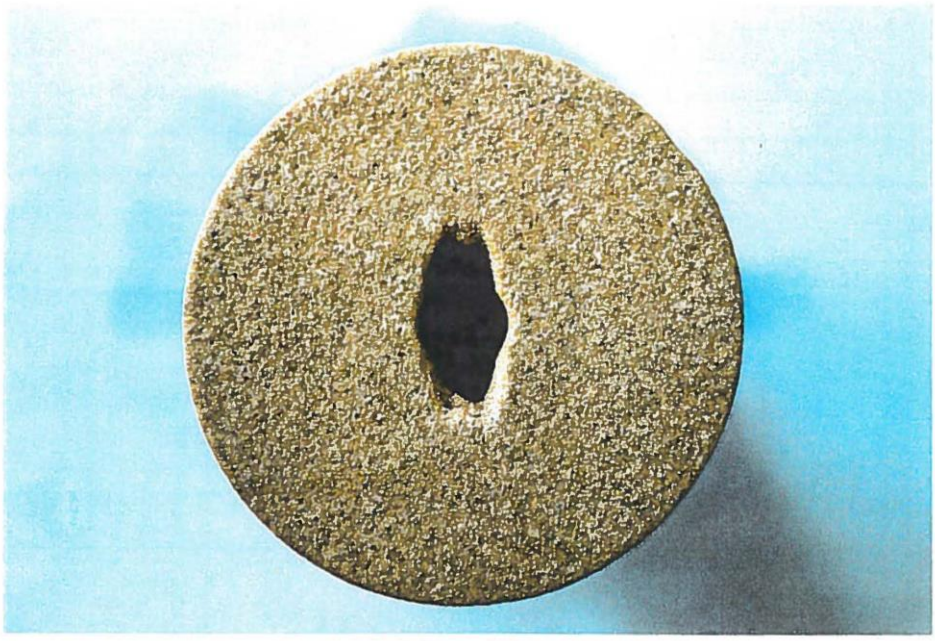

Fig. 4.6: Cavity shape of sample A after sand production – experimental data

Fig. 4.7: Cavity shape of sample B after sand production – experimental data

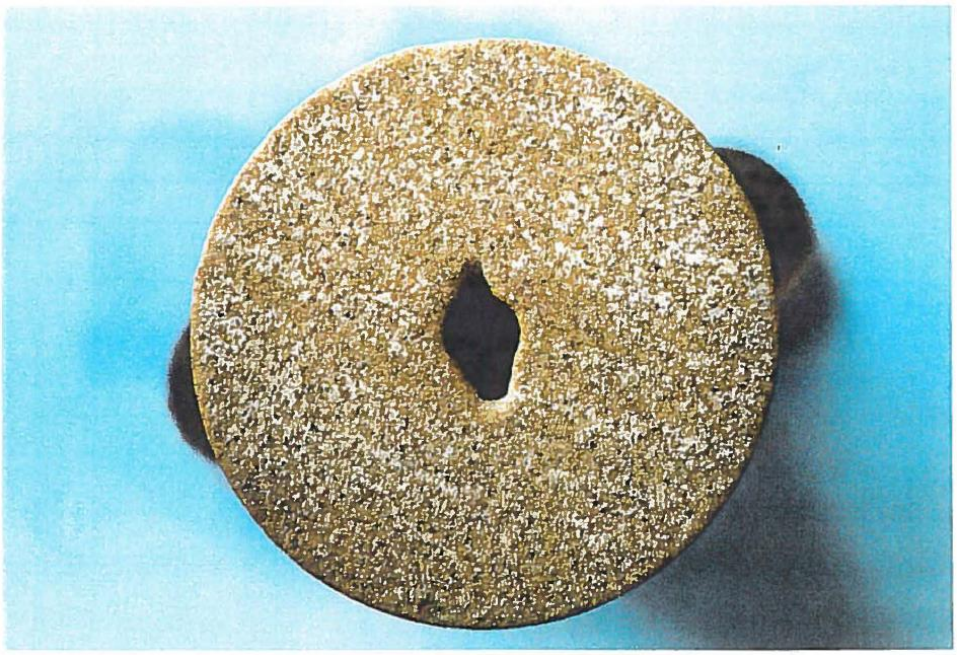

Fig. 4.8: Cavity shape of sample C after sand production – experimental data

4.3.2 Rock Properties Calibration

Prior to sand production prediction, it is essential to obtain accurate rock properties. Based on the fundamental physics of sand production, the necessary rock properties include both elastic and plastic properties, which can be obtained from triaxial tests.

Fig. 4.9 shows the relation between shear stress and shear strain under different total confining stresses on Castlegate outcrop from triaxial tests. For all the samples, they are initially saturated with fluid and the pore pressure remains at 500psi. At low confining stresses, strain hardening and then softening is observed as the post yield behavior, along with a constant residual shear stress at the end. At high confining stresses (8500psi), strain hardening is observed, followed by perfect plasticity behavior.

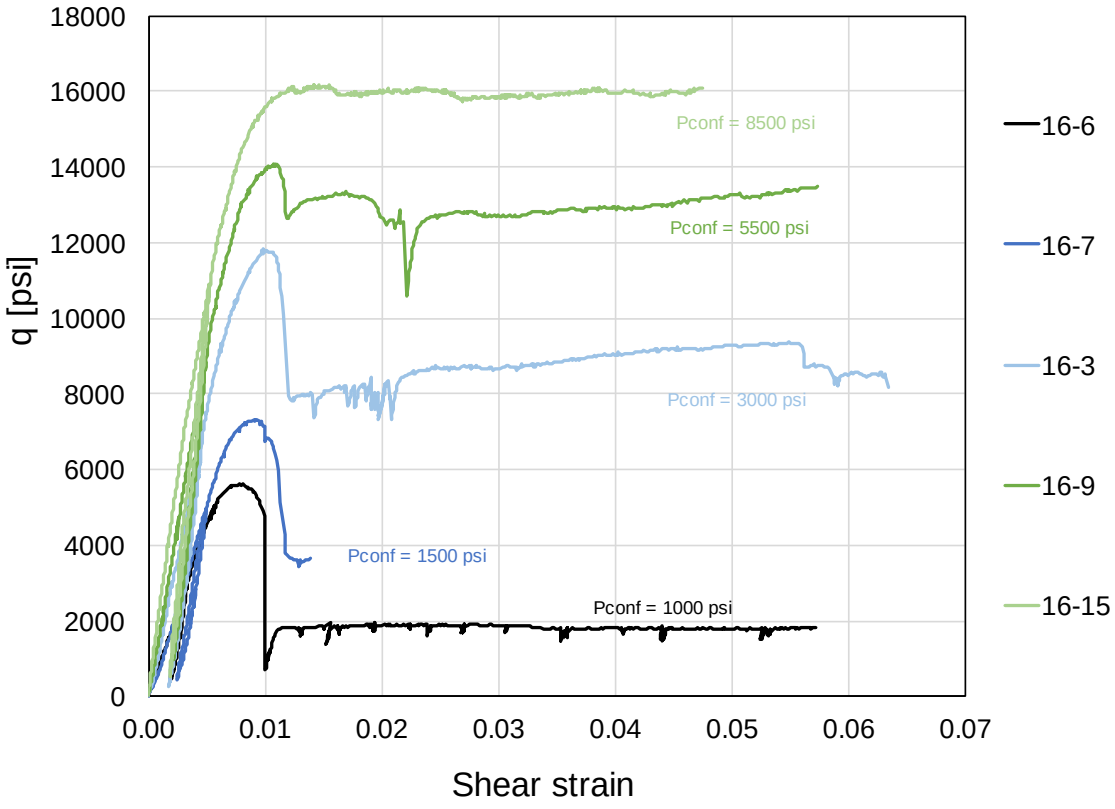

Fig. 4.9: Shear stress vs. shear strain under different total confining stresses on Castlegate rock

4.3.2.1 Elastic Properties

Young's modulus and Poisson's ratio can be calculated from the linear elastic deformation region. For Young's modulus calibration, we recall the generalized Hooke's Law in 3-D,

$$\varepsilon_{zz} = \frac{1}{E}\left(\sigma_{zz} - \upsilon\sigma_{xx} - \upsilon\sigma_{yy}\right) \tag{4.8}$$

From triaxial compression tests we can derive from Eqn. (4.7)

$$\varepsilon_1 = \frac{1}{E}(\sigma_1 - 2\upsilon\sigma_3)$$

$$\varepsilon_1 + d\varepsilon_1 = \frac{1}{E}(\sigma_1 + d\sigma_1 - 2\upsilon\sigma_3)$$

By subtracting the above two equations, we have

$$E = \frac{d(\sigma_1 - \sigma_3)}{d(\varepsilon_1)} \tag{4.9}$$

Thus, by plotting shear stress and axial strain, we can calculate Young's modulus from the linear slope during elastic deformation.

On the other hand, by definition, Poisson's ratio is calculated as,

$$\upsilon = -\frac{d(\varepsilon_r)}{d(\varepsilon_1)} \tag{4.10}$$

A plot of radial strain vs. axial strain will yield the Poisson's ratio.

4.3.2.2 Plastic Properties

Plastic properties, especially post-yield properties, are much more complex to determine. As rock strength is changing during plastic deformation, we calibrate the mobilized strength under four critical points in these experiments: strength for intact rock, peak strength, strength at sharp reduction, and residual strength. As discussed before, mobilized strength is a function of plastic strain, therefore, the strength at each point is related to an equivalent plastic strain.

Strength for Intact Rock

Strength for intact rock represents the strength at the instant the rock turns from elastic to plastic. From stress-strain relations in Fig. 4.9 we can pick up these critical points and draw the Mohr circles according to each confining stress, shown in Fig. 4.10. As observed in the figure below, only one shear yield line is not enough to cover all critical points of yielding from low confining stress to high. Instead, it is necessary to use a bi-linear shear yield function to capture the yielding points under various stresses. Based on the yield function, shear strength for the intact rock can be obtained, where equivalent plastic strain is 0.

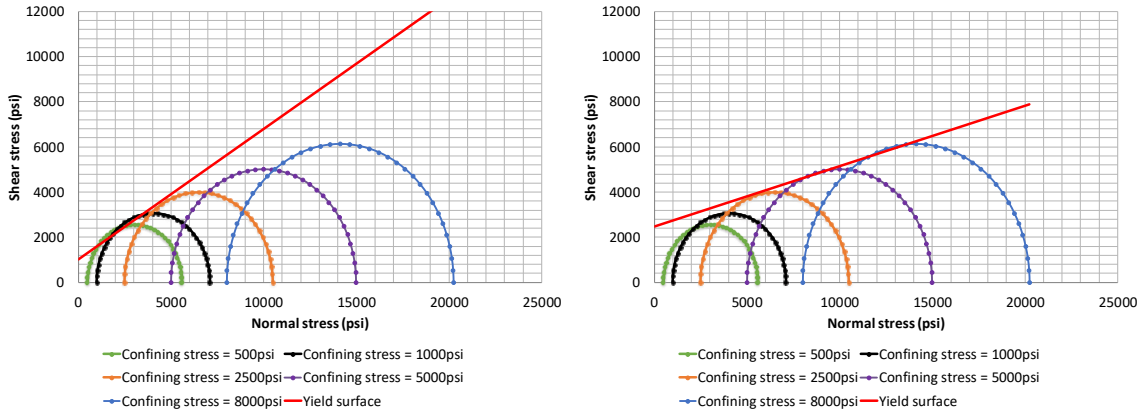

Fig. 4.10: Mohr circles for intact rock strength with bi-linear shear yield surface: low confining stress (left) and high confining stress (right)

Peak Strength

The next critical property for rock strength is peak strength, which represents the highest strength the rock can sustain, and this is also the conjunction point from strain hardening to strain softening. By extracting these points in Fig. 4.9, the corresponding Mohr circles can be plotted in Fig. 4.11. Similarly, from the bi-linear yield function, peak strength for each confining stress can be calculated.

Another important parameter is the corresponding equivalent plastic strain, as in our model the mobilized parameters are the function of it. To illustrate this calculation, we take the sample with 2500psi confining stress (total confining stress is 3000psi) as an example. At peak strength for this case, we have

$$\sigma_{shear}^{peak} = 11833.7psi$$

With unloading stress path to 0psi, we can calculate elastic axial strain and elastic radial strain as

$$\varepsilon_{e\_axial}^{peak} = \frac{\sigma_{shear}^{peak}}{E} = \frac{11833.7}{1133786.848} = 0.010437$$

$$\varepsilon_{e\_radial}^{peak} = -\varepsilon_{e_{axial}}^{peak} \times \nu = 0.010437 \times 0.12 = -0.001252$$

From the experiment data, we know that at peak strength the total strains are

$$\varepsilon_{t\_axial}^{peak} = 0.011622$$

$$\varepsilon_{t\_radial}^{peak} = -0.003173$$

Plastic strains are calculated as

$$\varepsilon_{p\_axial}^{peak} = \varepsilon_{t\_axial}^{peak} - \varepsilon_{e_{axial}}^{peak} = 0.011622 - 0.010437 = 0.001185$$

$$\varepsilon_{p\_radial}^{peak} = \varepsilon_{t\_radial}^{peak} - \varepsilon_{e_{radial}}^{peak} = -0.003173 + 0.001252 = -0.001921$$

Finally, equivalent plastic strain for this case at peak strength can be obtained

$$\varepsilon_{p\_eqv}^{peak} = \frac{2}{3}\left(\varepsilon_{p\_axial}^{peak} - \varepsilon_{p\_radial}^{peak}\right) = 0.00207$$

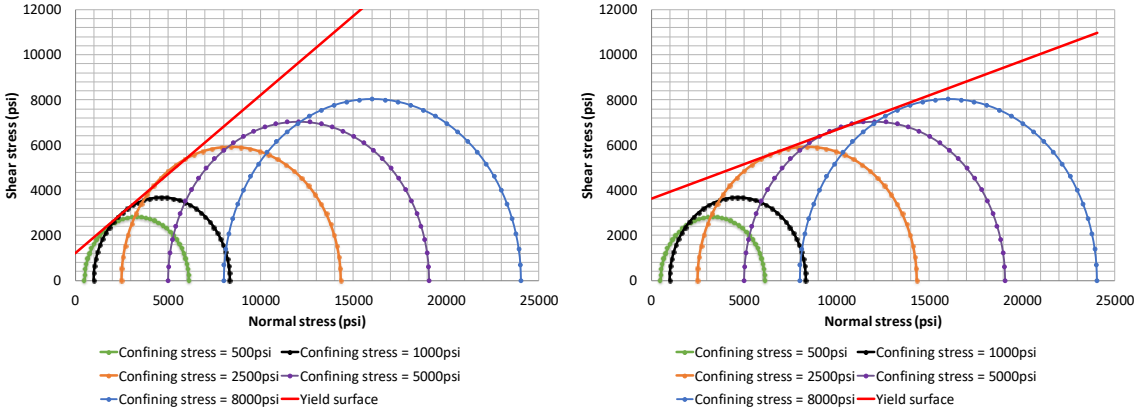

Fig. 4.11: Mohr circles for rock peak strength with bi-linear shear yield surface: low confining stress (left) and high confining stress (right)

Strength Reduction

With a further increase of plastic strain during post-yield deformation, we may observe a sharp reduction of rock strength, due to massive fractures developed from high compaction. This is also a critical status where stress and strain should be interpreted for the rock strength. By plotting these points in shear stress – normal stress curve, five Mohr circles under each confining stress are obtained. With the tangential lines of yield function, rock strength can be inferred. The corresponding equivalent plastic strain for each case is calculated as the same method elaborated before.

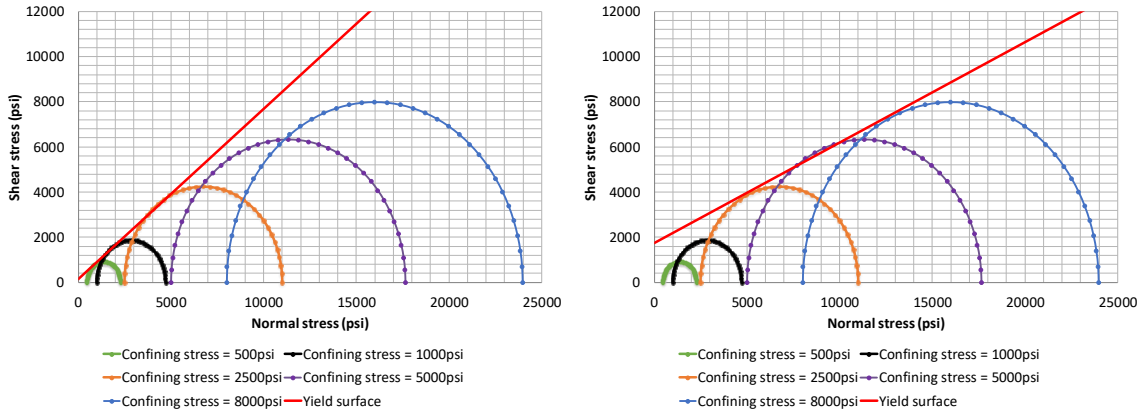

Fig. 4.12: Mohr circles for rock strength at sharp reduction with bi-linear shear yield surface: low confining stress (left) and high confining stress (right)

Residual Strength

The last critical strength is the residual strength, meaning the strength at which rock can sustain the compression before catastrophic failure. The residual strength at various confining stresses can be calculated from the same bi-linear yield function for Mohr circles at the status (Fig. 4.13). The associated equivalent plastic strain can be calculated from above equations.

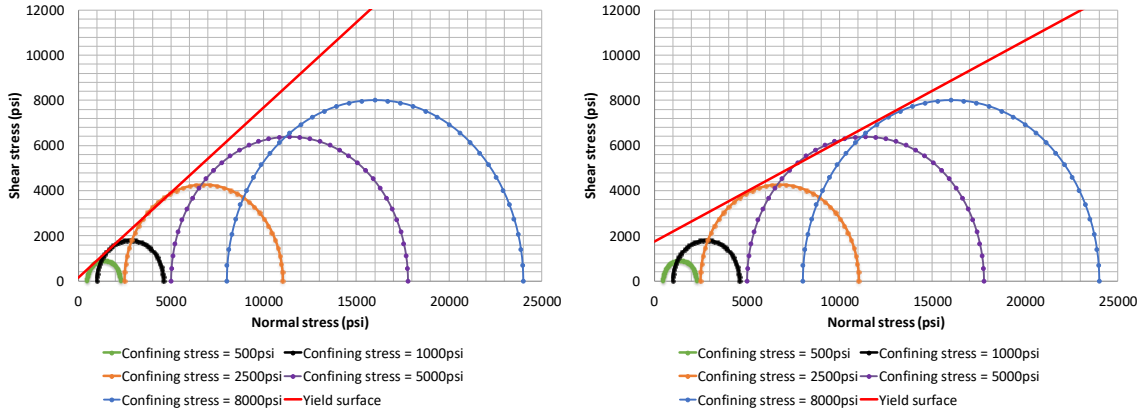

Fig. 4.13: Mohr circles for rock residual strength with bi-linear shear yield surface: low confining stress (left) and high confining stress (right)

From the above procedures, we can obtain rock mobilized plastic properties and corresponding equivalent plastic strain, as shown in Figs. 4.14 and 4.15. As the bi-linear yield function is used to better capture the yielding status for various confining stresses, two set of cohesion and internal friction angle are obtained.

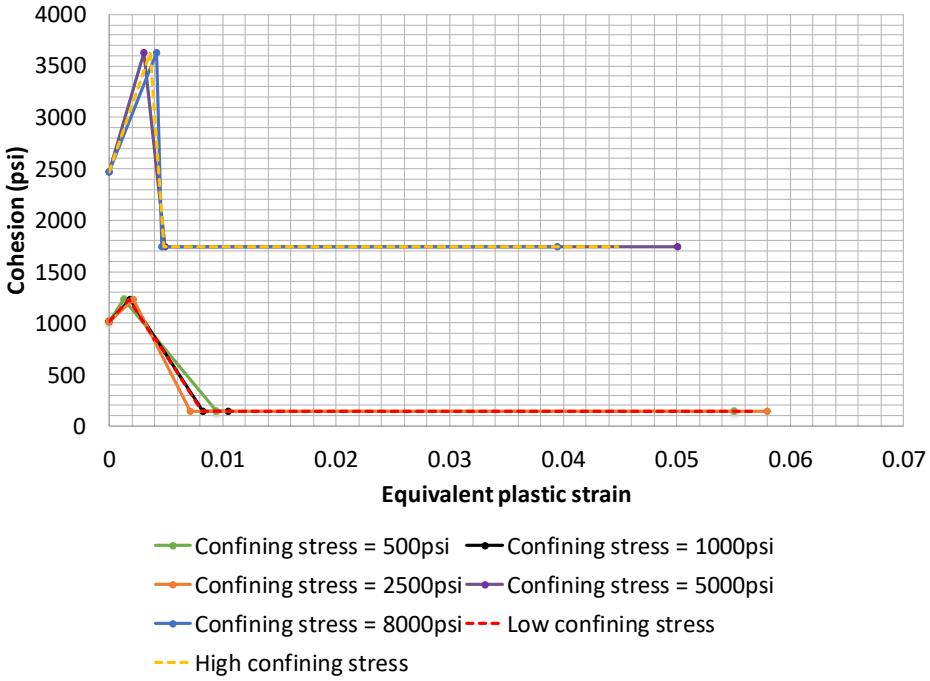

Fig. 4.14: Mobilized cohesions at low and high confining stresses

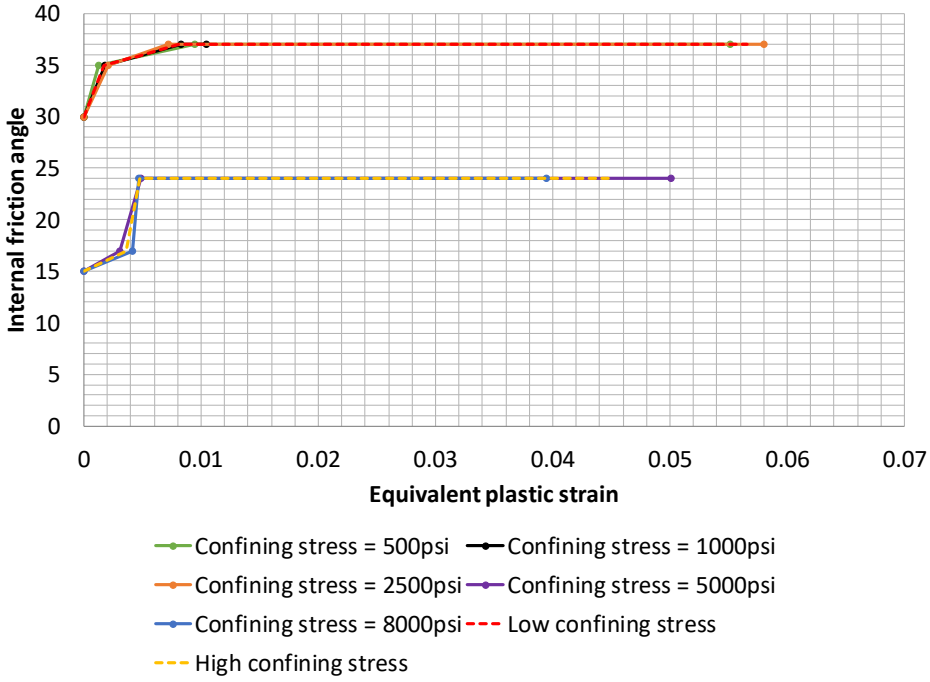

Fig. 4.15: Mobilized internal friction angles at low and high confining stresses

With all the calibrated elastic and plastic rock properties we can benchmark the stress-strain relation used in the simulation with those obtained from experiments and displayed in Fig. 4.16. The results show good agreement, suggesting that the calibrated rock properties are accurate enough to represent the mechanical properties of the rock.

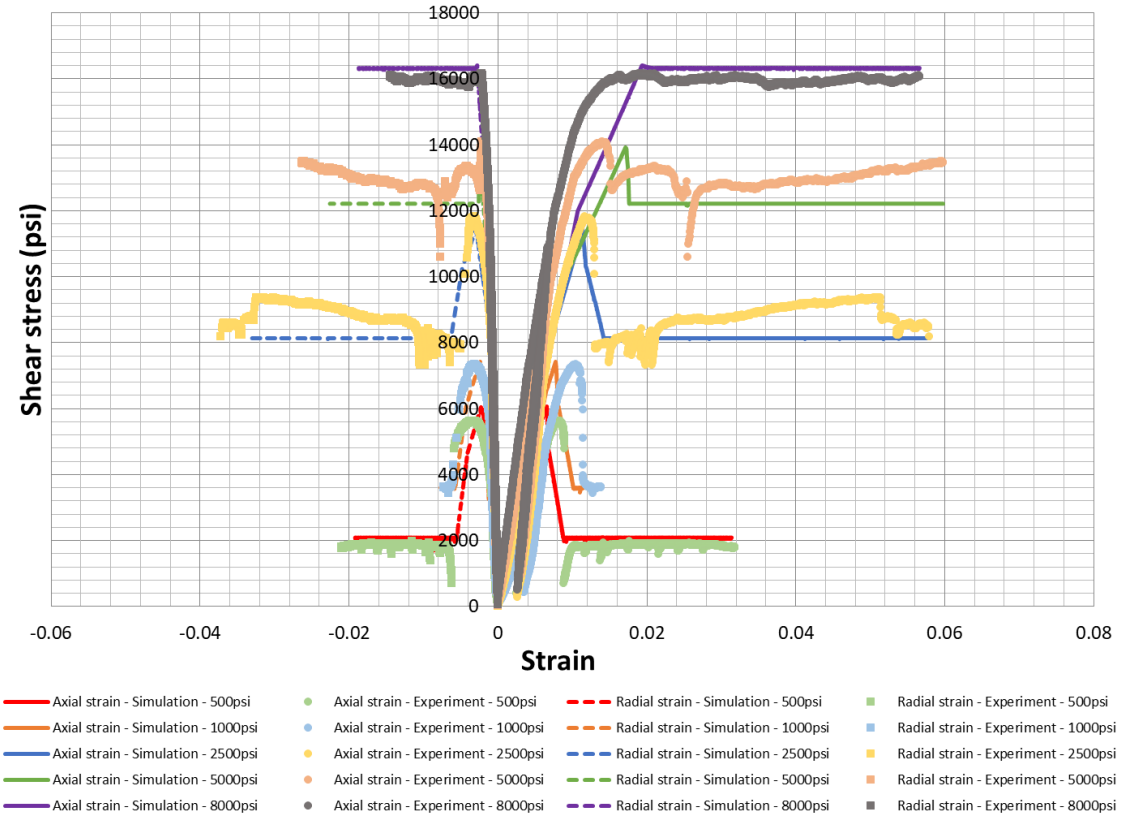

Fig. 4.16: Comparison of stress-strain curve between simulation and experiment

4.3.3 Validation of Sand Production

After the rock mechanical properties have been calibrated with experiments, we are able to model sand production for the thick-walled cylinder test. Results of sand production with confining stress in three cases are shown in Figs. 4.17 to 4.19. Both the onset of sanding sand sanding rate from simulations are comparable with the experiment data. In addition, the cavity shapes from the model after sanding are the same as those observed in the experiments (Figs. 4.20 to 4.22). To the best of our knowledge, this is the first model that can accurately predict both sand production and cavity shape after sanding.

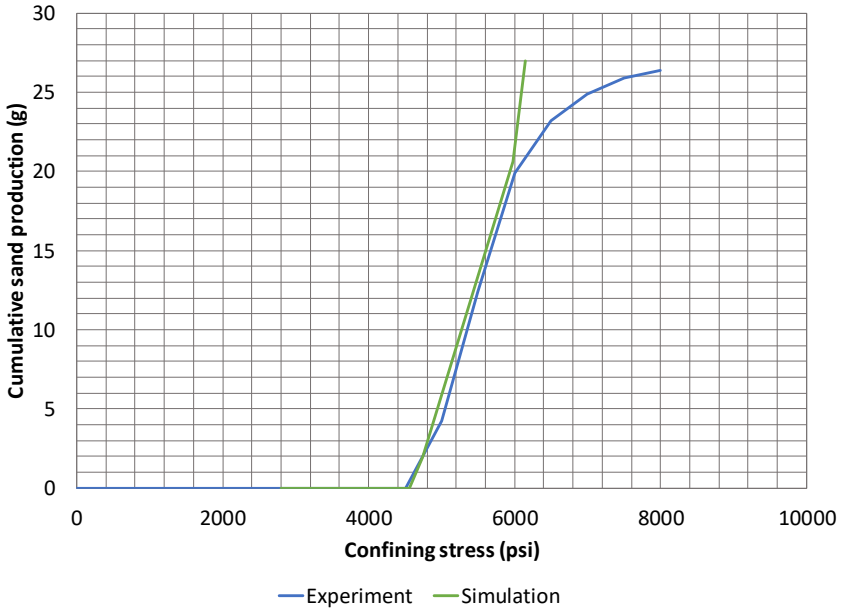

Fig. 4.17: Validation of sand production model with experiments for both the onset of sanding and sand production volume – sample A (4”×8”×0.63”)

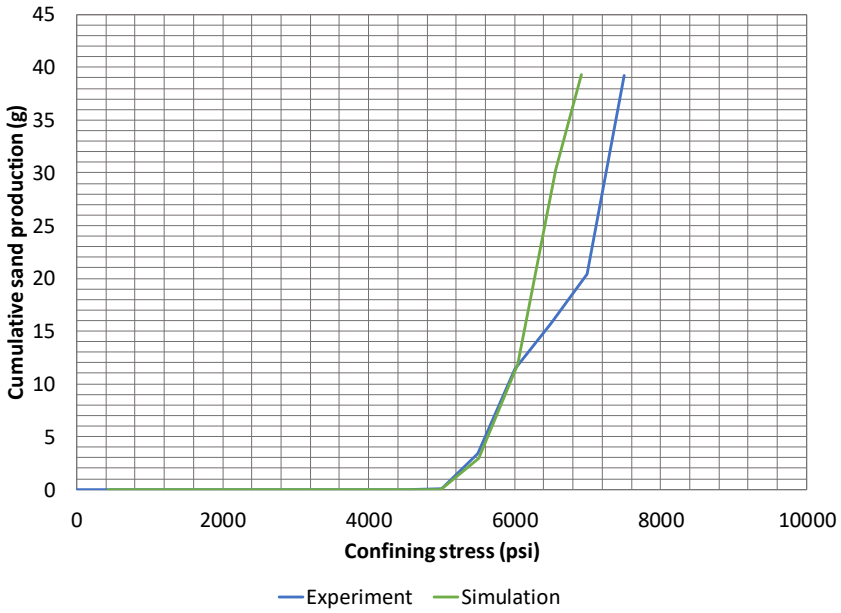

Fig. 4.18: Validation of sand production model with experiments for both the onset of sanding and sand production volume – sample B (3”×6”×0.5”)

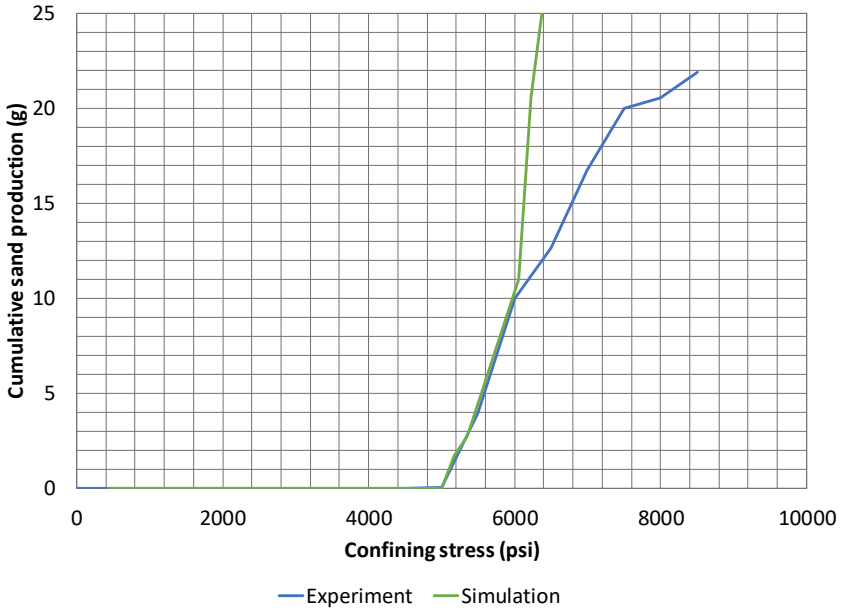

Fig. 4.19: Validation of sand production model with experiments for both the onset of sanding and sand production volume – sample C (4”×8”×0.5”)

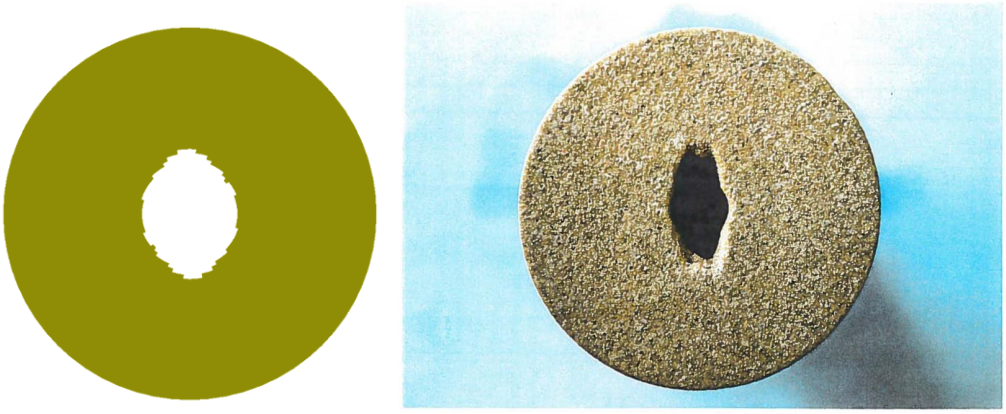

Fig. 4.20: Comparison of cavity shape after sanding: modeling result (left) and experimental result (right) – sample A (4”×8”×0.63”)

Fig. 4.21: Comparison of cavity shape after sanding: modeling result (left) and experimental result (right) – sample B (3”×6”×0.5”)

Fig. 4.22: Comparison of cavity shape after sanding: modeling result (left) and experimental result (right) – sample C (4”×8”×0.5”)

4.4 CONCLUSIONS

A sand production model has been developed using a general poro-elasto-plastic model. In the model, sanding criteria for the entrainment of sands consists of both mechanical failure (shear/tensile/compressive failure) and fluid erosion. Furthermore, a dynamic cell removal algorithm has been implemented to simulate cavity propagation during sand production and to calculate sanding rate and cumulative sand production. In

addition, to efficiently capture the transient plastic zone (especially shear/compaction bands), dynamic mesh refinement/un-refinement has been incorporated in the model.

The model is further compared with sand production experiments for validation. All rock properties are carefully calibrated using triaxial test data before using the model for sand prediction. The model shows good agreement with the experiment for the onset of sanding, cumulative sand production, as well as cavity shape after sanding. This is the first sand production model that has matched such experiments both quantitatively and qualitatively.

The model that is presented here is capable of predicting both the onset of sanding and sand production under single/multi-phase fluid flow in various well completions. It can be used to discover sanding mechanisms, determine sand control methods, and provide operational guidance on critical drawdown/velocity and well completion design. These aspects of the problem are explored in subsequent chapters.

REFERENCES

Bird, R. B., W. E. Stewart, and E. N. Lightfoot. 2007. Transport phenomena. *John Wiley & Sons.*

Barry, W. J., M. T. Jones, and P. E. Plassmann. 1998. Parallel adaptive mesh refinement techniques for plasticity problems. *Advances in Engineering Software, 29(3-6),* 217-225.

Deb, A., J. H. Prevost, and B. Loret. 1996. Adaptive meshing for dynamic strain localization. *Computer methods in applied mechanics and engineering, 137(3-4),* 285-306.

Morita, N., D. L. Whitfill, O. P. Fedde, and T. H. Lovik. 1989. Parametric study of sand production prediction: Analytical approach. *SPE Prod. Eng., 4:* 25–33.

Rahmati, H., M. Jafarpour, S. Azadbakht, A. Nouri, H. Vaziri, D. Chan, and Y. Xiao. 2013. Review of Sand Production Prediction Models. *Journal of Petroleum Engineering*, 2013, 1-16. doi: 10.1155/2013/864981.

Risnes, R., R. K. Bratli, and P. Horsrud. 1982. Sand stresses around a wellbore. *SPE J., 22:* 883–898.

Wang, Y. and M. B. Dusseault. 1996. Sand production potential near inclined, perforate wellbores. *CIM 47th Annual Technical Meeting. June10–12, Calgary, Alberta, Canada. Paper No. 96–27.*

Weingarten, J. S. and T. K. Perkins. 1992. Prediction of sand production in gas wells: Methods and Gulf of Mexico case studies. *J. Pet. Tech., 47:* 596–600.

Chapter 5: The Role of Elasto-Plasticity on Cavity Shape and Sand Production in Oil and Gas Wells[1]

5.1 INTRODUCTION

Previous experimental observations have shown the formation of distinct failure patterns and cavity shapes. When sands fail and produce, excessive deformations or cavities may form around wells and perforations, exhibiting different patterns due to different rock properties and stress conditions. Papamichos et al. (2000) quantitatively studied sand production under various flow and stress conditions. Results for isotropic stress conditions show a failure pattern that is dominated by shear failure bands with sand being produced from a localized region. This failure pattern has also been observed in other experiments (Meier et al., 2013). V-Shape and dog-ear breakouts are other common cavity shapes frequently observed in experiments conducted under anisotropic stress conditions (Papamichos et al., 2008; Sinaki, 2012; Haimson, 2007; Addis et al., 1990). On the other hand, in sandstones with high porosity a distinctive cavity shape, known as slit mode breakout, is found in several experiments under either isotropic (Papamichos et al., 2008) or anisotropic stress conditions (Haimson and Kovacich, 2003). Haimson and Kovacich (2003) further concluded that with a higher stress contrast, a longer slit length can be obtained. These cavity shapes are induced by different failure mechanisms, and these failure mechanisms have a significant effect on both the onset of sanding and the sand production rate. Comparing with experimental observations, Papamichos et al. (2004) numerically studied the propagation of breakouts for spiral shear banding, and further analyzed the breakout stability with circular holes and holes with pre-cut elliptical breakouts. However, very little research has been conducted to systematically study the different mechanisms of various breakouts and the conditions for distinguished cavity types

[1] The original source of this chapter is from Wang and Sharma (2017). Sharma supervised the project.

after sanding. The latter is found to be crucial in sand production prediction and sand control design.

5.2 Studying Failure Patterns in Various Cavity Shapes Around the Hole

So far, the most classic near-well failure patterns observed in the experiments or fields can be summarized as: Spiral shear band, V-Shape cavity, Dog-Ear cavity, and Slit mode cavity. The developed sand production model is used here to qualitatively benchmark these cavity shapes and study the mechanisms and conditions for each type of these patterns from the perspective of stress conditions, rock properties, and failure type.

5.2.1 Spiral Shear Band

Papamichos et al. (2000) conducted sand production tests on a thick-wall-cylinder rock sample. Under isotropic stress conditions, a spiral shear band cavity forms during sand production (left in Fig. 5.1). Later, Meier et al. (2013) observed a similar spiral shear band cavity from the experiment (right in Fig. 5.1). This distinct cavity shape is studied in our simulation to explore how and why such spiral patterns are formed.

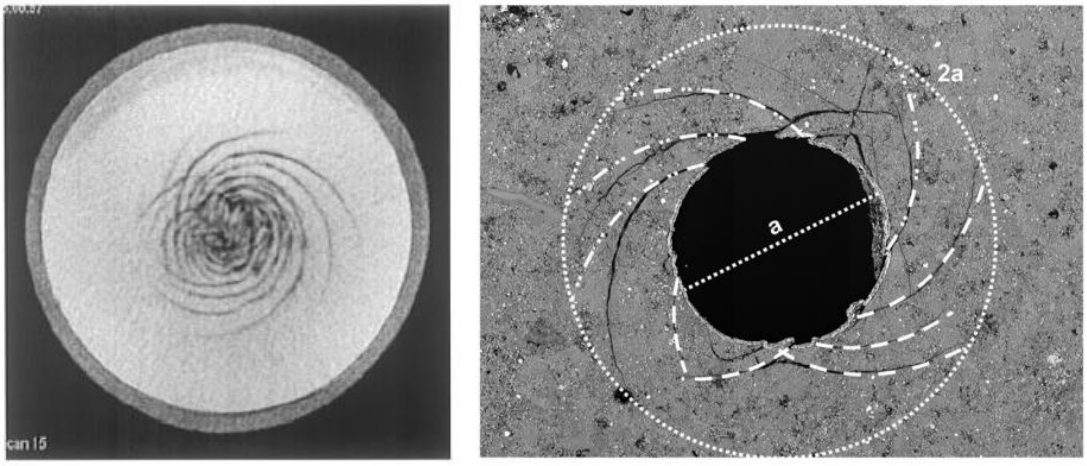

Fig. 5.1: Evidence of shear band cavity in experiments: Papamichos et al., 2000 (left) and Meier et al., 2013 (right)

Table 5.1 Rock and fluid properties for spiral shear band case

Parameters	Value	Unit
Young's modulus	0.3	GPa
Poisson's ratio	0.05	
Cohesion	0.5	MPa
Internal friction angle	30	deg
Tensile strength	0.173	MPa
Critical plastic strain	0.15	
Sand density	2650	kg/m^3
Sand grain diameter	180	micron
Porosity	0.36	
Permeability	3.6	Darcy
Biot's coefficient	1	
Fluid viscosity	0.001	Pa•s

Table 5.2 Dimensions of the TWC geometry

Dimension	Value	Unit
Cylinder diameter	0.06	m
Inner hole diameter	0.006	m

The inputs for the rock and fluid properties and the dimensions of the thick-wall-cylinder sample in our simulation case are displayed in Tables 5.1 and 5.2. In Case 1 we use non-associated plastic flow, where the dilation angle is 0, to represent shear compaction behavior of the rock. In Case 2, associated plastic flow is modeled to represent shear dilation behavior. Perfect plasticity is assumed to describe the post-yield behavior. Zero pressure and effective normal stress are applied on the inner hole surface, while a constant fluid pressure (2MPa) and increasing compressive stress are applied on the outside cylinder surface.

In Case 1, during early stages of the simulation when compression is small, the sand yields in shear and uniform shear plastic strain is developed around the hole (left figure in Fig. 5.2). However, when confining stress reaches the critical value, the hole loses its stability and hole surface becomes non-circular with a non-circular plastic strain contour

shown in Fig. 5.3. With further increase of confining stress, plastic strain is localized and gradually forms a spiral shear band (right figure in Fig. 5.2). The red colored zone in the right picture of Fig. 5.2 represents the shear failure zone, where sand has failed and is likely to be produced. With shear dilation behavior, however, we always observe uniform shear plastic strain around the hole from the simulation. Fig. 5.4 shows a comparison of the plastic strain for these two cases under the same confining stress.

To obtain this failure pattern, an isotropic stress is required to avoid any preferred localization path, and rock deforms with shear compaction. Also, shear failure is the main mechanism for sand production along the spiral shear band zone. During shear yield, strain softening is not necessary for this failure pattern, but it can accelerate the shear band localization (lower confining stress is required for the onset of failure). Furthermore, instead of increasing the compression on the outside cylinder boundary, if we maintain the compression to be the same while decreasing pore pressure on the inner hole surface, the same failure trend can be observed.

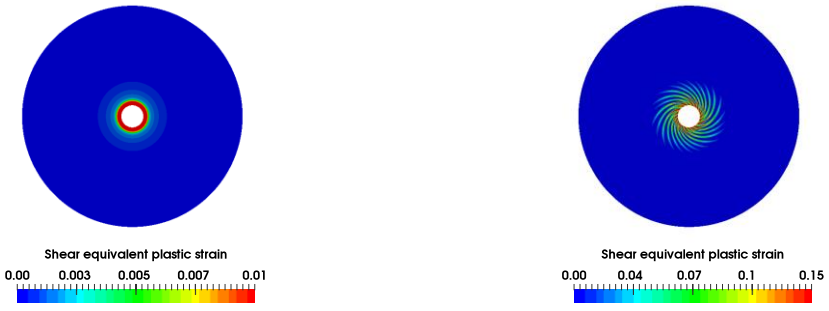

Fig. 5.2: Shear compactive rock - shear equivalent plastic strain with different compressive stress: 3MPa (left) and 5MPa (right)

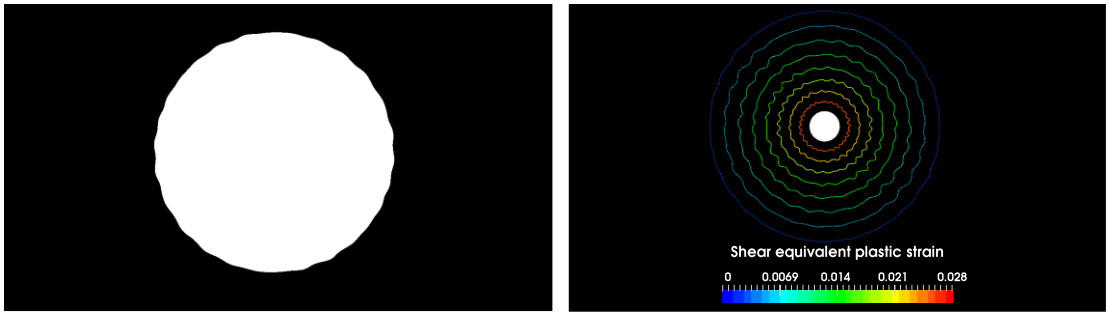

Fig. 5.3: Shear compactive rock - inner hole starts deforming non-circularly (left) with non-circular plastic strain (right)

Fig. 5.4: Comparison of shear plastic strain: shear compaction (left) and shear dilation (right)

5.2.2 V-Shape Cavity

Another cavity type commonly seen is a V-shape breakout. Fig. 5.5 shows the final cavity shape after sand production under anisotropic stresses (Sinaki, 2012). Two V-shape cavities are formed in the minimum horizontal stress direction around the hole. Haimson (2007) conducted tests on core samples from the Austin Chalk and also observed a V-shaped cavity after rock failure (right picture in Fig. 5.6). Two shear fractures first propagate from the borehole surface, and gradually interact with each other, leaving an isolated failure zone behind that forms the cavity. In our study, when we simulate sand failure and production from the low-cohesion, ductile rock under anisotropic stress, we obtained the same cavity type.

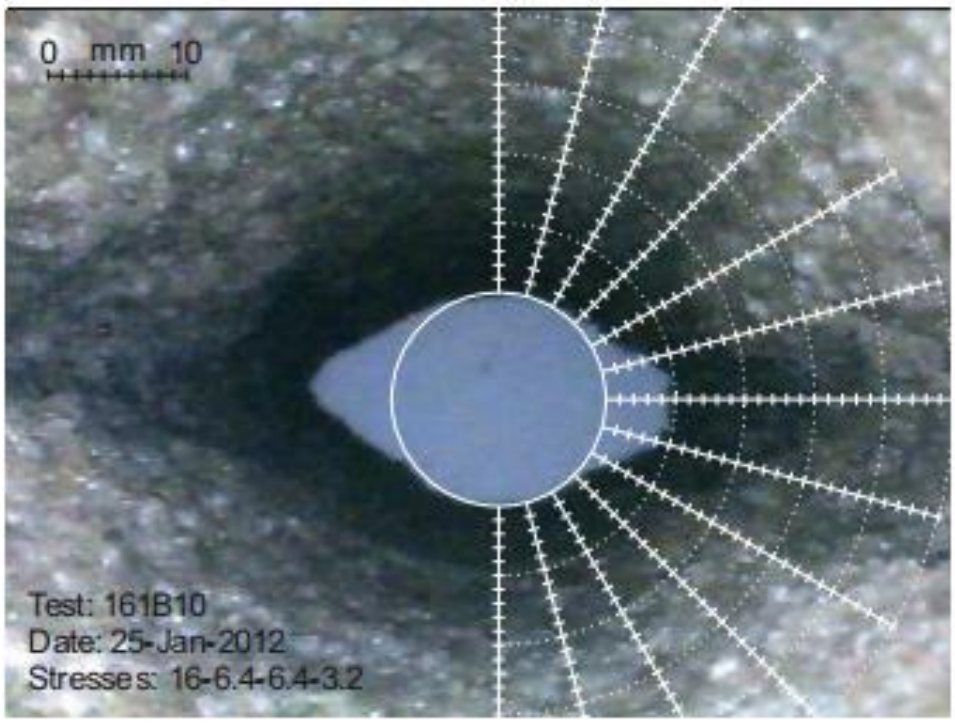

Fig. 5.5: Evidence of V-shaped cavity in the experiment (Sinaki, 2012)

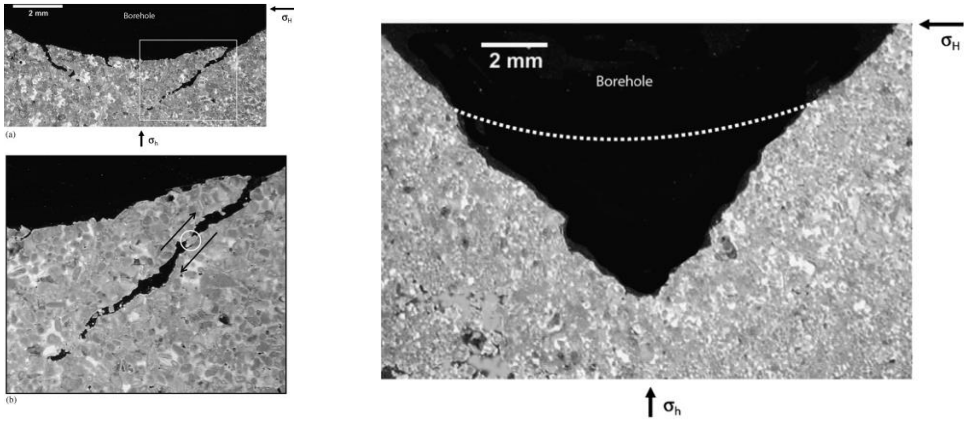

Fig. 5.6: The development of a V-shape cavity for Austin Chalk (Haimson, 2007)

Table 5.3 displays the inputs for the case, which are typical values for a poorly consolidated reservoir. The post-yield behavior is modeled with a strain hardening/softening model (details in Wang et al, 2016). The wellbore pressure decreases

from 25MPa to 21MPa (Fig. 5.7) to represent oil production. Anisotropic far field stresses are applied to model conditions as set up in the experiments above.

Table 5.3 Reservoir properties and dimensions in V-shaped cavity case

Parameters	**Value**	**Unit**
Young's modulus	1	GPa
Poisson's ratio	0.25	
Cohesion	2	MPa
Internal friction angle	20	deg
Dilation angle	0	deg
Tensile strength	0.57	MPa
Critical plastic strain	0.15	
Sand density	2650	kg/m^3
Sand grain diameter	100	micron
Porosity	0.25	
Permeability	1	Darcy
Biot's coefficient	1	
Fluid viscosity	0.005	Pa•s
Initial pore pressure	25	MPa
Minimum horizontal stress	28	MPa
Maximum horizontal stress	32	MPa
Vertical stress	35	MPa
Reservoir length	20	m
Reservoir width	20	m
Reservoir height	10	m
Wellbore diameter	0.2	m

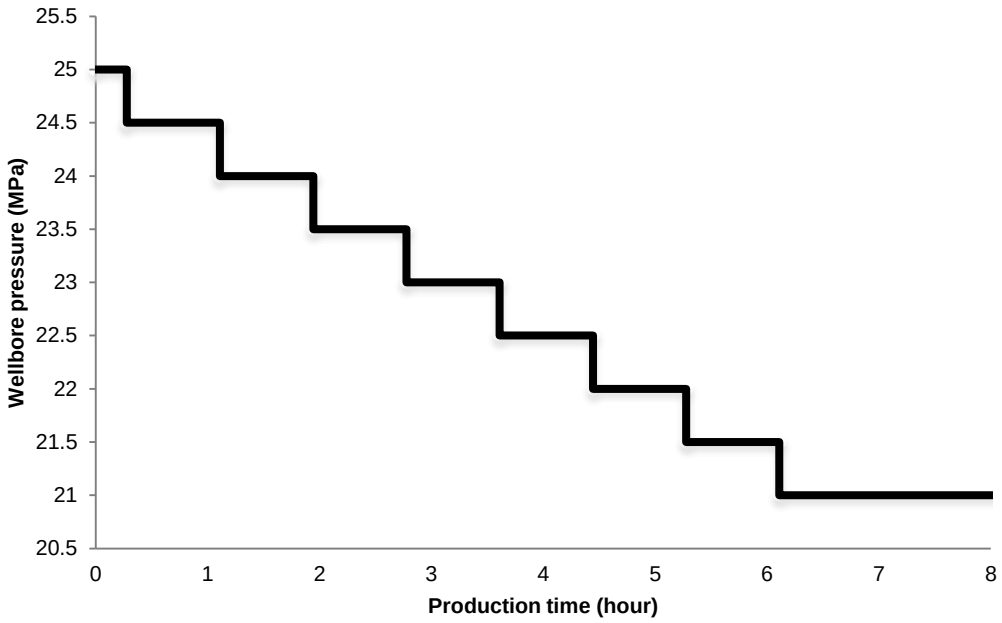

Fig. 5.7: Wellbore pressure changes with time

The shear equivalent plastic strain and cavity shape around the wellbore are shown in Figs. 5.8 to 5.10. During early time (3.06 hour), strain localization develops along the minimum horizontal stress direction, and sanding initiates on the wellbore surface where the equivalent plastic strain is larger than the critical plastic strain. The cavity continues to propagate along the shear bands due to high plastic strain and sufficient fluid velocity to erode failed sand grains (Fig. 5.9). At a production time of 3.61hr, the two shear fractures on each side intersect, detaching a portion of intact sand from the main sand body. The cavity propagation process and the final V-shaped cavity from the simulation are exactly the same as observed in the experiments. It can be concluded that the V-shaped cavity can be induced by the anisotropic stresses and the resulting shear failure that is induced. In addition, we found during sand production, the produced sands are composed of both sand grains and sand in bulk.

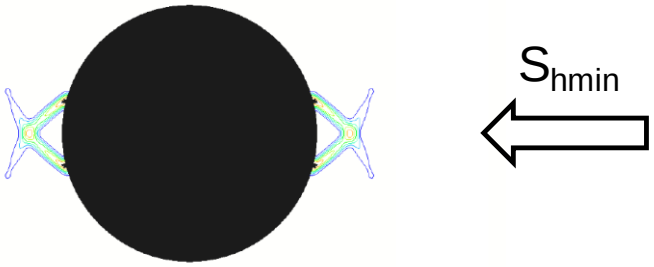

Fig. 5.8: Sand initiation at production time = 3.06h

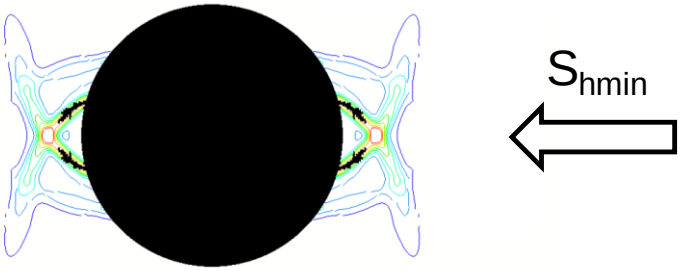

Fig. 5.9: Cavity production along shear band at production time = 3.33h

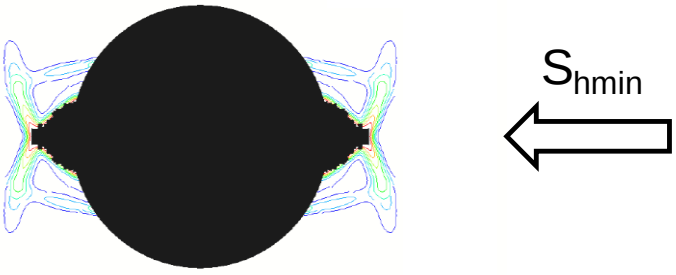

Fig. 5.10: V-Shape cavity forms at production time = 3.61h

5.2.3 Dog-Ear Cavity

The third cavity type caused by sand production is the dog-ear breakout. It has been observed under both isotropic and anisotropic stress conditions, along with large plastic deformations in localized bands. Fig. 5.11 shows how the shear bands develop along the minimum horizontal stress direction around the hole, leading to plastic deformations in a dog-ear shape where sand is likely to fail and produce (Addis et al., 1990). Other experiments show the dog-ear shaped cavities resulting from sand production. Such cavities continue to propagate along the strain localized region with a preferred direction, even under isotropic stress conditions (Papamichos et al., 2008). It may be caused by the heterogeneity of the sample. This cavity type was also studied in our simulations with the same parameter set as for the in V-shaped cases, but for a longer time.

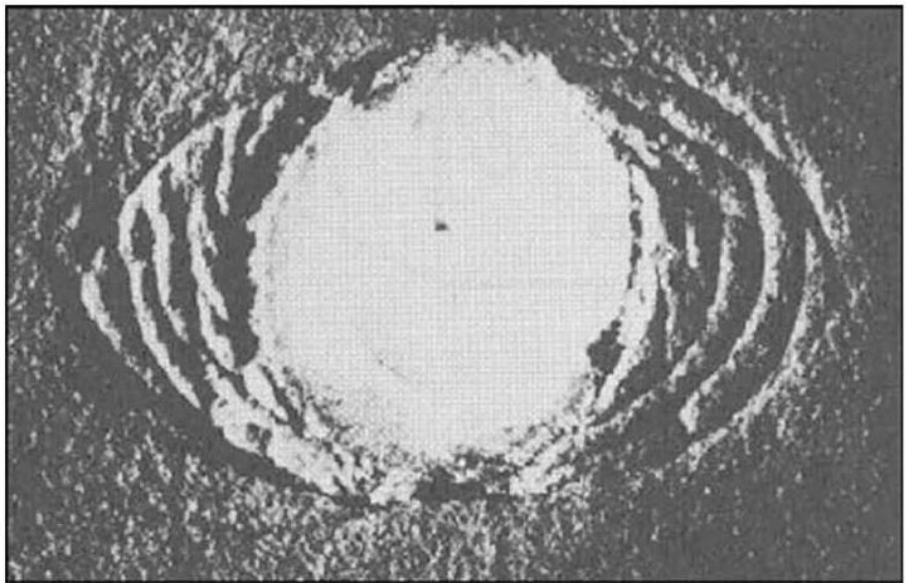

Fig. 5.11: Shear bands develop around a hole in a dog-ear shape (Addis et al., 1990)

Fig. 5.12: Dog-ear cavity around hole after sand production (Papamichos et al., 2008)

After the V-shaped cavity forms (Fig. 5.10), the arch is relatively stable and can hold in a sand free condition until the bottom-hole pressure decreases further. At a lower wellbore pressure, sand starts to be produced again with a high flow rate, along the failure region where the equivalent plastic strain is larger than the critical one. A dog-ear cavity forms after 5 hours of fluid production in the simulation, as shown in Fig. 5.13. The sanding occurs both ahead of the tip of the V-shaped cavity and on the surface of the borehole surface. Due to strain localization, the cavity always propagates along these shear bands. This agrees with the dog-ear cavity in the experiment (Fig. 5.12). On the other hand, rock may experience extensive plastic strain if flow rate is not sufficient to erode sands. To obtain the observation similar to Fig. 5.11, we simply turn off the sand erosion criterion so

that rock continues to deform without being removed. Consequently, the result of plastic strain is plotted in Fig. 5.14, which is constant with the experiment. Based on the model, anisotropic stresses are required for a dog-ear cavity shape. In addition, shear failure triggered by the localized plastic strain is the dominant sanding mechanism for this type of cavity.

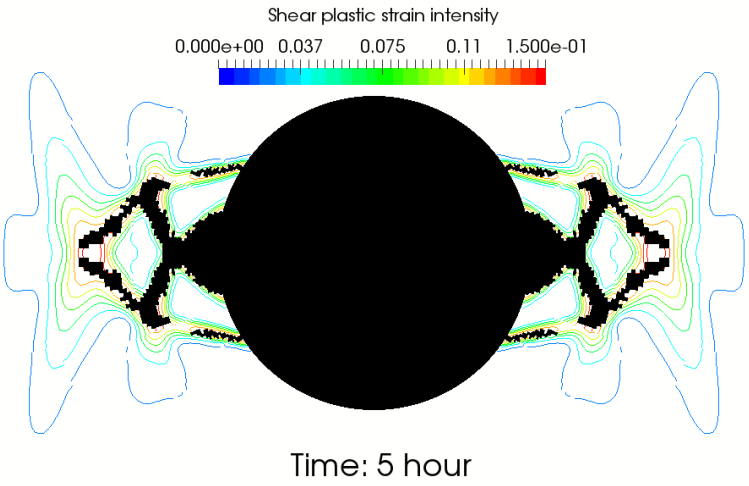

Fig. 5.13: Dog-ear cavity around the borehole with sand production in the simulation

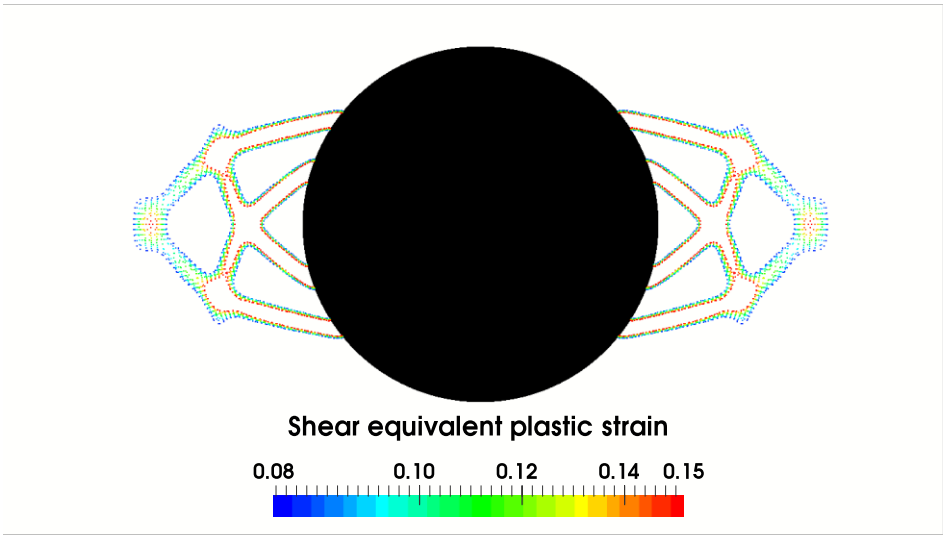

Fig. 5.14: Dog-ear cavity around the borehole without sand production in the simulation

5.2.4 Slit Mode Cavity

The last cavity type frequently observed in experiments is the slit mode cavity. Unlike previous failure patterns, this cavity type often appears in rocks with high porosity and low compressive strength. Fig. 5.15 shows the experiment results of slit mode cavity propagation under isotropic stress (Papamichos et al., 2008). However, this cavity mode is more commonly observed under anisotropic stress conditions. Haimson and Kovacich (2003) conducted tests and revealed the relationship between the cavity length and stress contrast (Fig. 5.16). The larger the stress contrast, the longer the slit mode cavity length. In addition, they showed the breakouts extend to the bottom of the rock, all along remaining orthogonal to maximum horizontal stress direction. In order to study this cavity shape, the cap model is implemented to capture compressive failure.

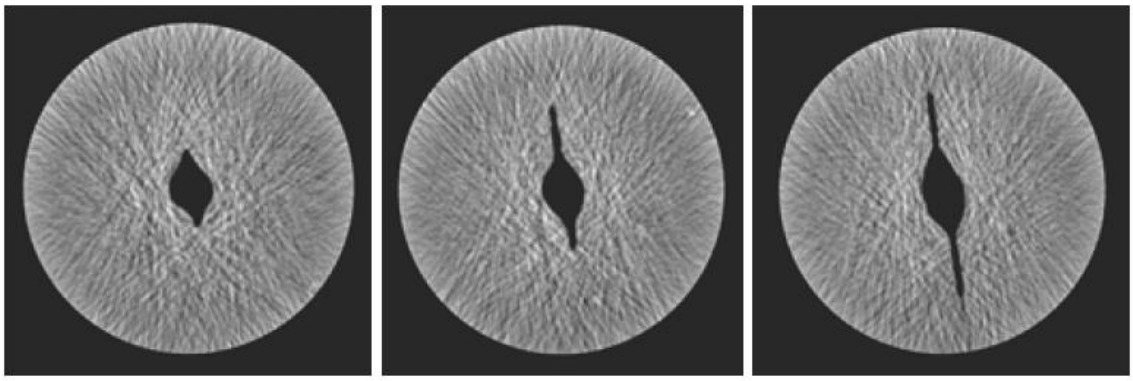

Fig. 5.15: Slit mode cavity under isotropic stress conditions in experiments (Papamichos et al., 2008)

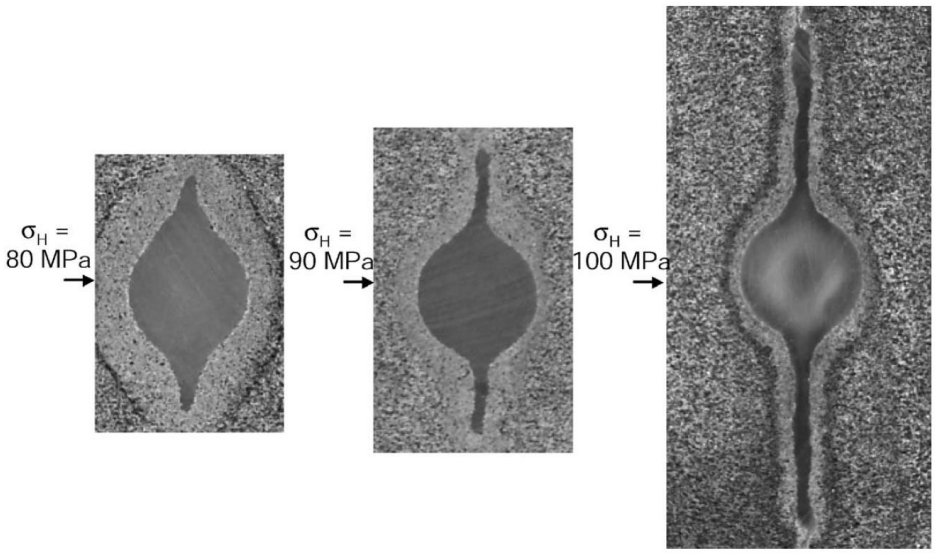

Fig. 5.16: Slit mode cavity under anisotropic stress conditions in experiments (Haimson and Kovacich, 2003)

In this study, we set up a thick wall cylinder test simulation (2D plane strain) to simulate sand production under isotropic stress. Table 5.4 shows the rock properties used for this simulation. Cohesion and tensile strength are set as large values to avoid shear and tensile failure. The cap pressure remains constant throughout the simulation. A smaller cap pressure is applied on two cells opposite on the hole surface representing a small heterogeneity in the compressive strength. Results for cavity development are shown on Fig. 5.17 along with the pressure distribution. With an increase in compression on the outside cylinder surface, a large region of compaction forms until gradually the mean effective stress exceeds the cap pressure, resulting in the compressive yielding of the rock. When the compressive plastic strain exceeds the critical plastic strain, sanding occurs first on the two cells with low cap pressure (higher compressive plastic strain) and they eventually propagate like a fracture.

Table 5.4 Rock properties in slit mode cavity case

Parameters	Value	Unit
Young's modulus	3	GPa
Poisson's ratio	0.15	
Cohesion	70	MPa
Internal friction angle	35	deg
Dilation angle	35	deg
Tensile strength	25	MPa
Critical plastic strain	0.2	
Sand density	2650	kg/m^3
Sand grain diameter	100	micron
Porosity	0.25	
Permeability	1.2	Darcy
Biot's coefficient	1	
Fluid viscosity	0.005	Pa•s
Cap pressure	15	MPa

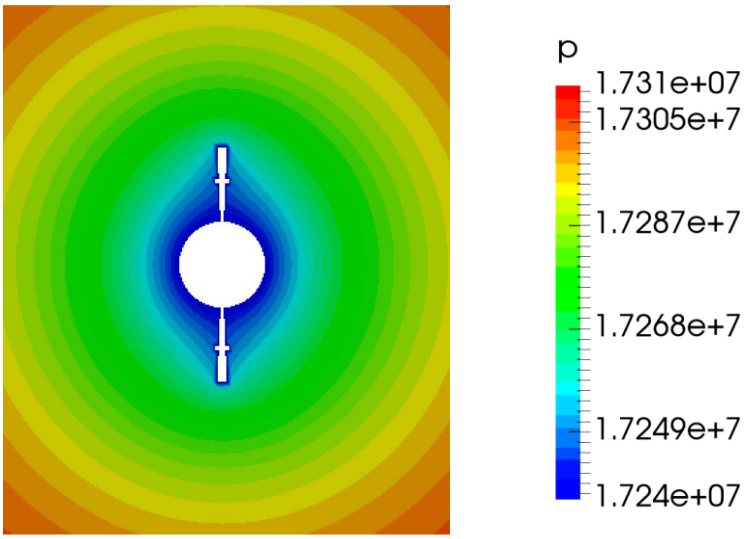

Fig. 5.17: Slit mode cavity under isotropic stress conditions from the simulations

5.3 Factors Controlling the Cavity Shape

It is evident from the simulation results presented thus far that the cavity shape and the rate of sand production depend on the stress and pressure conditions as well as the properties of the sand. A parametric study was conducted to study the effect of the different

parameters on the onset of sand production and the rate of sand production. While it is not possible to capture all these trends in a simple manner some general trends are qualitatively illustrated in Fig. 5.18. If the mean effective stress is high (rock is more likely to fail in compression), a slit mode cavity is likely to form. Otherwise, the cavity shape is dependent on the stress contrast and drawdown. With a small stress contrast, spiral shear band cavities may develop after the hole loses its integrity. On the other hand, if the stress contrast is high, a small drawdown may result in a V-shaped cavity, while a large drawdown will lead to a dog-ear breakout. These trends are qualitative, since the magnitude for each parameter is also a function of rock intact and post-yield strength. More quantitative trends depend on the magnitude of a range of parameters that include the mechanical properties of the sand and many other fluid and failure parameters.

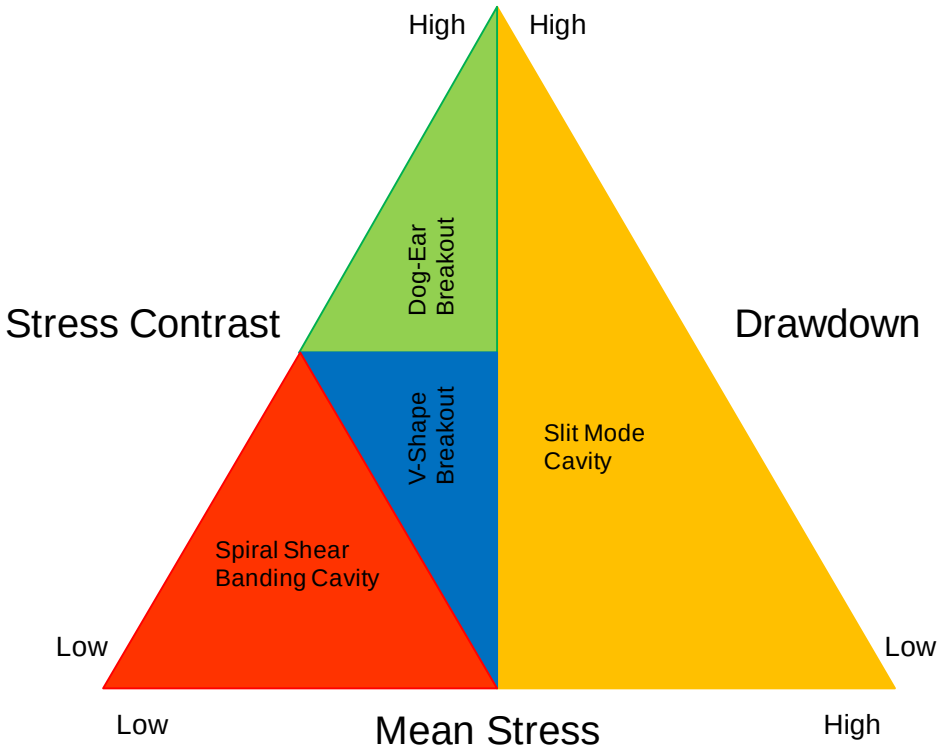

Fig. 5.18: Likely cavity shapes under different conditions

5.4 CONCLUSIONS

We have developed a fully coupled poro-elasto-plastic, 3D sand production model. It has been validated with various analytical solutions. The model is applied to study sanding mechanisms for the different cavity shapes that have been observed in experiments and in the field. Some key conclusions are summarized below:

- The model results match very well with experiments for all cavity shapes;
- For spiral shear band cavities, V-shaped cavities and dog-ear cavities, shear failure is the main mode of sand failure;
- For slit mode cavity, compressive failure dominates sand production;
- Strain localization plays an important role in the development of V-shaped cavities and dog-ear shaped cavities;
- In field operations, during early production (when mean effective stress and drawdown is small), a spiral shear banding cavity and V-Shaped breakouts are more likely to form if sand production occurs. With larger drawdown, a V-shape cavity cannot remain stable and the sand production induced cavity may propagate like a dog-ear.
- For a depleted reservoir, we should expect a slit mode cavity caused by high mean effective stress.

In addition to the mechanical properties of the sand, it is shown that the stress contrast, drawdown, and the mean effective stress are the primary parameters that determine the type of failure mechanism and the shape of the cavity formed. Based on a parametric study conducted with the model, general qualitative guidelines are obtained that define the conditions for which each type of cavity will form.

REFERENCES

Addis, M. A., N. R. Barton, S. C. Bandis, and J. P. Henry. 1990. Laboratory studies on the stability of vertical and deviated boreholes. *In SPE Annual Technical Conference and Exhibition. Society of Petroleum Engineers, 1990.*

Dake, L. P. 1978. Fundamentals of Reservoir Engineering. *Elsevier Scientific Publishing Co., NY.*

Detournay, E. and A. H. D. Cheng. 1993. Fundamentals of poroelasticity. *In Comprehensive Rock Engineering: Principles, Practice & Projects, Vol. II, Analysis and Design Method: 113-171.* Pergamon Press.

Haimson, B. 2007. Micromechanisms of borehole instability leading to breakouts in rocks. *International Journal of Rock Mechanics and Mining Sciences, 44(2),* 157-173.

Haimson, B. and J. Kovacich. 2003. Borehole instability in high-porosity Berea sandstone and factors affecting dimensions and shape of fracture-like breakouts. *Engineering Geology, 69(3),* 219-231.

Meier, T., E. Rybacki, A. Reinicke, and G. Dresen. 2013. Influence of borehole diameter on the formation of borehole breakouts in black shale. *International Journal of Rock Mechanics and Mining Sciences, 62,* 74-85.

Papamichos, E., A. Skjærstein, and J. Tronvoll. 2000. A volumetric sand production experiment. *Paper presented at the 4th North American Rock Mechanics Symposium. American Rock Mechanics Association, 2000.*

Papamichos, E., J. Stenebraten, P. Cerasi, A. Lavrov, I. Vardoulakis, G. F. Fuh, M. Brignoli, Goncalves CJ de Castro, and O. Havmoller. 2008. Rock type and hole failure pattern effects on sand production. *Paper presented at the 42th US Rock Mechanics Symposium and 2th US-Canada Rock Mechanics Symposium, San Francisco, CA, USA, June 2008.*

Papamichos, E., P. Liolios, and P. J. Van den Hoek. 2004. Breakout stability experiments and analysis. *Paper presented at the 6th North America Rock Mechanics Symposium (NARMS). American Rock Mechanics Association.*

Salencon, J. 1969. Contraction quasi-statique d'une cavite a symetrie spherique ou cylindrique dans un milieu elastoplastique. *In Annales des ponts et chaussées*, 4: 231-236.

Sinaki, A.R.Y. 2012. Sand production simulation under true-triaxial stress conditions.

Wang, H. and M. M. Sharma. 2016. A fully 3-D, multi-phase, poro-elasto-plastic model for sand production. *In SPE Annual Technical Conference and Exhibition. Society of Petroleum Engineers, 2016.*

Wang, H. and M. M. Sharma. 2017. The Role of Elasto-Plasticity in Cavity Shape and Sand Production in Oil and Gas Wells. *In SPE Annual Technical Conference and Exhibition. Society of Petroleum Engineers, 2017.*

Wang, H., P. Cardiff, and M. M. Sharma. 2016. A 3-D poro-elasto-plastic model for sand production around open-hole and cased & perforated wellbores. *Paper presented at 50th US Rock Mechanics Symposium, Houston, Texas, USA, June 2016.*

Chapter 6: Effect of Well Completions on Sand Failure and Production[2]

6.1 INTRODUCTION

In unconsolidated reservoirs, minimizing the sand failure is one of the most crucial components in the oil and gas production well design. Geometry of the well and its operational conditions can substantially impact the integrity of the wells. Understanding the significance of sand failure affected by well designs and operational conditions can help to maintain the operability of the well over a long period of time without decreasing the well's performance.

For production wells handling high flow rates, high drawdown in the near-wellbore region over long-term production significantly affects the integrity of the well as sand is produced due to shear or compressive failure (Wang and Sharma, 2017). In producers, the evidence of sand production is obvious since failed sands are transported to the surface if the flow rate is sufficient. In injection wells, unexpected shut-in induced water hammer may lead to dramatic sand failure around the well and perforations (Wang et al., 2018; Vaziri et al., 2007). Further, water injection induced fractures may change the flow pattern and redistribute the stresses around the well (Ye et al., 2017).

Maintaining wellbore integrity is a critical operational issue for production wells in poorly consolidated sands. Designing production wells and determining their safe operational conditions requires careful attention. Prediction of sand failure caused by high pressure drawdown or high flow rate can be used to optimize choke operations. Simulation and analysis can help explain the physics of sand failure and predict the integrity of well completions in poorly consolidated reservoirs. Sizing of well completion components and understanding its impact on sand failure are the key decisions in the design of well

[2] The original source of this chapter is from Wang et al. (2016) and Hwang et al. (2017). Sharma supervised all the projects. Hwang plotted and analyzed the results.

completions. They can be optimized to soften the impact of prolonged high drawdown and the associated sand production.

Another crucial factor for sand control design is the well completion type. So far, most sanding-related studies have focused on sanding prediction and control in open-hole completions by assuming axisymmetric conditions or plane strain, which is enough for such simple geometries (Papamichos et al., 2001; Nouri et al., 2006). However, few models are able to predict sand production in complex geometries, i.e. perforated wellbores with multiple oriented perforations, with or without fractures. Wang and Dusseault (1996) implemented a poroelastic approach for sand production initiation showing that perforation orientation is a first-order factor in sand initiation. Later, Papanastasiou and Zervos (1998) performed a comprehensive stress analysis around perforated wellbores and showed that all perforations have high hoop stress in the lateral faces, caused by vertical in-situ stress. They also found that both wellbore and perforation orientation have a great effect on sanding potential. Zhang et al. (2007) studied the perforation tunnel stability by analyzing the stress distribution for different perforation density, implying that tunnels with lower perforation density are more stable. These results qualitatively and indirectly demonstrate that wellbore and perforation geometries are crucial to sand production. On the other hand, many other well completions including frac-packs have shown their effectiveness in sand control (Hainey and Troncoso, 1992). Papanastasiou and Zervos (1998) conducted a 3-dimensional stress analysis of a wellbore with a fracture and concluded that a propped fracture will give rise to an increase in compressive stress around a perforation, which increases with propped width. However, the impacts of different well completions on wellbore stability and sand failure/production have not been systematically studied or compared.

Numerically simulating sand failure and production can help understand the mechanism of sand failure. However, the geometric effects of the well, well completion types, failure mechanisms involving plasticity and compressive failures, have not been systematically investigated with numerical simulations. In this work, a 3-dimensional finite-volume sand production simulator which fully couples multi-phase fluid flow and poro-elasto-plasticity with a Modified Mohr-Coulomb Cap model, is used to study the sanding mechanism around the well and fracture. It is then used to predict the potential region of sand failure and the severity of sand production.

We constructed simulation cases for well completions used in unconsolidated sand reservoirs including open-hole frac-pack (OHFP), cased-hole frac-pack (CHFP), and open-hole completions with stand-alone screen (OH-SAS) or open-hole gravel packs (OHGP). In this chapter, we address the OH-SAS or OHGP as the same type of open-hole (OH) completions for simplicity to better understand near-wellbore rock failure mechanisms. Completion types are implemented by using different geometries and boundary conditions. Pore pressure, effective stresses, plastic strain, and the extent of sand failure are computed and presented in this chapter for various simulation cases representing well completion types.

6.2 Stress and Sand Failure Analysis in Multiple Well Completions

In this section, we evaluate the effect of well completion design on sand failure with numerical simulation methods (Hwang et al., 2018). The sand failure/production model developed in earlier chapters is used to predict the risk and severity of sand failure and production. The detailed objectives of this study include:

- Predict sand failure and sand production caused by well completion designs including OH, OHFP and CHFP.

- Show the effects of well designs, such as fractures, frac-pack width, pressure drawdown pattern on shear failure, hoop stress, compressive failure, and sand failure patterns.
- Study the impact of rock properties such as the post-yield behavior on high-drawdown-induced sand failure.

6.2.1 Simulation Setup

The mechanical integrity of the well after the drilling and completion is different from the state before the well is drilled. For example, the application of a frac-pack completion changes the hoop stress of the well substantially. The proppant placed in the frac-packs keep the fracture open during production over a long period of time. The impact of stress conditions altered by well completions, must be accounted for to comprehend the sand failure mechanisms.

The sand-control performance of a well in a poorly consolidated sand, is affected by several factors. For the type of well completions, the existence of a fracture with proppant greatly alters the initial hoop stress of the production well. The pattern of pressure drawdown influences the plastic strain distribution. The shear failure pattern in a frac-packed well can be significantly different from an open-hole well completion without a fracture.

The width of the frac-pack is also a critical parameter that determines the altered hoop stress condition. If the well is cased, the bore-hole boundary condition is no-flow and no-displacement due to the casing and cement. In such a completion, the hoop stress effect diminishes, and sand failure occurs primarily around the perforation and shear failure is minimized with the application of cased-hole completions. We also focused on the

individual impact of rock properties including post-yield behavior. Strain-softening rocks exhibit a large increase in the extent of shear failure.

Table 6.1 Input parameters for studying the impact of completion types

Parameters	**Value**	**Unit**
Oil viscosity	0.005	Pa·s
Young's modulus	15	GPa
Poisson's ratio	0.25	
Cohesion	0.5	MPa
Friction angle	30	deg
Dilation angle	0	deg
Tensile strength	0.78	MPa
Critical plastic strain	0.008	
Porosity	0.25	
Permeability	0.0001	Darcy
Initial pore pressure	56.55	MPa
Minimum horizontal stress	63	MPa
Maximum horizontal stress	68	MPa
Vertical stress	70	MPa
Reservoir length, *x*-direction	100	m
Reservoir length, *y*-direction	100	m
Wellbore diameter	0.2	m
BHP drop rate	10	MPa/day
Residual cohesion	0.3	MPa
Critical cap pressure	15	MPa

To take into account the impact of the above factors, Base Case simulations were set up for well completion cases including open-hole, open-hole frac-packs, and cased-hole frac-packs. The individual effects of the factors influencing sand production are simulated by modifying relevant parameters. The input parameters for the Base Case simulations are summarized in Table 6.1. The table also contains parameters used for strain-softening and

compressive failure. The following factors are changed to simulate the pressure/stress distributions, plastic strain, and sand failure responses:

- Borehole flow/deformation boundary conditions
- Existence of fracture
- Frac-pack width
- Constitutive formulations (Poro-elasto-plasticity and poro-elasticity)
- Rock post-yield behavior (strain softening or perfect plasticity)
- Failure criterion in shear and compression (Mohr-Coulomb model with and without a cap model)

6.2.2 Effect of Well Completions on Sanding

The type of well completion in a poorly consolidated reservoir impacts the sand failure behavior substantially. The flow-mechanics boundary conditions on the borehole surface and the existence of fractures are the crucial controlling parameters for stress distributions and failure patterns.

By using the input parameters in Table 6.1, the pressure and mechanical responses, and failure regions are simulated as shown in Fig. 6.1 for an open-hole (OH) completion with no frac-pack. The well radius of 0.1m was used for all the simulations in this section. The initial reservoir and wellbore pressures are kept constant with a constant pressure drawdown rate of 10 MPa/day for all simulations in this work. The simulations were run for 1 day of production, unless otherwise indicated.

In Fig. 6.1a, the radial pressure gradient is observed for a single vertical well. The maximum plastic strain is approximately 8.5×10^{-2} at the sand face. The shear failure region propagates in a V-shaped pattern in the horizontal minimum stress (S_{hmin}) direction. Note that S_{hmin} is in the y-direction and S_{Hmax} is in the x-direction for all cases in this chapter.

For this particular simulation, a gradual profile of plastic strain and associated V-shaped wellbore breakout are induced by production. Under a different set of parameters, a band-type of plastic strain and associated failures can be observed.

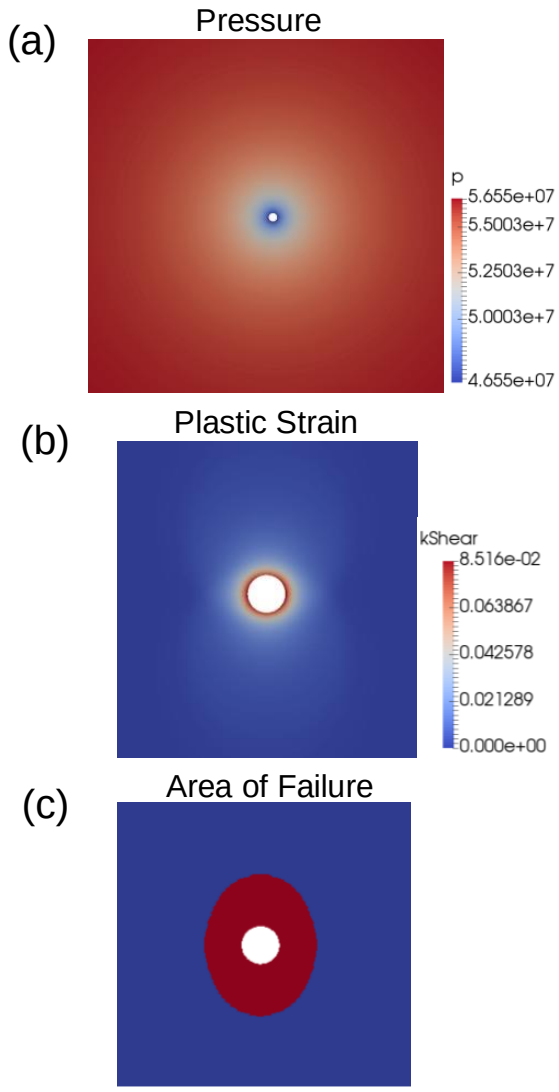

Fig. 6.1: Results of sand failure simulation for open hole completions (without frac-pack) at t =1 day. The radius of hole is 0.1 m. For all simulation cases shown in this paper, the hole size remains the same as 0.1 m radius, and the final simulation time is 1 day unless otherwise mentioned. (a) Pressure profile in map-view. The unit of pressure is Pa. (b) Magnitude of plastic strain. (c) Area of failure

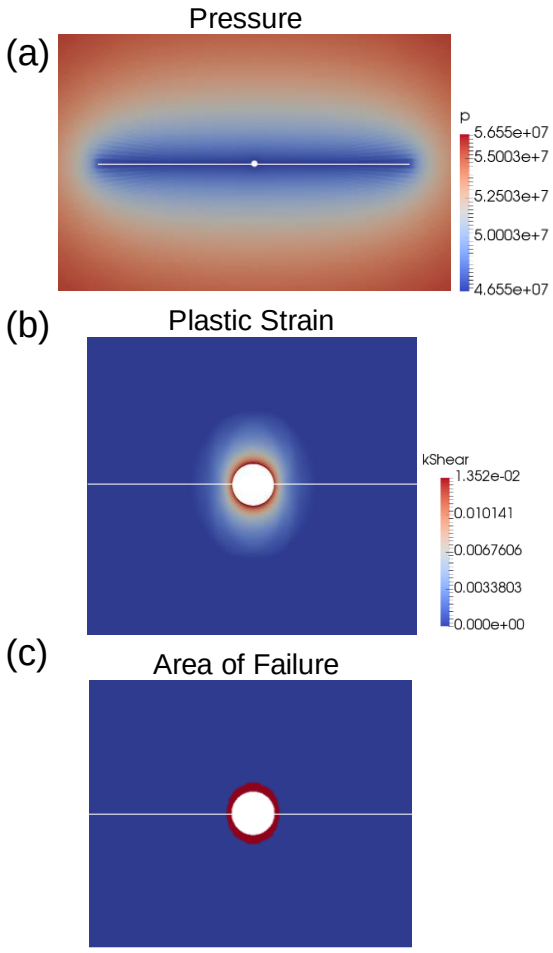

Fig. 6.2: Sand failure simulation results for open hole frac-packed well. The white line crossing the well denotes the frac-pack. (a) pressure profile. (b) plastic strain. (c) area of failure. Note that frac-pack is along the S_{Hmax} direction

As compared with Fig. 6.1 for OH completions, Fig. 6.2 shows the shear failure behavior in open-hole frac-packed (OHFP) completion. The fracture conductivity is assumed infinite, and the fracture half-length is 10 m. The pressure profile shows linear flow in the direction perpendicular to the fracture. The fracture width was assumed to be zero to make the mechanical effect of fracture width (which will be shown later) negligible and to highlight the poro-elasto-plastic effect. In Fig. 6.2b, the maximum magnitude of plastic strain is decreased from 8.52×10^{-2} to 1.35×10^{-2} when compared to the case without

the frac-pack. The extent of shear failure is significantly reduced. This is a result of the decreased plastic strain and linearly dispersed pressure drawdown in the frac-pack case.

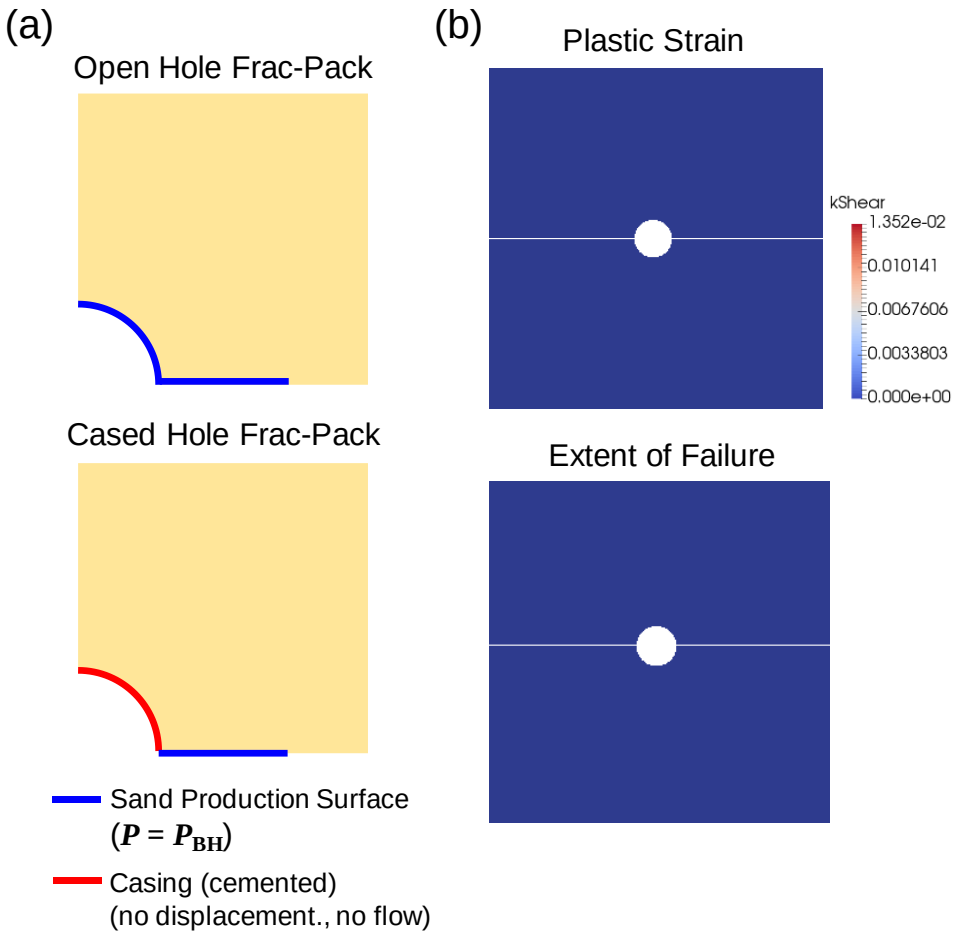

Fig. 6.3: (a) Treatment of boundary conditions in open hole and cased hole frac-pack models. (b) Simulation results for cased hole frac-pack case. No significant increase or failure have been observed

For cased-hole frac-pack (CHFP) completions, the casing is assumed cemented and the circumferential surface of the wellbore is fixed in-place by the high modulus of casing and cement. Hence at the wellbore, a no-displacement BC is used for the mechanical constitutive equation and a no-flow boundary condition is used for the fluid flow equations. For frac-packs, an infinite conductivity fracture with no width is shown as in Fig. 6.3a. The

boundary conditions result in negligible hoop stress in the CHFP simulation case. Shear failure is negligible in the CHFP case despite the fracture-dominated linear fluid flow (Fig. 6.3b).

To compare the impact of poro-elasto-plastic stress changes on the shear failure patterns, the tangential stress ($\sigma_{\theta\theta}$) profile from the well center in the perpendicular direction to the frac-pack is shown in Fig. 6.4. The tangential stress profiles are shown at the early production time (t = 1600 s) and the late production time (t = 1 day). At an early production stage, t = 1600 s, the profile is determined primarily by the in-situ stresses, and partially by the initial pressure drawdown. At a late production stage, t = 1 day, the poro-elasto-plastic effect alters the tangential stress from the initial profiles.

At early time, CHFP case shows almost a constant tangential stress distribution along the radius due to the fixed casing. In both open-hole cases (OH and OHFP), a typical tangential stress profile is seen where the near-well region is dominated by plasticity. The $\sigma_{\theta\theta}$ decreases with radius, beyond the near-well increasing region, and is dominated by an elastic response. Later in time, the poro-elasto-plastic response can be observed as in Fig. 6.4b. The fluid production from the well as a pressure point-sink increases the tangential effective stress to a more compressive state in all cases.

Our results show that there are notable differences in OHFP and OH cases. The OH case moves the peak in the tangential stress further away from the well center. This originates from the difference in the pressure gradient profile where radial flow is shown for the OH case and linear flow for the frac-pack case. In radial flow without a frac-pack, a higher pressure gradient is anticipated and this results in a larger tangential stress gradient. In the OHFP case, the peak in the tangential stress has not moved much from the well center, but the maximum magnitude of the tangential stress is larger than the OH case without a frac-pack. Due to the near-well high tangential stress in the OHFP case, the extent

of shear failure has decreased when compared with the OH case. Implementing a frac-pack completion substantially reduced shear failure primarily by changing the radial flow to the linear flow pattern and consequently altering the pressure gradient.

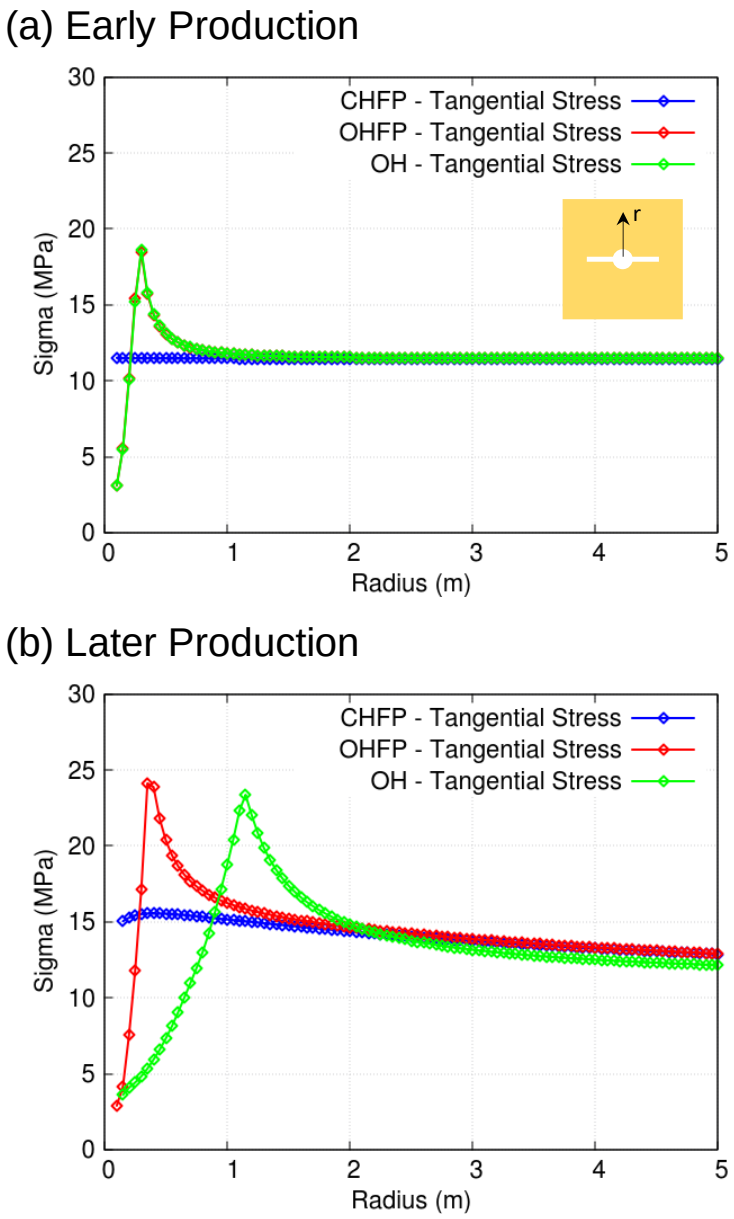

Fig. 6.4: Tangential stress profiles from the well center in the perpendicular direction to the fracture. Each line represents the type of well completions. (a) at t = 1600 sec (b) at t = 1 day

6.2.3 Mechanical Effect of Frac-Pack Width on Wellbore Integrity

Along with the pressure gradient effect discussed previously, another important factor that influences the stress profile and the sand failure response is the mechanical stresses created by the frac-pack width. The mechanical stress condition is altered substantially by the opening of the proppant-packed fracture. From the hoop-stress condition reached after drilling, the opening of the frac-pack again alters the hoop stress. Subsequent fluid production from the OHFP impacts the plastic strain and shear failure pattern and is a strong function of the frac-pack width.

In Fig. 6.5, plastic strain and shear-failure regions are shown in a map view for the cases with frac-pack widths of 0, 2 and 4 cm. As the frac-pack width increases, the plastic strain magnitude increases, and disperses towards the frac-pack faces. The shear failure region increases with increasing width. In the small-width case, the sand fails with the typical V-shape cavity pattern centered in the S_{hmin} direction in both OH and OHFP cases as compared in Figs. 6.1 and 6.2. However, the mechanical effect of the frac-pack width alters the shear failure pattern from the V-shape in the S_{hmin} direction to the frac-pack-centered V-shape. When a wide frac-pack is implemented in the field for the sake of conductivity enhancement, it must be taken into consideration. Sand failure will exhibit a frac-pack-oriented failure pattern.

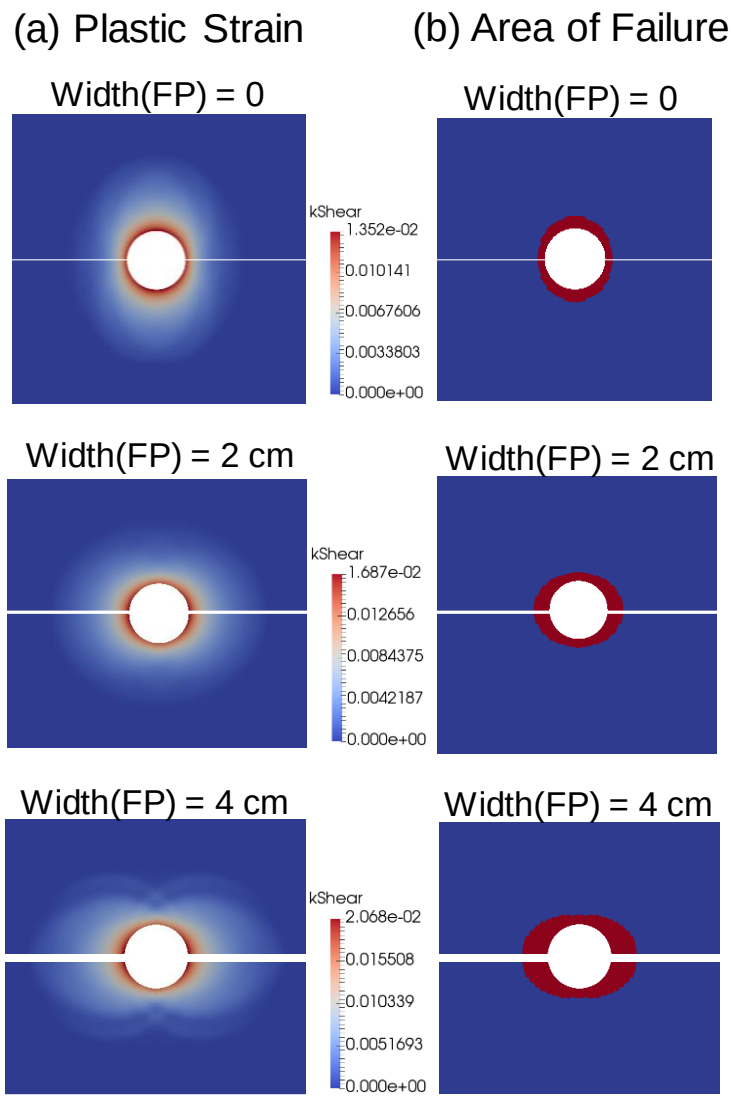

Fig. 6.5: Map view of simulation results for production wells completed with an open hole frac-pack (OHFP). (a) plastic strain and (b) regions of failure are presented for various frac-pack widths

It is evident that this width effect arises from mechanical stress effects and not from pressure gradient effects. This can be confirmed by an analysis of the hoop stress at the beginning of production. In Fig. 6.6, the tangential stress profiles on the wellbore from 0 to 90 degrees are shown for different width cases. On the fracture face, the tangential stress

is smallest for the no-width case as the mechanical effect is the lowest. At the 90 degree position, the tangential stress is the largest and determined only by the maximum and minimum horizontal stresses. However, the larger frac-pack width completely alters the trend of the hoop stress. The tangential stress increases with increasing width at the 0-degree location, and decreases at the 90-degree position. This initial hoop stress re-distribution by the frac-packing is a critical factor for production-induced sand failure and wellbore integrity during production.

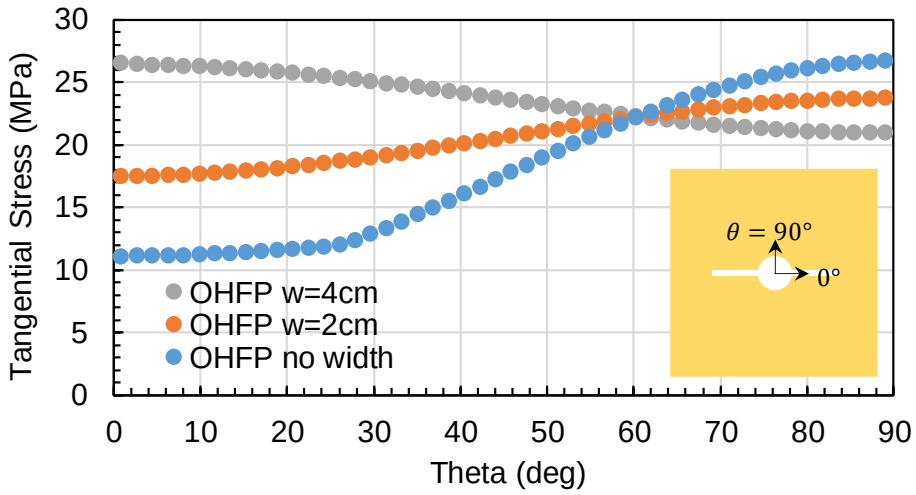

Fig. 6.6: Tangential stress along the wellbore circumferential face in open-hole frac-packed wells with different widths at an early production stage (t = 1600 s). The angle theta starts from 0 degree in the direction of frac-packs and increases to 90 degrees in the direction perpendicular to the fracture

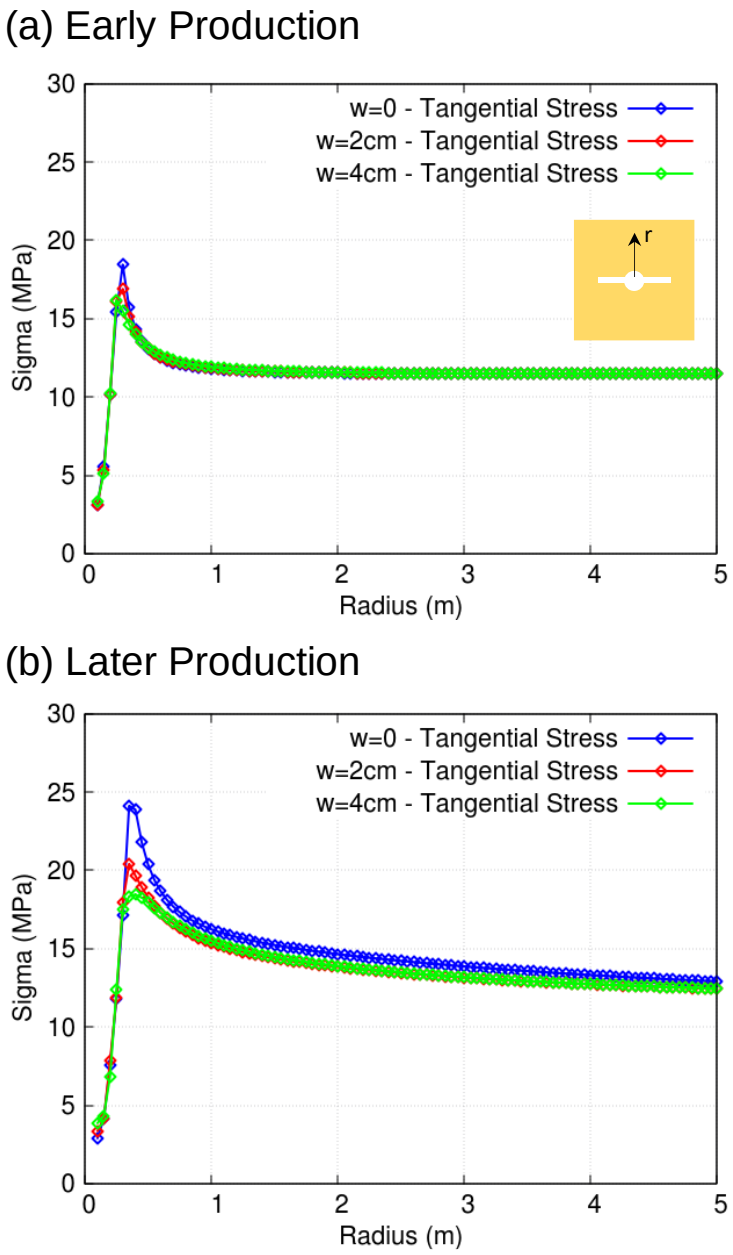

Fig. 6.7: Tangential stress profiles from the well center in the perpendicular direction to the fracture. Each line represents simulation cases with different frac-pack widths. (a) at t = 1600 sec (b) at t = 1 day

The effect of mechanical opening of the fracture in OHFP completions can be confirmed by the shear stress distributions as shown in Fig. 6.7. This figure is compared

with Fig. 6.4 to show the difference between the pressure-gradient and mechanical effects on the tangential stress along the line shown in the diagram. As opposed to the pressure gradient effect, the mechanical effect does not move the peak location of the tangential stress along the radius after production. The maximum tangential stress increases after production. The largest increase is observed in the no-width case as the increase of effective stresses due to pore pressure reduction is not compensated for by the fracture opening effect. Thus, the impact of fracture opening re-distributes the hoop stress and generates excessive shear stress in the frac-pack direction.

6.2.4 Role of Plasticity on Sand Failure in OHFP

The failure patterns shown in the previous section demonstrated the pressure-gradient and mechanical influences on poro-elasto-plastic responses in OH, OHFP and CHFP completions. To identify the impact of plasticity on frac-pack completions, OHFP cases were compared by using poro-elasto-plastic and poro-elastic models. In Fig. 6.8, tangential stress profiles in the radial direction are presented for poro-elastic and poro-elasto-plastic models. The tangential stress continuously decreases with radius in the poro-elastic case. With the addition of plasticity, the tangential stress increases in the near-well region and decreases further away from the well. For frac-pack widths of 0, 2 and 4 cm, the difference in poro-elastic (p-e) and poro-elasto-plastic (p-e-p) tangential stresses at the wellbore, $\Delta\sigma_{\theta\theta,WB} = \sigma_{\theta\theta,WB(p\text{-}e)} - \sigma_{\theta\theta,WB(p\text{-}e\text{-}p)}$, decreases with increasing frac-pack width. The difference, $\Delta\sigma_{\theta\theta,WB}$, is proportional to the magnitude of plastic strain created by the shear stress. This indicates that, at the wellbore in the Shmin direction, the no-width case (Fig. 6.8a) will experience a greater chance of shear failure. Fracture width, proppant size, and tip screen out can be optimized to minimize the sanding risk according to the results presented here.

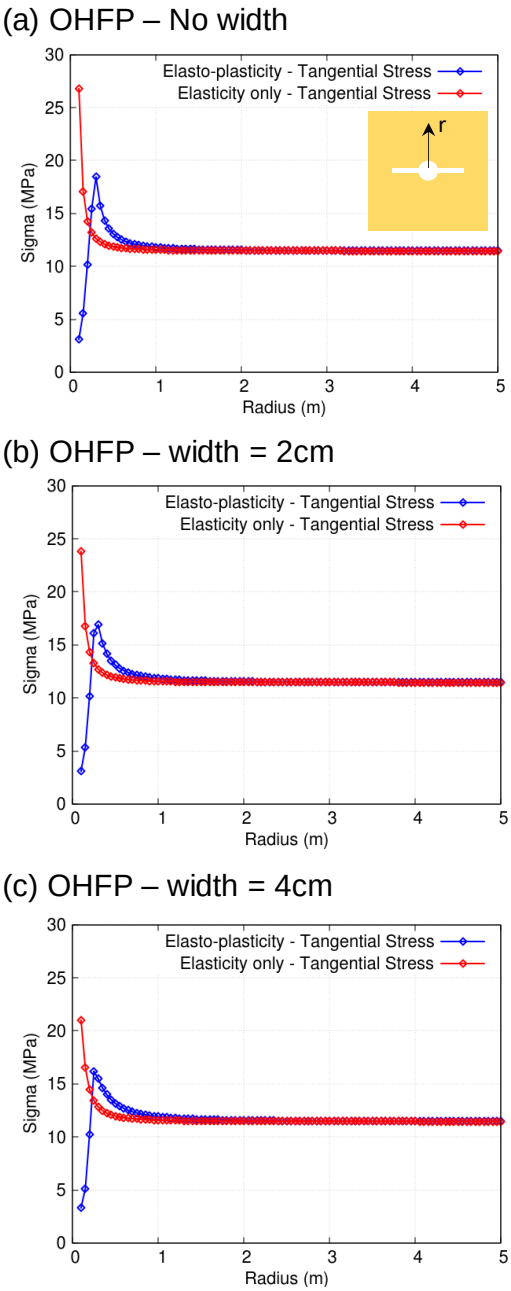

Fig. 6.8: Tangential stress profiles at early production time (t = 1600 s) from the well center perpendicular to the fracture. The well completion type is open-hole frac-pack. Each figure represents a different width of frac-pack. The blue lines show the results with poro-elasto-plasticity, and red lines are from poro-elastic simulations

6.2.5 Post-Yield Behavior

The post-yield behavior of the rock formation can substantially impact the plastic strain and subsequent rock failure patterns. In this section, the impact of strain softening is presented by comparing with results assuming perfect plasticity. In Fig. 6.9, the plastic strain and failure regions are shown for perfect plasticity and strain softening cases for the OHFP completions where the frac-pack width is assumed to be zero. In rocks with strain softening behavior, the plastic strain increased in magnitude and the region of increased strain expanded. It must be noted that, in contrast to the V-shaped failure patterns in the perfect-plasticity case, the straining-softening rock exhibits shear-band patterns in plastic strain. The failure regions of strain-softening rocks are broader in area than for perfect-plasticity as shown in Fig. 6.9b. It can be expected that with continued production, the failure pattern can have shear bands as well.

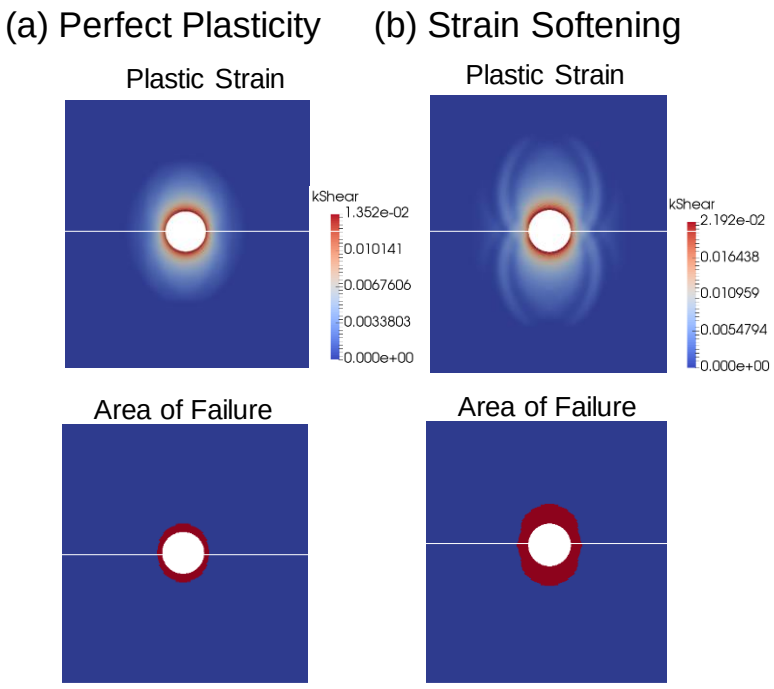

Fig. 6.9: Map view of the plastic strain and the failure region from the open-hole frac-pack completion. The fracture width was assumed zero. Each simulation assumed (a) perfect plasticity and (b) strain softening behavior

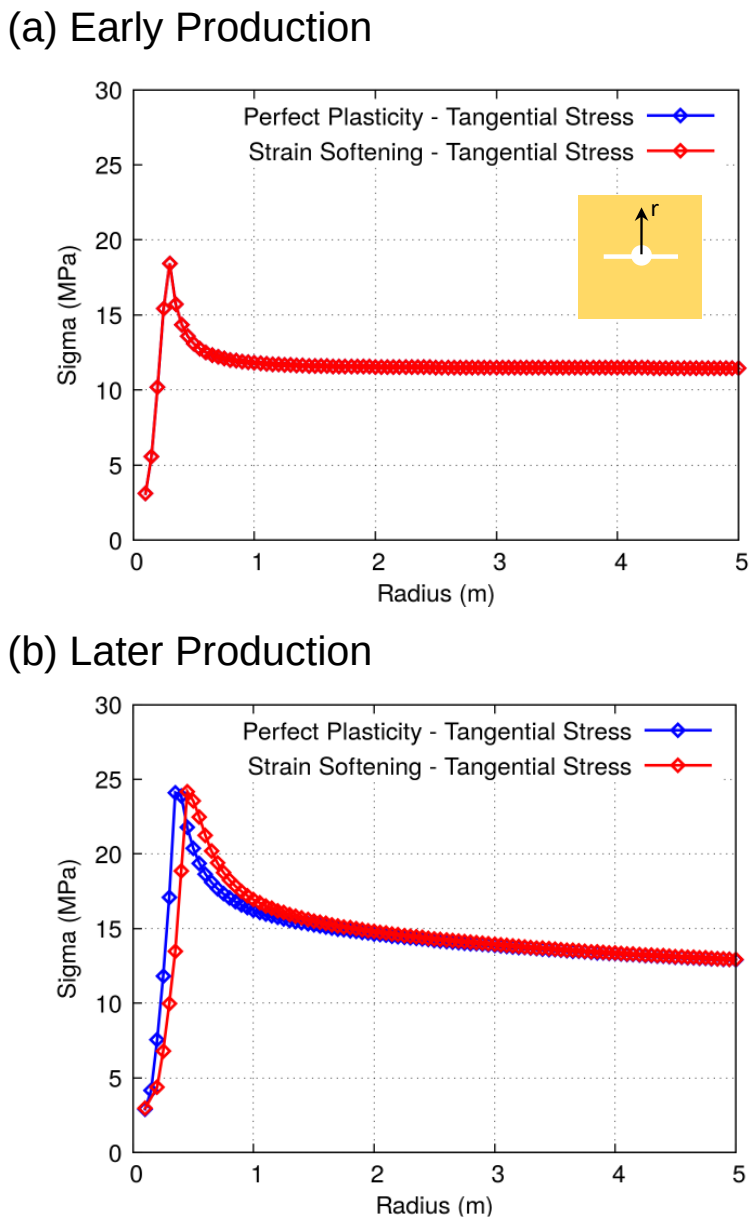

Fig. 6.10: Tangential stress profiles from the well center in the direction perpendicular to the fracture. Blue line represents simulation case with perfect plasticity, and the red line shows the strain softening case. (a) at t = 1600 sec (b) at t = 1 day

The tangential stress profiles in the above cases are compared in Fig. 6.10. The initial tangential stresses (Fig. 6.10a) do not show any difference caused by the rock post-

yield behavior. After some production, as shown in Fig. 6.10b, the peak in the tangential stress moved away from the strain-softening case further than the perfect-plasticity case. This indicates the larger areal extent of shear failure in the strain-softening case.

For the open-hole completion without a frac-pack, the influence of strain-softening compared to perfect plasticity is shown in Fig. 6.11. As in Fig. 6.9, strain softening increases the tendency of spiral shear band formation in the failure patterns.

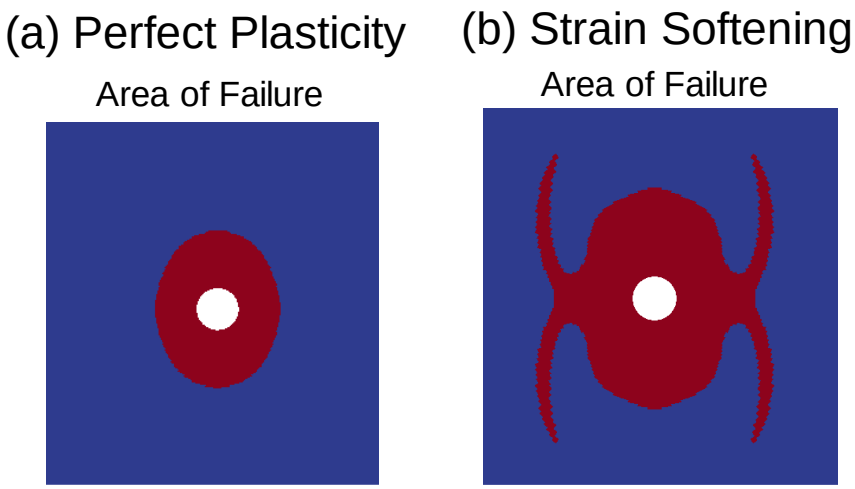

Fig. 6.11: Map view of the failure region in the well with open-hole completions without a frac-pack. (a) perfect plasticity and (b) strain softening as post-yield behavior

6.2.6 Compressive Failures in Frac-Packed Wells

In OH and OHFP completions, near-well shear failures can provide a pre-existing discontinuity where the rock can continue to yield in a compressive failure mode. To capture the impact of compressive failure, a Mohr-Coulomb model with a cap developed by Wang & Sharma (2017) was used for the current simulations. In this model, the rock experiences compressive yielding when the mean effective stress exceeds the cap pressure.

In Fig. 6.12, production from OHFP completions are simulated to examine both shear and compressive failure. Simulations were conducted for cases with no-width and 2

cm width, and the resulting plastic and volumetric strains are shown to represent the severity of shear and compressive failure respectively. As explained previously, the shear strain is spread over the frac-pack by the opening of the frac-pack width. It must be noted that the implementation of a Mohr-Coulomb with a cap model changed the plastic strain results in Fig. 6.5 compared to when the cap model was not applied.

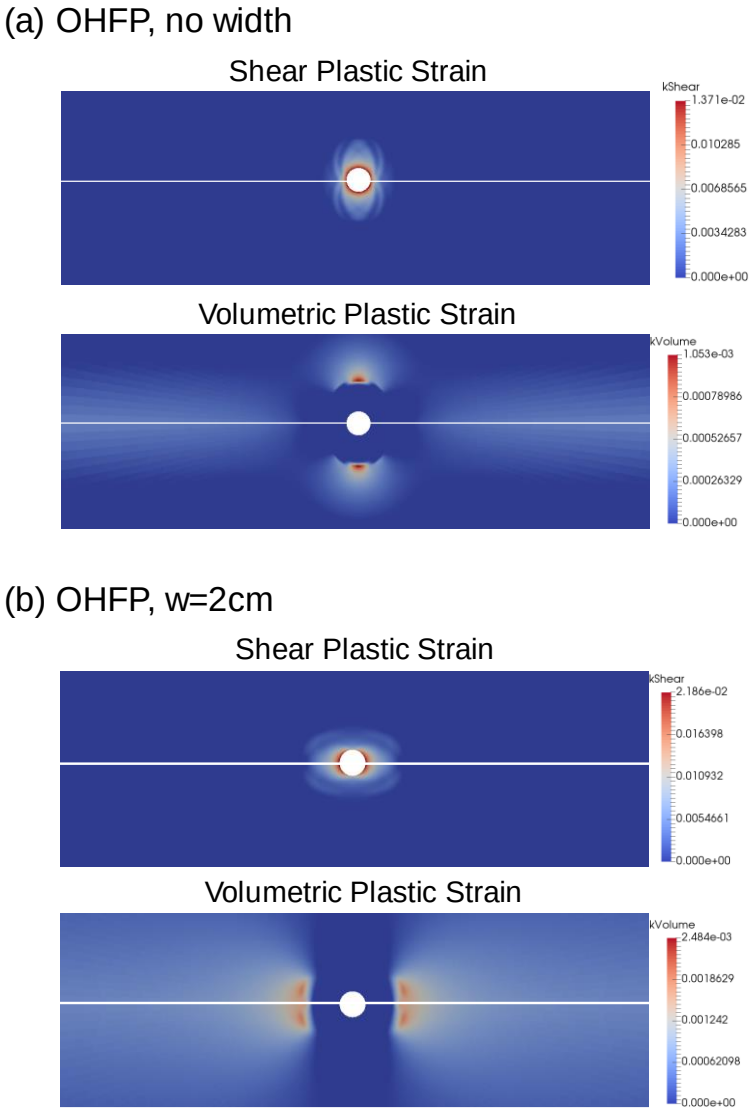

Fig. 6.12: Map view of plastic (shear-plastic) and volumetric (volumetric-plastic) strains at a production time t = 1 day. Both cases are for open-hole frac-packs. (a) no width (b) 2 cm of frac-pack width are assumed

In the no-width OHFP case, the volumetric plastic strain increases moderately along the frac-pack. The maximum volumetric plastic strain is, however, located in the minimum horizontal stress direction, slightly further away from the potential shear-failure regions of high plastic strain. When the frac-pack width is increased to 2 cm as shown in Fig. 6.12b, the volumetric strain profile changes significantly. The volumetric strain is concentrated along the frac-pack, primarily in the maximum horizontal stress direction indicating a high possibility of compressive yielding and failure along the frac-pack.

The inclusion of the compressive failure model in the rock-yield criteria using the Mohr-Coulomb cap model, alters the shear-failure region of the OHFP cases. In Fig. 6.13, the shear failure area is shown to extend along the frac-pack directions. Taking into account the shear and compressive failure behavior in Figs. 6.12 and 6.13 with non-zero width of frac-packs. Simulations indicate that both shear and compressive yield of the rock mainly occur along the frac-pack.

The tangential stress profiles from the simulations by a Mohr-Coulomb cap model with the compressive failure criteria (Fig. 6.14) show the lowered tangential stress profiles in the 2 cm width case. This indicates a transition from shear failure near the well to compressive failure in the outer frac-pack area. This suggests that failure in shear and compressive modes can occur in a connected pattern from the wellbore along the frac-packs. The combined shear and compressive failures can create cavities that worsen the well integrity in OHFP completions. The compressive failure along the frac-pack can intensify the severity of sand failure by crushing the proppants to reduce the frac-pack conductivity.

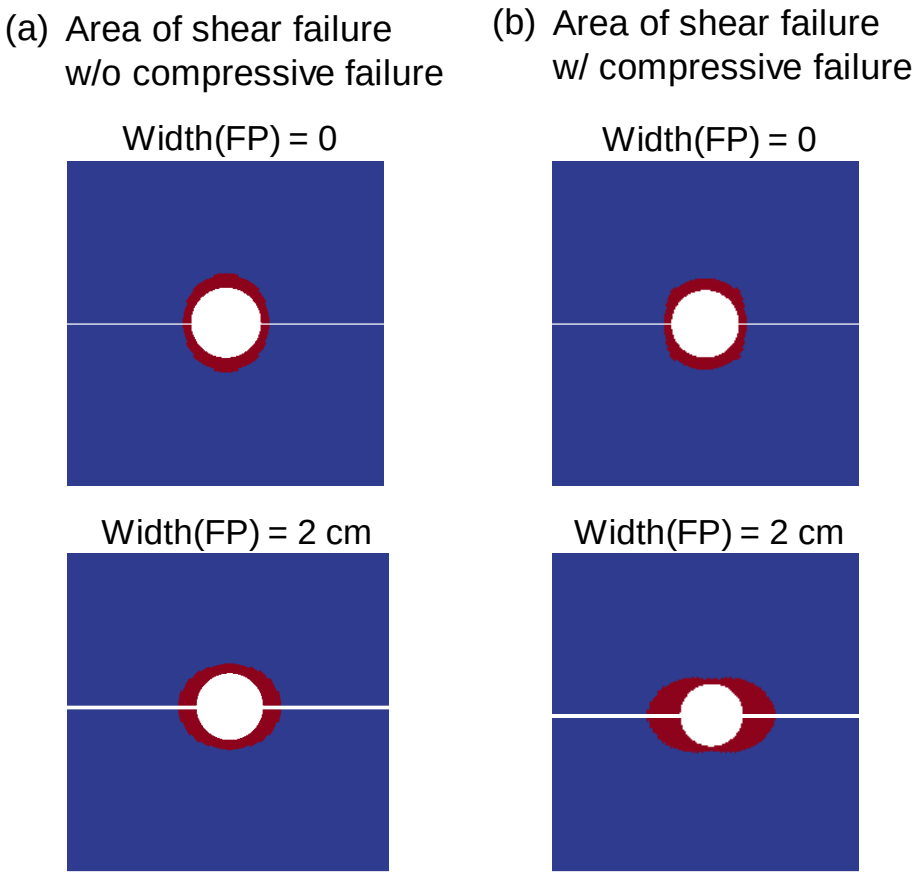

Fig. 6.13: Map view of the shear failure regions at the later production time (t = 1 day). Results from four simulation cases are compared. (a) Simulations without compressive failure. (b) Simulations with compressive failure

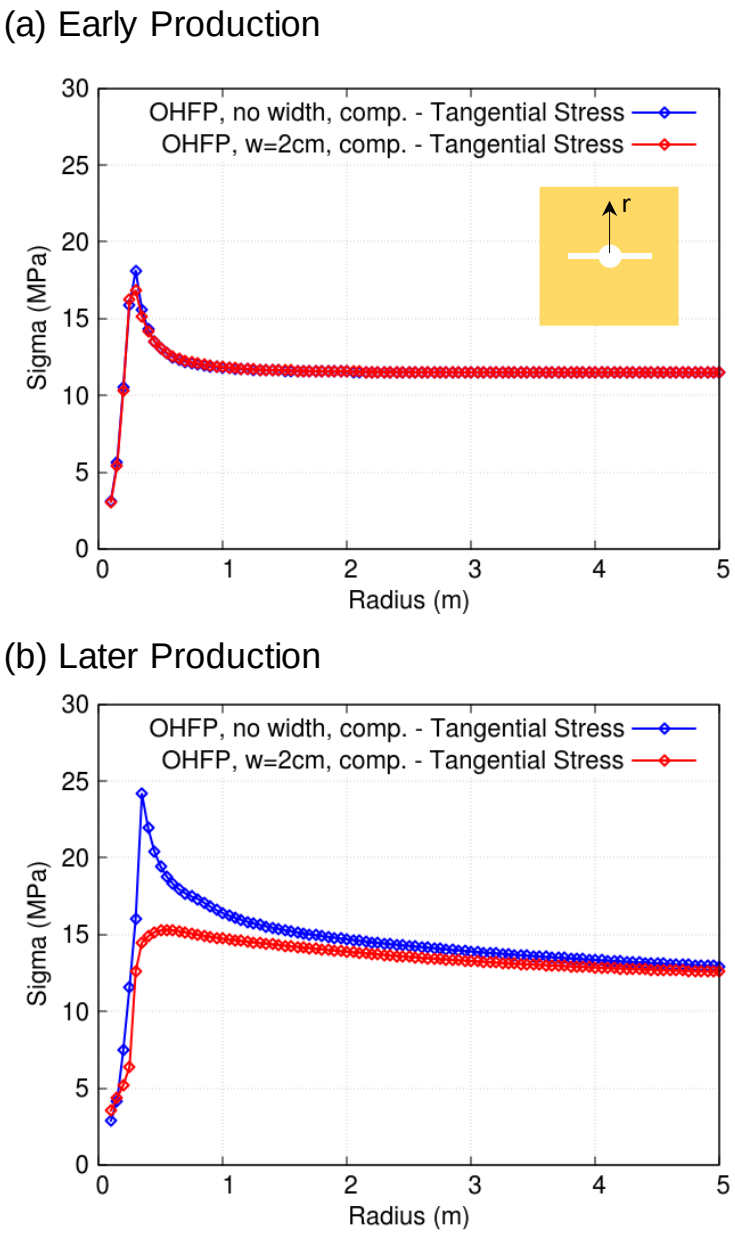

Fig. 6.14: Tangential stress profiles from the well center in the perpendicular direction to the fracture. Simulations are conducted with compressive failure model. Each line represents simulation case with different frac-pack widths. (a) at t = 1600 sec (b) at t = 1 day

(a) Early Production

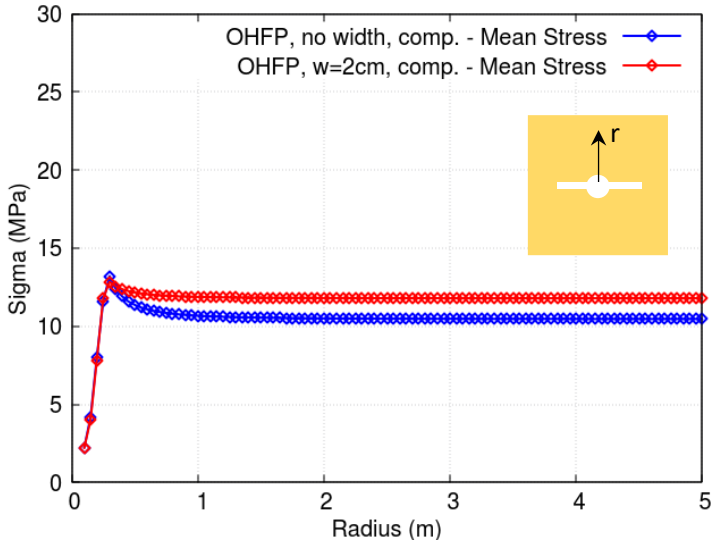

(b) Later Production

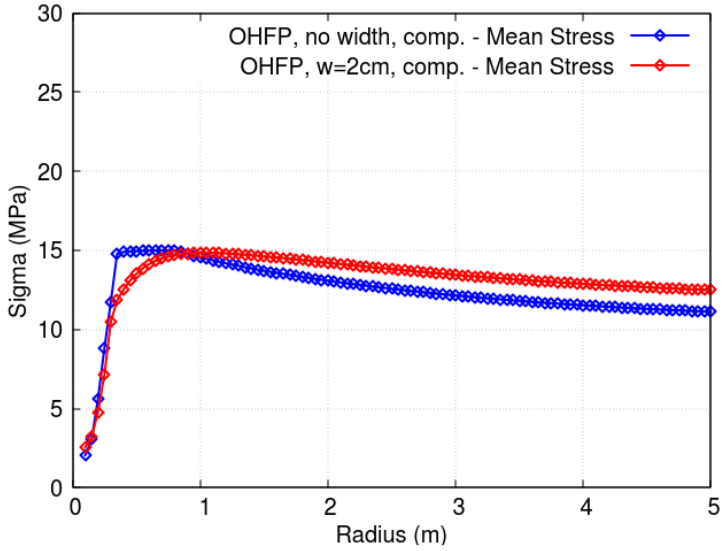

Fig. 6.15: Mean stress profiles from the well center in the perpendicular direction to the fracture. Each line represents simulation case with different frac-pack widths. (a) at t = 1600 sec (b) at t = 1 day

To better understand the possibility of compressive failure, we plot the mean stress as in Fig. 6.15. The mean stress in the radial direction perpendicular to the frac-pack shows

the increasing trend over the duration of production. When the mean effective stress exceeds the rock compressive strength, the rock yields in compressive mode and may cause pore collapse if the yielding persists. In Fig. 6.15, the rock compressive strength is 15 MPa, and the region between a radius of 0.3 and 0.8 m has a larger mean stress magnitude indicating a potential compressive failure region.

6.3 Effect of Rock Properties on Sand Production in OH Completion

As a fluid-geomechanics coupled problem, sand production is determined by pressure transients, stresses and rock deformation/failure. Therefore, rock mechanical properties and fluid flow properties play important roles in the onset of sanding and sanding behavior. Most past studies showed some simple trends in the onset of sanding, however, few have quantitatively studied the effect of these properties on failure and sanding behavior. It is important to predict the full sanding history so that the need for sand control completions can be assessed.

The Base Case for this study is set up with a rectangular reservoir with a vertical wellbore at the center. Table 6.2 shows the reservoir properties and geometry. The post-yield behavior under different confining pressures, which determines the mobilized cohesion, mobilized friction angle, and mobilized dilation angle after plastic yield point, is presented in Fig. 6.16.

Table 6.2 Reservoir properties and geometry for the Base Case

Parameters	Value	Unit
Fluid density	900	kg/m^3
Fluid bulk modulus	1	GPa
Fluid viscosity	0.005	Pa·s
Young's modulus	1	GPa
Poisson's ratio	0.25	
Cohesion	2	MPa
Friction angle	20	deg
Dilation angle	0	deg
Tensile strength	5.5	MPa
Critical plastic strain	0.15	Darcy
Sand density	2650	kg/m^3
Sand grain diameter	100	microns
Porosity	0.25	
Permeability	9.87E-13	m^2
Initial pore pressure	25	MPa
Minimum horizontal stress	28	MPa
Maximum horizontal stress	32	MPa
Vertical stress	35	MPa
Reservoir length	20	m
Reservoir width	20	m
Reservoir height	10	m
Wellbore diameter	0.2	m

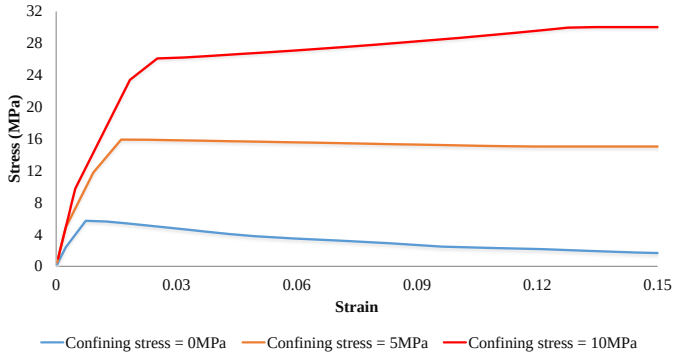

Fig. 6.16: Stress-strain curve for the rock for the Base Case

Initially the wellbore pressure is equal to the reservoir pressure. At equilibrium the rock suffers from shear yield and the shear plastic strain intensity is shown in Fig. 6.17(a). As the wellbore pressure starts decreasing (Fig. 6.18) rapid strain softening occurs around the wellbore. We observe strain localization (Fig. 6.17(b)), which dominates the sanding location. As seen in Fig. 6.17(c), at time = 3.06 hours, sanding occurs and the degraded sands are eroded along the shear band as long as the hydrodynamic force is larger than the resistant force. Once sand particles are removed from the shear band, an isolated rock chunk is left and will be transported by fluid, resulting in a sudden increase of produced sand (Fig. 6.17(d)). The cumulative sand production is shown in Fig. 6.18.

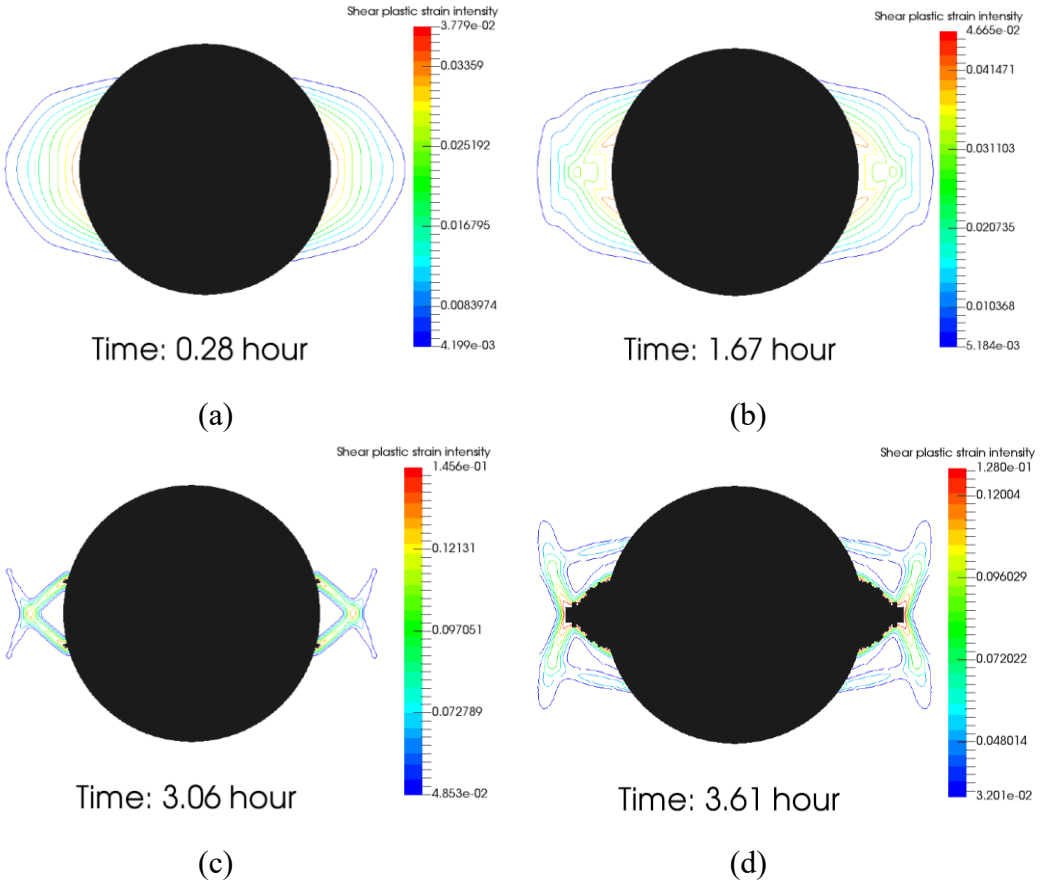

Fig. 6.17: The contour of shear plastic strain intensity: (a) time = 0.28hour; (b) time = 1.67hour; (c) time = 3.06hour; (d) time = 3.61hour

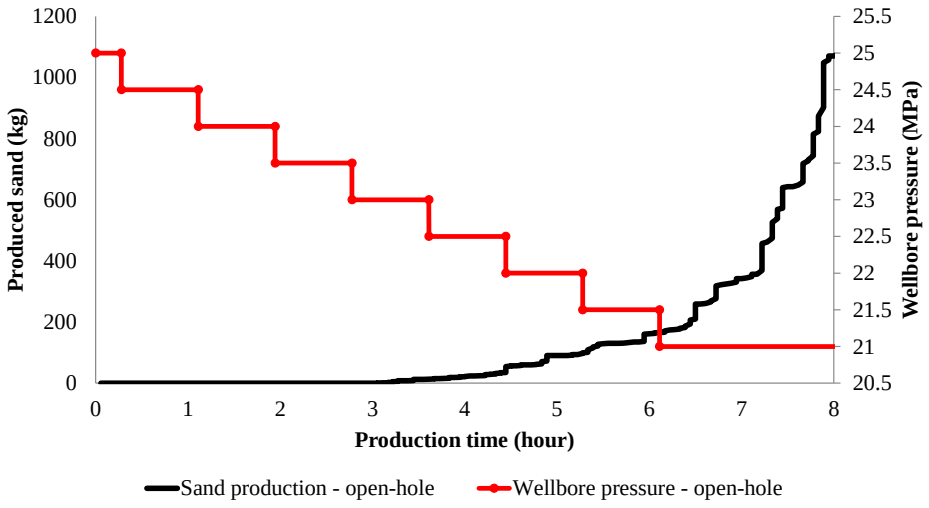

Fig. 6.18: Production scheme and sand production, results for the Base Case

To better understand the relation between reservoir properties and sand production (including both the onset of sanding and sand production rate), we perform a comprehensive sensitive study for the open-hole case.

6.3.1 Cohesion/Friction Angle/Dilation Angle

Figs. 6.19 to 6.21 show the effect of Mohr Coulomb parameters (cohesion, friction angle and dilation angle) on sand production. With lower cohesion and friction angle, the rock yields more easily and is likely to produce sand sooner. On the other hand, dilation angle determines the plastic flow rule and is proportional to the plastic strain. Therefore, rocks with a larger dilation angle generate a larger plastic strain, leading to earlier sanding. From the perspective of the sand production rate, rocks with lower cohesion/friction angle or higher dilation angle tend to produce massive sand bursts immediately after the onset of sanding. This results from the failure and erosion of large chunks and sufficient hydrodynamic force around the wellbore, while sanding for high cohesion/friction angle or lower dilation angle rock results in more smooth and continuous production rate. During

the late stages of sand production, sanding is more dominated by the cavity arch and fluid flow velocity in the rock with lower cohesion/friction angle and higher dilation angle. The sand rate for these rocks becomes steady due to a stable cavity arch and/or insufficient flow velocity around the cavity.

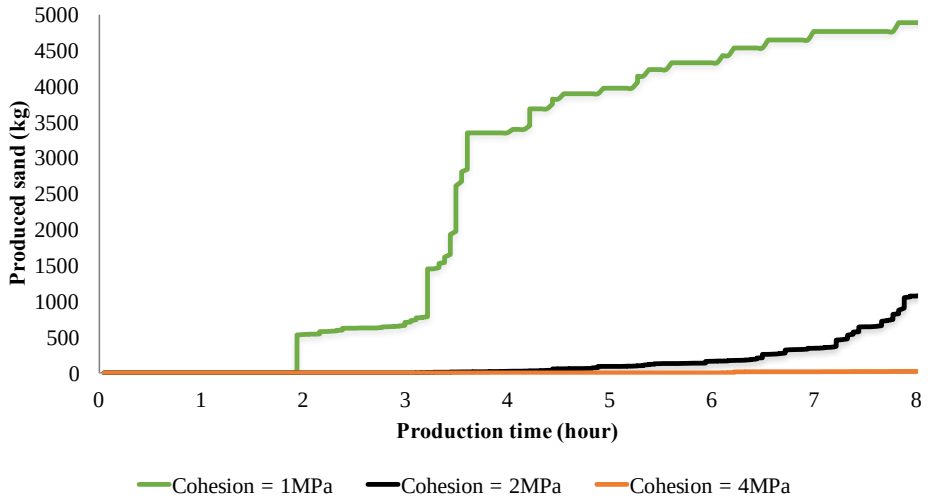

Fig. 6.19: Effect of cohesion on sand production

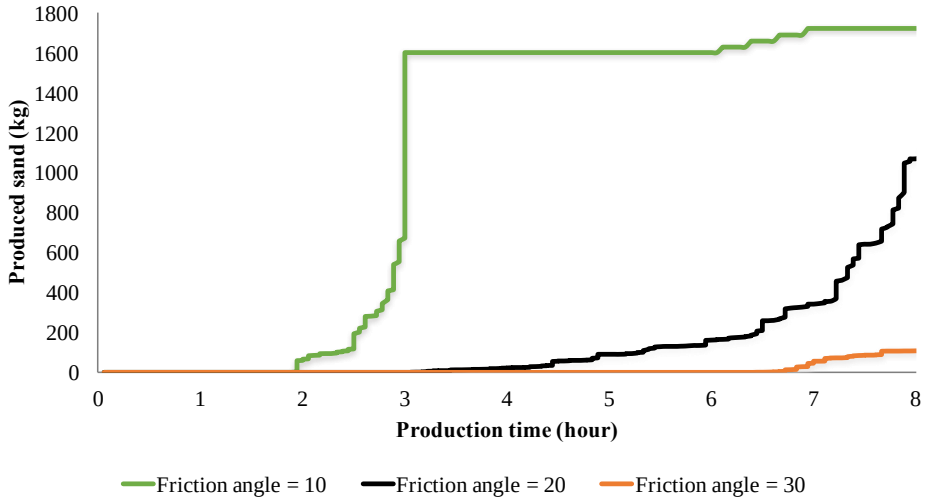

Fig. 6.20: Effect of friction angle on sand production

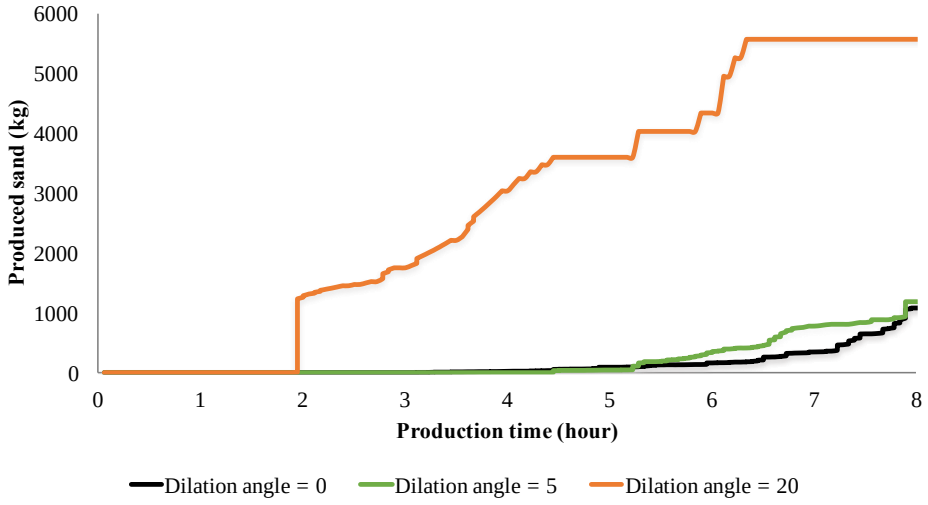

Fig. 6.21: Effect of dilation angle on sand production

6.3.2 Post-yield Parameters

The effects of post-yield parameters (residual cohesion, residual friction angle and residual dilation angle) on sand production are illustrated in Figs. 6.22 to 6.24. Since these parameters are all residual values, they do not influence the onset of sanding significantly. However, they do affect the sanding rate. With a lower residual cohesion/friction angle and higher residual dilation angle, the sanding rate is higher and an increase in the final sand production is observed. In addition, the sanding pattern tends to be similar for different values of post-yield parameters. That is, sands are produced with a relatively smooth rate instead of suddenly massive production.

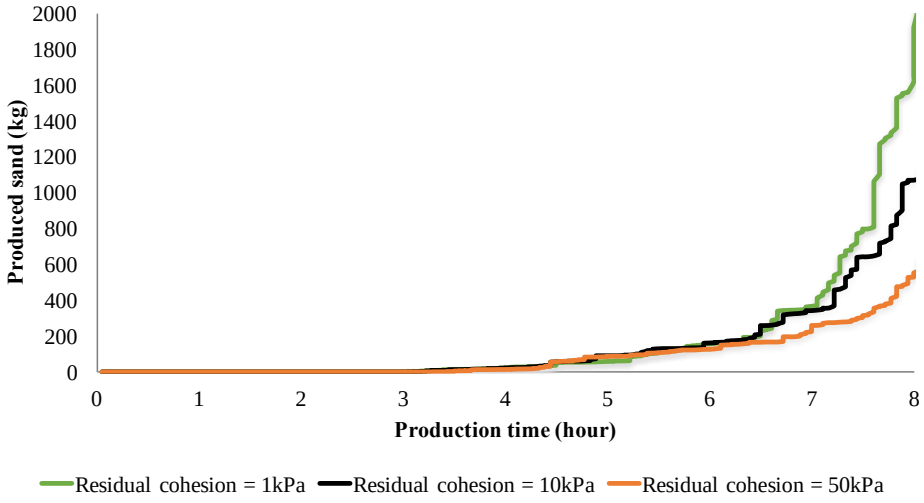

Fig. 6.22: Effect of residual cohesion on sand production

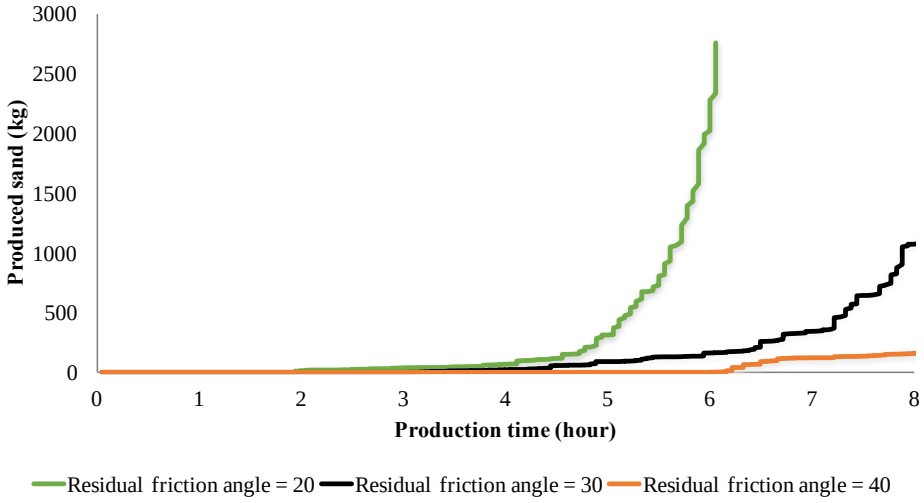

Fig. 6.23: Effect of residual friction angle on sand production

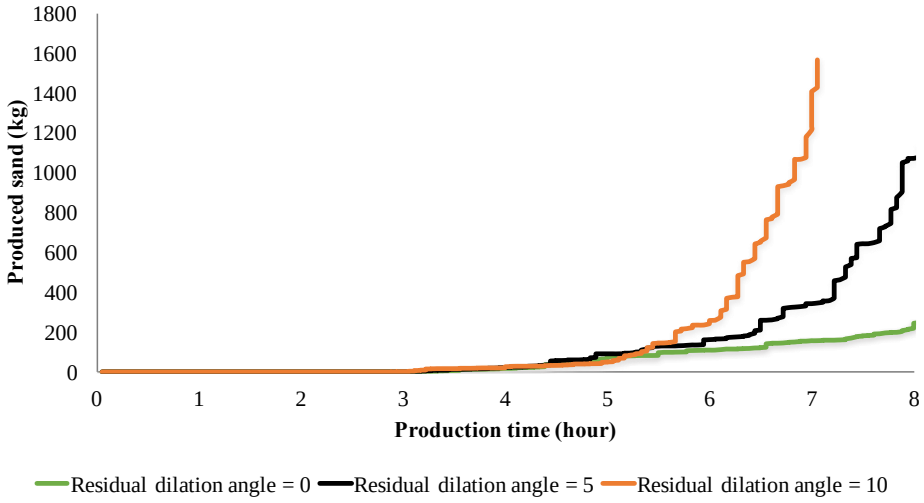

Fig. 6.24: Effect of residual dilation angle on sand production

6.4 Effect of Fluid Erosion on Sand Production in OH Completion

6.4.1 Permeability

Besides the influence of mechanical properties on sanding, fluid flow also plays an important role on degraded sand erosion. Results in Fig. 6.25 indicate that permeability is one of the key factors for sand production rate. If permeability is small (0.2 Darcy), fluid flow rate is not sufficient to bring failed sands out. On the other hand, larger permeability results in higher fluid velocity. If the velocity is satisfied with the erosion criteria as discussed before, failed sands around cavity will be eroded away and increase the sand production.

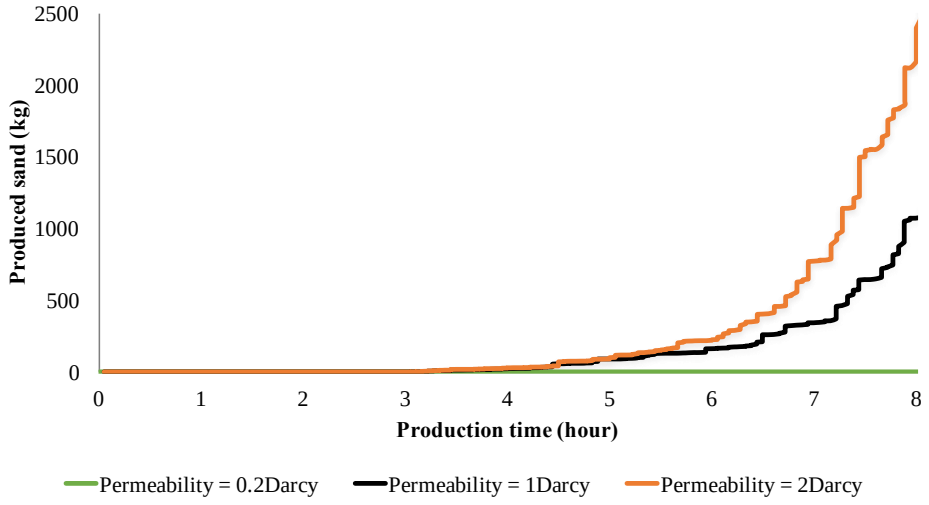

Fig. 6.25: Effect of permeability on sand production

6.4.2 Sand Grain Size

The erosion equation in this model indicates that sand grain size affects both hydrodynamic force and resistant force. To study this effect, we compared three cases with different grain sizes (assume grain diameter is uniform in each case). Fig. 6.26 present the results of sand production. For a rock composed of larger grain sizes (200 microns), no sands are produced. In this case, even some part of rock has degraded, the hydrodynamic force on these failed sands is always less than the resistance force. For rocks with smaller grain size (50 microns and 100 microns), we observe sanding happens at the same time, but gradually the sanding rate diverges. Smaller grain size yields higher sanding rate and results in higher sand production.

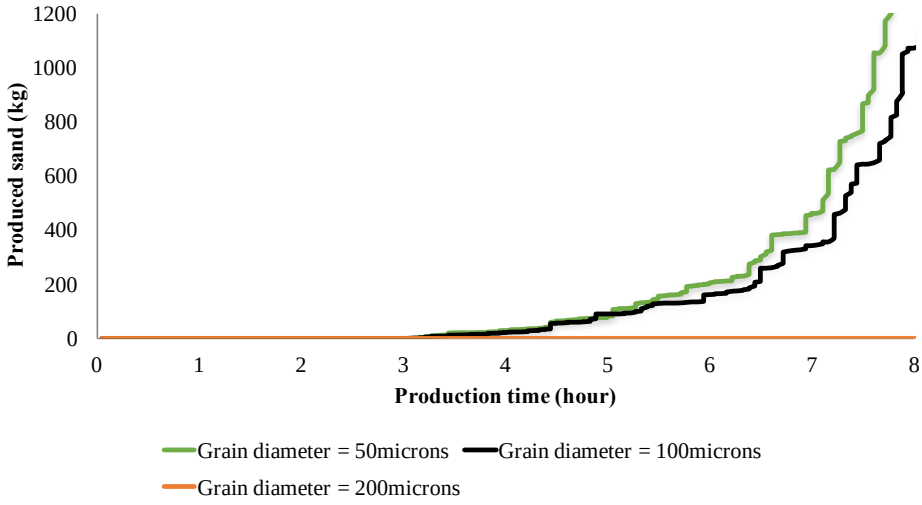

Fig. 6.26: Effect of sand grain size on sand production

6.5 Effect of Stress Contrast on Sand Production in OH Completion

Besides rock and fluid flow properties, in-situ stress also plays an important role on sand production. As shown in Fig. 6.27, larger stress contrast can accelerate the onset of sanding and change the sanding pattern (from steady and continuous sanding to massive burst of sand production). In addition, the large stress contrast leads to higher sand production, while in the low stress contrast case, we can hardly see sands being produced.

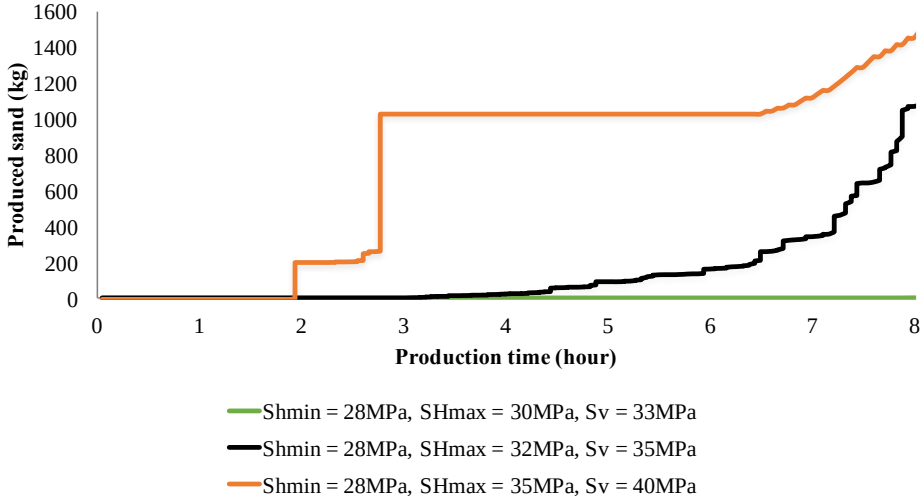

Fig. 6.27: Effect of stress on sand production

6.6 Effect of Perforation Design on Sand Production

In this section, the onset of sanding and the severity of sand production are analyzed in cased & perforated well completions, and we mainly focus on the effect of perforation geometry, including perforation orientation and perforation length.

Assume we have a rectangular reservoir and a vertical wellbore at the center, with the same dimensions and reservoir properties presented in Table 6.2. Two perforations are distributed perpendicular to the wellbore (Fig. 6.28), and are described in detail in Table 6.3. The wellbore is assumed to be cased such that there's no displacement and fluid flow across it. The pressures on two perforations are decreasing with time at the same rate of 1.8MPa per hour.

Table 6.3 Perforations geometry: cased & perforated well

Perforations dimension	
Length (m)	0.2
Diameter (m)	0.015
Perforation spacing (m)	0.2
Perforation direction	
Perforation A	parallel to S_{hmin}
Perforation B	parallel to S_{Hmax}

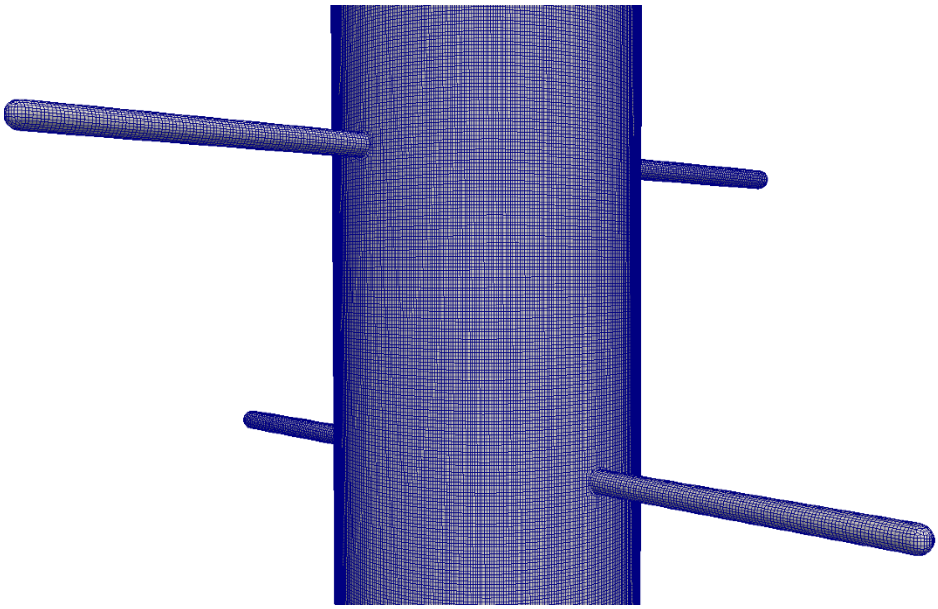

Fig. 6.28: Geometry and mesh of perforated wellbore

Fig. 6.29 shows the shear plastic strain intensity for perforation A and B at the initial equilibrium state. Plastic strain is concentrated on lateral face of two perforations, where larger stress and stress contrast are located and sanding is likely to start. After sand production, perforation boundary changes due to sands are removed, and is displayed in Fig. 6.30.

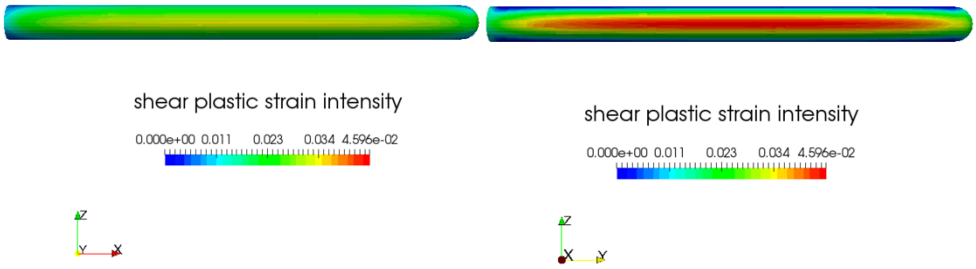

Fig. 6.29: Shear plastic strain intensity on two perforations' faces at initial equilibrium (left: perforation A; right: perforation B)

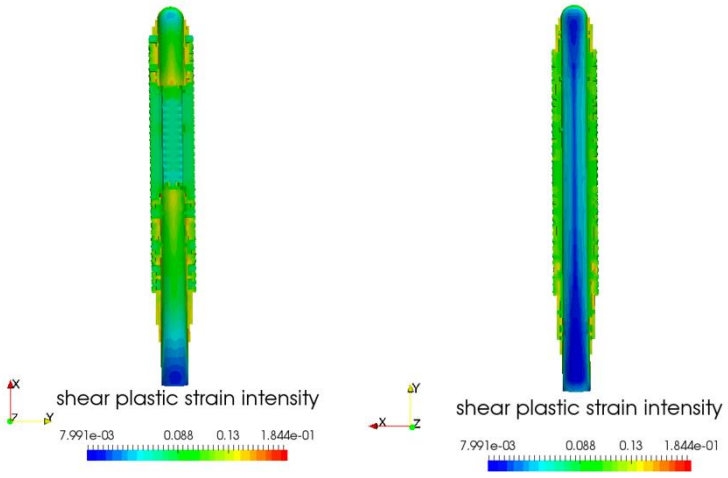

Fig. 6.30: Perforations in horizontal plane after sand production (left: perforation A; right: perforation B)

6.6.1 Perforation Orientation

We first compared the effect of perforation orientation on sanding, and the results are displayed in Fig. 6.31. The onset of sanding for perforation B is earlier than that of perforation A. This can be explained from a mechanical aspect: perforation B sees the higher hoop stress caused by the vertical stress and minimum horizontal stress, resulting in a higher shear plastic strain (see in Figure 19) and higher possibility to fail. Around 3.8 hours after fluid production, we notice a massive sand production for perforation A, yielding higher sand production than perforation B later on. It is caused by the stability of cavity, and will be discussed in the next section.

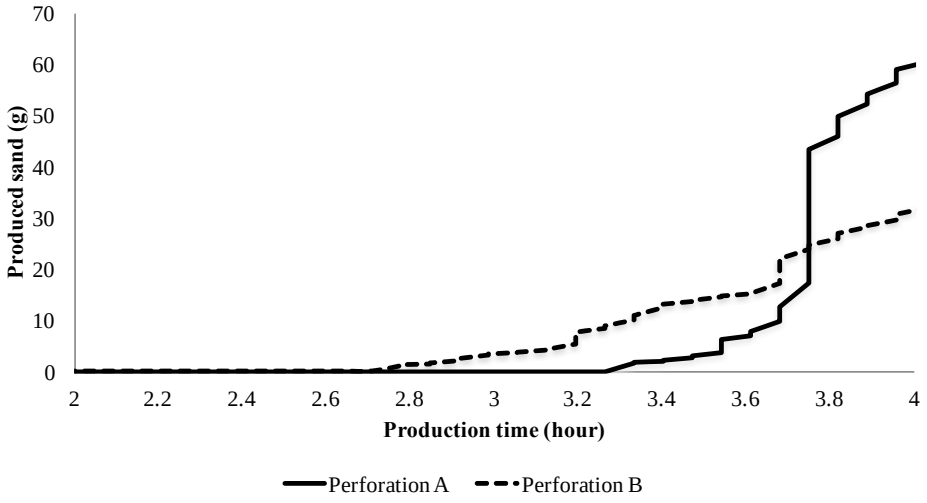

Fig. 6.31: Effect of perforation orientation on sand production

6.6.2 Perforation Cavity Stability

After sands being initialized, for perforation A, stress contrast is smaller, and the cavity propagates more radially (more circular shape, see left side in Fig. 6.32). On the contrary, perforation B suffers a larger stress contrast, leading the cavity to mainly grow in the Shmin direction (more elliptical shape, see right side in Fig. 6.32). Due to a weaker stability of the circular hole than that of the elliptical, rapid sanding rate and sand burst occur for perforation A, while the sand rate for perforation B tends to be stable and steady (Fig. 6.31). Thus, even though we concede that perforation A is more stable than perforation B before sanding, the former may tend to be less stable as the cavity grows, due to arch stability.

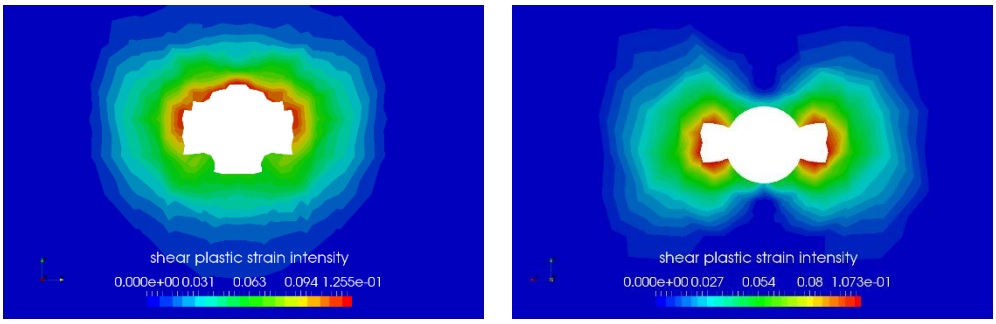

Fig. 6.32: Perforations in horizontal plane after sand production (left: perforation A; right: perforation B)

6.6.3 Perforation Diameter

Perforation hole size also has a great effect on sanding. From the results in Fig. 6.33, we observe earlier sanding and more sand production with larger perforation diameter for both perforations, inferring that smaller hole has a better stability.

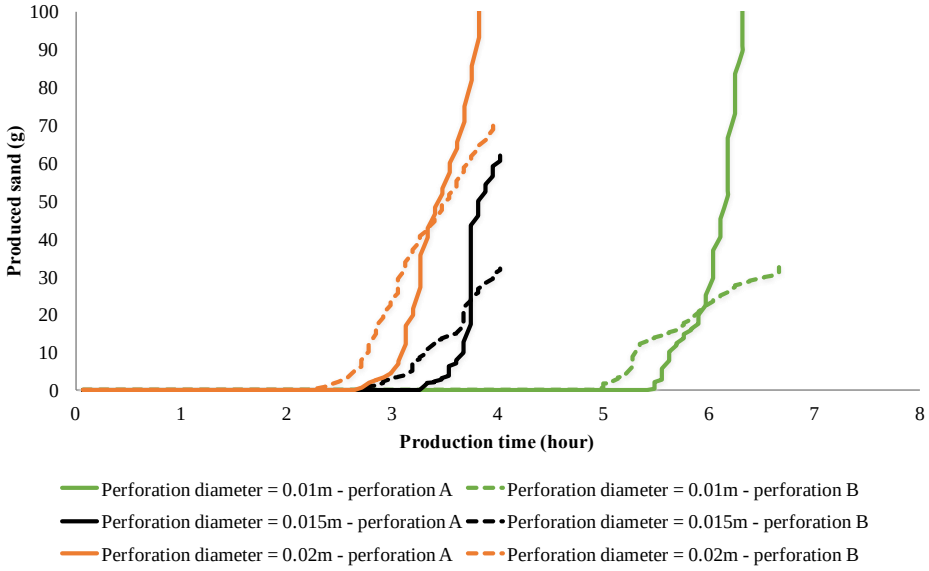

Fig. 6.33: Effect of perforation diameter on sand production

6.6.4 Perforation Length

The results for sand production with different perforation lengths are shown in Fig. 6.34. It indicates that perforation length can affect not only produced sand mass, but also

the onset of sanding. In addition, with a longer perforation, sanding is more likely to occur and have a higher production.

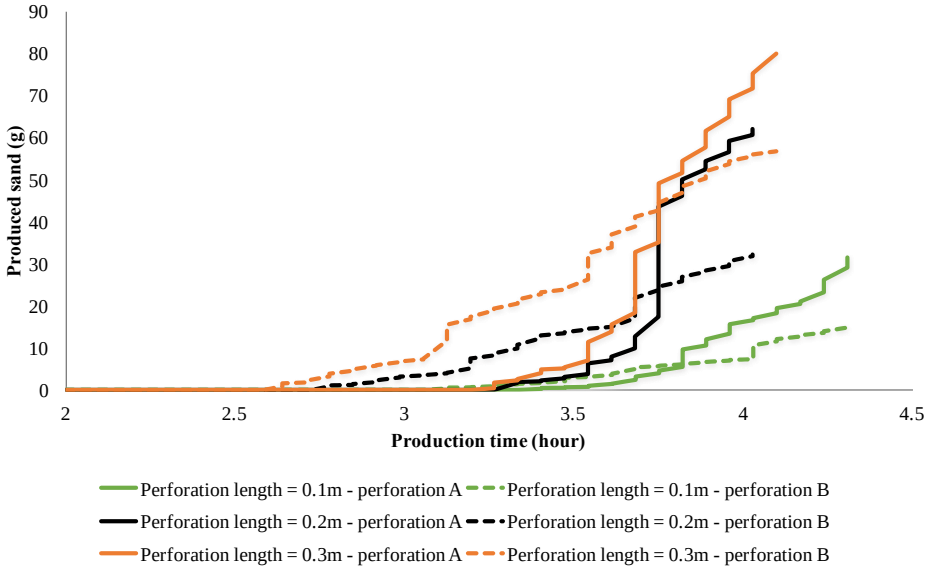

Fig. 6.34: Effect of perforation length on sand production

6.7 CONCLUSIONS

We have studied sand failures in the wells completed with open-hole without fracture, open-hole frac-pack, and cased-hole frac-pack through the numerical simulation. Various factors controlling the sand failure behavior in these completion types are investigated, which includes pressure-gradient effect, mechanical effect of frac-pack width, post-yield behavior of rocks, and compressive failures.

The results presented in this chapter, for the first time, allows us to fully understand the role of well completion designs and reservoir pressure drawdown on sand failure mechanisms and severity of damage. Sanding mechanisms are identified to show how the frac-pack designs results in less sand production and how their dimensions impact the failure mechanisms. The simulation results clearly show the important factors in sand

production, and suggest changes to frac-pack well designs and operations that help to minimize the risk of sand production in the unconsolidated reservoirs.

In addition, a comprehensive parametric study including rock strength, post-yield properties, fluid flow properties and stresses have been conducted for their impacts on both onset of sanding and sand production rate based on the open-hole completion. The model shows the capability of capturing the strain localization and steady/burst sanding rate caused by mechanical or fluid flow properties.

Furthermore, sand production around a perforated well has been studied to show the importance of perforation design on perforation orientation, perforation diameter and perforation length relative to perforation stability and the mount of produced sands.

REFERENCES

Hainey, B. W. and J. C. Troncoso. 1992. Frac-pack: an innovative stimulation and sand control technique. *In SPE Formation Damage Control Symposium. Society of Petroleum Engineers.*

Hwang, J., H. Wang, and M. M. Sharma. 2018. Wellbore Integrity and Sand Failure Mechanisms of Frac-Packed Wells in Unconsolidated Sand Formations. *In 52nd US Rock Mechanics/Geomechanics Symposium. American Rock Mechanics Association, 2018.*

Nouri, A., H. H. Vaziri, H. A. Belhaj, and M. R. Islam. 2006. Sand-production prediction: a new set of criteria for modeling based on large-scale transient experiments and numerical investigation. *SPE Journal, 11(2):* 227-237.

Papamichos, E., I. Vardoulakis, J. Tronvoll, and A. Skjaerstein. 2001. Volumetric sand production model and experiment. *Intl J for Numerical and Analytical Methods in Geomechanics, 25(8):* 789-808.

Papanastasiou, P. and A. Zervos. 1998. Three-dimensional stress analysis of a wellbore with perforations and a fracture. *In SPE/ISRM Rock Mechanics in Petroleum Engineering.*

Vaziri., H, A. Nouri, K. Hovem, and X. Wang. 2007. Computation of Sand Production in Water Injectors. *Presented at the European Formation Damage Conference held in Scheveningen, The Netherlands, 2007.*

Wang, H. and M. M. Sharma. 2017. The Role of Elasto-Plasticity in Cavity Shape and Sand Production in Oil and Gas Wells. *In SPE Annual Technical Conference and Exhibition. Society of Petroleum Engineers, 2017.*

Wang, H., P. Cardiff, and M. M. Sharma. 2016. A 3-D poro-elasto-plastic model for sand production around open-hole and cased & perforated wellbores. *Paper presented at 50th US Rock Mechanics Symposium, Houston, Texas, USA, June 2016.*

Wang, H., D. P. Gala, and M. M. Sharma. 2017. Effect of Fluid Type and Multi-Phase Flow on Sand Production in Oil and Gas Wells. *In SPE Annual Technical Conference and Exhibition. Society of Petroleum Engineers, 2017.*

Wang, H., J. Hwang, and M. M. Sharma. 2018. Sand Production Caused by Water Hammer Events: Implications for Shut-In Protocols and Design of Water Injection Wells. *In SPE International Conference and Exhibition on Formation Damage Control. Society of Petroleum Engineers.*

Wang, Y. and M. B. Dusseault. 1996. Sand production potential near inclined, perforated wellbores. *In CIM Annual Technical Meeting, Calgary.*

Ye, Z., M. Janis, and A. Ghassemi. 2017. Injection-driven Shear Slip and The Coupled Permeability Evolution of Granite Fractures for EGS Stimulation. *In 51st US Rock Mechanics/Geomechanics Symposium. American Rock Mechanics Association.*

Chapter 7: Effect of Multi-Phase Fluid Flow and Fluid Type on Sand Failure and Production[3]

7.1 INTRODUCTION

A great deal of effort has focused on sand production from the perspective of mechanical failure in past years. However, there are relatively few studies on the effect of fluid properties and flow mechanisms, which are also important in determining the onset of sanding and controlling the sand production rate. There are two major impacts of fluid properties and multi-phase flow on sand production; (a) the change in rock strength for both intact and post-yield stages, (b) the change in drag force required to carry the sand particles against the resistance force.

Ray et al. (2014) recently tested sand production characteristics in three different sandstone outcrops under varying fluid flow conditions, and observed different sanding behavior for brine, oil and gas flow. Later, Cerasi et al. (2015) conducted a systematic series of experiments, demonstrating the same phenomenon that higher compressive stresses are required for the onset of sand production with compressed air flow when compared with liquid flow. One possible reason is rock strengthening due to water drying effect in gas flow. Mahadevan and Sharma (2006) showed that the flow of gas near the well can result in drying of the porous medium even when the gas enters the region fully saturated in water vapor. This is due to a reduction in pressure of the gas as it flows towards the wellbore. The mole fraction of water in the gas increases as the gas pressure decreases. This results in drying and salt precipitation. This drying increases the capillary cohesion between the sand grains and has a significant impact on the strength of the sand around the wellbore.

[3] The original source of this chapter is from Wang et al. (2017) and Wang et al. (2018). Sharma supervised all the projects. Gala provided simulations of compositional fluid flow. Hwang provided simulations of water hammer.

Another issue that has received considerable attention in the past in sand production is multi-phase fluid flow. It has been widely observed in the field that water breakthrough prompts the onset of sand production. From the mechanical point of view, Tronvoll et al. (2001) claimed that water inflow changes the relative permeability and capillary pressure. The presence of water can also dissolve cement bonds and weaken the strength of the porous medium. From the fluid erosion perspective, Skjaerstein et al. (1997) suggested that water and gas breakthrough may increase the drag forces acting on the sand near the wellbore. In addition, Vaziri et al. (2002) proposed that capillary cohesion serves as resistance force, when the dis-aggregated rock around the wellbore is held together by capillary forces. With water saturation increasing, the capillary forces are reduced or eliminated, prompting sand production.

Besides production wells, injection wells also face sanding issues and injectivity loss caused by water hammer events. A water hammer event is a pressure fluctuation originating from the momentum change due to a sudden change of flow in a confined system, e.g., pipes and wellbores. The sudden change in the injection rate into a wellbore causes a pressure pulse to propagate through the wellbore and the fluctuation of pressure attenuates over time as the pressure pulse travels up and down the wellbore. Such water hammer events are observed across various facilities in the oil and gas industry, but they are often ignored despite the fact that they can affect injection and production operations and they contain valuable information.

For example, in unconventional shale reservoirs, water hammer signatures have been used for hydraulic fracture diagnosis by simulating the transient pressure after shut-in of fracture treatments. As almost all the fracture treatment data contain this water hammer signature, the water hammer simulation for the wellbore-fracture system provides a viable alternate option over other expensive fracture diagnostic methods. This application

of the water hammer simulation has been used in a series of fracture diagnosis papers by Carey et al. (2015); Carey et al. (2016); Hwang et al. (2017). In the current work, the same water hammer simulation is used to calculate the transient pressure change in the injection wells completed in the poorly consolidated reservoirs. In water injectors, water hammer responses caused by shut-in of injectors have been simulated as in Wang et al. (2008) and Choi & Huang (2011). However, the impact of water hammer on well integrity and formation damage has not been well studied. Hence, it is crucial to integrate the water hammer model with a sand failure model to fully understand the physics in the water-hammer-induced sand failure.

In this chapter, the sand production model is applied to study the effect of fluid flow on sand failure and sand production from the above prospects (Wang et al., 2017; Wang et al., 2018). Results here will explain the effects of water drying, non-Darcy flow and multiphase flow on sand production onset and sanding rate. In addition, reasons for the different sanding behavior in oil and gas fluid flow experiments and the effect of water breakthrough and water cut on sanding are studied in detail. At last, for the water hammer study, the primary results allow us to quantitatively understand the role of well shut-downs and subsequent water hammer pressures on sand production. The failure of unconsolidated sands near the wellbore is affected by water hammer events, their amplitude, period, and attenuation. If a water hammer event occurs during shut-in of water injectors, the extent of the sand failure becomes larger and the failure zone continues to propagate along the stress concentration direction. The simulation results clearly show which parameters are important and suggest changes to well operations such as proper shut-in protocols that help to minimize the possibility of sand production. The results also suggest ways in which injectors can be designed to minimize the impact of water hammer events.

7.2 Effect of Fluid Type on Sand Production

Previous experiments have shown that sand production requires higher compressive stresses in gas flow, compared with brine and oil flow (Ray et al., 2014; Cerasi et al., 2015). Cerasi hinted at two possible reasons for the observation: 1) Non-Darcy effects, 2) Rock strengthening due to water drying. However, the exact reasons for this observation remained unclear. In this section, we verify this experimental observation through numerical simulations and study the above two potential reasons.

In the model, the non-Darcy velocity for any fluid phase is given as follows using the multi-phase extension of the Forchheimer equation

$$v_j + k\frac{k_{rj}}{\mu_j}\beta_j\rho_j|v_j|\cdot v_j = -k\frac{k_{rj}}{\mu_j}\nabla(p + p_{cj}) \tag{7.1}$$

The non-Darcy coefficient is an input in the model and is typically calculated using the following correlation (Wu et al., 2014), where the unit of permeability in this equation is mD,

$$\beta = \frac{1.485 \times 10^9}{k^{1.021}\phi} \tag{7.2}$$

Water evaporation due to expanding gas flow is implemented using Raoult's law (Mahadevan et al., 2006). The water evaporation option in the model is only applicable to ideal gases and is an approximation that can be relaxed. The mole fraction of water in the gas phase ($x_{w,g}$) is calculated using the following formula, where p^{sat} is the water vapor pressure

$$x_{w,g} = \frac{p^{sat}}{p_g} \tag{7.3}$$

The water vapor pressure is a function of the reservoir temperature and is calculated using the following empirical correlation (Buck, 1981), where T is in ^oC and p^{sat} is in kPa

$$p^{sat} = 0.61121 \times exp\left[\left(18.678 - \frac{T}{234.5}\right)\left(\frac{T}{257.14 + T}\right)\right] \tag{7.4}$$

The dependence of UCS on water saturation has been studied in detail in the past (Hawkins and McConnell, 1992; Vasarhelyi and Van, 2006; Zhou et al., 2016; Masoumi et al., 2017). All the experiments show a similar trend of decreasing UCS with increasing water saturation. The UCS as a function of water saturation is calculated using the equation below in our model, where 'a' is the ratio of UCS at fully saturated water condition and UCS_{dry} and b* typically depends on the rock type. Parameters a and b* can be obtained by fitting experimental data for any rock/brine combination.

$$UCS = UCS_{dry}\left[1 - \frac{1-a}{1-\exp(-b^*)} + \frac{1-a}{1-\exp(-b^*)}\exp(-b^* S_w)\right] \qquad (7.5)$$

Table 7.1 Rock and fluid properties in the cases of fluid type on sand production

Parameters	**Value**	**Unit**
Young's modulus	3	GPa
Poisson's ratio	0.2	
Cohesion of dry rock	2	MPa
Internal friction angle	30	deg
Dilation angle	0	deg
Tensile strength	0.69	MPa
Critical plastic strain	0.01	
Sand density	2650	kg/m^3
Sand grain diameter	100	micron
Porosity	0.25	
Permeability	1	Darcy
Biot's coefficient	1	
Initial water saturation	0.2	
Oil viscosity	0.005	Pa•s
Non-Darcy coefficient	1.69E+07	m^{-1}

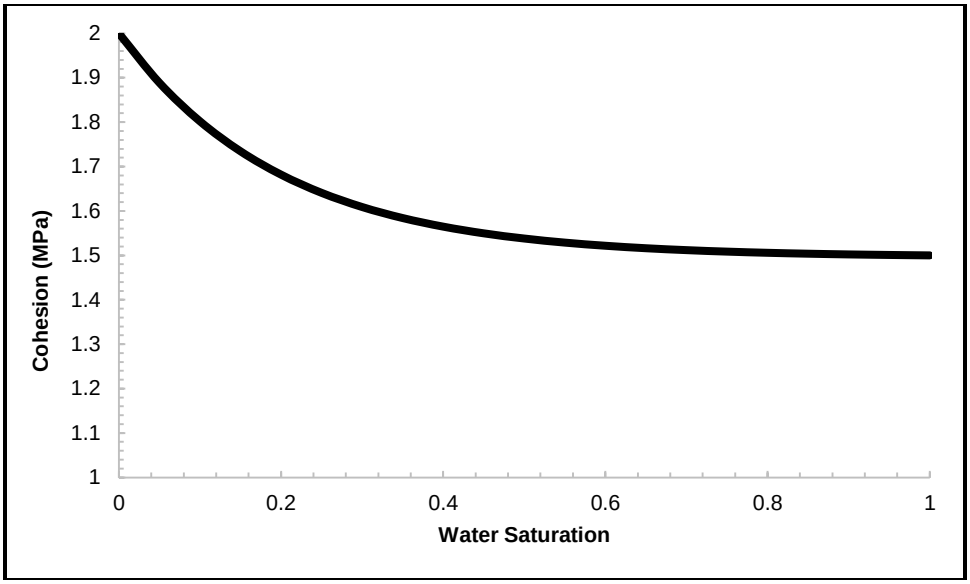

Fig. 7.1: Cohesion as a function of water saturation

The analysis requires two scenarios due to two sanding mechanisms. In the first scenario, the flow rate is large enough so that before mechanical failure, the drag force already exceeds the resistance force, and sanding is dominated by mechanical failure. In the second scenario, mechanical failure happens before the fluid erosion criterion has been met, and sanding is dominated by fluid erosion. The general inputs for both scenarios used in this experimental case study are shown in Table 7.1.

For all the cases in this experimental case study, the cohesion of the rock is a function of water saturation. From the experimental data set for sandstone strength in water content (Hawkins and McConnell, 1992), typical values are assumed in this study as a = 0.75 and b* =5, with a dry rock cohesion value of 2 MPa. The cohesion as a function of water saturation with the assumed parameters is shown in Fig. 7.1.

7.2.1 Effect of Rock Weakening with Saturated Water

In this scenario, four cases are tested: oil flow, base case of gas flow without any non-Darcy and water-drying effect, gas flow with non-Darcy effect, and gas flow with water-drying effect. To obtain mechanical failure dominated sanding, the thick wall cylinder in the model is subjected to increasing compression on the outside cylinder surface (from 0.1MPa to 10MPa), while fluid pressures on the inner borehole surface (atmosphere pressure) and outside cylinder surface (0.3MPa) remain constant to allow for radial flow. Under such conditions, the drag force exceeds the resistance force before the rock fails. With an increase of external traction, the rock goes into shear yield status and starts to produce sand once the failure criterion is met. Fig. 7.2 shows the critical external traction required for the onset of sanding under different conditions. For the first three cases, the critical external tractions are the same, while for the last case, the rock can withstand larger external traction (10% higher) before producing sand.

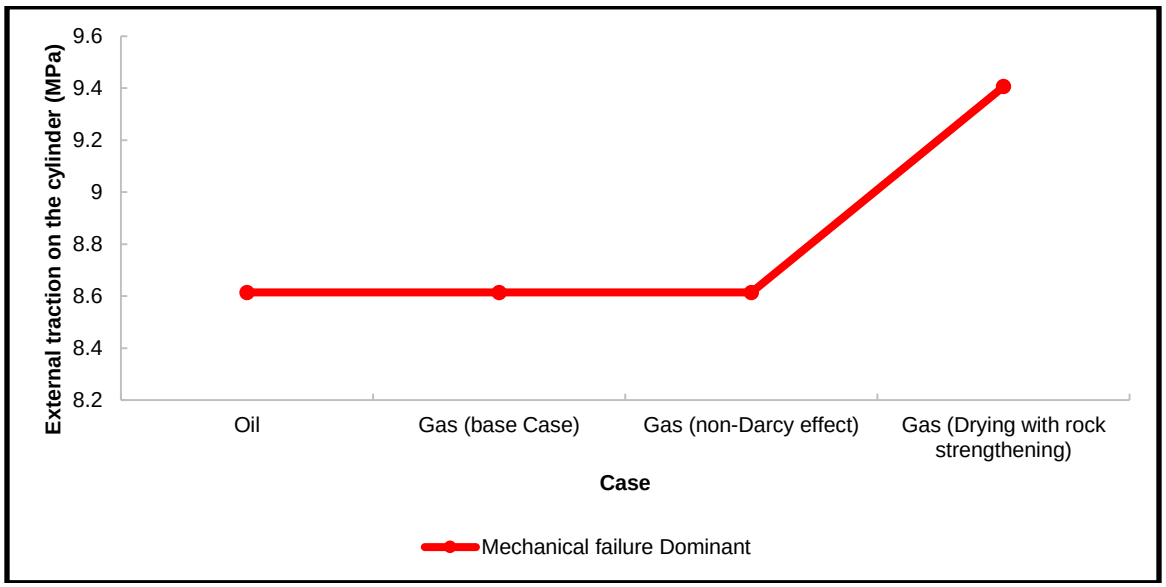

Fig. 7.2: Comparison of critical external traction at the onset of sanding

To study the delay of sanding caused by water evaporation, detailed results are plotted on Figs. 7.3 to 7.5. In gas flow, water drying effects are considered by allowing water evaporation into the gas (vapor) phase. Since the pressure of the gas phase is low near the well, the water mole fraction in the gas phase is greater near the well and water saturation decreases with time. Once the water saturation near the well reaches zero, there is no more evaporation of water into the gas phase and the water mole fraction in gas phase becomes zero. Due to water drying, the cohesion near the hole increases and reaches the completely dry rock cohesion value of 2 MPa. This drying effect results in an increase in the value of cohesion in the sand near the hole. However, if water drying effects are not considered the cohesion everywhere in the cylinder remains at a constant value of 1.68 MPa, which is the value at initial water saturation. Thus, water evaporation strengthens the rock around the hole and prevents sand failure at the same compressive stress level, compared with no water evaporation (in the first three cases). This explains why sand production requires higher compressive stresses for gas flow when water evaporation effects are considered. Note that evaporation occurs only in gas wells and does not occur in oil reservoirs.

Fig. 7.3: Comparison of water saturation for gas flow with (left) and without (right) drying effects

Fig. 7.4: Comparison of water mole fraction in gas phase for gas flow with (left) and without (right) drying effects

Fig. 7.5: Comparison of cohesion for gas flow with (left) and without (right) drying effects

7.2.2 Effect of Non-Darcy Flow

In the second scenario, the same four cases are simulated and compared for the conditions at the onset of sanding. The cylinder in this set of simulations is subjected to increasing fluid pressure on the outside cylinder surface (from atmosphere pressure to 0.3MPa), while fluid pressure on the inner borehole surface (atmosphere pressure) and traction on the outside cylinder surface (10MPa) remain constant throughout the simulation. For all these four cases, due to excessive shear stresses, rock fails at the beginning. However, sanding does not occur immediately because fluid flow rate is not sufficient to remove these failed sands. The comparison of the critical fluid velocity for the onset of sanding in each case is displayed in Fig. 7.6.

For the case with oil flow, a much smaller flow rate is required to meet the erosion criterion and produce the failed sands, compared with gas flow. This is because there is no sand strengthening due to water evaporation with oil flow. In addition, with gas flow, non-Darcy effects tend to slightly increase the critical fluid velocity (4% higher) for sand erosion. Thus, with increasing flow rate, the oil flow case is the first to produce sand, while sand production in the gas flow case (with non-Darcy flow) is delayed. Non-Darcy effects are not significant in this case because the Reynolds number is very low for this experimental setup. The Reynolds number is shown in Fig. 7.7 below. These effects may be much more important in the field where the flow velocities are expected to be much higher.

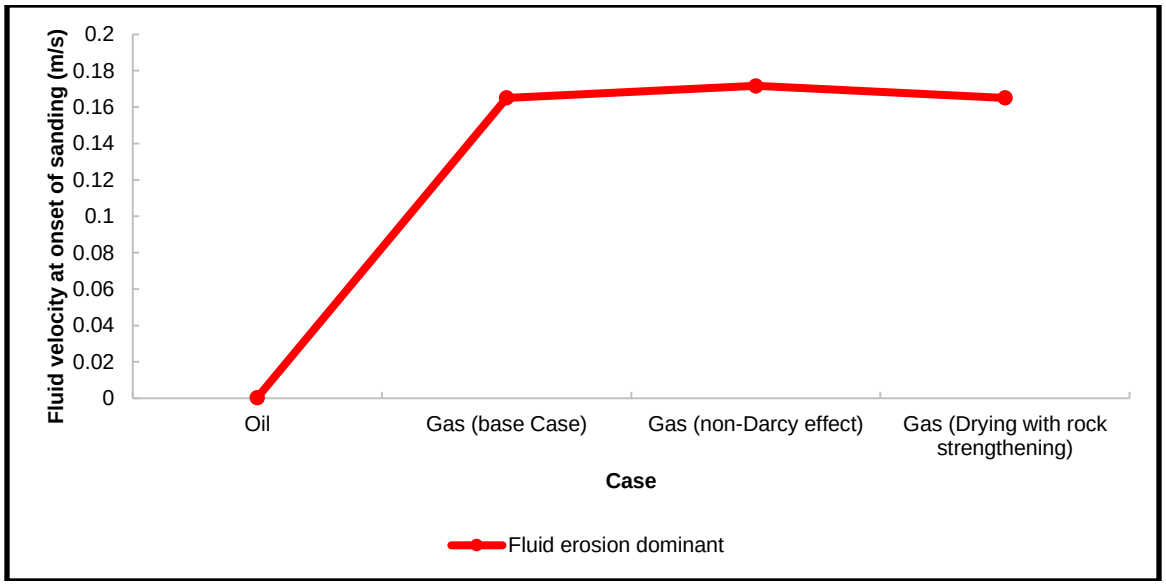

Fig. 7.6: Comparison of critical fluid velocity at the onset of sanding

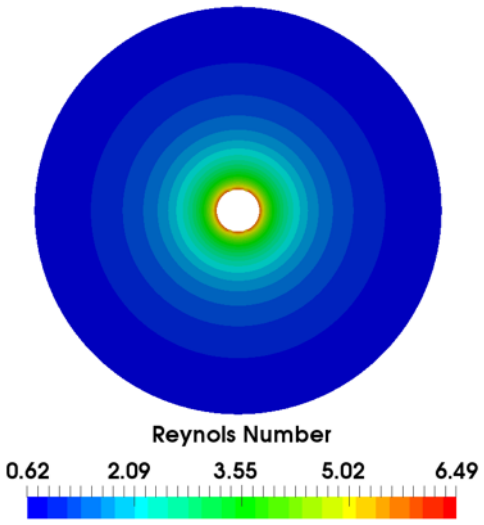

Fig. 7.7: Reynolds number for gas flow with non-Darcy effects

Next, the relation of sanding and pressure gradient is analyzed by comparing the difference between drag and resistance forces for each case. Since the fluid flow conditions are the same for the second and fourth case, only three cases are compared. Fig. 7.8 illustrates the evolution of drag force and resistance force with external fluid pressure during the injection period. As the resistance force is only a function of sand and fluid properties, it remains constant during injection. Nevertheless, as oil density is larger than gas density, the resistance force in oil flow is smaller when compared to gas. On the other hand, with the same external fluid pressure (same pressure gradient), the drag force for oil flow is the smallest due to the small fluid velocity caused by the larger oil viscosity. The drag force for gas flow with non-Darcy effects is slightly smaller than for Darcy gas flow, and this can be inferred from Eqn. (7.1) and Eqn. (4.1). As a result, oil flow requires the largest pressure gradient to produce sand, while the critical pressure gradient in gas flow without non-Darcy effects is the smallest.

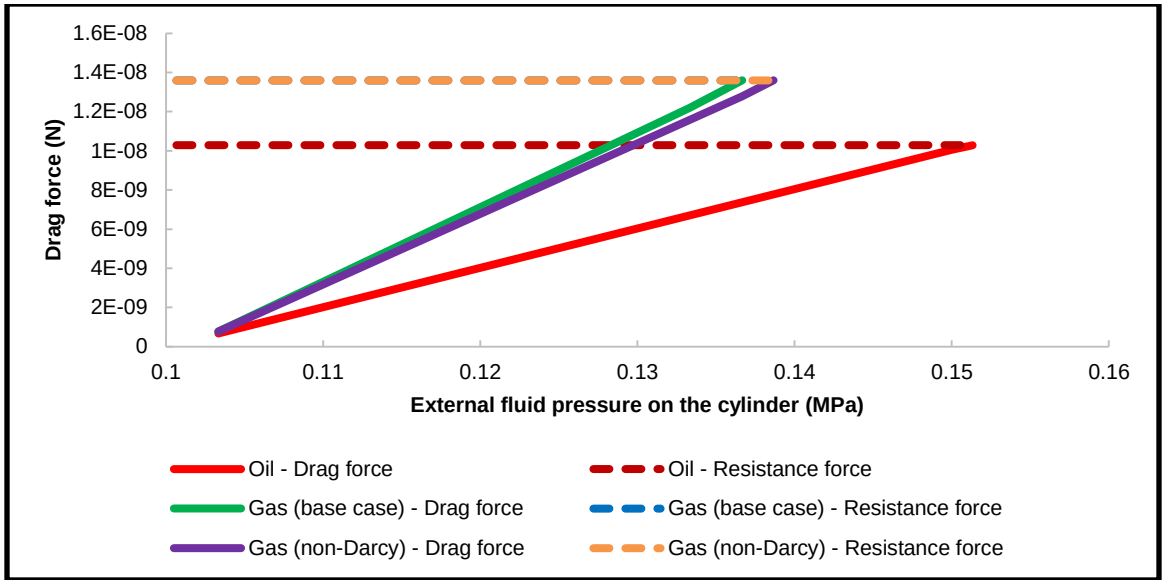

Fig. 7.8: Comparison of critical external fluid pressure with drag and resistance forces

7.3 Multiphase Fluid Flow on Sand Production

In this section, sand production in multi-phase fluid flow (oil and water) is simulated and analyzed. The multi-phase fluid properties are shown in Table 7.2. Initially, the reservoir is saturated with oil at an irreducible water saturation of 0.3. The pressure in the producer well is decreased from 25MPa while water is injected from wells in a 5-spot pattern. Three cases with different capillary pressure exponents (2, 4, and 6) are compared to study the effect of water breakthrough and water cut on sand production.

Table 7.2 Multi-Phase fluid flow parameters

Parameters	Value	Unit
Swr	0.3	
Sor	0.35	
Rel perm exponent	2	
Water end point rel perm	0.4	
Oil end point rel perm	0.75	
Capillary pressure at Swr (Pc^0)	2.00E+04	Pa
Capillary pressure exponent (Epc)	2,4,6	

The effect of capillary pressure exponents (Epc) on capillary cohesion is shown in Fig. 7.9. This governs the fluid erosion criterion. With a higher Epc value, capillary cohesion decreases more rapidly, resulting in a lower resistance force at the same water saturation. Fig. 7.10 shows the onset of sanding and the sanding rate in three cases with different Epc (until 1637s). The case with Epc = 6 shows that sanding happens at around 1619s, with increasing sanding rate. On the other hand, the cases with lower Epc do not result in any sand production at the end of 1637s. This is because in the case Epc = 6, the resistance force is lower than the drag force at the time sanding initiates, while for other two cases with lower Epc, the erosion criterion is not yet met due to larger capillary cohesion, which holds the sand together and prevents any sanding.

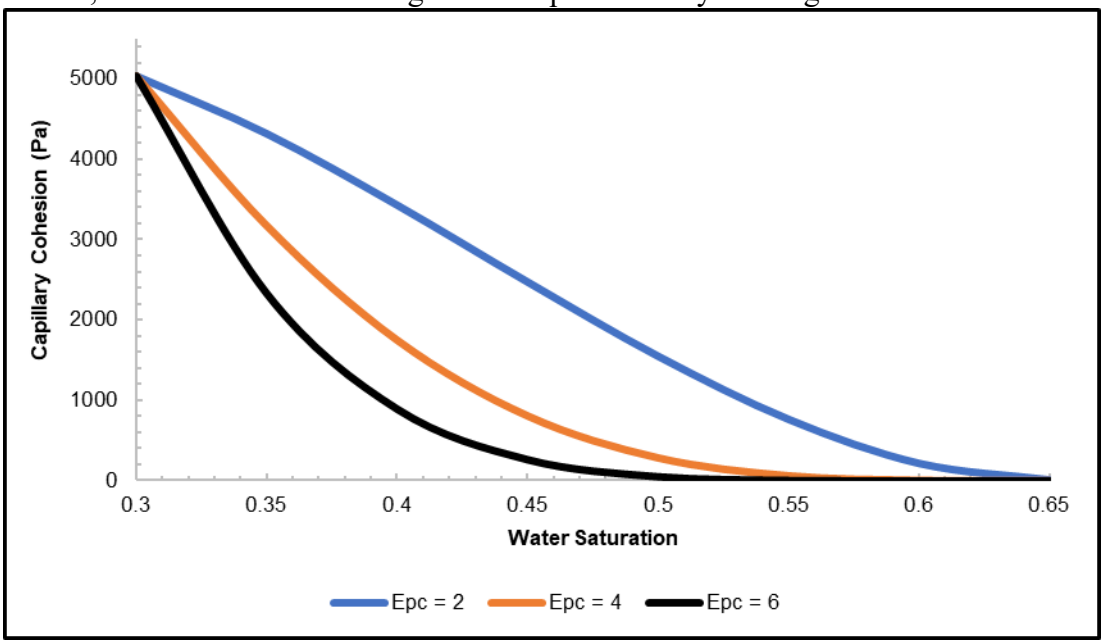

Fig. 7.9: The effect of capillary pressure exponent on capillary cohesion

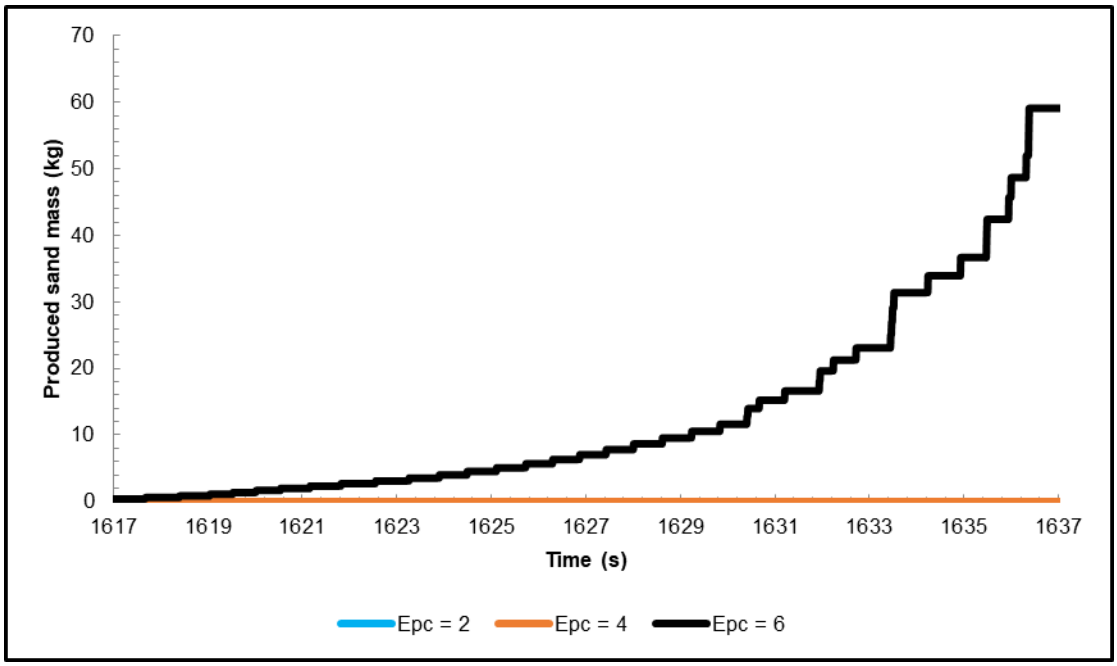

Fig. 7.10: The onset of sanding and sanding rate in three cases at wellbore pressure = 22MPa

More detailed results for the Epc = 6 case can be seen in Figs. 11 to 13. At time = 1500s (before the onset of sanding), the equivalent plastic strain forms a dog-ear shape due to the anisotropic stress condition, indicating the potential failure zone. However, at this time the rock has not yet failed. The water saturation profile is displayed in Fig. 12. With four wells injecting water, water breakthrough happens, yet no sanding is observed. The change of water saturation around the production well has three important impacts: 1) The cohesion decreases in the high water saturation region (left in Fig. 13), which will accelerate the mechanical failure process; 2) Capillary cohesion is reduced in high water saturation region (as discussed above), decreasing the force needed to erode the sand away; 3) The water saturation front increases the relative permeability of water and thus water velocity, which increases the drag force. In summary, water breakthrough and the increase

of water cut at the production well will prompt sanding, and the water cut plays an important role in determining the onset of sanding and the sanding rate.

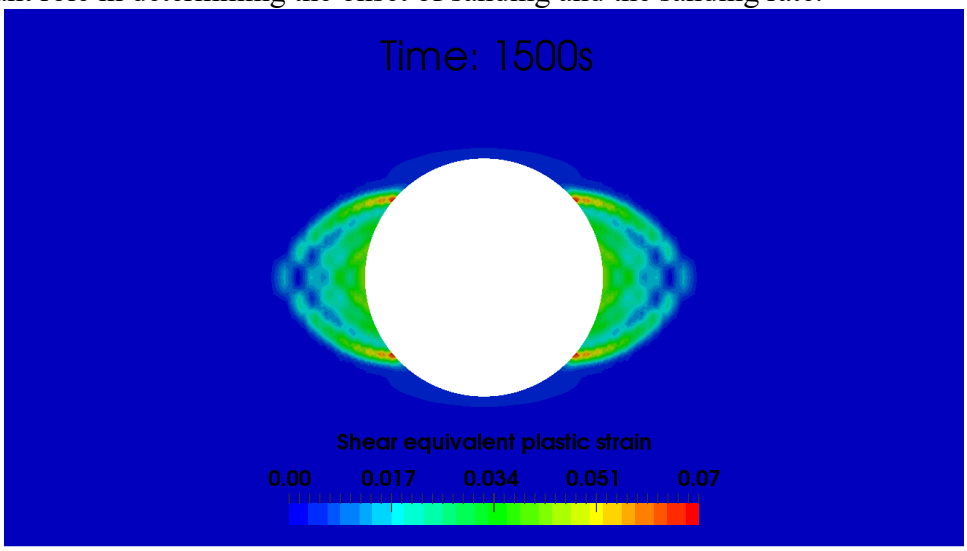

Fig. 7.11: Shear equivalent plastic strain distribution at time = 1500s, Epc = 6

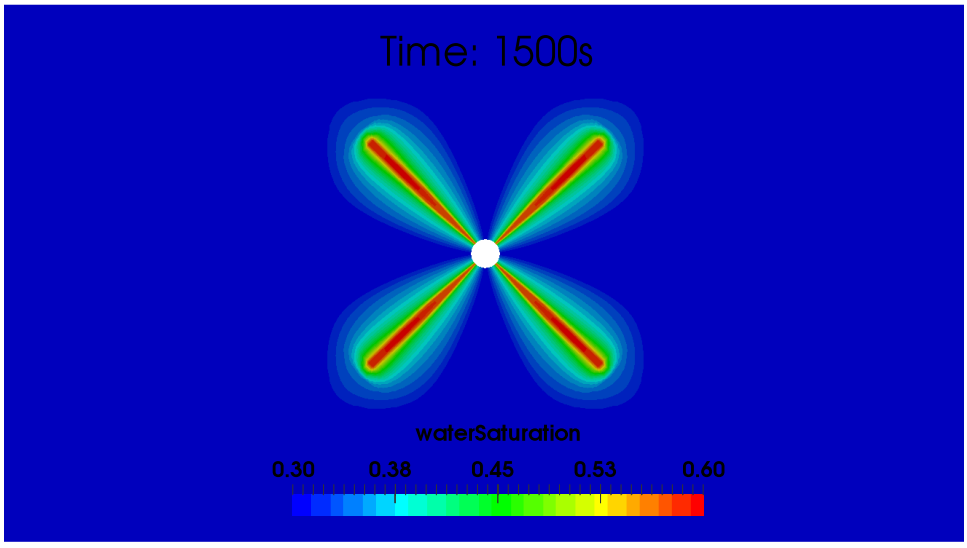

Fig. 7.12: Water saturation profile (with 4 injection wells around production well) at time = 1500s, Epc = 6

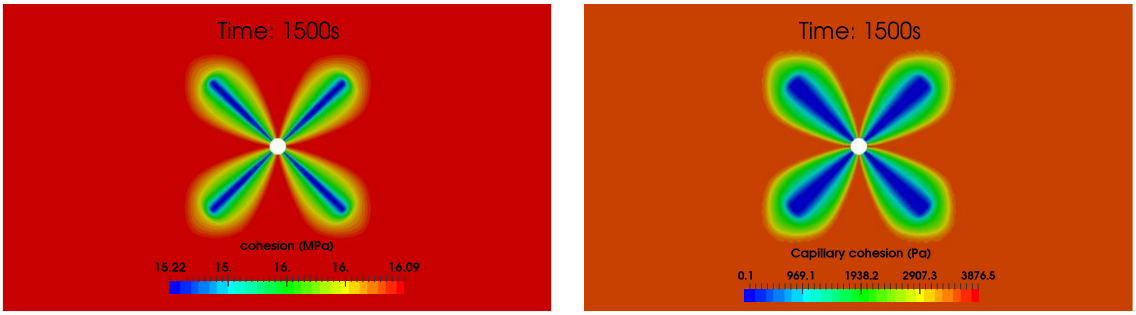

Fig. 7.13: Properties affected by water saturation in the case Epc = 6: cohesion (left) and capillary cohesion (right)

7.4 Sand Failure Caused by Water Hammer Event

For water injection wells handling high injection rates, water hammer signatures are observed when water injection is stopped. Maintaining wellbore integrity is a critical operational issue for water injection wells in poorly consolidated sands (Feng et al., 2015). Designing water injectors and deciding how quickly or slowly to shut-in wells requires careful attention. Prediction of sand failure caused by water hammer events can help design shut-in protocols for water injectors. The new workflow developed in this paper integrates water hammer simulations with sand stability and production predictions. The water hammer simulation shows that the rate changes during shut-in affects the water hammer amplitudes and attenuations significantly. Large pressure fluctuations, or large amplitudes in the water hammer signature after a quick shut-in are shown to result in significant sand failure, and a slow shut-in procedure can minimize sand production. Sizing of well completion components and locations of subsurface valves are key decisions in the design of injection wells and can be optimized to soften the impact of water hammer events and the associated sand production.

In producers, the evidence for the sand production is usually clear since failed sands can usually be transported and detected at the surface if the flow rate is sufficient. However, in injectors, failed sands stay in the well. Thus, there is no direct field data available on

when sanding in injectors begins and how much sand is produced with each shut down (Vaziri et al., 2007). Morita et al. (1998) studied the sand failure in injector wells with repeated shutdowns by reviewing the injectivity. Later, Santarelli et al. (2000) presented a field case of sand failure and sand production around a series of water injectors in the North Sea, showing extreme amounts of sand fill above the top perforation, and concluding that the consequences of sand failure around injectors could be dramatic in terms of injectivity losses and well performance. This mutual interaction between the formation damage and sand failure is a crucial factor which influences the long-term injectivity significantly. Sand failure and associated formation damage behavior can affect the induced fracture growth as well as the fluid leak-off pattern (Hwang & Sharma, 2013). This proves the sand failure prediction is the crucial component in the long-term injectivity prediction.

Vaziri et al. (2007) developed a numerical model for sand production prediction, and conducted a parametric study on sand production in terms of rock stress/strain behavior (brittle or ductile), injection pressure, frequency of shutdowns, magnitude of crossflow, and water hammer pressure pulses, concluding that a reduction in the frequency of shutdowns can be helpful in minimizing sanding issues.

In this section, we evaluate the effect of water hammer on sand failure with numerical simulation methods. Two numerical simulators, a water hammer model, Water Hammer (Mondal, 2011) and a sand production prediction model, Sand Manager (Wang et al., 2016) are integrated to help predict the risk and severity of sand failure and production. The detailed objectives of this study include:

- To predict sand failure and sand production caused by water hammer events
- To show the effect of well designs, such as the location of subsurface valves, shut-in procedures, and multiple shut-in events on both bottomhole pressure (BHP) and sand failure responses

- Study the impact of rock properties such as the post-yield behavior and rock strength, on water-hammer-induced sand failure.

The workflow in the current work integrates simulations of water hammer events after shut-in, with the associated sand failure/production. Water hammer signatures are simulated by solving mass and momentum balances in the wellbore-fracture system immediately after shut-in. The important parameters that control the pressure oscillations in the wellbore include wellbore geometry/properties, reservoir/fluid properties, and fracture dimensions connected to the wellbore. The shut-in procedure, can also greatly affect the water hammer amplitudes and attenuation time. This simulated pressure pulse at the sand-face is used in the sand production simulator, which fully couples multi-phase fluid flow and elasto-plasticity with a Mohr-Coulomb model, to predict the potential region of sand failure and the severity of sand production. Both the onset and volume of sand production are numerically computed as a function of time.

The water hammer simulation model used in this work was developed by Mondal (2010) and Carey (2014). The model solves the continuity and momentum balances in the wellbore filled with a slightly compressible single-phase fluid. The boundary condition at the wellhead is the transient change of the injection rate as the valve is being closed. The bottomhole boundary condition is an effective reservoir system composed of resistance-capacitance-inertance (R-C-I) components (Fig. 7.14a). Carey et al. (2016) was able to match water hammer field data by this simulation model, and predicted fracture dimensions that compared well with those estimated from microseismic data. Haustveit et al. (2017)'s work verified the simulation's ability to match the water hammer signals from the field data. Hwang et al. (2017) also matched the water hammer field data and showed that water hammer signatures show stress alterations over the fracture stages in a horizontal well. The simulation can predict the bottomhole pressure as well as the wellhead pressure (Fig.

7.14b). As shown earlier, the water hammer simulation model has been proven to provide a reliable prediction of the transient BHP.

In this work, the water hammer simulation model was used to predict transient changes of bottomhole pressure in water injectors. The model accounts for reservoir, fluid properties, wellbore trajectory, and rate change during shut-in. The simulated pressure in the wellbore is a combined result of all parameters and is impacted by the physical components specified in the simulation. The resulting amplitude, period, and the rate of decay change significantly as the input parameters are changed. For example, the resistance value represents the near-wellbore frictional pressure drop corresponding to the near-wellbore frictional resistance of the well. In water injectors, the resistance can be understood as the filter cake accumulated near the sandface. The capacitance and inertance values are specified so that the fracture volume is small enough in this work. During long-term water injection, a fracture may be induced, and this can be also simulated.

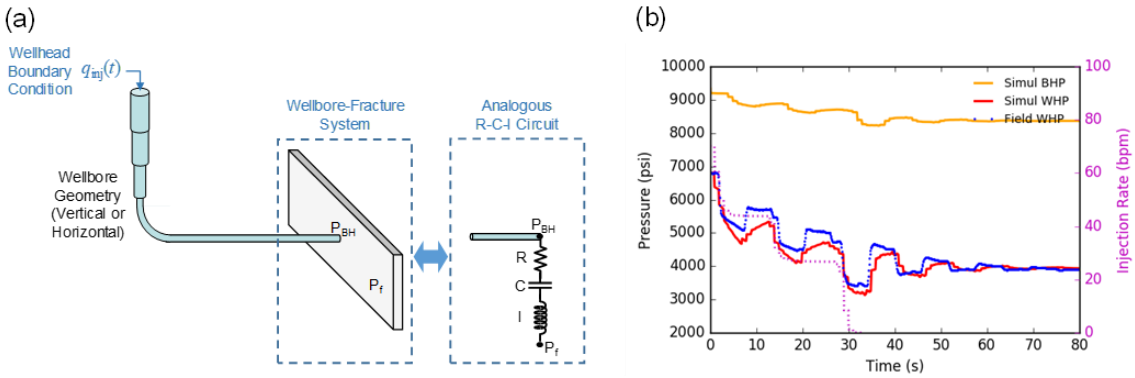

Fig. 7.14: (a) Components of the water hammer simulation model including boundary conditions at the wellhead and bottomhole. (b) Example results from the water hammer simulation and its comparison with the field wellhead pressure data

Over the life of injectors, the performance of the injection well can be affected by many factors. Suspended solids or oil droplets in the injection water can plug the matrix

near the sandface, and form a filter cake on the sand at the wellbore. Santarelli et al. (2000) showed that the injectivity decline process is mainly impacted by filter cakes and cross-flow between layers, and their impacts can be enhanced by water hammer pressure pulses during shut-in. While considering these factors, we will focus on the impact of water hammer on sand failure and sand production issues. The existence of water hammer, its period, amplitude, and the decay rate are shown to vary depending on injection well design and shut-in procedure.

Continuity and momentum balance equations are solved for the fluid in the wellbore after shut-in of water injectors. Simulated bottomhole pressure containing water hammer signatures are used as a boundary condition for the sand production simulation. The input parameters for the vertical well base case are summarized in Table 7.3. For a horizontal well, the input parameters are summarized in Table 7.4. The wellbore trajectory of the horizontal well was assumed to have four sections as shown in the table.

Table 7.3 Inputs for the water hammer simulation in the base case for vertical well

Parameter	Value	Unit	Parameter	Value	Unit
R-C-I Parameters			**Fluid Properties**		
R	2.67×10^{-3}	psi/bpd	Fluid density in wellbore	8.34	ppg
C	4.34×10^{-2}	bbl/psi	Fluid density in fracture	8.34	ppg
I	9.77×10^{-10}	psi/(bbl/d2)	Fluid viscosity in wellbore	1	cp
Initial Conditions			Fluid viscosity in fracture	1	cp
WHP before shut-in	3420	psi	Fluid modulus in wellbore	322000	psi
Injection rate before shut-in	18000	bpd	**Wellbore Properties**		
Reservoir Properties			Deviation from horizontal	90	deg
S_{hmin}	7542	psi	length	12000	ft
TVD	12000	ft	ID	7.87	in
Young's modulus	2170000	psi	OD	9.84	in
Poisson's ratio	0.25		Young's modulus	29000000	psi
			Poisson's ratio	0.25	
			roughness factor	6×10^{-5}	

Table 7.4 Inputs for the water hammer simulation in the base case for horizontal well

Parameter	Value	Unit	Parameter	Value	Unit
R-C-I Parameters			**Fluid Properties**		
R	8.44×10^{-3}	psi/bpd	Fluid density in wellbore	8.34	ppg
C	4.34×10^{-1}	bbl/psi	Fluid density in fracture	8.34	ppg
I	3.09×10^{-9}	psi/(bbl/d2)	Fluid viscosity in wellbore	1	cp
Reservoir Properties			Fluid viscosity in fracture	1	cp
S_{hmin}	6300	psi	Fluid modulus in wellbore	320000	psi
TVD	5600	ft	**Initial Conditions**		
Young's modulus	1740000	psi	WHP before shut-in	5300	psi
Poisson's ratio	0.24		Injection rate before shut-in	36000	bpd
Wellbore Properties					

	Section 1	**Section 2**	**Section 3**	**Section 4**	**Unit**		
Section deviation from horizontal	90	60	30	0	deg		
Section length	7700	800	1000	4000	ft		
Section ID	4.76	4.76	4.76	4.76	in		
Section OD	5.51	5.51	5.51	5.51	in		
Section Young's modulus	29000000	29000000	29000000	29000000	psi		
Section Poisson's ratio	0.25	0.25	0.25	0.25			
Section roughness factor	6×10^{-5}	6×10^{-5}	6×10^{-5}	6×10^{-5}			

In the following sections, the parameters noted below are varied to simulate the water hammer bottomhole pressures, and the subsequent sand failure responses in the openhole completion caused by water hammer BHP are simulated:

- Near-wellbore frictional pressure drop (skin caused by filter cake)
- Location of surface-controlled subsurface safety valve (SCSSV) in the wellbore
- Shut-in procedure

The values of parameters are changed as shown in Table 7.5.

Table 7.5 Parameters for the sensitivity study in water hammer simulations

	Well Orientation	**Parameter**	**Value**	**Unit**
Effect of Near-Well Friction (Skin)				
WH Case 01 (Base case for vert. well)	Vertical	Δp (near-well) =	48	psi
WH Case 02	Vertical	Δp (near-well) =	95.9	psi
WH Case 03	Vertical	Δp (near-well) =	240.8	psi
Effect of SCSSV Depth				
WH Case 01 (Base case for vert. well)	Vertical	Distance (SCSSV-Reservoir) =	12,000	ft
WH Case 04	Vertical	Distance (SCSSV-Reservoir) =	10,000	ft
WH Case 05	Vertical	Distance (SCSSV-Reservoir) =	8,000	ft
Effect of Shut-In Procedure				
WH Case 06 (Base case for horiz. well)	Horizontal	Quick shut-in		
WH Case 07	Horizontal	Slow and gradual shut-in		
WH Case 08	Horizontal	Slow and step-wise shut-in		

7.4.1 Effect of Filter Cake on Sandface

The filter cake is formed on the sandface over a long-term water injection, which impacts the sand failure behavior significantly. The presence of filter cake on the sandface can shield the reservoir formation from the water hammer pressure pulse in the bottomhole. The filter cake controls the frictional pressure drop at the interface of wellbore-reservoir system, and is represented as the skin of the well. Depending on the pressure drop across the filter cake, the actual transient pressure exhibited at the sandface differs significantly from the water hammer pressure in the wellbore.

In the water hammer simulation, the near-wellbore frictional pressure drop is represented as the pressure drop across the filter cake, which is calculated by the resistance component of the R-C-I circuit analogue. Higher pressure drop represents a thicker and low-permeability filter cake. With a large resistance value, the high near-well pressure drop as the well as the high skin is simulated. The skin of injectors also adversely impacts the injectivity of the well.

By using the input parameters in Table 7.3 and 7.5, the water hammer responses are simulated as shown in Fig. 7.15a. The higher skin (higher near-well pressure drop, higher resistance, thicker filter cake and lower injectivity index) results in a quicker attenuation and smaller initial amplitude of the water hammer. With a near-wellbore pressure drop (across filter cake) of 241 psi, the bottomhole pressure experienced at the sandface contains almost no water hammer pulses. With lower pressure drops, water hammer amplitudes and duration increase. With a 48 psi pressure drop with less filter cake deposition, the initial water hammer amplitude is approximately 220 psi, and the water hammer continues over 50 seconds at the sandface.

Table 7.6 shows the parameters used in the sand production model. In this section, we assume perfect plasticity during the yield process. The cohesion value is set as 72.5 psi

to represent unconsolidated sands, and the critical equivalent plastic strain is 0.4% to model quick failure after yield. BHP responses from three different skins, as described above, are applied to the sand production model to study the corresponding sand failure behavior and severity.

Table 7.6 Parameters used for the sand production simulations

Parameter	**Value**	**Unit**
Fluid density	1000	kg/m3
Fluid compressibility	3.10×10^{-6}	psi^{-1}
Fluid viscosity	0.001	Pa•s
Young's modulus	2170000	psi
Poisson's ratio	0.25	
Cohesion	72.5	psi
Friction angle	30	deg
Dilation angle	0	deg
Tensile strength	25	psi
Critical plastic strain	0.004	
Porosity	0.25	
Permeability	0.3	Darcy
Initial pore pressure (before shut-in)	8202	psi
Minimum horizontal stress	8557	psi
Maximum horizontal stress	8992	psi
Vertical stress	9427	psi
Reservoir length	20	m
Reservoir width	20	m
Wellbore diameter	0.2	m

Sand failure behaviors for the three cases are shown in Fig. 7.15. With low pressure change caused by small skin, a smooth plastic strain distribution is obtained which propagates along the minimum horizontal stress direction around the well. As the skin-induced pressure change increases (from 48 psi to 96 psi, and further to 241 psi), the plastic

strain distribution shown in Fig. 7.15c, becomes more and more localized, resulting in the development of shear bands. This is because the water hammer allows less time for the plastic strain to be localized during the deformation transient period, and the sudden decreases in bottom hole pressure cause the plastic strain to grow with a continuous gradient. On the other hand, a steady pressure drop with no water hammer signature allows the strain to be concentrated gradually.

Fig. 7.15d displays the failure area around the well in the three cases, and the magnitudes of the failed sand area (failed sand volume per unit height of the reservoir) are shown in Fig. 7.15b. The largest failure area is obtained in the case with the smallest frictional pressure drop (thinnest filter cake and smallest skin factor), where the water hammer has a larger number of cycles and larger amplitude. The failure area decreases monotonically when the water hammer effect becomes less significant, as the plastic strain concentrates in the narrow shear band rather than growing widely. To summarize, a case with a significant water hammer event, resulting from small near-wellbore frictional pressure drop (least filter cake deposition and small skin factor), gives rise to more sand failure than a case with no water hammer.

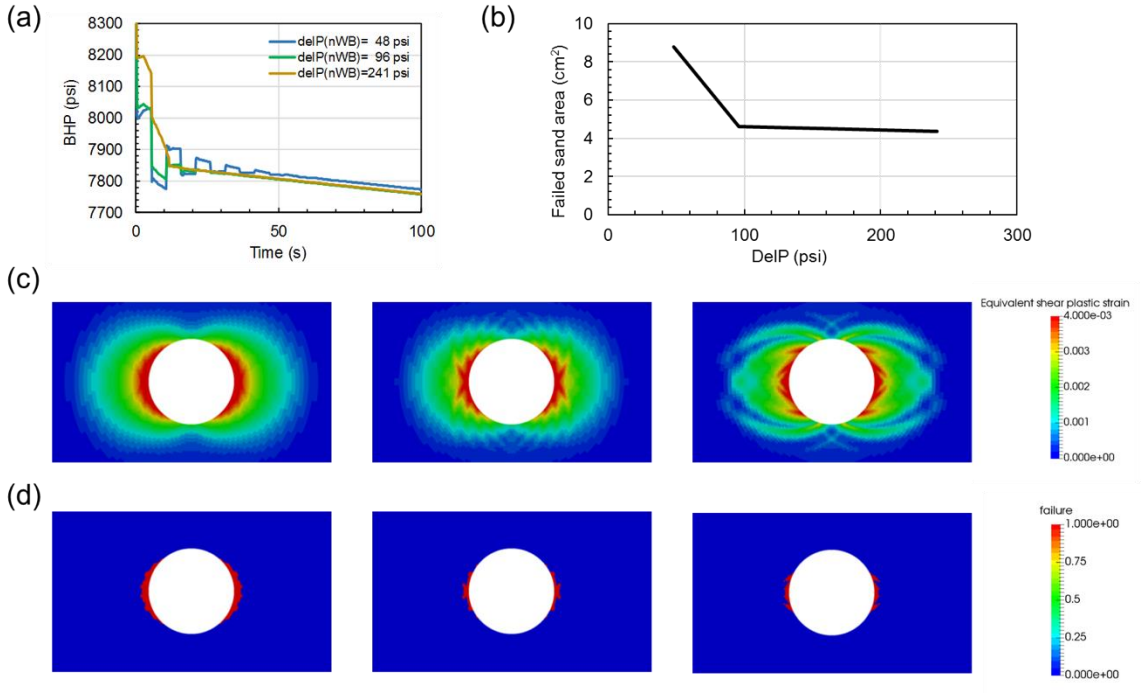

Fig. 7.15: (a) The effect of near-well frictional pressure drop (skin factor) on BHP after shut-in. (b) The effect of well skin on cumulative failure area. (c) The effect of well skin on plastic strain distribution (left: delP = 48 psi; middle: delP = 96 psi; right: delP = 241 psi). (d) The effect of well skin on sand failure distribution around wells (left: delP = 48 psi; middle: delP = 96 psi; right: delP = 241 psi). Note that the wellbore diameter is 0.2 m in all figures

7.4.2 Effect of Subsurface Valve Location

The emergency shut-down of a water injection well can be controlled by a surface-controlled subsurface safety valve (SCSSV). When the SCSSV is closed, water hammer pulses are transferred through the wellbore section from the SCSSV to the sandface as shown in Fig. 7.16a. Depending on this distance of the wellbore section, the water hammer signatures change in their amplitudes, wavelength, and decay rate. When the SCSSV is located at a deeper location in the wellbore, the distance that the water hammer pulse propagates becomes shorter. With this shorter length, the wavelength of the water hammer fluctuation becomes shorter. As the fluid volume is smaller in the wellbore when the

SCSSV is located deeper, the water hammer signature decays quicker in the deeper SCSSV case as shown in Fig. 7.16b.

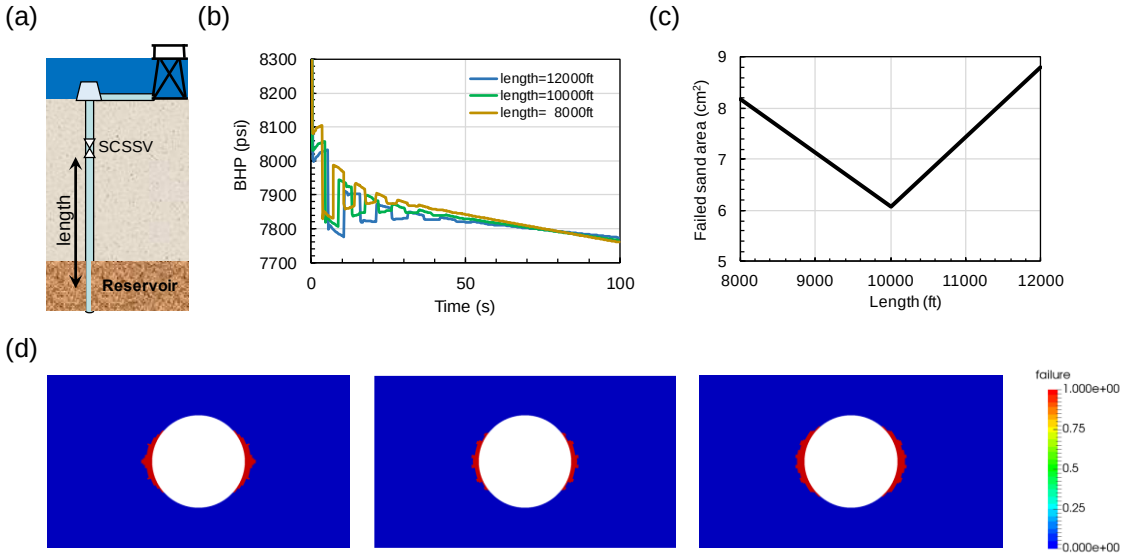

Fig. 7.16: (a) Location of subsurface valve. (b) The effect of subsurface valve location on BHP after shut-in. (c) The effect of subsurface valve location on cumulative failure area. (d) The effect of subsurface valve location on sand failure distribution around wells (left: length = 8000 ft; middle: length = 10000 ft; right: length = 12000 ft)

The impact of these three different water hammer events on sand failure behavior is similar. As seen in Fig. 7.16d, failure zones are all developed in the minimum horizontal stress direction, due to larger stress concentration and ultimate shear failure. However, Fig. 7.16c implies that the optimum location of subsurface valve to minimize sand failure is neither at the upper depth (toward surface) nor at the lower depth (toward reservoir). Instead, it should be located somewhere between the two limits. By comparing the two cases with length = 8,000 ft and length = 10,000 ft, we see larger pressure pulses in the latter case, which promote sand failure. On the other hand, under the same frequency of pressure pulses, the duration of each cycle of pressure fluctuation is longer in the latter case, which may inhibit sand failure. Thus, the cumulative sand failure region depends on

the combination of the magnitude of the pressure pulse and the duration of each cycle. Each potential location of the SCSSV in a well will, therefore, must be modeled to determine the best location from a sand control point of view.

7.4.3 Effect of Shut-In Procedure

The procedure of closing the valve results in how quickly or slowly the transient injection rate is changed from the initial injection rate to the complete shut-in state. This procedure of valve closure and associated rate changes are used for the water hammer simulation to show the response of bottomhole pressure. Three different shut-in procedures are tested, which are: a quick shut-in in 5 seconds; a slow/gradual shut-in over 50 seconds; and a step-wise shut-in in 20 seconds. The transient rate change in injection rates are plotted in Fig. 7.17a. It is noted that the step-wise shut-in process is comparable with the slow/gradual shut-in but with three times of sudden rate changes. The water hammer simulations are conducted with parameters in Table 7.4. The resulting bottomhole pressures are shown in Fig. 7.17a. In the quick shut-in, the bottomhole pressure drops over 450 psi in less than 10 seconds, and the water hammer attenuates in more than 50 seconds. In contrast, the slow shut-in process results in a very gradual pressure decay without a water hammer signature. The step-wise shut-in creates water hammer pulses, but the maximum amplitude is approximately 200 psi. Each of rate changes during step-wise shut-in create water hammer pulses, and they are superposed and decay over time.

Using these bottomhole pressures as boundary conditions, sand failure simulations are conducted with the in-situ stresses and initial pore pressure as shown in Table 7.7.

Table 7.7 Parameters used for shut-in procedure study

Parameter	Value	Unit
Initial pore pressure (before shut-in)	8992	psi
Minimum horizontal stress	9282	psi
Maximum horizontal stress	9718	psi
Vertical stress	10153	psi

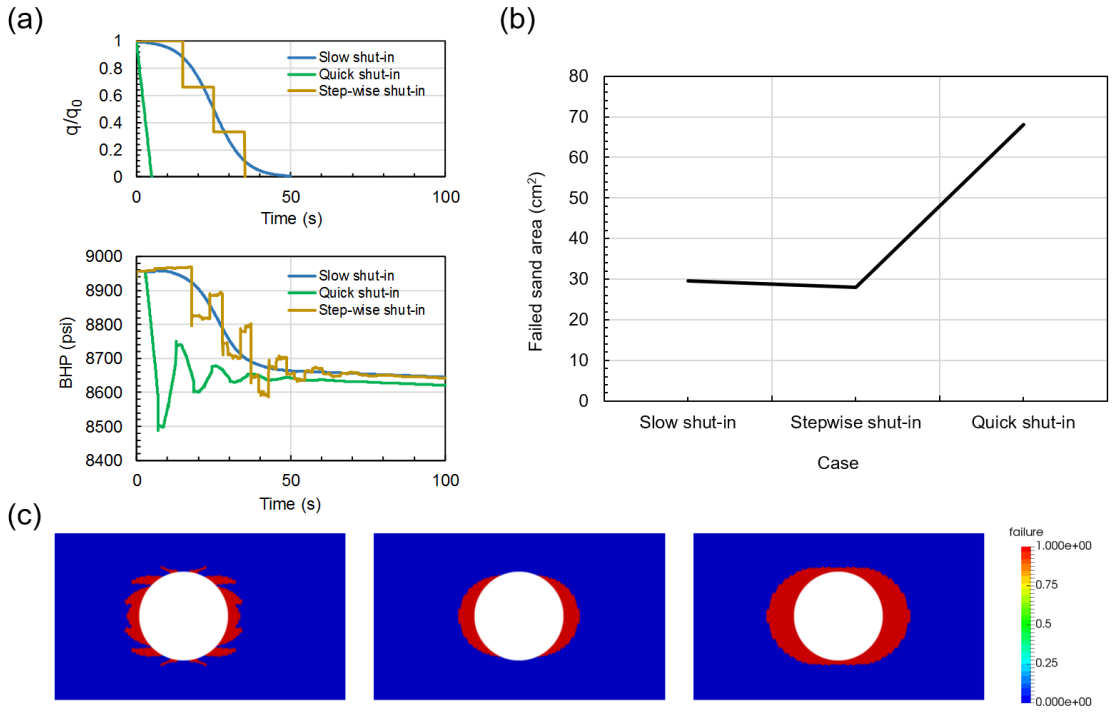

Fig. 7.17: (a) The effect of shut-in protocol on BHP. (b) The effect of shut-in protocol on cumulative failure area. (c) The effect of shut-in protocol on sand failure distribution around wells (left: slow shut-in; middle: stepwise shut-in; right: quick shut-in)

Since there is no water hammer event for the slow shut-in case, the development of sand failure is more localized, as discussed in the previous section, and its failure region is displayed in the left of Fig. 7.17c, whereas the water hammer caused by step-wise shut-in and quick shut-in lead to a global propagation of the failure region. In Fig. 7.17b, the results clearly demonstrate that a quick shut-in produces the largest failure area. However, the

difference between slow shut-in and step-wise shut-in is negligible for this particular case. Thus, based on our simulation workflow, it is recommended that operators avoid a quick shut-in to prevent massive sand failure.

7.4.4 Permeability Reduction by Sand Failure During Water Hammer Events

Injectivity loss due to sand failure and sand production is a common issue related to shut-in and restart of injection wells. In unconsolidated formations, a severe injectivity loss can be triggered by several phenomena related to the sand failure:

i. Aggregation of degraded sands (Fig. 7.18a),
ii. Re-injection of accumulated fines and produced sands during water hammer events (Fig. 7.18b),
iii. Accumulation of produced sands in the wellbore and perforation tunnel,
iv. Invasion of fines (from accumulated filter cakes on the formation face) into the failed sand regions.

The above factors can dramatically decrease the formation permeability in the damaged zones, and this phenomenon has been studied in this section. Permeability reduction in the formation is used to represent injectivity loss due to the formation damage. The solid particles residing over the long-term injection can move with the water hammer pressure pulses and the failed area is subject to severe plugging of these suspended particles. The particle plugging causes substantial impact on the rock permeability. The internal plugging and the external forming of filter cakes can incur substantial permeability damage. In order to take injectivity loss into account, we assume that, once sands fail, the permeability in the failed region is reduced by 100 times. The simulations in the previous sections, including wellbore skin factor, location of subsurface valves and shut-in protocol,

have been re-evaluated with the injectivity-loss assumption to analyze their impacts on sand failure.

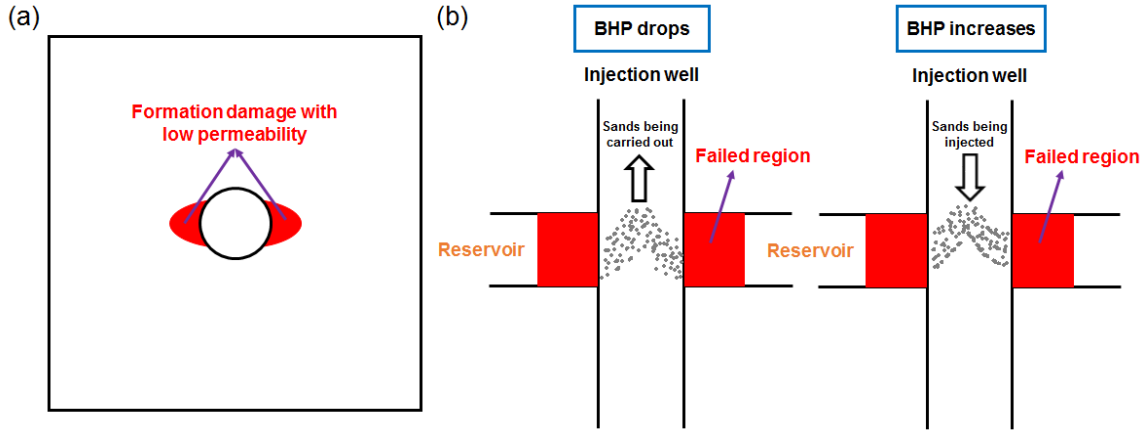

Fig. 7.18: (a) Degraded sand aggregation in the formation. (b) Fines, particles and sands reinjected into formation due to water hammer

The effect of well skin factor (filter cake) on sand failure is shown in Fig. 7.19 with the injectivity-loss assumption. This result is comparable with Fig. 7.15, which assumed no injectivity loss. Similar trends are observed for the cumulative failed sand area; with higher near-wellbore friction, formation tends to be more stable. However, the difference between the failed regions with and without water hammer is significant when we include the injectivity loss (Fig. 7.19c). As we reduce formation permeability within the damage zone, the pore pressure distribution varies dramatically, as seen in Fig. 7.19b. A large pressure gradient is generated due to fines reinjection, increasing sand failure. By comparing Fig. 7.15d and Fig. 7.19c, we find that with water hammer (cases with Δp_{nw} = 48 and 96 psi), injectivity loss increases the extent of sand failure dramatically, whereas without water hammer (case with high filter cake deposition with Δp_{nw} = 241 psi), the difference in sand failure is minimal no matter if there is an injectivity loss or not. This

indicates that a decrease in near wellbore permeability increases water-hammer-induced sand failure significantly.

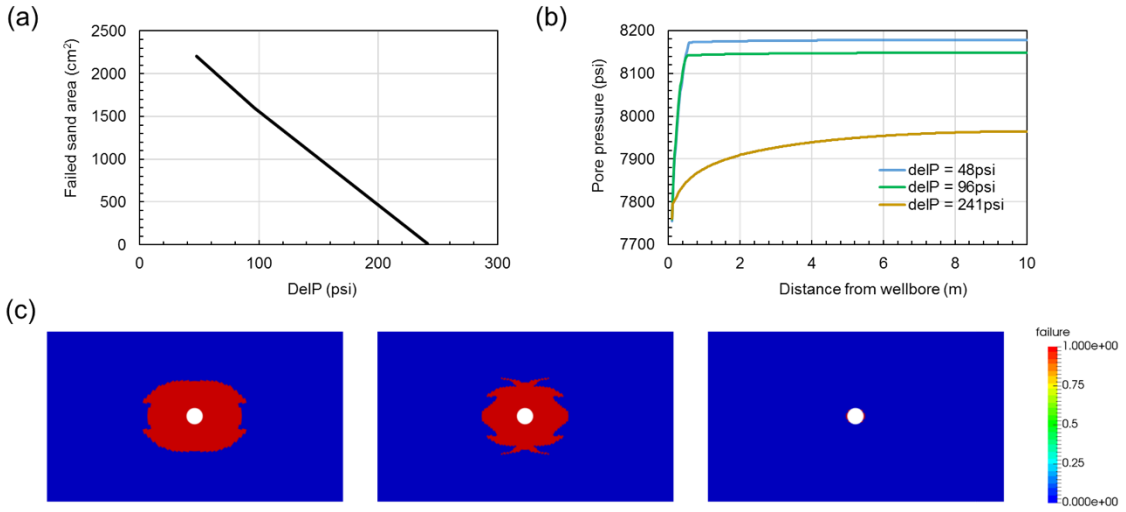

Fig. 7.19: Injectivity loss due to fines reinjection: (a) The effect of well skin on cumulative failure area. DelP in x-axis represents the pressure drop caused by the near-wellbore friction. This is the skin caused by the external filter cake formed by suspended particles in the injection water. (b) Pore pressure distribution after 100s of shut-in along a line in the radial direction from the wellbore toward the reservoir boundary. (c) The effect of well skin (filter cake) on sand failure distribution around wells (left: delP = 48 psi; middle: delP = 96 psi; right: delP = 241 psi)

Fig. 7.20 illustrates the sand failure results for different subsurface valve locations. By taking permeability loss into account, we arrive at the same conclusion on valve location: the optimum valve location needs to be determined for each well through simulations to minimize sanding risk. On the other hand, by comparing Fig. 7.16d and Fig. 7.20b, we observe a large difference in the extent of the sand failure region. As discussed previously, this is caused by the fact that near wellbore permeability loss leads to a much larger failure area when water hammer events appear after shut-in.

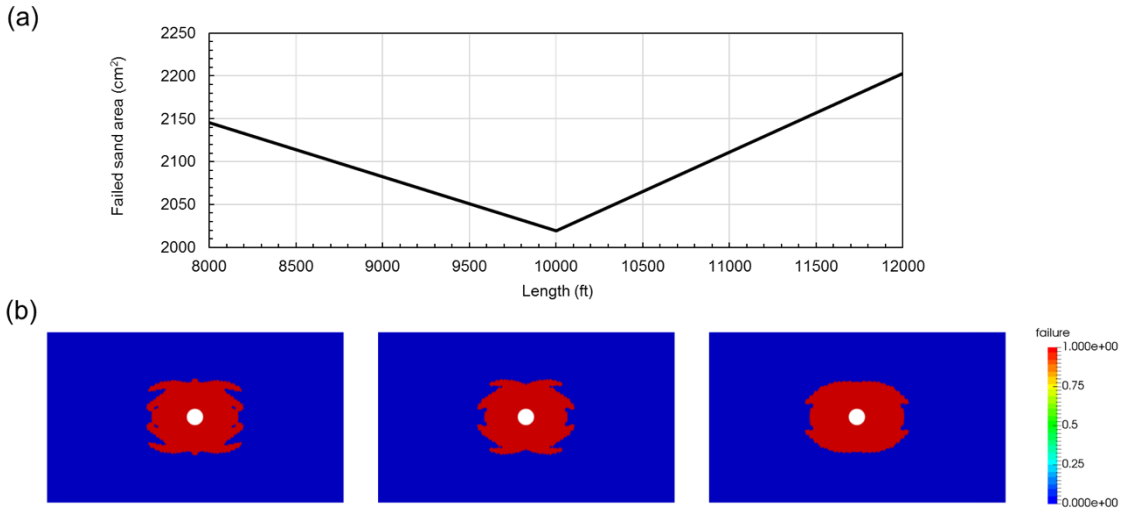

Fig. 7.20: Injectivity loss due to formation damage: (a) The effect of subsurface valve location on cumulative failure area. (b) The effect of subsurface valve location on sand failure distribution around wells (left: length = 8000 ft; middle: length = 10000 ft; right: length = 12000 ft)

The fines induced permeability-loss assumption is applied again to re-evaluate the impact of the shut-in procedure, and this result is shown in Fig. 7.21 (and can be compared with Fig. 7.17). We can see that the trends in Fig. 7.17b and Fig. 7.21a are not the same. As seen before, a reduction in near wellbore permeability (due to fines reinjection or other mechanisms) magnifies the impact of water hammer on sand failure. As can be seen in Fig. 7.21a, a slow shut-in is the best procedure to minimize sand failure.

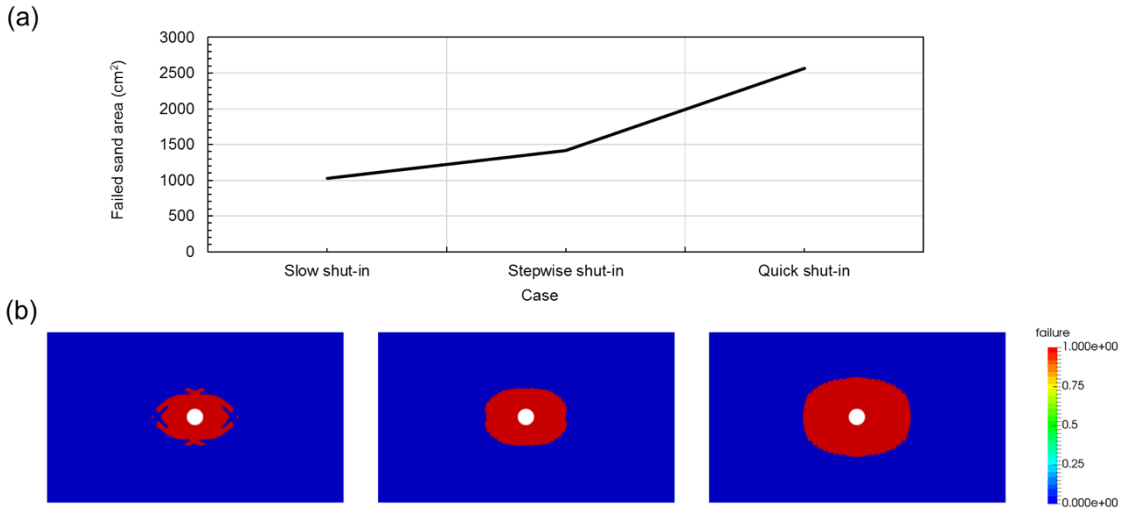

Fig. 7.21: Injectivity loss due to formation damage: (a) The effect of shut-in protocol on cumulative failure area. (b) The effect of shut-in protocol on sand failure distribution around wells (left: slow shut-in; middle: stepwise shut-in; right: quick shut-in)

7.4.5 Effect of Multiple Shut-In Events

Next, we compared the severity of sand failure with and without water hammer events for multiple shut-in events (Fig. 7.22). In the example shown here, a total of 5 shut-in events have been simulated for the injection well, and the inputs are the same as in the case of Δp_{nw} = 48 psi (with water hammer) and Δp_{nw} = 241 psi (no water hammer). Assuming a near wellbore permeability loss we observe a big difference in the sand failure region for these two scenarios as shown in Fig. 7.22c. As expected, at the end of the last shut-in event, much more sand failure is predicted under water hammer conditions. Also, Fig. 7.22b indicates that with a water hammer, the extent of the sand failure region continuously increases with the number of shut-in events. However, if there is no water hammer, sand failure occurs in the second and third shut-in events, while for the other events the sand failure rate is relatively small.

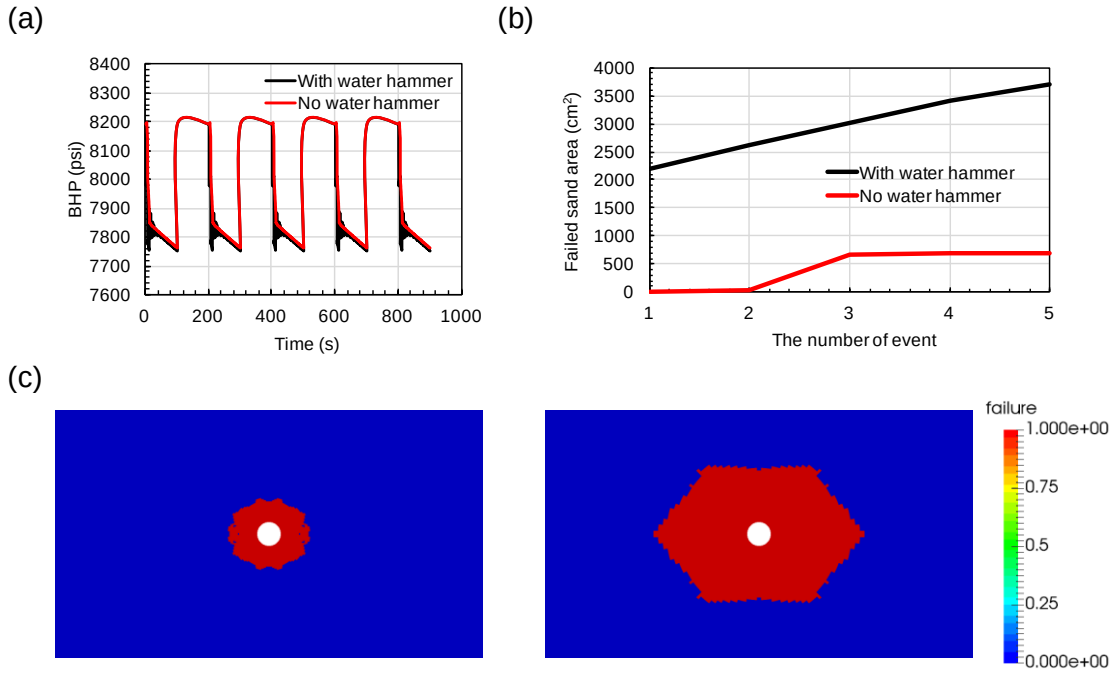

Fig. 7.22: (a) BHP with and without water hammer for 5 shut-in events. (b) The effect of water hammer on cumulative failure area during each shut-in event. (c) The effect of water hammer on sand failure distribution around wells at the end of 5 shut-in events (left: no water hammer; right: with water hammer)

7.4.6 Effect of Rock Mechanical Properties: Strain Softening Behavior

In this section, we will discuss the role of rock strain softening behavior. We use the data from the previous three shut-in protocol cases (without permeability loss), with the only difference being that instead of assuming perfect plasticity after yield, here we allow the cohesion to decrease during yielding to represent the rock degradation process. The intact rock cohesion is 72.5 psi, and during post-yield, it linearly decreases to 43.5 psi (the residual cohesion).

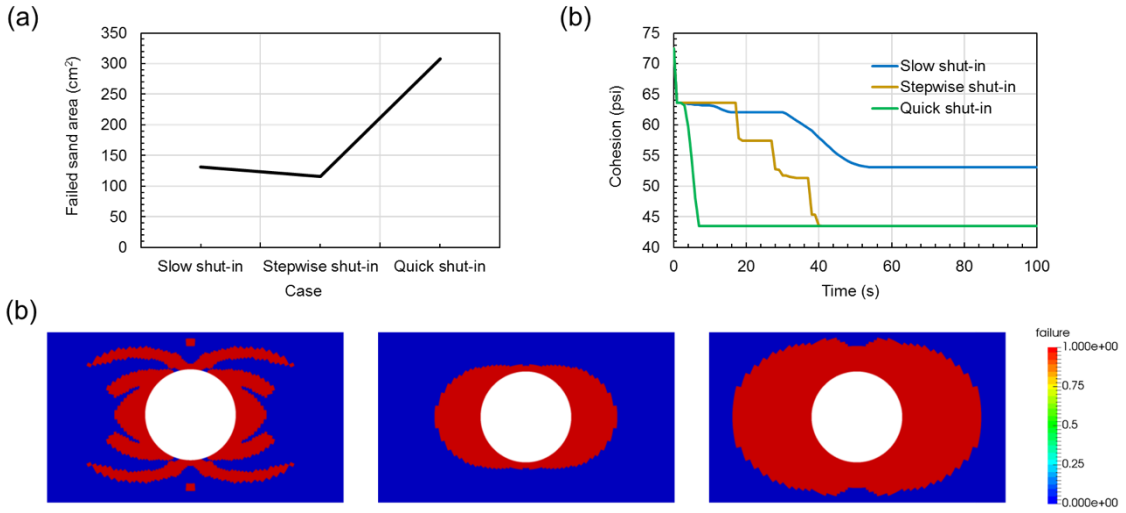

Fig. 7.23: Strain softening after yield: (a) The effect of shut-in protocol on cumulative failure area. (b) The reduction of rock cohesion after yield in three shut-in protocols. (c) The effect of shut-in protocol on sand failure distribution around wells (left: slow shut-in; middle: stepwise shut-in; right: quick shut-in)

By comparing Fig. 7.17b and Fig. 7.23a, we see the same trend for the cumulative sand failure area. In the slow shut-in case, shear bands dominate the failure region, whereas with step-wise and quick shut-in procedures, failure develops in a smoother region along the concentrated-stress direction. On the other hand, with strain softening, failure areas in all three shut-in protocols are more than 3 times larger than those with perfect plasticity. This is because, after sands yield, with strain softening, cohesion starts to decrease towards to the residual cohesion, and the sands can sustain smaller stress due to stress relaxation. Since boundary conditions for stress and BHP are given, the total strain obtained after yielding with strain softening is larger, and the neighboring intact rock is more likely to yield and further fail. Fig. 7.23b illustrates how sand cohesion changes after yielding under three different shut-in procedures. The cohesion values are obtained at the location of 0.2 m on the right side from the wellbore. With quick shut-in, sands at this location quickly

lose their strength and fail (to the residual cohesion). With stepwise shut-in, the cohesion has three sharp reductions, corresponding to the three pressure drops in water hammer response (Fig. 7.17a). With slow shut-in, since there is no water hammer, cohesion decreases gradually, however at this location, sands do not reach failure due to the failure pattern (failure distribution with shear banding).

7.4.7 Effect of Unconfined Compressive Strength (UCS)

Previously we have studied the effect of different BHP responses on sand failure after shut-in, and we have observed that both sand failure behavior and cumulative sand failure area are different with and without water hammer events. Fig. 7.24a shows the BHP change with and without water hammer events. We evaluate the impact of this pressure response under three groups of unconfined compressive strength (UCS), and the results are shown in Fig. 7.24b. When the UCS is small (below 240 psi), the impact of water hammer on sand failure is significant, compared with no water hammer. The difference of cumulative failed sand areas caused by water hammer compared to no water hammer becomes larger as the rock becomes more poorly consolidated. For reservoirs with low UCS, water hammer events may result in much more sand failure and the water hammer must be carefully controlled during the shut-in process. On the other hand, when the UCS is larger (above 240 psi), we can see a smaller impact of water hammer on sand failure.

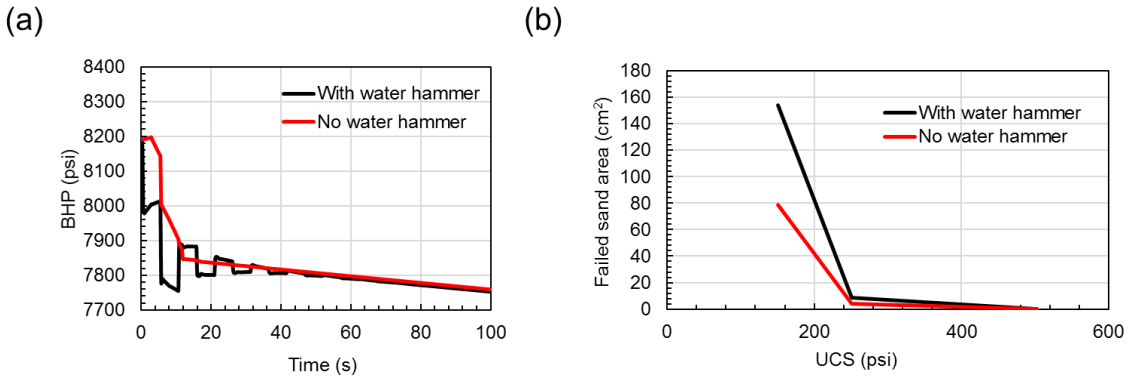

Fig. 7.24: (a) The effect of water hammer on BHP. (b) The effect of water hammer on cumulative sand failure for different UCS

7.5 CONCLUSIONS

In this chapter, we have explored the reasons for the experimental observation that higher compressive stresses are needed for the onset of sanding in compressible gas flow compared with oil flow. The impact of water breakthrough and water cut on the onset of sand production and sanding rate are also studied. We have developed a numerical 3-D multi-phase fluid flow sand production model which considers several important effects such as (a) non-Darcy flow (b) rock strength as a function of water saturation (c) water evaporation (d) flow-regime-dependent drag force calculation and (e) erosion resistance force which depends on capillary cohesion.

For the first time we have also numerically simulated water-hammer-induced sand failures to understand the impact of well geometry, rock properties and shut-in procedures. We have developed a workflow that integrates simulation of water hammer events with geomechanical sand failure/production models. Water hammer signatures have been simulated to understand their impact on sand failure. The workflow has been applied to quantitatively predict the BHP response and induced sand failure during different shut-in protocols in injection well operations. Factors such as wellbore skin in the form of filter

cake, subsurface valve location, shut-in protocols and the number of shut-in events have been studied.

REFERENCES

Bird, R. B., W. E. Stewart, and E. N. Lightfoot. 2007. Transport phenomena. *John Wiley & Sons.*

Buck, A. L. 1981. New equations for computing vapor pressure and enhancement factor. *J. Appl. Meteorol., 20:* 1527–1532.

Carey, M. A. 2014. Water Hammer Fracture Diagnostics. Thesis. *The University of Texas at Austin.*

Carey, M. A., S. Mondal, and M. M. Sharma. 2015. Analysis of Water Hammer Signatures for Fracture Diagnostics. *Paper SPE 174866. https://doi.org/10.2118/174866-MS.*

Carey, M. A., S. Mondal, M. M. Sharma, and D. B. Hebert. 2016. Correlating Water Hammer Signatures with Production Log and Microseismic Data in Fractured Horizontal Wells. *Paper SPE 179108. https://doi.org/10.2118/179108-MS.*

Cerasi, P., A. Berntsen, L. E. Walle, and E. Papamichos. 2015. Sand production delay in gas flow experiments. *Paper presented at the 49th US Rock Mechanics Symposium, San Francisco, CA, USA, June 2015.*

Chang, Y. -B. 1990. Development and Application of an Equation of State Compositional Simulator. *Ph.D. Dissertation, University of Texas at Austin, Austin, Texas.*

Choi, S.-K. and W. S. B. Huang. 2011. Impact of Water Hammer in Deep Sea Water Injection Wells. *Paper SPE 146300. https://doi.org/10.2118/146300-MS.*

Feng, Y., C. Arlanoglu, E. Podnos, E. Becker, and K. E. Gray. 2015. Finite-element studies of hoop-stress enhancement for wellbore strengthening. *SPE Drilling & Completion, 30 (01): 38-51. https://doi.org/10.2118/168001-PA.*

Haustveit, K., K. Dahlgren, H. Greenwood, T. Peryam, B. Kennedy, and M. Dawson. 2017. New Age Fracture Mapping Diagnostic Tools-A STACK Case Study. *Paper SPE 184862. https://doi.org/10.2118/184862-MS.*

Hawkins, A. B. and B. J. McConnell. 1992. Sensitivity of sandstone strength and deformability to changes in moisture content. *Quarterly Journal of Engineering Geology and Hydrogeology25.2 (1992):* 115-130.

Hwang, J. and M. M. Sharma. 2013. A 3-Dimensional Fracture Propagation Model for Long-Term Water Injection. *ARMA 13-575. https://www.onepetro.org/conference-paper/ARMA-2013-575.*

Hwang, J., M. J. Szabian, and M. M. Sharma. 2017. Hydraulic Fracture Diagnostics and Stress Interference Analysis by Water Hammer Signatures in Multi-Stage Pumping Data. *Paper URTeC 2687423, SPE/AAPG/SEG Unconventional Resources Technology Conference. https://www.onepetro.org/conference-paper/URTEC-2687423-MS.*

Mahadevan, J., M. M. Sharma, and Y. C. Yortsos. 2006. Flow-through drying of porous media. *AIChE Journal, 52(7),* 2367-2380.

Masoumi, H., J. Horne, and W. Timms. 2017. Establishing empirical relationships for the effects of water content on the mechanical behavior of Gosford sandstone. *Rock Mech. Rock. Eng. 50,* 2235–2242.

Mondal, S. 2010. Pressure Transients in Wellbores: Water Hammer Effects and Implications for Fracture Diagnostics. *Thesis, The University of Texas at Austin.*

Morita, N., E. Davis, and L. Whitebay. 1998. Guidelines for solving sand problems in water injection wells. *In SPE Formation Damage Control Conference. Society of Petroleum Engineers.*

Ray, P., M. Rijken, J. Cameron, C. Jones, and A. EI-Fayoumi. 2014. Estimating sand production volume in Oil and Gas Reservoir. *Paper presented at the SPE Annual Technical Conference and Exhibition, Amsterdam, The Netherlands, October 2014.*

Santarelli, F. J., E. Skomedal, P. Markestad, H. I. Berge, and H. Nasvig. 2000. Sand Production on Water Injectors: How Bad Can It Get? *SPE Drilling & Completion, 15(2), 132–139. https://doi.org/10.2118/64297-PA.*

Skjaerstein, A., J. Tronvoll, F. J. Santarelli, and H. Joranson. 1997. Effect of water breakthrough on sand production: experimental and field evidence. *Paper presented at the SPE annual technical conference and exhibition.*

Tronvoll, J., M. Dusseault, F. Sanfilippo, and F. Santarelli. 2001. The tools of sand management. *Paper presented at the SPE Annual Technical Conference and Exhibition.*

Vasarhelyi, B. and P. Van. 2006. Influence of water content on the strength of rock. *Engineering Geology 84:* 70-74.

Vaziri, H., B. Barree, Y. Xiao, I. Palmer, and M. Kutas. 2002. What is the magic of water in producing sand? *Paper presented at the SPE Annual Technical Conference and Exhibition.*

Vaziri., H, A. Nouri, K. Hovem, and X. Wang. 2007. Computation of Sand Production in Water Injectors. *Presented at the European Formation Damage Conference held in Scheveningen, The Netherlands, 2007. SPE-107695-MS.*

Wang, H., P. Cardiff, and M. M. Sharma. 2016. A 3-D poro-elasto-plastic model for sand production around open-hole and cased & perforated wellbores. *Paper presented at 50th US Rock Mechanics Symposium, Houston, Texas, USA, June 2016.*

Wang, H., D. P. Gala, and M. M. Sharma. 2017. Effect of Fluid Type and Multi-Phase Flow on Sand Production in Oil and Gas Wells. *In SPE Annual Technical Conference and Exhibition. Society of Petroleum Engineers, 2017.*

Wang, X., K. A. Hovem, D. Moos, and Y. Quan. 2008. Water Hammer Effects on Water Injection Well Performance and Longevity. *Paper SPE 112282.*

Wang, H., J. Hwang, and M. M. Sharma. 2018. Sand Production Caused by Water Hammer Events: Implications for Shut-In Protocols and Design of Water Injection Wells. *In SPE International Conference and Exhibition on Formation Damage Control. Society of Petroleum Engineers.*

Wu, Y.-S., J. Li, D. Ding, C. Wang, and Y. Di. 2014. A Generalized Framework Model for the Simulation of Gas Production in Unconventional Gas Reservoirs. *SPE Journal, 19(05):* 845-857.

Zhou, Z., X. Cai, W. Cao, X. Li, and C. Xiong. 2016. Influence of water content on mechanical properties of rock in both saturation and drying processes. *Rock Mech Rock Eng 49:*3009–3025.

Chapter 8: Sand Production Prediction in Tarim Field[4]

8.1 INTRODUCTION

Sand production is a common issue throughout the life of many wells. It is likely to happen in poorly consolidated sands, due to low rock strength. However, it has also been observed frequently in HPHT wells, where formation damage can be triggered through drilling, cementing, completion and production.

In some fields, formation damage, caused by drilling and completion process, play an important role in sanding issues. This has been reported in VLG 3676, Block VII, one of the most important fields in Ceuta, which is located in the deep and layered Eocene reservoirs of southern Lake Maracaibo, Western Venezuela (Tovar et al., 1999). As observed in the field, most of the wells produced sand from the very beginning in manageable quantities. However, sand production became more critical, resulting in severe consequences when depletion effects started to add to the in-situ stresses. Finally, throughout the field, some wells suffered catastrophic failure (casing collapse), while others consistently produced sand at higher levels than the specified limit

In HPHT reservoirs, high stresses and high initial pore pressure can result in high drawdowns which can be another culprit for sand failure and sand production. Vaziri (1986) stated that creation of wellbores in deep reservoirs leads to significant changes in stress and pore pressure around the well cavity. The shear stresses developed and the pressure gradients established are sufficient to cause instability over a long distance beyond the stress relieved zone, giving rise to sand production. Later, Allen and Waters (1999) analyzed the early operating experience in Erskine field, which is the first High Pressure High Temperature field in production on the UK continental shelf, and concluded that due

[4] The original source of this chapter is from Wang et al. (2018). Sharma supervised all the projects. Yang and Zhang provided field data and collaborated on the analysis.

to very high initial pressures, there would be tremendous decline in pore pressure over the field life. With the combination of initial high stress, this depletion induced some localized formation collapse, giving rise to the production of sand.

Experience in HPHT fields in Louisiana has shown that initially the sand production will occur in small and controllable bursts, which has been explained on the basis of the grain-to-grain frictional resistance and the capillary cohesion, binding the individual sand grains (Glass, 2005). This favorable sand behavior has also been confirmed in North Sea HPHT fields. By investigating completion strategies and field validation, Palmer et al. (2006) proposed that for deviated wells, oriented perforations can help to reduce the risk of sanding, compared to non-oriented, phased perfs.

Another important factor for sand production is rock strength. Sand failure and further production is also common in reservoirs with low rock strength and weak cements. The Marnock field, which is a retrograde gas condensate accumulation in the central area of the North Sea, is classified as a HPHT reservoir, with a pressure of 9123 psia and a temperature of 310F (Law et al., 2000). According to a review of the laboratory core work from the exploration wells and petrophysical analysis, the rock is identified with an unconfined compressive strength in the range 1250 – 4500 psi, and with the presence of weak chlorite cement in places. These lead to rock failure and sand production during the early years of field life.

8.2 Background of Tarim KeS Field

The KeS block is recognized as a low porosity, low permeability, deep and tight gas reservoir with a large amount of natural fractures. It is cretaceous in age (Fig. 8.1). The lithology consists of mainly fine sandstone, a small amount of clay, fine to coarse quartz grains, siltstone and gravel. The porosity is around 6 to 10% at a formation depth of 6500m

to 7000m. The permeability varies from 0.1~1×10-3μm2. Rock strength is relatively high due to compaction in the intact rock zone, and cementation is dominated by calcite and clay. Fig. 8.2 shows the detailed lithology of the KeS block at different depths. One important feature in the KeS block is that it includes a high content of clay and natural fractures (fully filled or half filled by calcite), and the rock strength in the natural fracture zone can be affected significantly by the fractures. On the other hand, heterogeneity plays an important role in the KeS block. Figs. 8.3 and 8.4 present the porosity and the rock strength as a function of depth. Rock properties change dramatically with depth, as the change in porosity can be 4 to 8 times and the difference of UCS can be more than 3 times.

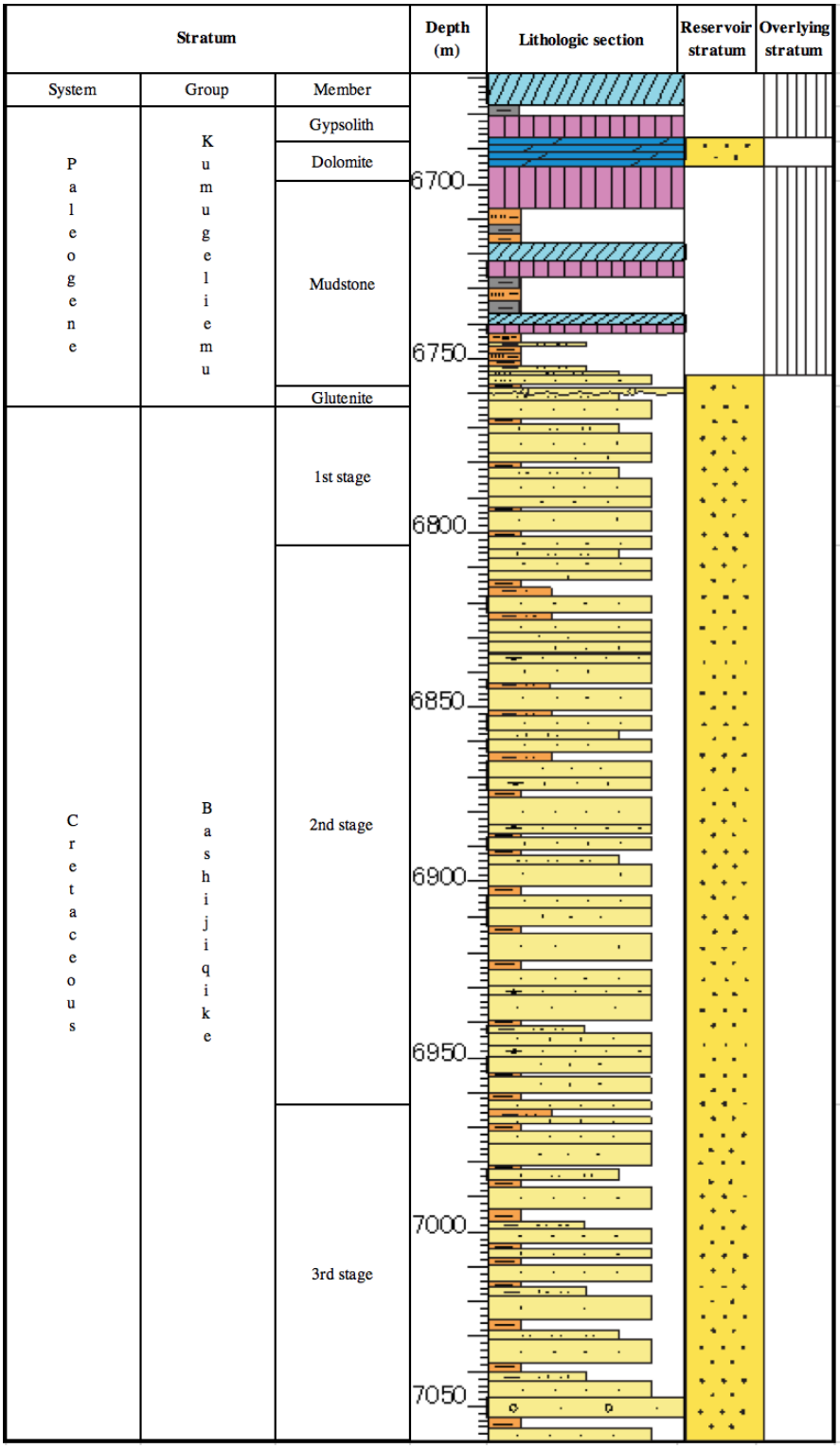

Fig. 8.1: Rock characterization in Tarim KeS block

Sample	Depth (m)	Terrigenous clastic content (%)						Contact	Main grain size range (mm)	Debris size range (mm)
		Quartz	Potash feldspar	Plagioclase	Rock debris					
					Sedimentary rock	Metamorphic rock	Magmatic rock			
R2014-1121	6580.08	45	17	15	2	8	13	Point	0.0625 - 0.25	0.04 - 0.38
R2014-1122	6580.42	46	18	17	2	7	10	Point	0.0625 - 0.25	0.03 - 0.65
R2014-1123	6580.82	44	20	17	2	6	11	Point - line	0.125 - 0.5	0.04 - 0.7

Fig. 8.2: Lithology of Tarim KeS block

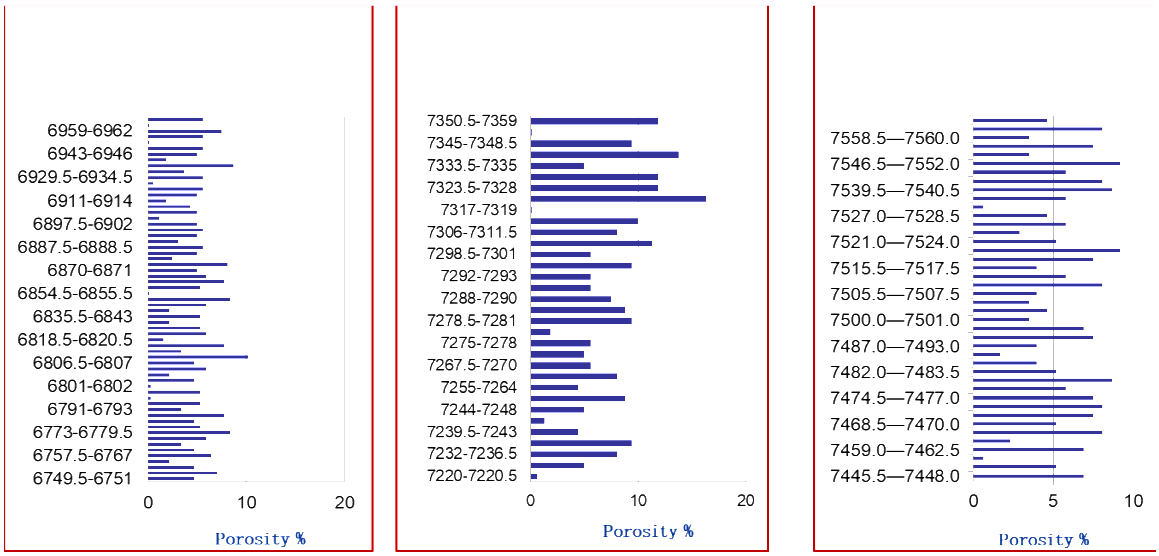

Fig. 8.3: Porosity vs depth for different wells

Sample No.	Depth	Cohesion
	m	psi
3-2	6799.48	4751
4-1	6799.61	2857
11-2	6800.62	7682
43-2	6804.48	5805
85	6811.38	5245
92-2	6869.14	7985
95-2	6869.63	6066
132	6875.59	4090
140-1	6876.44	5634
150	6878.28	9082
166	6881.04	6173

Fig. 8.4: Rock strength at different depth

8.3 Background of Sand Production Wells in Tarim Field

In the KeS block there are 49 production wells that have been producing or are shut-in since 2013. Through analysis of samples collected from the well head and analysis of production data, 26 wells are suspected of having a sand production issue, which accounts for 53.06% of existing wells. Due to severe sand accumulation and blockage, 9 wells have had to be shut-in for a long term, which is 34.6% of sand production wells. In addition, there are more production wells in the KeS block that face sand production issues every year.

Fig. 8.5 lists some general information about the 26 production wells with sand production issues, including the severity of sanding, well stimulation method, production time, onset of sanding, as well as information about sand samples collected. The locations of these wells are shown in Fig. 8.6. Some wells have sand samples collected from well cleanouts, and the compositions include: fracturing sand, iron fillings, formation sand, cement and gravels (shown in Fig. 8.7 and Table 8.1). It is suspected that failure may happen throughout drilling, cementation, completion, fracturing, and production. However, sand from cementation and fracturing comes out in the early stages of production, while most of the produced sand is formation sand.

No.	Status	Stimulation Method	Production time	Sand production
1	Wellbore sand block	SRV Fracturing	Jul-13	Jan-14
2		SRV Fracturing	Jul-13	May-14
3		Frac Pack	Nov-11	Oct-13
4		SRV Fracturing	Oct-13	Jun-14
5	Wellbore sand and liquid accumulation	SRV Fracturing	Jun-13	Mar-14
6		SRV Fracturing	Dec-13	Mar-14
7		Temporary Plugging Acid Fracturing	Jul-13	Aug-13
8		Acidizing	Jun-13	Sep-14
9		Frac Pack	Nov-13	Mar-14
10	High level sand production	SRV Fracturing	Sep-14	Feb-15
11		SRV Fracturing	Sep-14	Mar-15
12		Temporary Plugging Acid Fracturing	Apr-14	Oct-14
13	Medium level sand production	SRV Fracturing	Mar-14	Nov-14
14		SRV Fracturing	Nov-14	Apr-15
15		SRV Fracturing	Aug-14	Mar-15
16		SRV Fracturing	Oct-14	Jan-15
17	Low level sand production	Frac Pack	Nov-12	Feb-16
18		Acid Fracturing	Sep-14	Aug-15
19		Acid Fracturing	May-13	Oct-15
20		SRV Fracturing	Jul-13	Aug-14
21		Temporary Plugging Acid Fracturing	Jan-14	May-15
22		Same as above	Aug-14	Dec-15
23		Same as above	Sep-14	Jun-15
24		Same as above	Apr-13	Aug-14
25		Same as above	Oct-14	Jul-15
26		Same as above	Sep-14	Feb-16

Fig. 8.5: Summary of 26 production wells with sanding issues

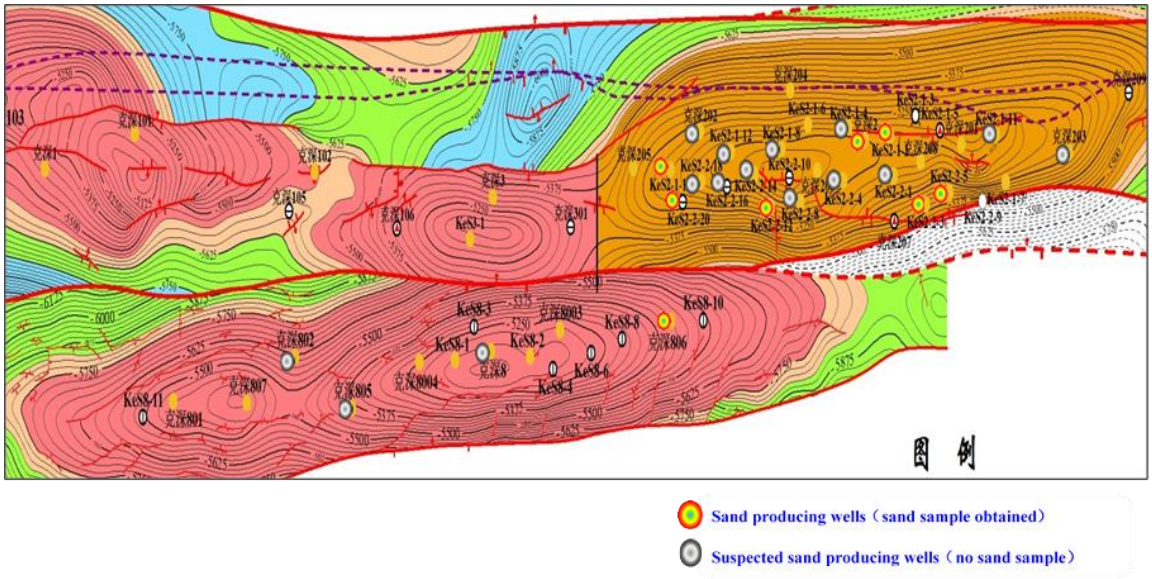

Fig. 8.6: Location of production wells with sanding issues

Fig. 8.7: Sand samples collected from sand production wells

Table 8.1 Sand sample analysis

Well No.	Sand sample analysis
1	Mainly brown granules (round - cone) and small brown-black long strips of argillaceous (iron) particles, small amount of iron, dolomite aggregate and individual calcite crystal grain and sporadic quartz grain, a grain of implicit crystalline silica plaque. The magnet adsorbs most of the particles and is magnetic, so the sand samples are mainly iron filings.
2	Sample comes from choke. Mainly medium sand, a small amount of coarse sand and fine sand. The components are mainly quartz, followed by feldspar (potassium feldspar, plagioclase), detritus (siliceous rock, quartzite, tuff, granite so on). Quartz has a secondary edge, and feldspar also has sodium feldspar. The interstitial materials are made of muddy iron, dolomite, siliceous, sodium feldspar and hard gypsum.
3	Mainly brown amorphous mixture, there is a small amount of clay mineral in it, silty - extremely fine felsic mineral, should be cement clast; then black soil shape, particle size 0.3-0.35 mm, round – cone particles, should be ceramic. Also see a small amount of plant fiber and cuttings.
4	Mainly medium sand, quartz grains has weak secondary increase. The feldspar is mainly plagioclase (sericite) and potassium feldspar. The cuttings include siliceous rocks, Phyllite, Andesite, tuff, quartzite, granite, acid extrusive rock and other cuttings. The filler is a small amount of muddy heterogeneity, dolomite, sodium feldspar (most of which are distributed in the form of the secondary edge of feldspar) and siliceous (the secondary increase of quartz particles). The rock is tight.
5	Among them are medium-grained litharenite sandstone and silvery fine grained litharenite. Medium-grained litharenite: the cuttings are mainly composed of medium sand, divided into quartz, feldspar, rock cuttings, etc. The fillings are brown clay, calcite, siliceous (secondary quartzite), and sodium feldspar (both for feldspar and interstitial distribution). Silty sandy feldspar sandstone: small fragment (0.03-0.125 mm), irregular angular shape, divided into quartz, feldspar, rock, mica and so on. The interstitial material is mainly iron and mud mixed, a small amount of calcite and sodium feldspar.
6	Barite: plate, colorless and dirty. Limonite: irregular granular, reddish brown. Magnetite: subround granular, iron black. White titanium stone: irregular granular, white, yellow and white. Pyrite: irregular granular, bright yellow. Anhydrite: columnar, colorless, bright-colored interference color.

Mechanical properties are crucial for determining rock deformation and failure. Properties including Young's modulus and compressive strength are displayed and compared for all sand production wells (Figs. 8.8 to 8.9). From the comparison, we do not see big differences in these properties between severe sand production wells and low sand production wells. For some low sand production wells, a surprisingly low rock shear strength can be observed, indicating that sand production should occur more easily. Therefore, by looking at the log derived mechanical property data, it is not obvious which wells will be prone to sand failure and production. Further detailed data such as post-yield behavior, compaction strength, etc. are required (from lab experiments) to obtain a comprehensive understanding on rock mechanical and failure behavior.

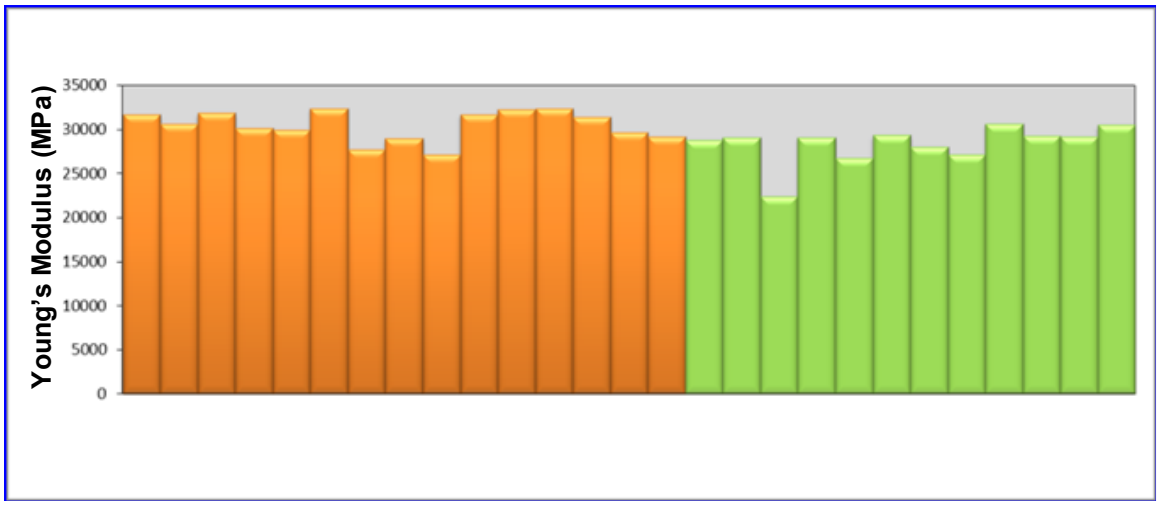

Fig. 8.8: Young's modulus for each sand production well

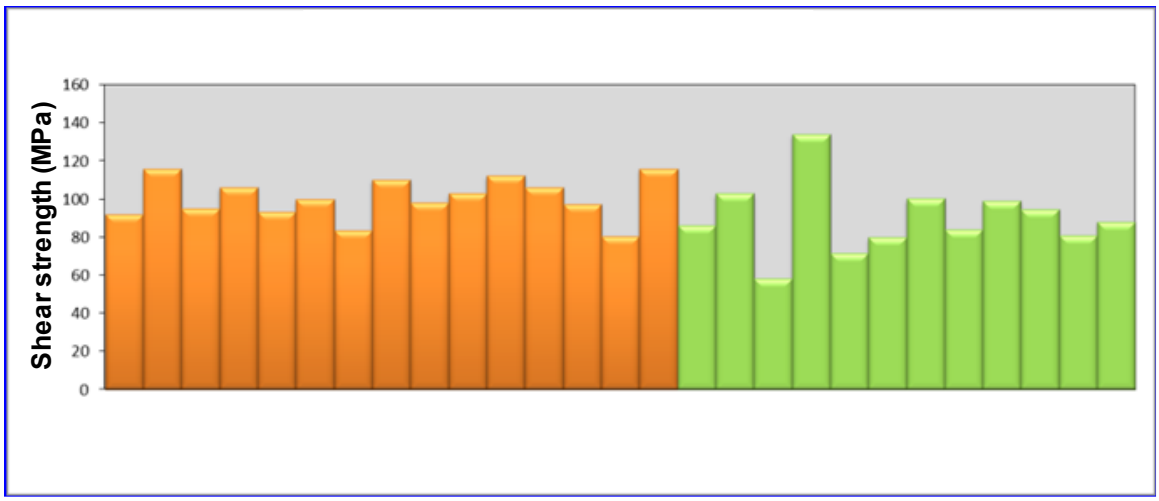

Fig. 8.9: Shear strength for each sand production well

8.4 Study of Sand Production in Tarim Wells

Due to availability of core data and core samples, we selected two wells representing different sanding severity. Well A, which has earlier onset of sanding and a smaller amount of sand, is still on production in the field. The other selected well is well B, reported to produce sands later, but with a larger amount of sand resulting in the wellbore experiencing well blockage. Production data for both wells are plotted in Fig. 8.10, along with the date for the onset of sanding.

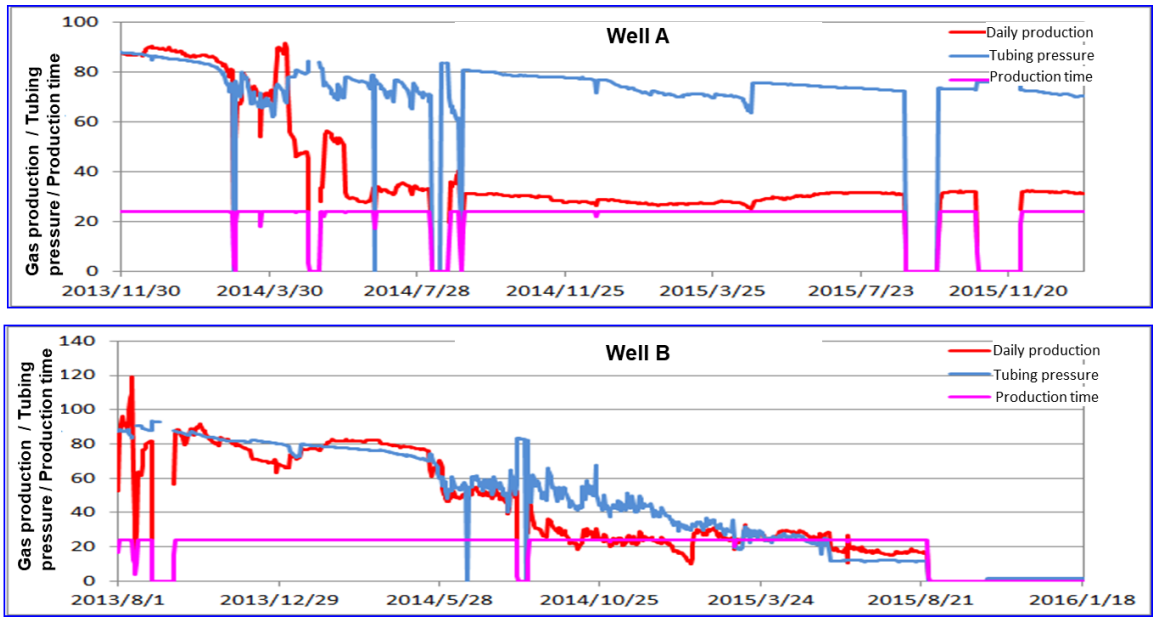

Fig. 8.10: Field data for gas production and the onset of sanding: well A (top) and well B (bottom)

Well A is a vertical HPHT gas well, located in Tarim Basin, KeS block. The well was drilled on May 3, 2012, with a total depth of 6853m. After casing and cementing, the well is perforated with two stages along the pay zone from 6602 to 6761.25m. In the first stage, 6 clusters are designed: 6696.00-6697.25m, 6673.00-6674.25m, 6656.00-6657.25m, 6633.00-6634.25m, 6617.00-6618.25m, and 6602.00-6603.25m. In the second stage, 3 clusters are opened: 6760-6761.25m, 6732-6733.25m, and 6718-6719.25m. Perforation density is 20spm, therefore 225 perforations were created. Perforation phasing, diameter, and length are 60°, 0.00762m and 0.44958m, respectively. From evaluation of the reservoir, it is categorized as a low permeability (0.9mD), low porosity (0.092) tight sand, where natural fractures are well developed.

Well B is also a vertical HPHT well for gas production. The well was drilled on May 19, 2012, with a total depth of 6975m. Like well A, the well is cased and cemented, and then perforated along the pay zone from 6513 to 6743m. Perforation density is

designed as 16spm, and a total of 384 perforations were created. Perforation phasing, diameter, and length are 60°, 0.0085m and 0.65m, respectively. Since the well location is closed to well A, the reservoir properties are similar, with low permeability (0.7mD), low porosity (0.076), and a high density of natural fractures.

To study the sanding mechanisms for these two wells, we use our sand production model to compare the effects of some key variables on both the onset of sanding and sand production volume. These variables include rock strength, in-situ stresses, BHP, perforation orientation, reservoir depletion, cement quality, and pressure fluctuation.

8.4.1 Rock Characterization in Two wells

Sand production is very sensitive to rock properties, as the onset of sanding and sand production rate are directly related to mechanical failure. Thus, it is important to estimate the rock mechanical properties, both pre-yield properties and post-yield properties, as accurately as possible. To determine these values, triaxial compression tests with multiple confining stresses were conducted experimentally by the Tarim project team. As shown in the left figure of Fig. 8.11, the stress increases linearly with strain at the beginning, representing an elastic region, and the slope reflects the value of Young's modulus. Once the stress-strain curve goes into the plastic region (non-linear region), the stress first increases with strain and then decreases abruptly or gradually (depending on confining stress), representing the strain-hardening and softening behavior. This means that the shear strength (from cohesion and internal friction angle) of the rock is not constant anymore once plasticity occurs. Instead, it changes non-linearly with an increase in the plastic strain. On the other hand, from Fig. 8.11b, we can see that initially the volumetric strain decreases linearly with axial strain (rock in elastic region), and from the slope Poisson's ratio can be calculated. Later, when plasticity dominates the rock deformation,

volumetric strain starts increasing, indicating that the rock dilates under shear. Now that the slope of volumetric strain vs. axial strain is changing, dilation angle (obtained from the slope) should also change with an increase in plastic strain.

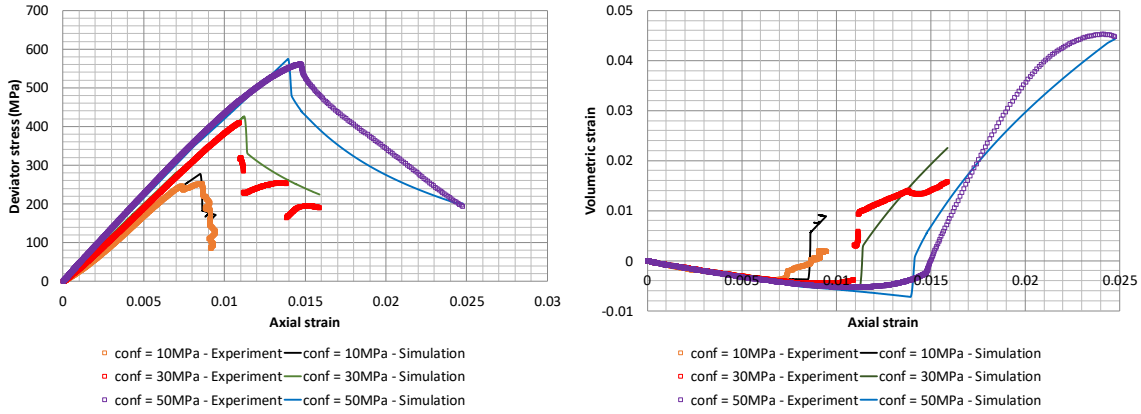

Fig. 8.11: Benchmark with experiment triaxial test for well A: stress-strain curve (left) and volumetric strain – axial strain curve (right)

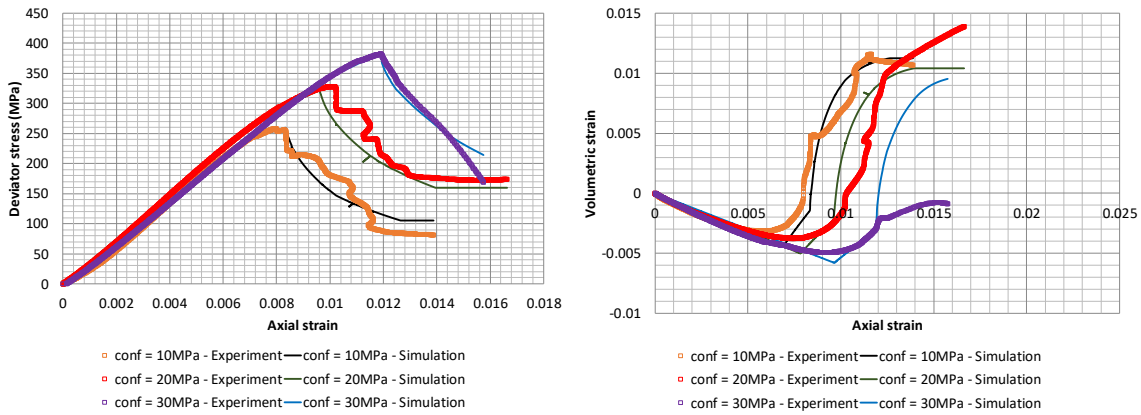

Fig. 8.12: Benchmark with experiment triaxial test for well B: stress-strain curve (left) and volumetric strain – axial strain curve (right)

Next, we fit the results for both the stress-strain curve and the volumetric strain-axial strain curve by using an elasto-plastic model. Simulation results are compared with experimental data in Figs. 8.11 and 8.12, and show very good agreement for all confining

stresses. Matching the core data in this manner allows us to obtain both pre-yield and post-yield rock properties for both wells (Wang et al., 2018).

8.4.2 Simulation Results for Well A

The base case in the model is set up using the field data from the reservoir evaluation report and the rock properties are obtained from the triaxial experiments conducted at different confining stress. The sand production results are shown in Fig. 8.13. Simulation results show that we do not observe any sand production in any oriented perforations. The reason is because the rock strength is high enough to prevent sand failure (even though it yields and deforms in the plastic region).

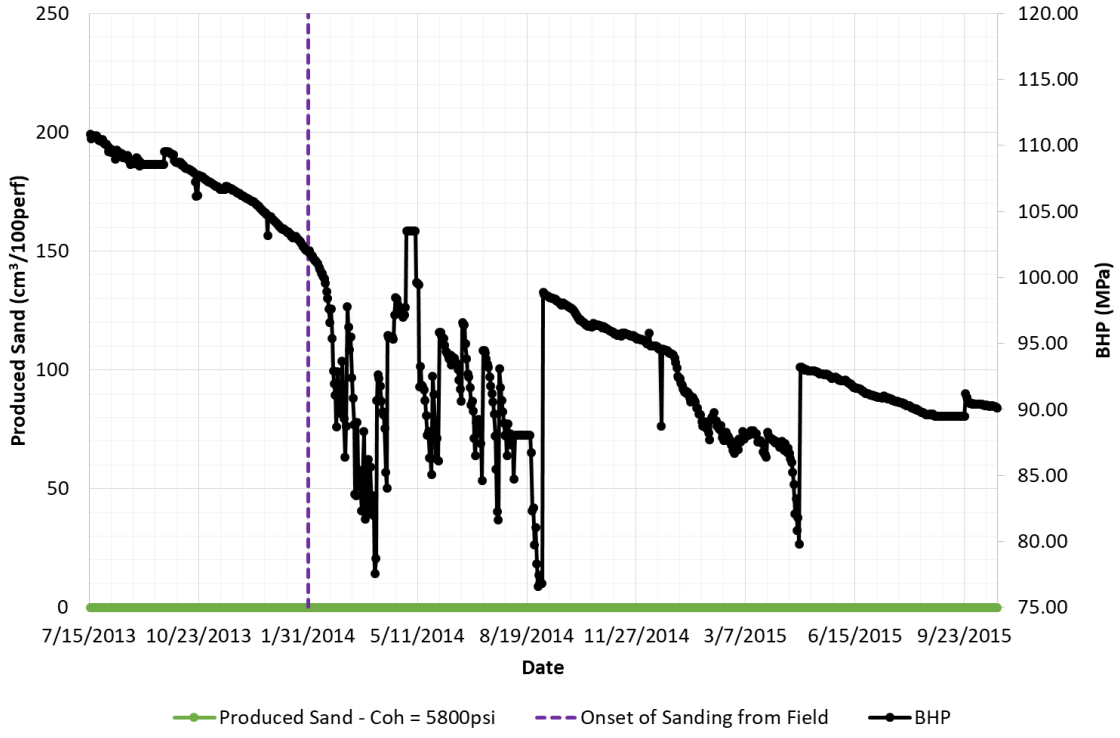

Fig. 8.13: Sand fill-up in well A – Base case

8.4.2.1 Effect of Rock Strength

In this section, the effect of cohesion on both the onset of sanding and sand production rate has been studied, and results are displayed in Fig. 8.14. With a high cohesion (5800psi, which is obtained from a triaxial test), there is no sand production predicted. When cohesion of the intact rock decreases to 4000psi, the sand around the perforations can reach shear failure and starts producing sands around March 2014. Sanding production is relatively steady, with a higher rate at the beginning (from March 2014 to September 2014) and a lower rate in the late production period (later than September 2014). If cohesion further decreases to 3000psi (closed to the lowest value of rock sample), we observe the onset of sand around January 2014, which is the same as observed in the field. This implies that perforations in this well may be drilled in the weak region of the rock (or the rock may be weakened during perforating). In addition, massive sand production is predicted from January 2014 to April 2014, while sands stop being produced later than May 2015.

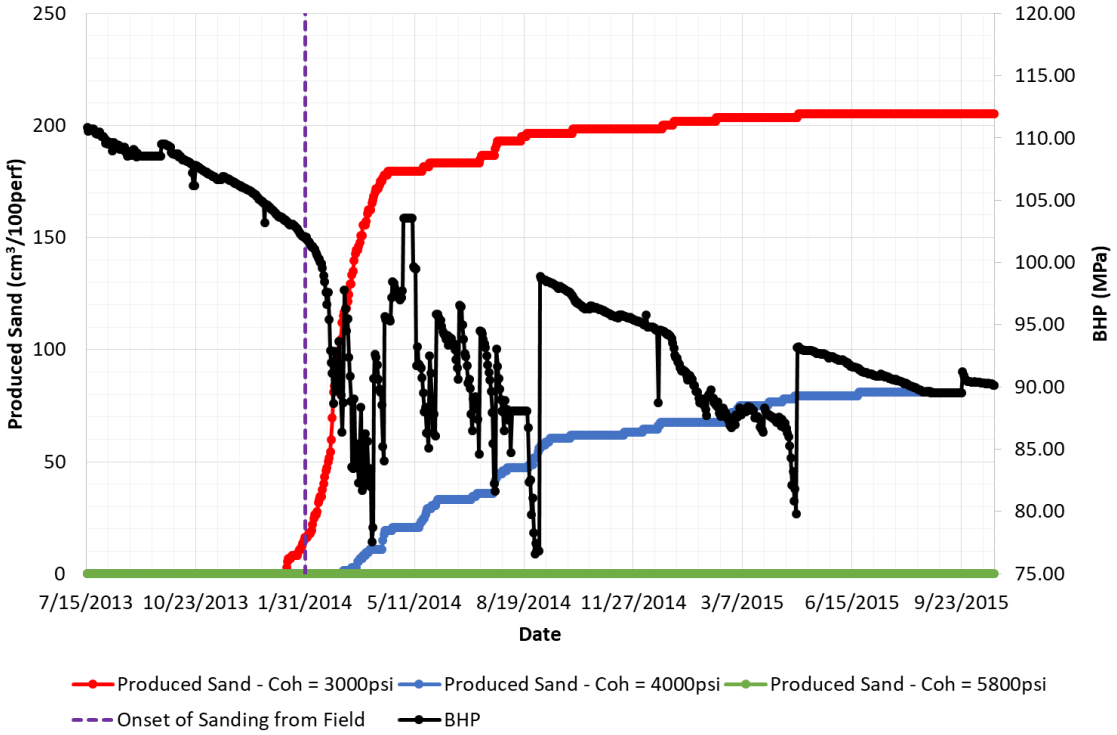

Fig. 8.14: Effect of cohesion on sand fill-up in well A

One justification for lowering the rock cohesion in the simulations is that the rock core samples in the triaxial experiments are likely sampled from the most competent part of the core. Weaker sections of the wellbore are either lost during the coring operation or may not be sampled because they are not recovered intact and are difficult to take core plugs from. The core samples used in the tri-axial tests are, therefore, unlikely to be representative of the weaker zones in the well. It is expected that heterogeneity and natural fractures will lead to large variations in cohesion from 2857psi to 9082psi (based on log data).

8.4.2.2 Effect of In-Situ Stresses

In-situ stresses and stress contrast around the perforation tunnel are crucial for sand mechanical yield and failure. Well A is in strike-slip faulting where the maximum

horizontal stress is the largest principal stress, followed by the vertical stress and the minimum horizontal stress. To understand the in-situ stresses on sand failure, the stress profile around the different oriented perforations during the initial period of production is plotted in Fig. 8.15. For perforations parallel to SHmax, the highest principal stress is observed at a circumferential angle = 90° (lateral face in Shmin direction), where failure is likely to occur. On the other hand, for perforations parallel to Shmin, the highest principal stress is obtained at a circumferential angle = 0° (vertical face in Sv direction), the location failure first starts. Furthermore, at this in-situ stress, the largest principal stress is 160MPa around the perforation parallel to Shmin, suggesting that sands around this oriented perforation will fail first, compared with other oriented perforations.

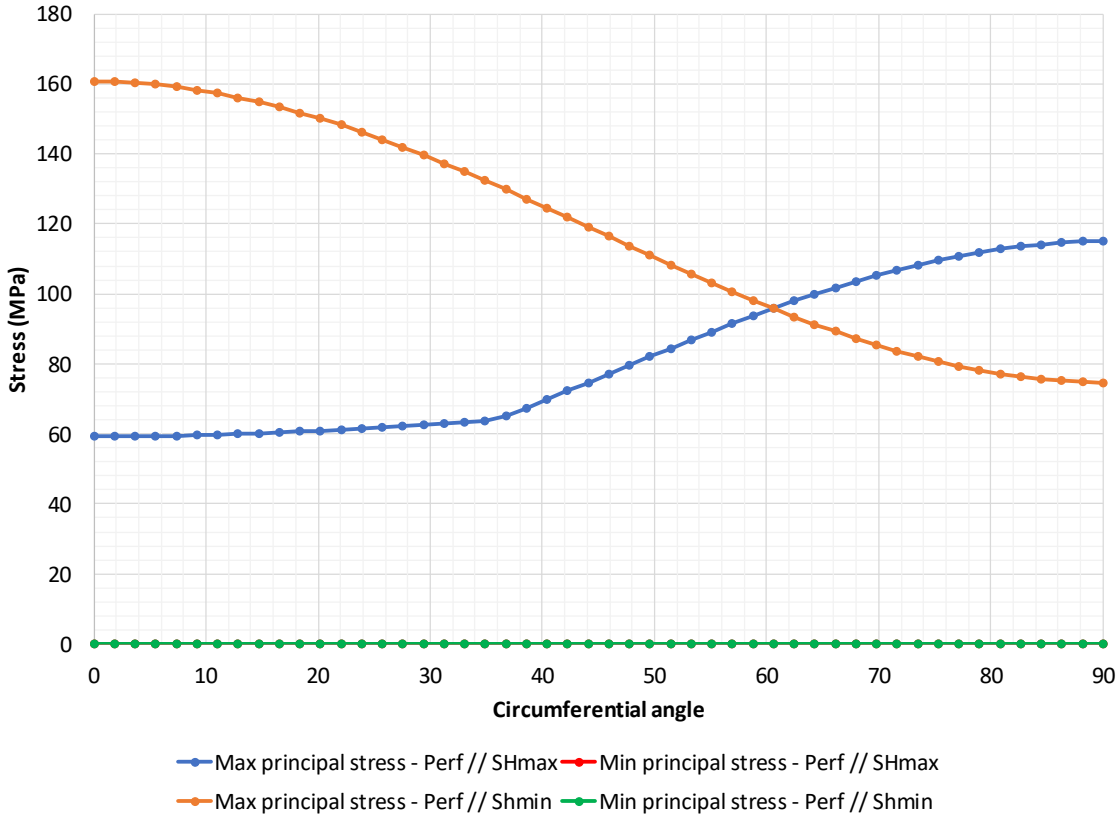

Fig. 8.15: Stress profile around perforations in well A. Note circumferential angle starts from Sv direction

8.4.2.3 Effect of Bottom Hole Pressure (BHP)

Changes in the BHP with time is another important factor affecting sand production. To study this effect, BHP and sand production in the rock with 3000psi cohesion are plotted in Fig. 8.16. From the sanding behavior, we observe that onset of sanding occurs when the BHP drops to 103MPa. This is because both the effective stresses and shear stress increase with pressure drop, leading to shear and/or compressive failure during production. Also, we observe massive sand production when the BHP drops quickly (from February to April 2014). There are two main reasons for this. Firstly, due to a large pressure drop, both the effective stresses and shear stress increase, leading to shear or compressive failure. Secondly, after the rock fails, sand production needs to be triggered by fluid erosion. With a sharp pressure reduction, the pressure gradient is large around the perforation, resulting in a large drag force that can bring the failed sands to the surface. This implies that BHP fluctuations also play an important role in sand production. It appears that a higher frequency and larger pressure pulses lead to more sand production. The effect of BHP fluctuation on sand production will be studied and discussed in more detail for Well B where more data is available.

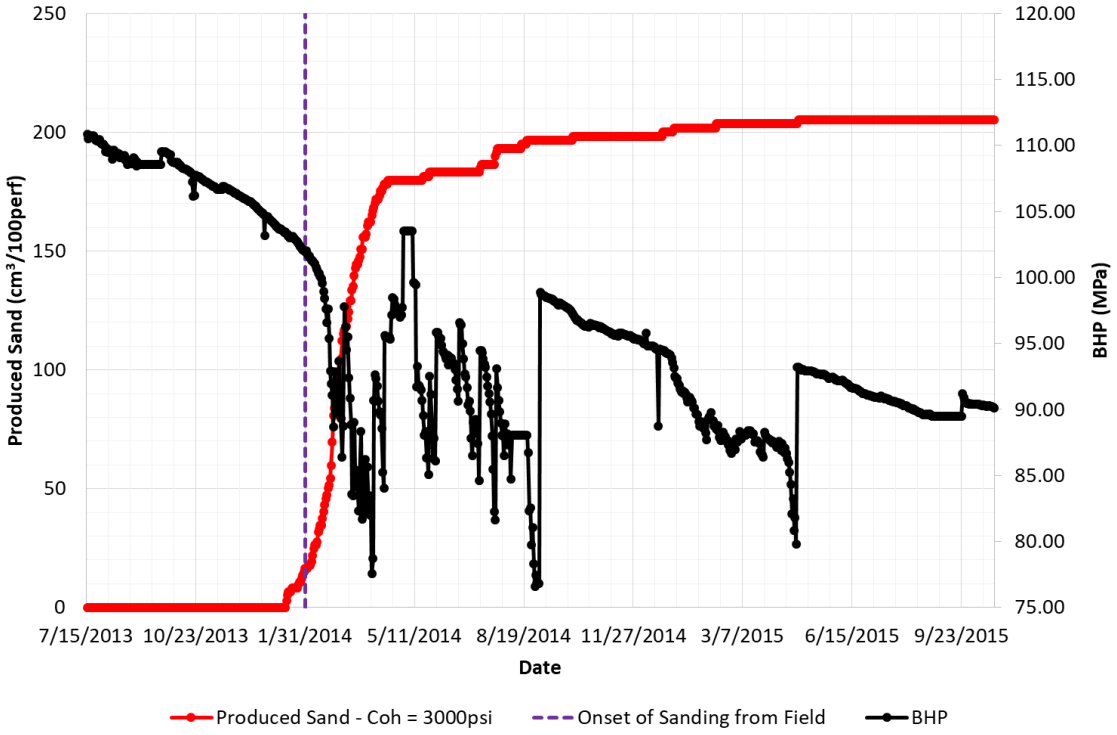

Fig. 8.16: Effect of BHP on sand fill-up in well A

8.4.2.4 Effect of Reservoir Depletion

Reservoir depletion is caused by production for a period, when average reservoir pressure decreases. The degree of reservoir depletion may dramatically affect the stresses in the reservoir and, therefore, the mechanical failure status of the rock. With reservoir depletion, effective stresses increase, leaving rock in a risky condition for either shear failure or compressive failure (as the effective mean stress increases).

From a practical perspective, reservoir depletion degree changes the critical drawdown for sand free production conditions. Figs. 8.17 and 8.18 show the critical bottom-hole pressure vs. average reservoir pressure for well A. The green zone in the plot represents the sanding free zone, where drawdown is allowable during the operation without any sand failure and production. The Yellow zone represents the sand failure zone,

indicating that the rock fails and the degraded sands may produce and fall into the perforation/well and may lead to well blockage and productivity loss. The Red zone represents the sand production zone. If drawdown falls into this zone, massive sanding can be observed at the surface. Clearly this condition should be avoided. For sand failure, with larger reservoir pressure, larger drawdown is allowable. This is because the effective stresses generated from larger reservoir pressure is small and can sustain more increase of the magnitude (caused by decrease of bottom-hole pressure) before failure is reached. With reservoir depletion, the allowable drawdown decreases and ultimately the rock can fail even without any drawdown. On the other hand, the critical drawdown for sand production increases with reservoir depletion, as a critical velocity needs to be reached.

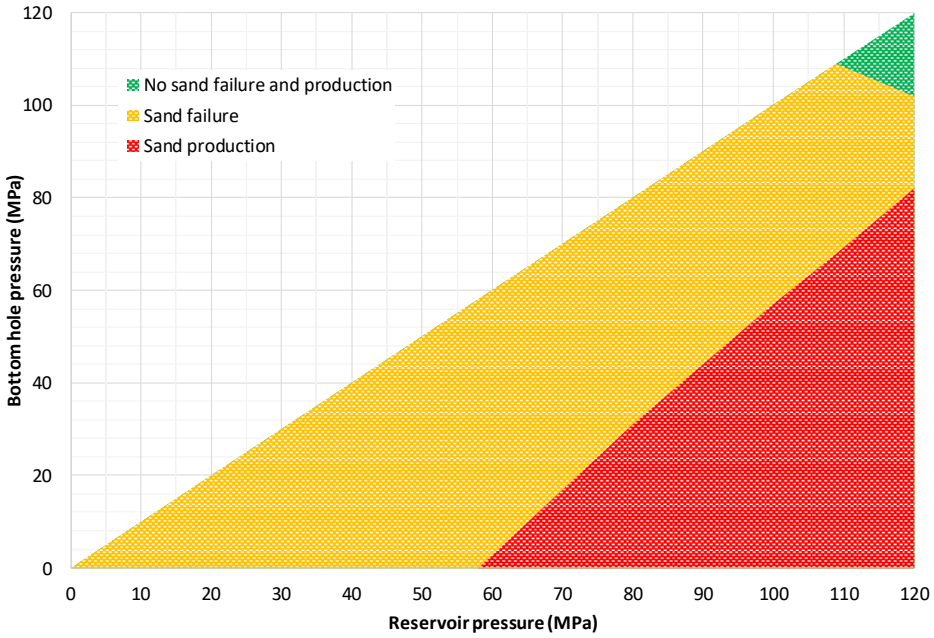

Fig. 8.17: Effect of reservoir depletion on critical drawdown: perf // Shmin in well A

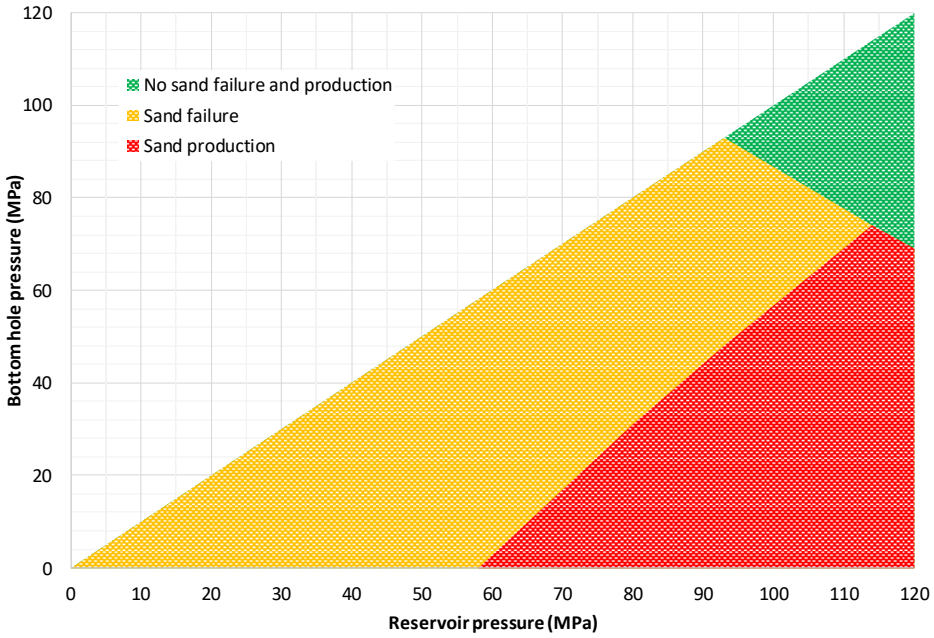

Fig. 8.18: Effect of reservoir depletion on critical drawdown: perf // SHmax in well A

8.4.2.5 Effect of Perforation Orientation

Perforation orientation plays an important role on sand production. As shown in Fig. 8.19, perforations parallel to SHmax are much more stable, compared with perforations in the other directions. In this well, perforations along SHmax suffer a stress contrast from vertical and minimum horizontal stress, while perforations along Shmin have a stress contrast from vertical stress and maximum horizontal stress. As discussed previously, due to the magnitude and stress contrast from in-situ stresses, perforations along Shmin suffer larger shear stress and are more likely to fail. This is why we expect to see sand production around these perforations.

Results for critical drawdown with depletion on two oriented perforations in Fig. 8.20 show the consistency of the previous conclusion. The Red line, representing critical bottom-hole pressure along reservoir depletion in perfs parallel to Shmin, shows the sand

free window is much smaller compared to the Blue line (perf parallel to SHmax). This suggests that rock failure occurs easier and earlier around perforations parallel to Shmin in well A, due to changes in drawdown.

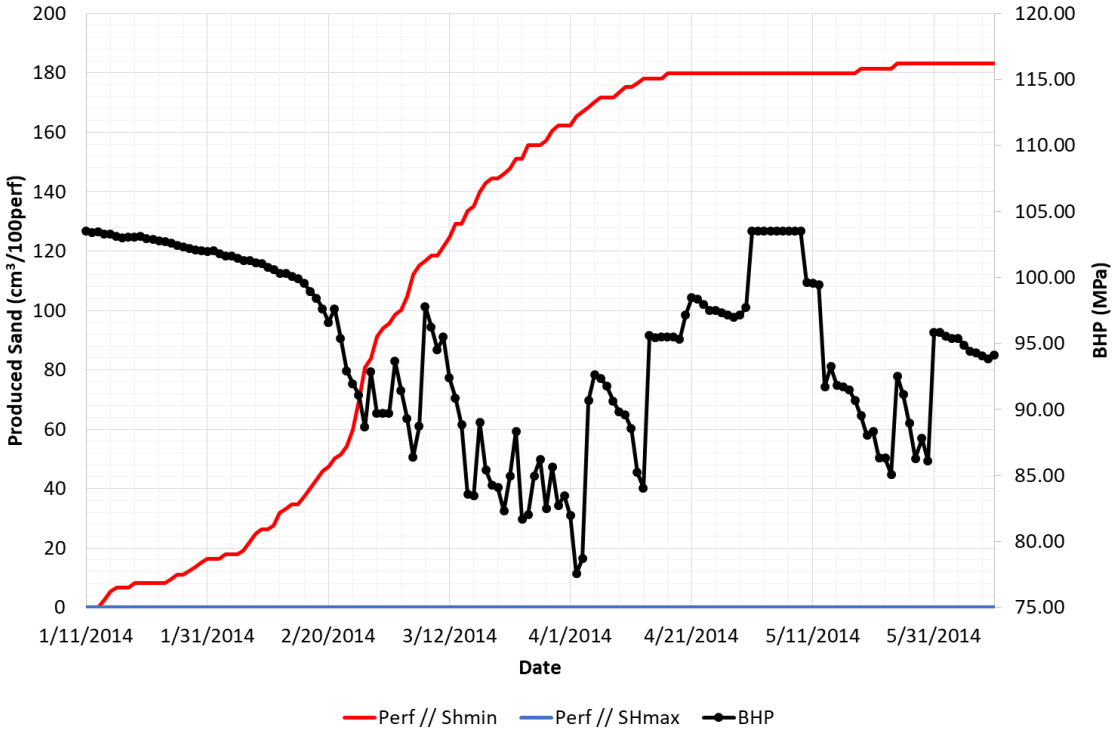

Fig. 8.19: Effect of perforation orientation on sand fill-up in well A

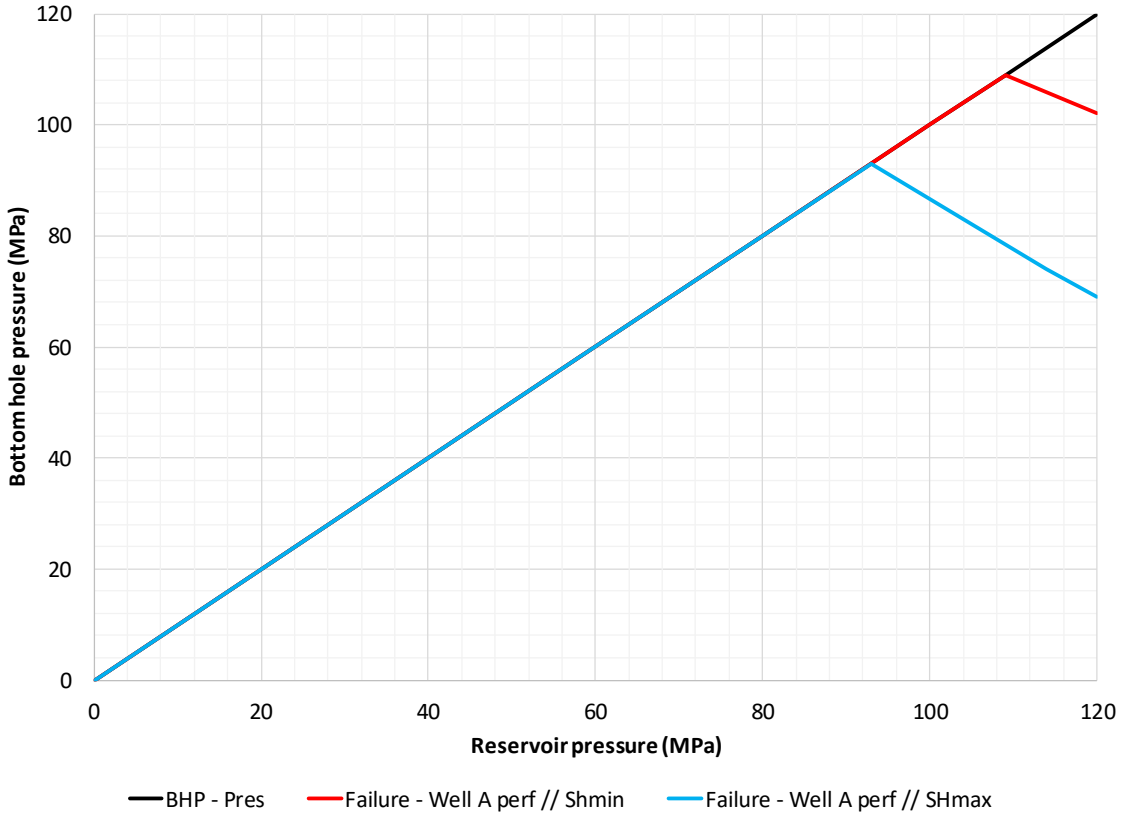

Fig. 8.20: Effect of perforation orientation on critical drawdown in well A

8.4.2.6 Effect of Cement Quality

The effect of cement quality is studied by comparing cement failure status with different cement strengths. Fig. 8.21 shows the Mohr circle for the rock parallel to Shmin, where sand suffers the largest hoop stress. From these results, if the cement cohesion is 50MPa, no yield occurs even if the BHP drops to 85MPa. Cement may fail if its cohesion decreases to 40MPa when BHP drops to 85MPa. If the cement cohesion drops below 40MPa, it may fail at the beginning of production. This situation will only occur if the cement is not properly placed all the way around the casing.

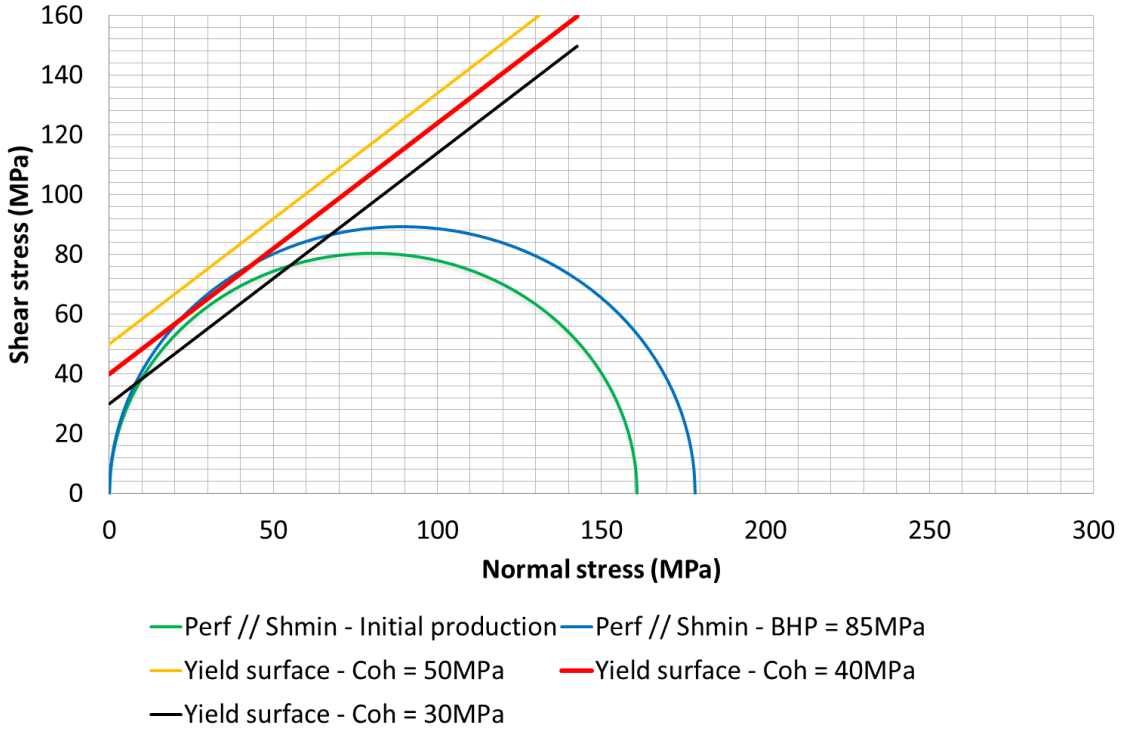

Fig. 8.21: Effect of cement quality on cement failure in well A

8.4.2.7 Effect of Natural Fractures

The existence of natural fractures and their interaction with production wells have an impact on both sand failure and sand production. Physically speaking, the existence of natural fractures reduces the rock strength to some extent. If more natural fractures are present, the rock strength will be lower. Therefore, rock with massive natural fractures has a higher potential risk of sand failure. In the meanwhile, the interaction of natural fractures with production wells results in an increase of productivity by enhancing the effective permeability in SRV zones, which may raise the possibility of sand erosion due to higher flow velocity and drag force.

The effect of natural fractures on sanding has been quantitatively studied in this work by showing its impact on critical drawdown for sanding free conditions, sand failure

conditions and sand production conditions from both strength reduction and permeability enhancement perspective. For strength reduction, three cases are compared, with cohesion reducing from 4000psi to 3000psi, and further to 2000psi due to different amount of natural fractures. For effective permeability, two cases are compared, with permeability increasing from the original matrix permeability of 0.9mD to 10 times of this value.

Figs. 8.22 to 8.27 compare the critical drawdown of both sand failure and sand production with reservoir depletion for different rock strengths and original permeability. There are several key observations:

1. For all oriented perforations, sanding free conditions can only occur for high reservoir pressure due to less effective stresses;
2. With high reservoir pressure, larger drawdown is acceptable. The allowable drawdown will decrease with the reduction of rock strength. For example, critical drawdowns at initial reservoir condition are 0, 18MPa and 37MPa corresponding to cohesion of 2000psi, 3000psi and 4000psi for perf parallel to Shmin. This trend is consistent for other oriented perfs;
3. Critical drawdown for sand failure decreases linearly with reservoir depletion. With low reservoir pressure, reservoir effective stresses are excessive to make rock fail easier, even with no drawdown;
4. Critical drawdown for sand production increases with reservoir depletion to make the drag force sufficiently large for sand erosion;
5. Mechanical failure is the most important first order effect that determines sand production and wellbore fill-up which can trigger well productivity loss, and dominate well performance;
6. For well A, perforations parallel to SHmax show a better stability under such in-situ stresses and a much larger drawdown (24MPa, 51MPa and

75MPa for different rock strength). Compared with perf parallel to Shmin, the difference between critical drawdown for sand failure tends to increase in higher strength regions.

Figs. 8.28 to 8.33 show a comparison of the critical drawdown for both sand failure and sand production with reservoir depletion for fractured and unfractured rocks with different rock strength and higher permeability. Results show agreement with the observations mentioned above, indicating that sand erosion is a second order effect of sand production as it requires the same or high drawdown for sand removal. In addition, enhancing the permeability by a factor of 10 reduces the difference of critical drawdown for sand failure and sand production, suggesting that massive sanding can happen soon after failure is achieved in highly natural fractured reservoirs.

By comparing the effect of natural fractures on sanding for well A (Figs. 8.34 to 8.36), we can clearly see the potential risk for both sand failure and a massive increase of sand production due to the impact of natural fractures on rock strength and flow conductivity.

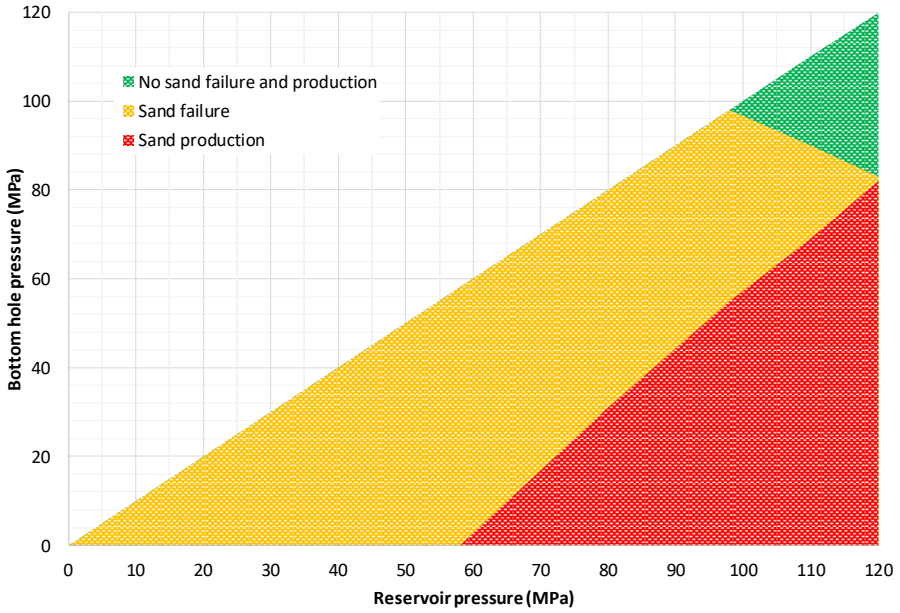

Fig. 8.22: Effect of natural fracture on critical drawdown in well A: perf // Shmin, coh = 4000psi, perm = 0.9mD

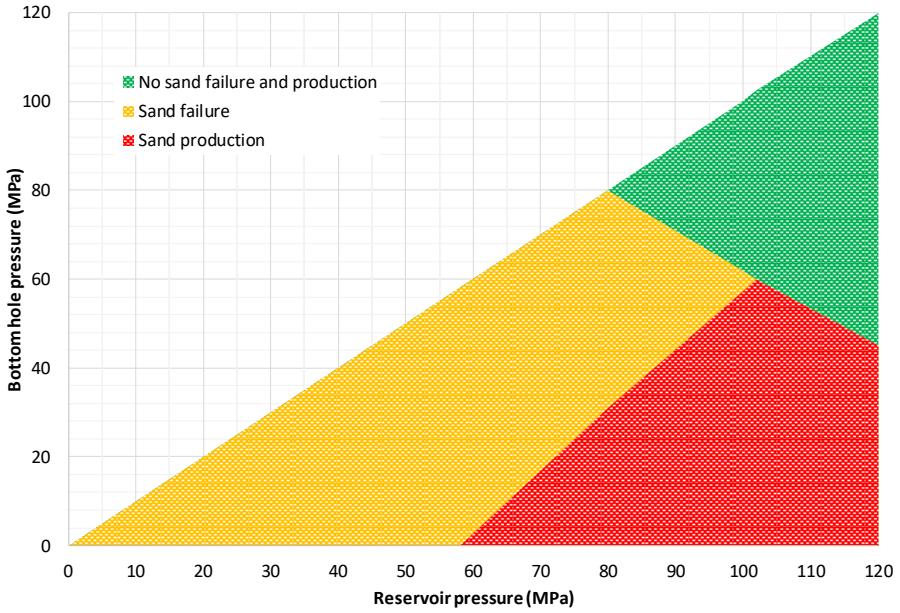

Fig. 8.23: Effect of natural fracture on critical drawdown in well A: perf // SHmax, coh = 4000psi, perm = 0.9mD

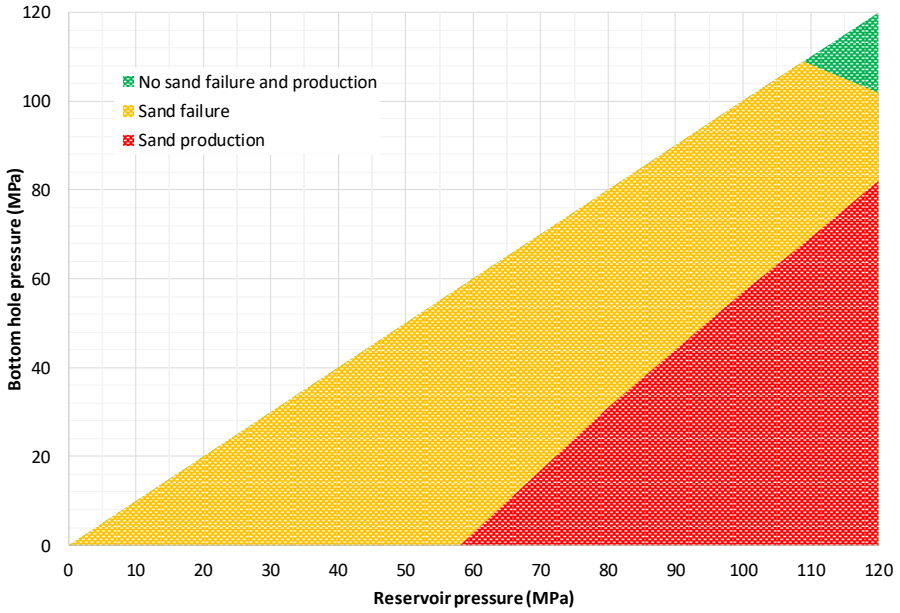

Fig. 8.24: Effect of natural fracture on critical drawdown in well A: perf // Shmin, coh = 3000psi, perm = 0.9mD

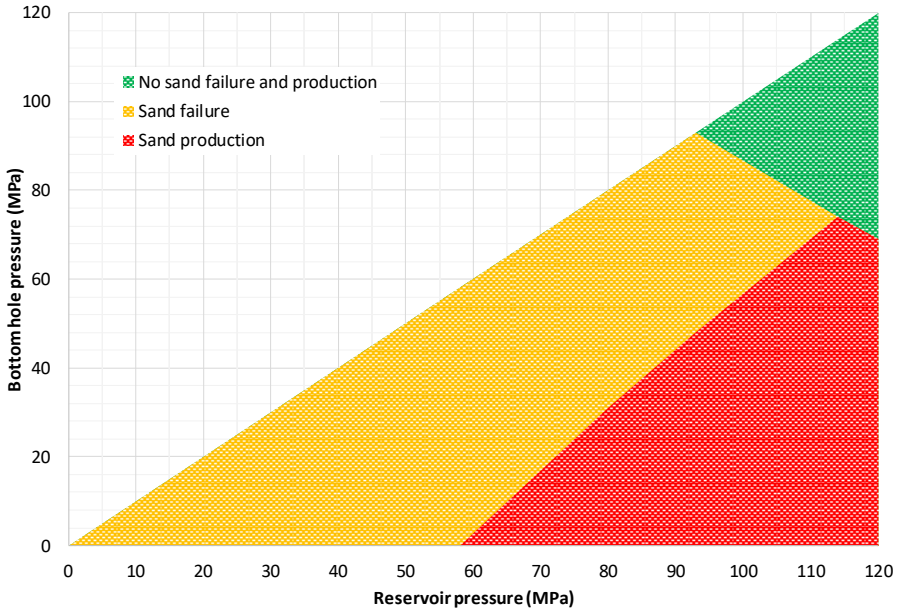

Fig. 8.25: Effect of natural fracture on critical drawdown in well A: perf // SHmax, coh = 3000psi, perm = 0.9mD

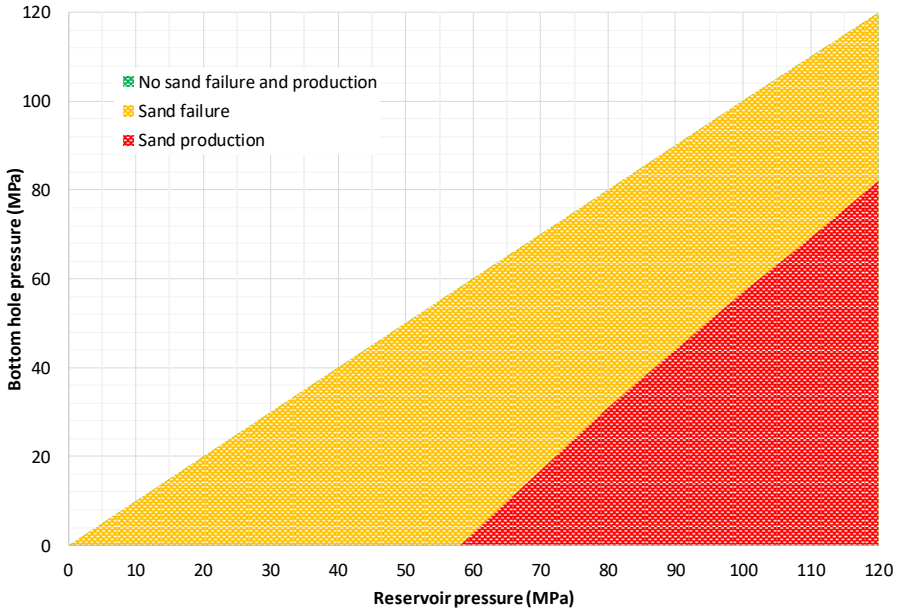

Fig. 8.26: Effect of natural fracture on critical drawdown in well A: perf // Shmin, coh = 2000psi, perm = 0.9mD

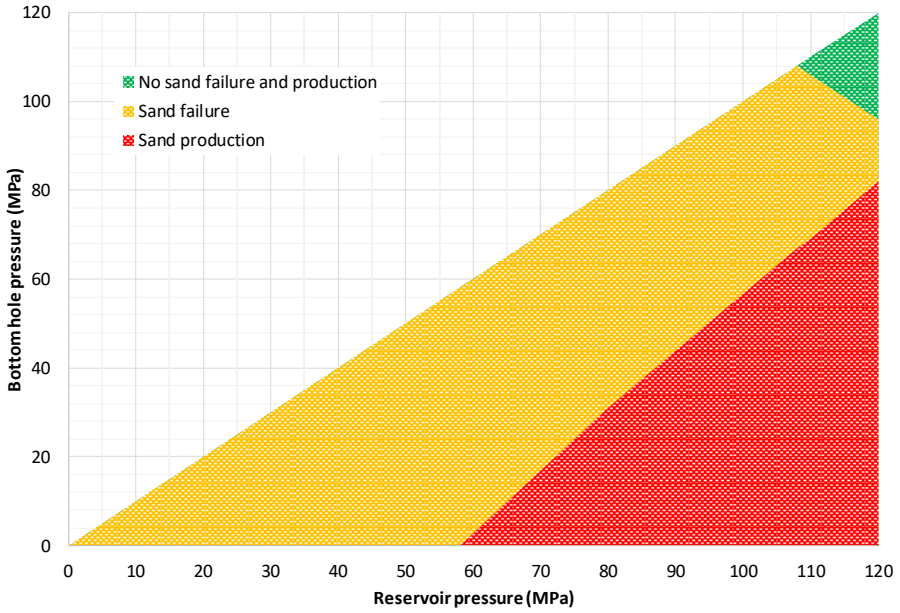

Fig. 8.27: Effect of natural fracture on critical drawdown in well A: perf // SHmax, coh = 2000psi, perm = 0.9mD

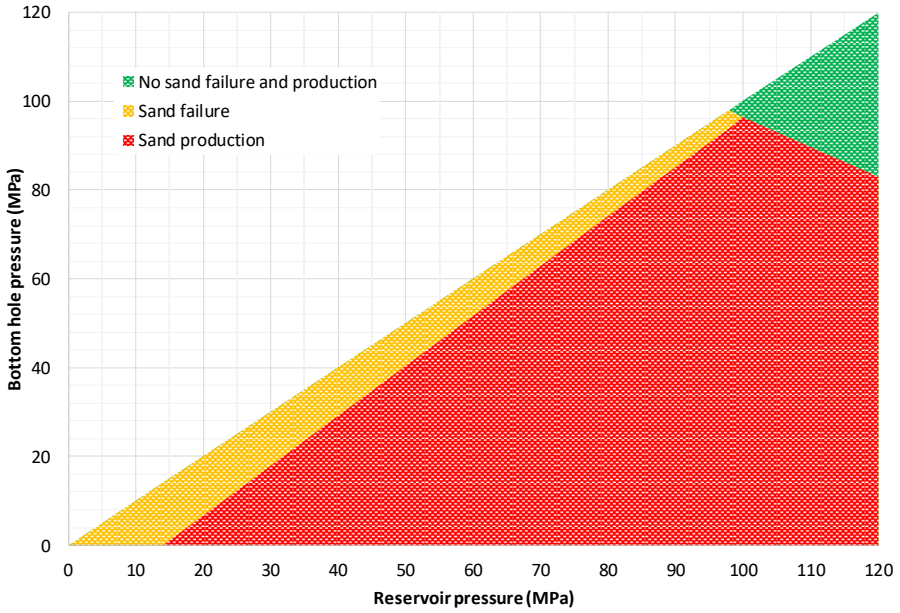

Fig. 8.28: Effect of natural fracture on critical drawdown in well A: perf // Shmin, coh = 4000psi, perm = 9mD

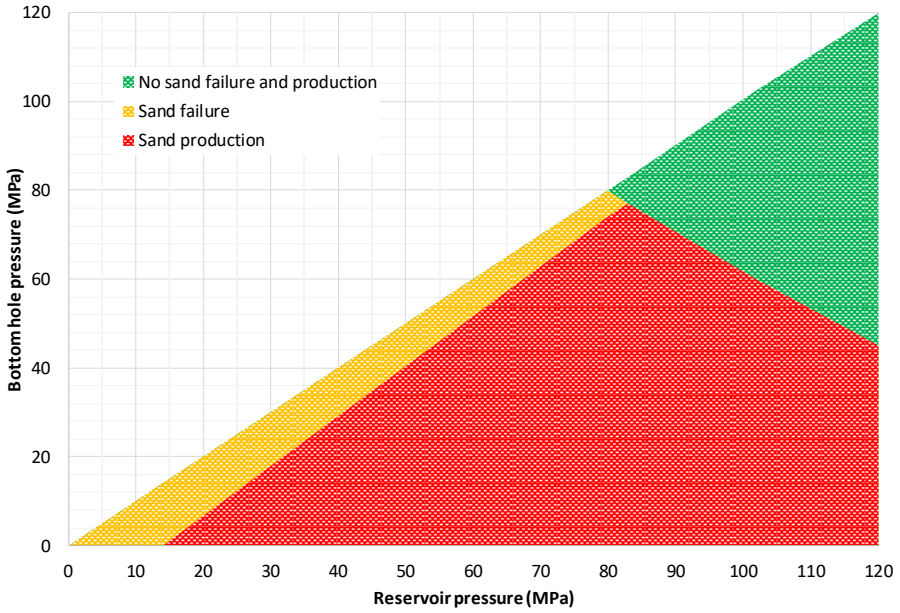

Fig. 8.29: Effect of natural fracture on critical drawdown in well A: perf // SHmax, coh = 4000psi, perm = 9mD

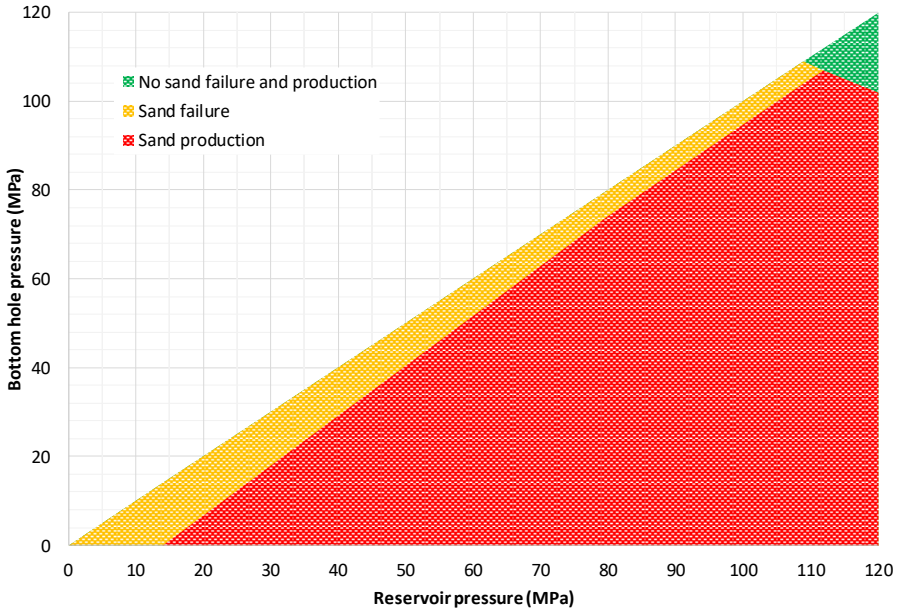

Fig. 8.30: Effect of natural fracture on critical drawdown in well A: perf // Shmin, coh = 3000psi, perm = 9mD

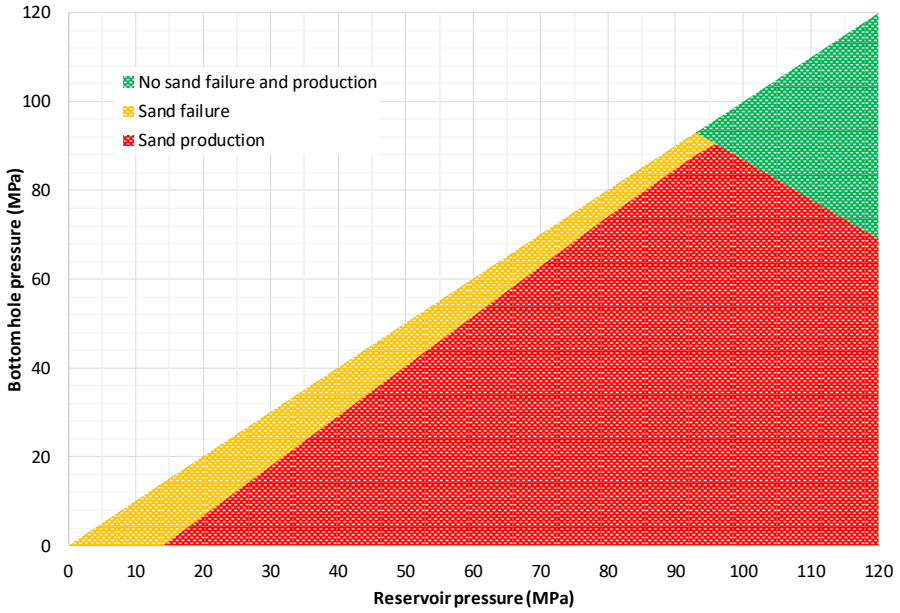

Fig. 8.31: Effect of natural fracture on critical drawdown in well A: perf // SHmax, coh = 3000psi, perm = 9mD

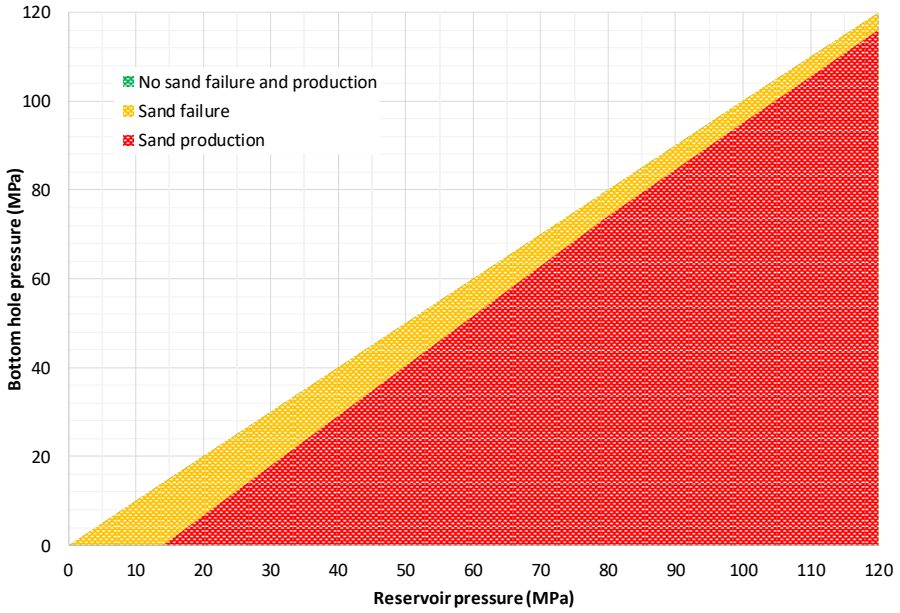

Fig. 8.32: Effect of natural fracture on critical drawdown in well A: perf // Shmin, coh = 2000psi, perm = 9mD

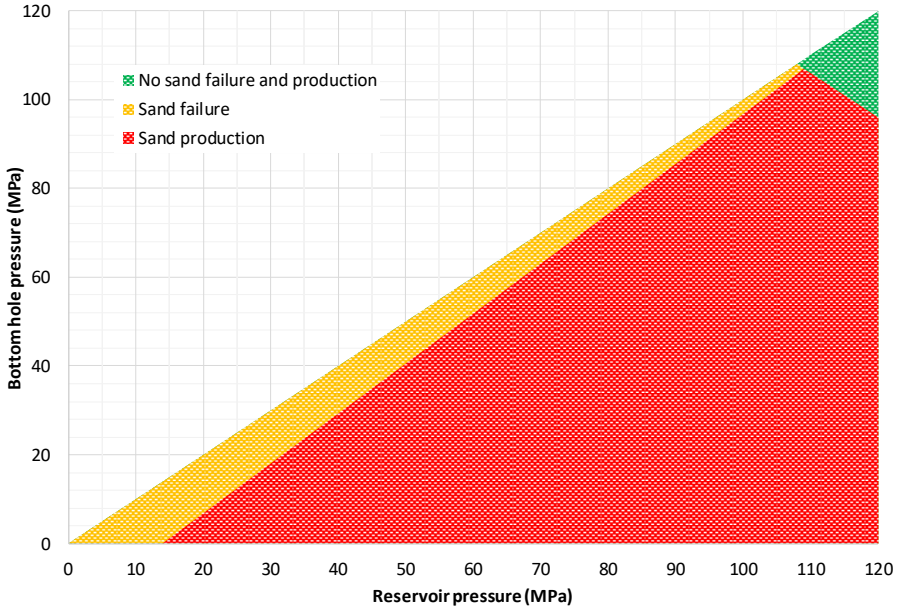

Fig. 8.33: Effect of natural fracture on critical drawdown in well A: perf // SHmax, coh = 2000psi, perm = 9mD

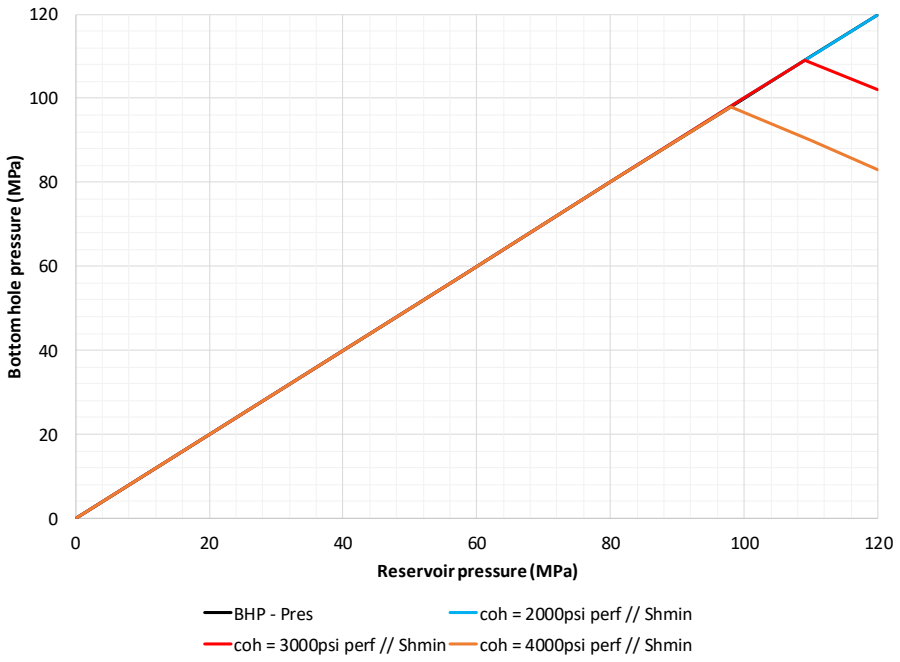

Fig. 8.34: Effect of natural fracture on sand failure critical drawdown in well A: perf // Shmin

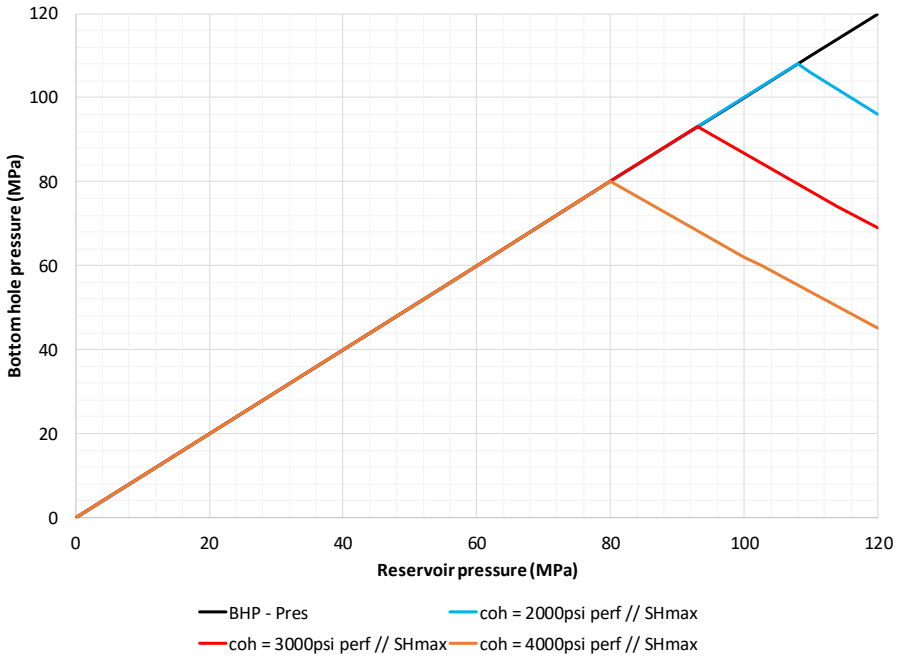

Fig. 8.35: Effect of natural fracture on sand failure critical drawdown in well A: perf // SHmax

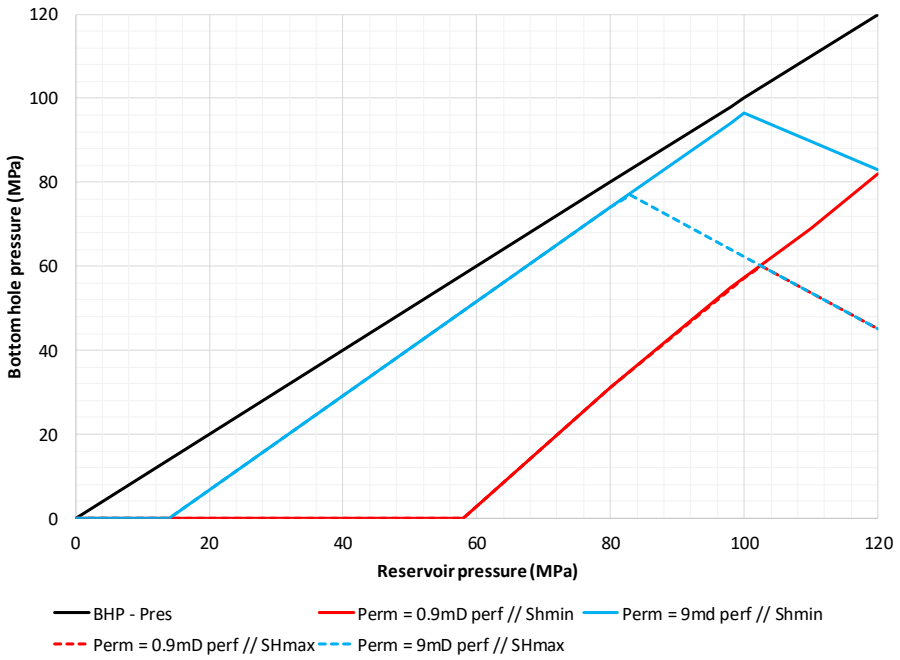

Fig. 8.36: Effect of natural fracture on sand production critical drawdown in well A

8.4.3 Simulation Results for Well B

The base case is set up using the rock and fluid properties obtained for well B. Simulation results for this well are shown in Figs. 8.37 and 8.38. This well varies from Well A, even though the rock is strong (cohesion is 5800psi), we observe sand production at the end of the production period. Also, sand is produced from perforations parallel to SHmax, rather than the other oriented perforations observed in well A. In well B, perforations parallel to Shmin tend to be stable and remain sand free with such a high rock strength.

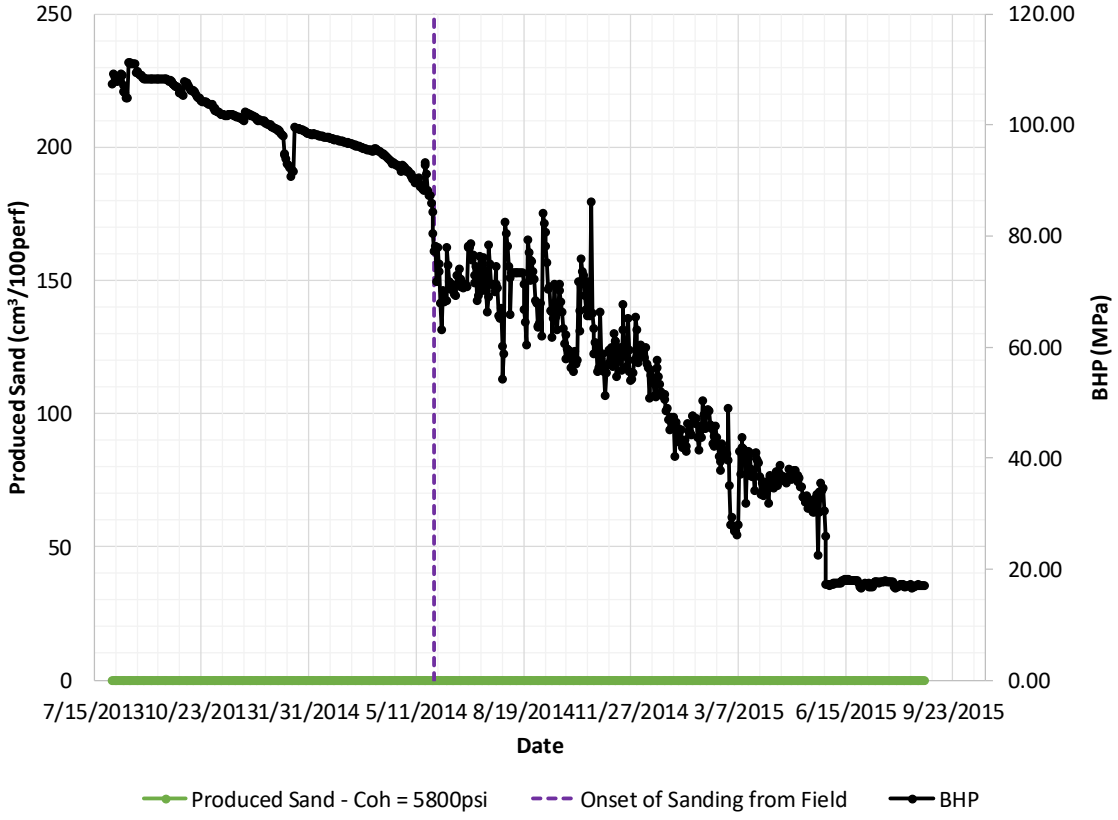

Fig. 8.37: Sand fill-up in well B – Base case: Perf // Shmin

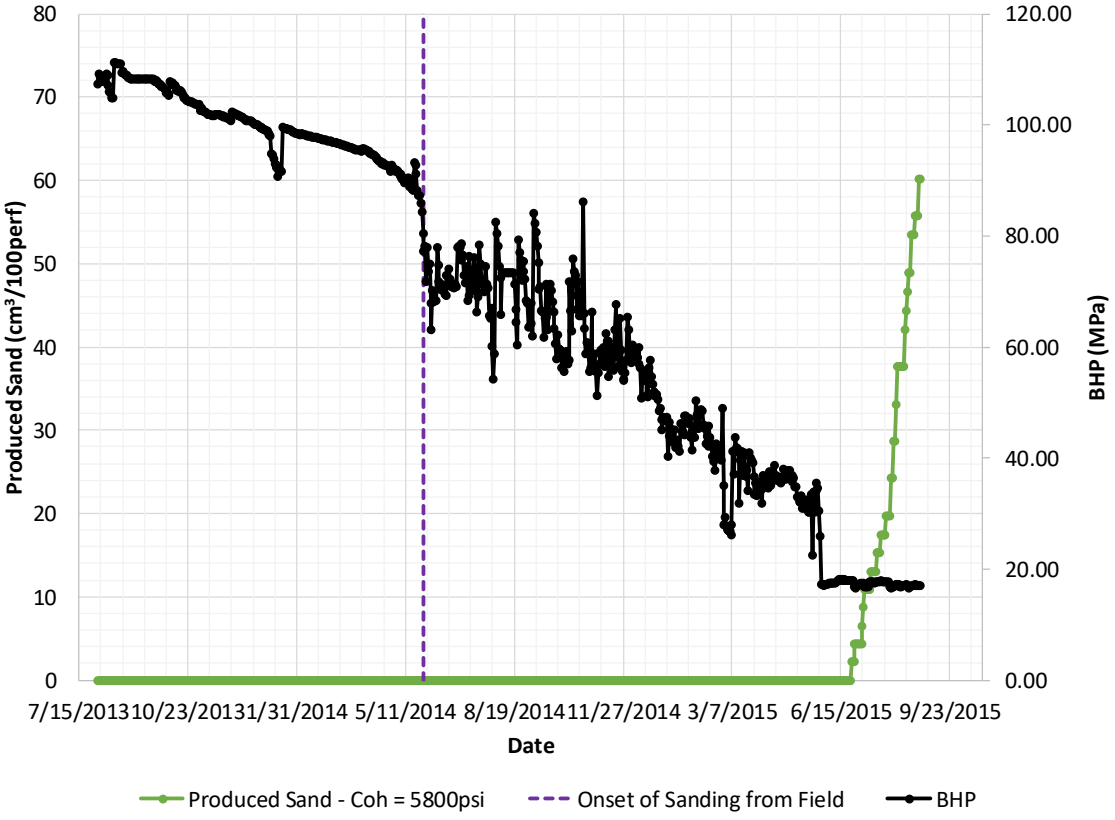

Fig. 8.38: Sand fill-up in well B – Base case: Perf // SHmax

8.4.3.1 Effect of Cohesion

The effect of cohesion on both the onset of sanding and sand production rate has been studied, and results are displayed in Figs. 8.39 and 8.40. For both oriented perforations, sand can be produced at low cohesion (3000psi and 4000psi). The effect of cohesion on sanding is the same as observed in well A: more sand production and earlier onset of sanding is observed with lower cohesion. With lowest cohesion (3000psi), onset of sanding from perforations parallel to SHmax is predicted, consistent with field data.

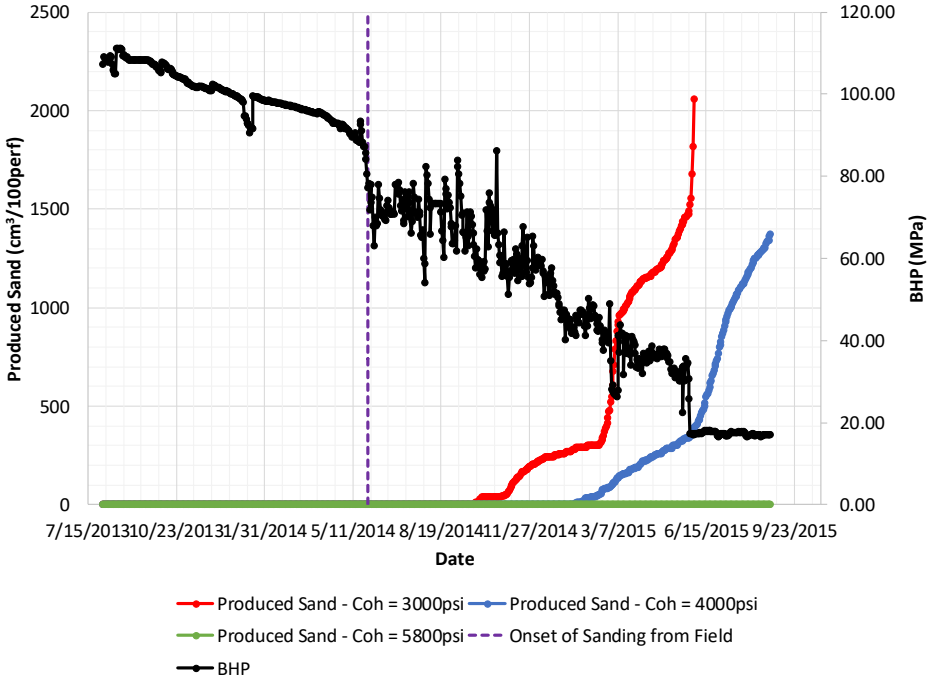

Fig. 8.39: Effect of cohesion on sand fill-up in well B: Perf // Shmin

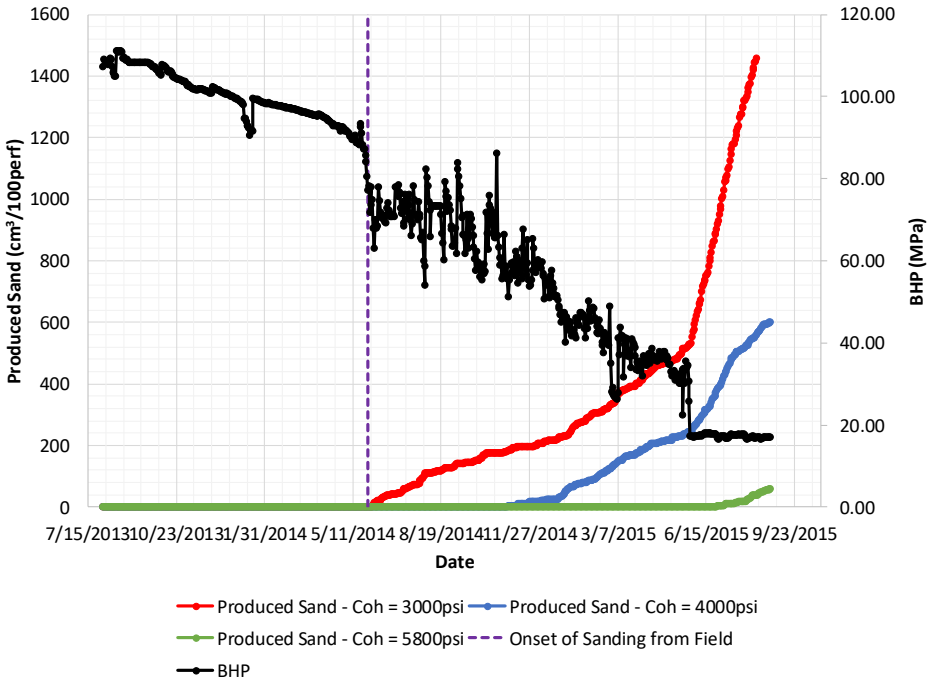

Fig. 8.40: Effect of cohesion on sand fill-up in well B: Perf // SHmax

8.4.3.2 Effect of In-Situ Stresses

Well B is also in the strike-slip faulting regime, where the maximum horizontal stress is the largest principal stress, followed by vertical stress and minimum horizontal stress. The main difference between this well and well A is that the maximum horizontal stress is much lower in this well. The consequence, as shown in Fig. 8.41, is that the largest principal stress and larger stress contrast are obtained around the perforation parallel to SHmax (which is different from well A). This explains the above results that onset of sanding occurs first around these perforations. In addition, the largest principal stress in this well is much lower than in well A (120MPa vs. 160MPa), this indicates the onset of sanding in well B is delayed, compared with well A.

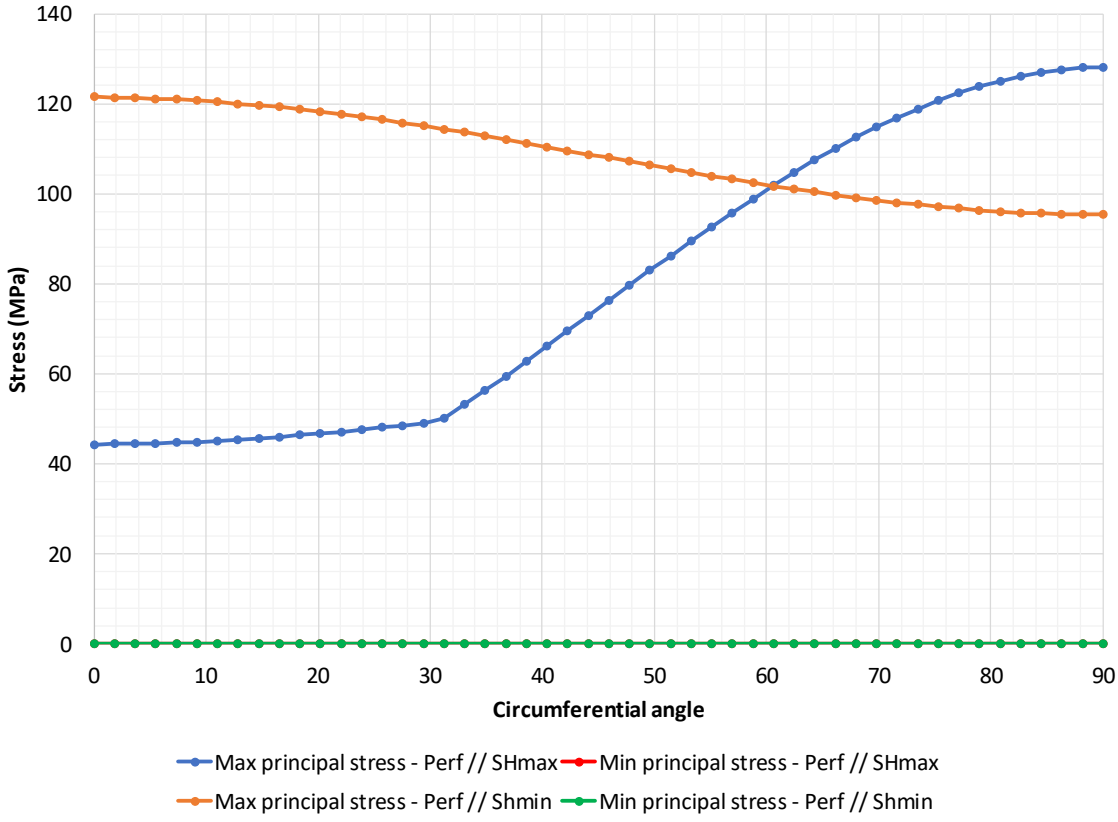

Fig. 8.41: Stress profile around perforations in well B. Note circumferential angle starts from Sv direction

8.4.3.3 Effect of BHP

The effect of BHP (varying with time) on sand production in well B is plotted in Fig. 8.42. After sanding occurs, sand production continues to increase as BHP decreases. The reason is the same as discussed for well A. Furthermore, the sanding rate tends to increase at the end of production, this is due to very low BHP around the exposed face, induced by a sudden drop in BHP. In addition, due to a much larger drop in BHP in this well, we observe much higher sand production compared with well A. Another difference is that sand keeps producing in this well due to the much lower BHP, while in well A, the BHP is maintained much higher, and sanding tends to be stable with sand production stopping at the end. The sand production volume in this well is much larger than in well A. The larger BHP drop suggests that the sanding issue in well B will be much worse than in well A, as observed in the field.

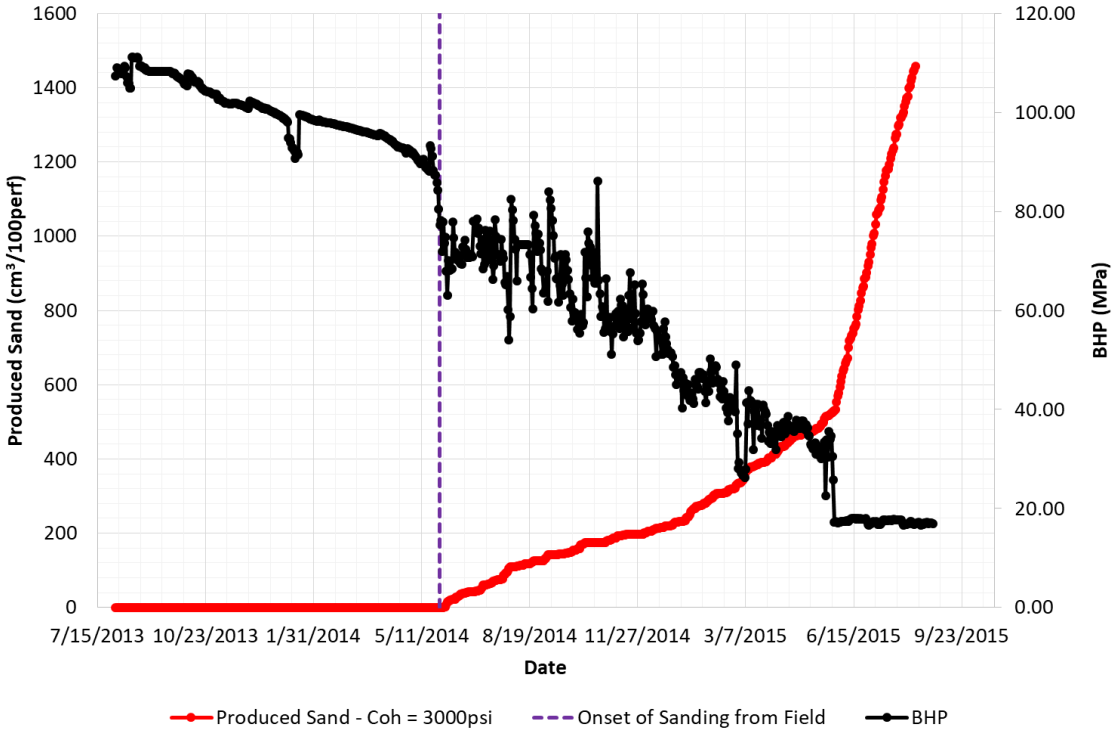

Fig. 8.42: Effect of BHP on sand fill-up in well B

8.4.3.4 Effect of Reservoir Depletion

Figs. 8.43 and 8.44 show the critical drawdown for sand failure and production in each oriented perforation in well B. With the decrease of reservoir pressure, sand failure is more likely to happen, while sand being eroded away is less possible as it requires a larger bottomhole pressure. Safe sand free zone is identified in the green region for the drawdown guidance. However, below certain reservoir pressures, sand failure can occur without any drawdown. In this case, reservoir pressure maintenance may help through injection.

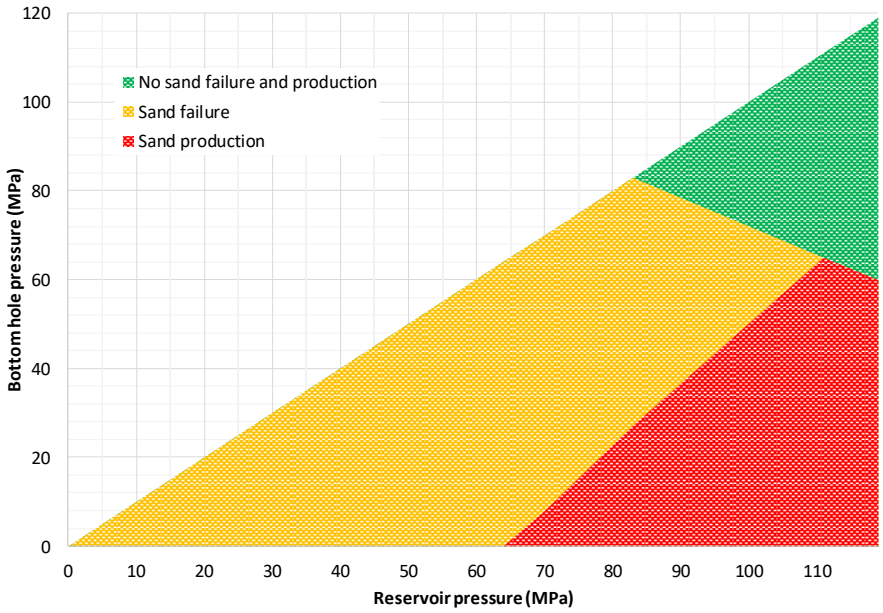

Fig. 8.43: Effect of depletion on critical drawdown in well B: perf // Shmin

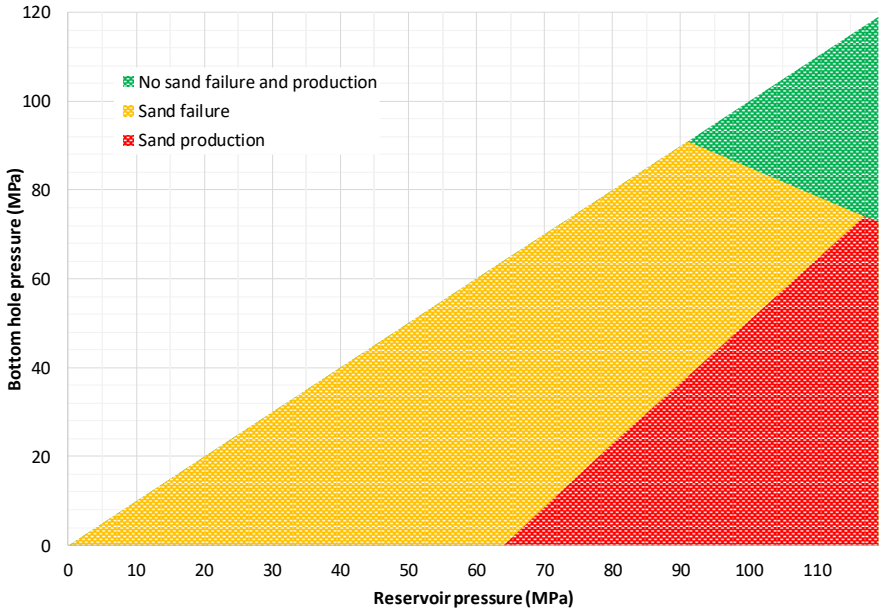

Fig. 8.44: Effect of depletion on critical drawdown in well B: perf // SHmax

8.4.3.5 Effect of Perforation Orientation

The effect of perforation orientation on sanding in this well (shown in Fig. 8.45) is completely different than in well A. Sanding occurs first around SHmax (as discussed above). Secondly, perforations along Shmin produce more sand during the late production period, due to the sand arch effect. As smaller stress contrast is obtained in this region, the cavity grows radially, which is less stable than an elliptical cavity from the other orientations (due to much larger stress contrast).

Fig. 8.46 illustrate the critical drawdown for sand failure in two oriented perforations. This well varies from well A such that the perforation parallel to Shmin has a larger sand free window, suggesting it's more stable compared with one parallel to SHmax. That is to say, there is no universal optimized orientation for perforation in general formations. Perforation orientation should be optimized based on the magnitude and contrast of in-situ stresses. The second discrepancy between this well and well A is the

difference of critical drawdown in two oriented perforations. In this well, the difference of critical drawdowns required for two perforations tends to be smaller, suggesting that perforation orientation design may not be most useful as a sand control method.

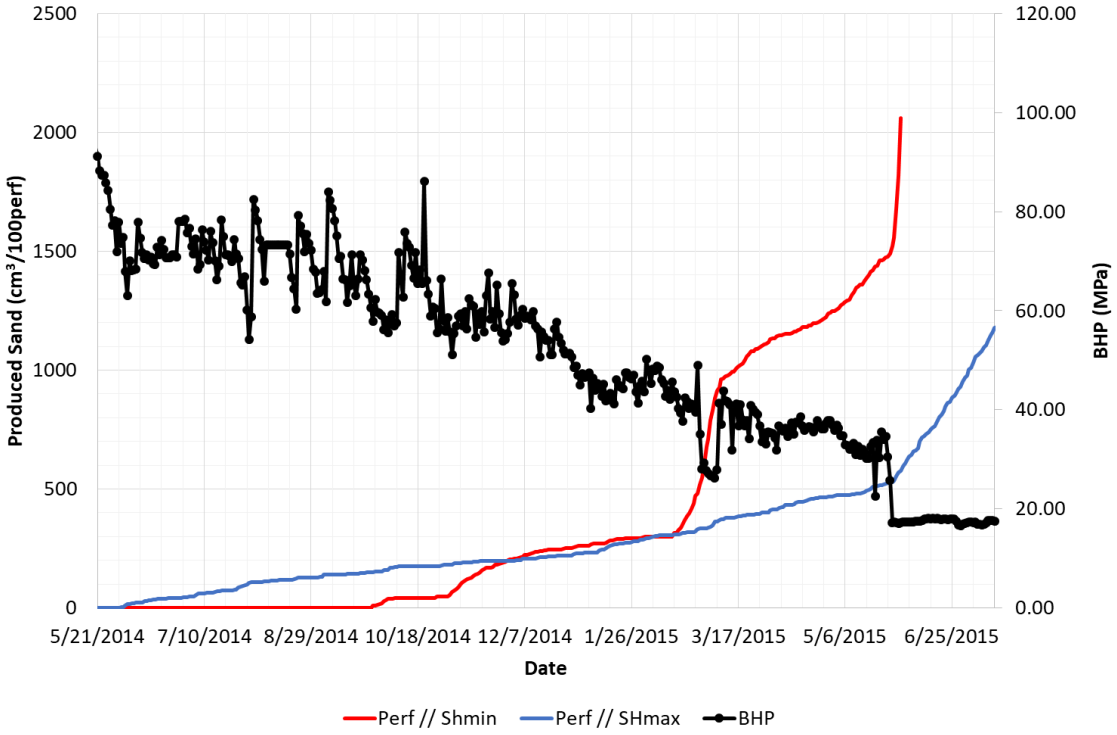

Fig. 8.45: Effect of perforation orientation on sand fill-up in well B

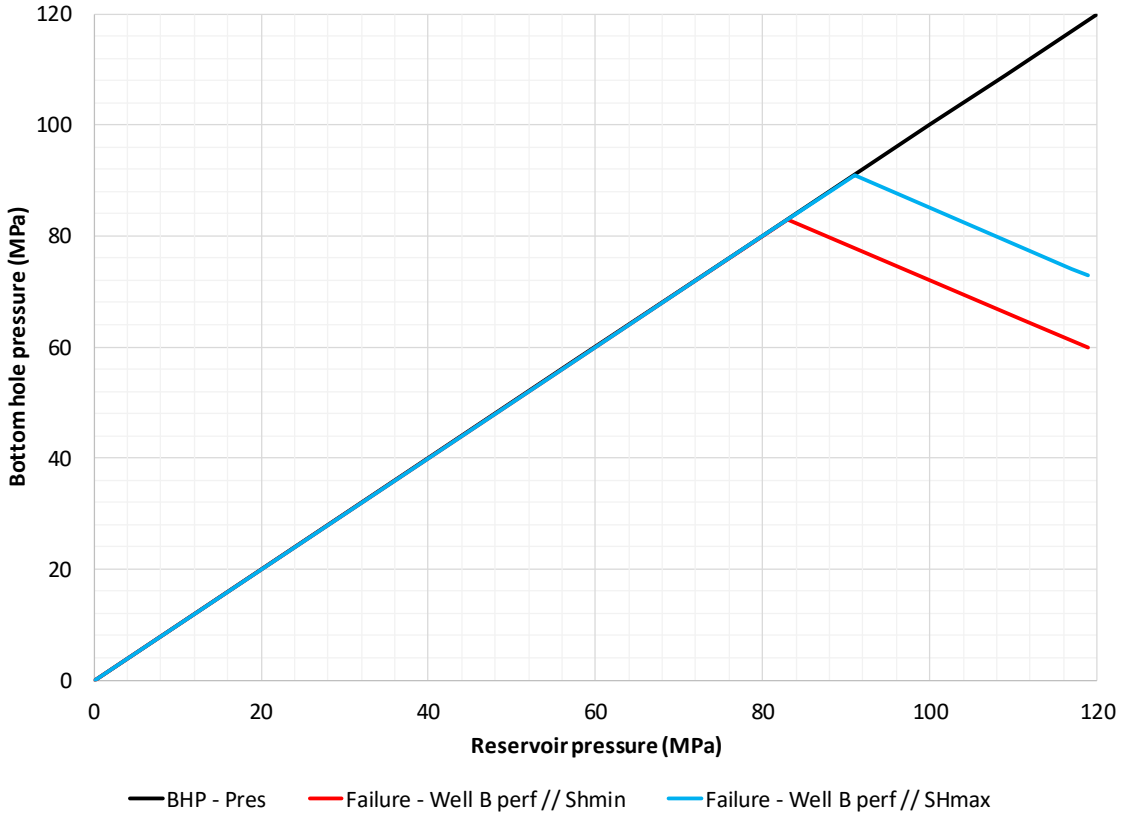

Fig. 8.46: Effect of perforation orientation on critical drawdown in well B

8.4.3.6 Effect of Cement Quality

Fig. 8.47 shows the Mohr circle for the rock parallel to SHmax, where sand suffers a slightly larger hoop stress. From the results, if cement cohesion is 50MPa, no yielding occurs even if the BHP drops to 77MPa. Cement starts to fail if its cohesion decreases to 40MPa when the BHP drops to 77MPa. If cement cohesion is below 30MPa, it may fail at the start of production. However, the cement in this well tends to be more stable than the same quality of cement in well A.

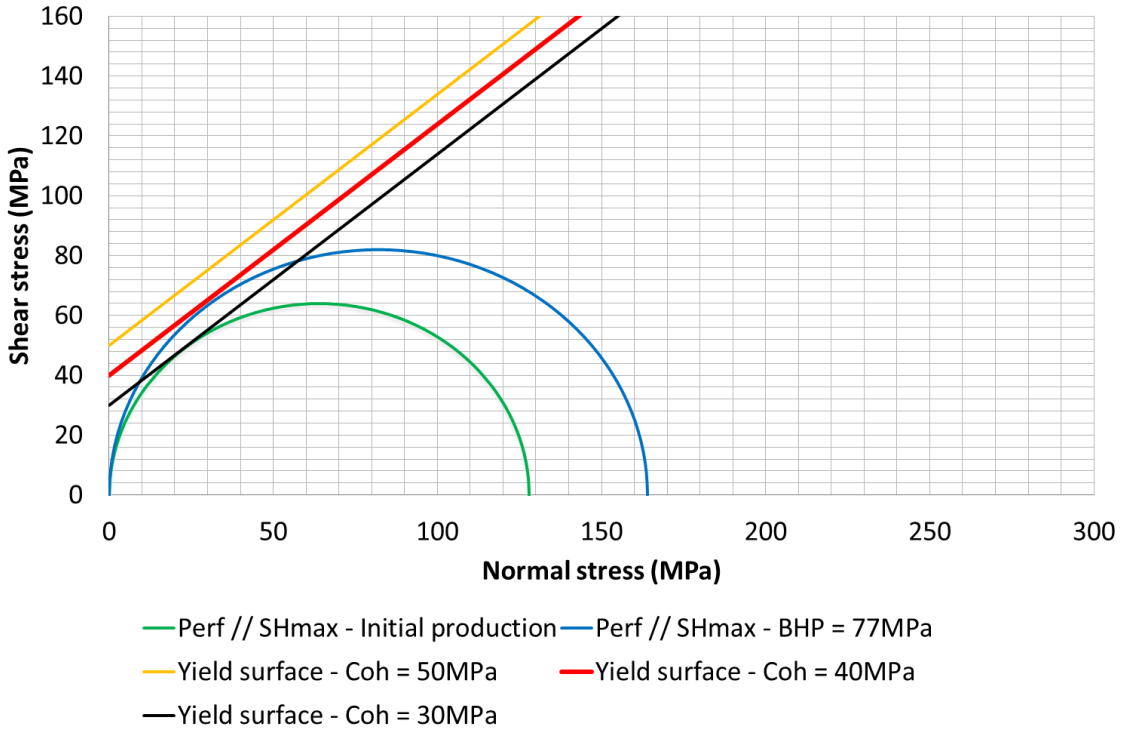

Fig. 8.47: Effect of cement quality on cement failure in well B

8.4.3.7 Effect of Pressure Fluctuation

Since we observe pressure fluctuations in production wells in the KeS block, it is important to study whether pressure fluctuations have an impact on sand failure and production. Field data for BHP with 6 min time interval is recorded and used in this study. The data set is from Oct 2013, where there is no sand production yet. The black dots in Fig. 8.48 show the field data at a time interval of 6min, while the red dots are extracted from the former with a time interval of 1day.

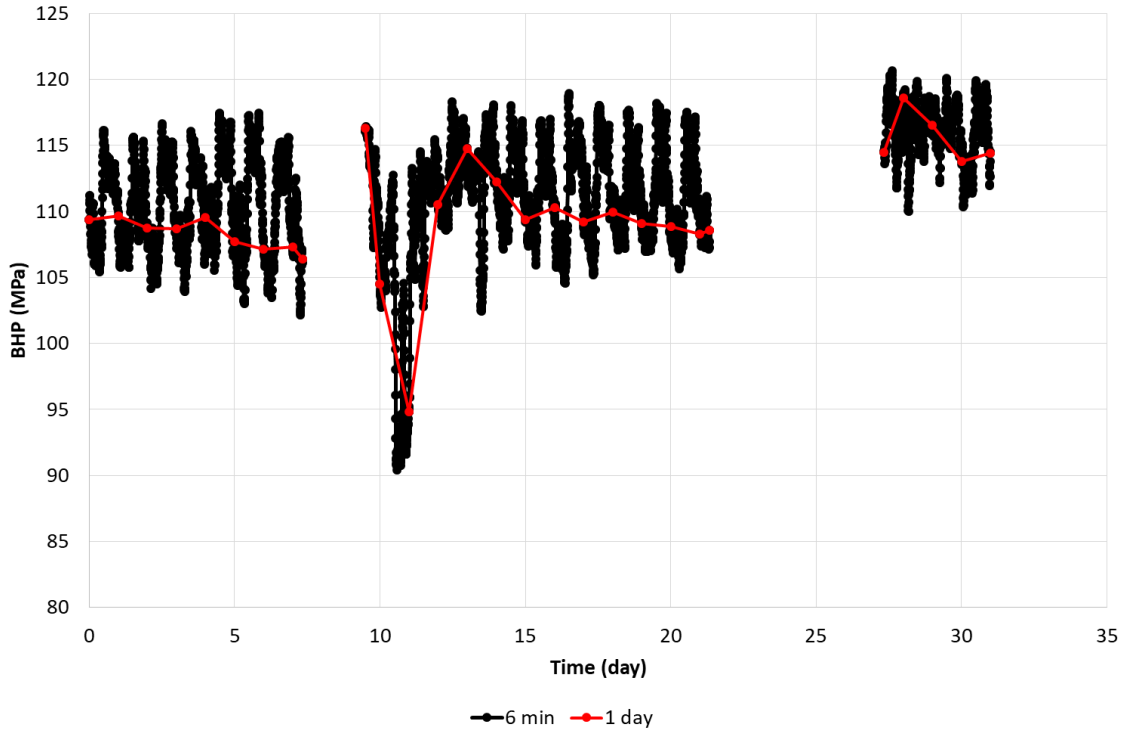

Fig. 8.48: Pressure fluctuation with different time interval in well B

Results of pressure fluctuation on plastic strain is shown in Fig. 8.49. With pressure fluctuations, the cumulative plastic strain is larger than without pressure fluctuations. Further, the difference tends to be larger with more cycles of pressure fluctuation. Besides, the larger pressure pulse and higher frequency of pressure fluctuation will lead to larger plastic strain, making the rock more prone to failure. The pressure fluctuations also result in larger pressure gradients around the wellbore and this promotes erosion of the sand. Therefore, both failure and erosion of the sand are much more likely to occur when pressure fluctuations occur in the wellbore.

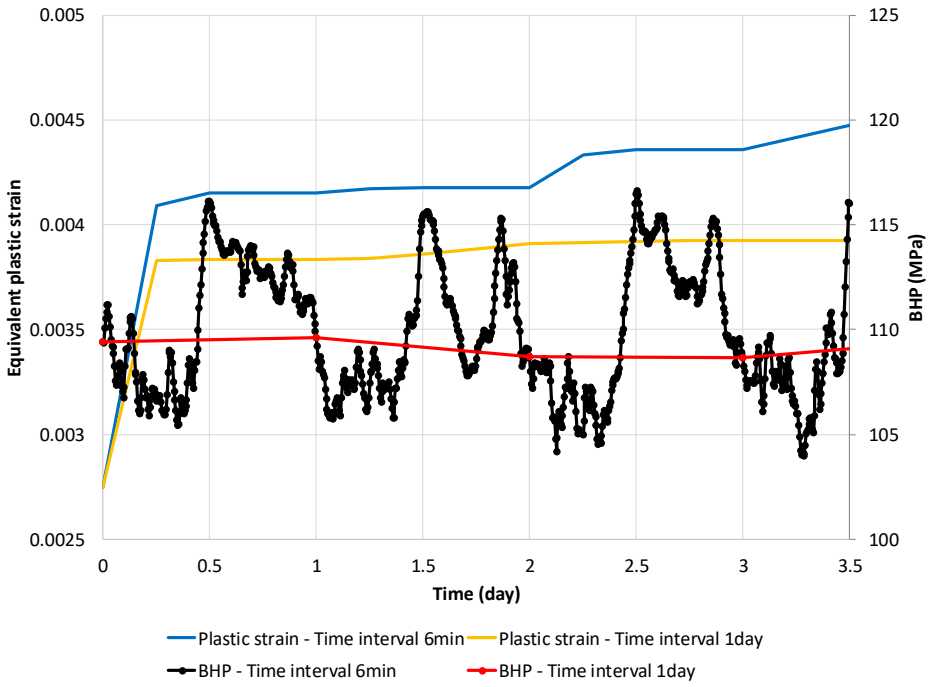

Fig. 8.49: Effect of pressure fluctuation on plastic strain in well B

8.4.3.8 Effect of Natural Fractures

Qualitative impact of the presence and interaction of natural fracture on sand failure and sand production has been discussed thoroughly in the well A study. For well B, we apply the same method and quantitatively study its effect on critical drawdown determination. In total we have six cases for each oriented perforation. For strength reduction, three cases are compared, with a cohesion reduction from 4000psi to 3000psi, and further to 2000psi due to various amounts of natural fractures. For effective permeability, two cases are compared, with permeability increases from original 0.7mD to 10 times of the value.

Figs. 8.50 to 8.55 show the critical drawdown for sand failure and sand production, corresponding to different reservoir depletion under various rock strength caused by the existence of natural fractures in the rock. The other set of figures, from Fig. 8.56 to 8.61,

representing the results in a higher permeability region as more natural fractures connected and interacted with the well/perforation. Some key conclusion can be obtained from these results:

1. The green area, representing a sand free production region, is only related to rock strength, rather than permeability. A larger green area gives rise to a larger acceptable drawdown within which no sand failure occurs.
2. The sand free area on these maps only appears at high reservoir pressure. As the reservoir pressure is depleted, sand failure will occur at any drawdown.
3. Sand free production conditions are more easily met and the green area becomes larger as less natural fractures are present;
4. Higher drawdowns are acceptable for larger cohesion. For example, critical drawdowns at initial reservoir conditions are 33MPa, 59MPa and 78MPa for the rock with cohesion of 2000psi, 3000psi and 4000psi for perforations parallel to Shmin. This trend is also true for other oriented perforations.
5. Larger drawdowns are acceptable at higher reservoir pressures, due to less effective stresses around the perforation/well. During reservoir depletion, the critical drawdown for sand failure continues decreasing to 0. After that, sand can fail without any drawdown;
6. Critical drawdown for sand production increases with reservoir depletion to make drag force sufficiently large for sand erosion. More interaction between natural fractures and well/perforation leads to a smaller drawdown for sand erosion. Below certain reservoir pressure, the drag force can never be sufficient enough to erode failed sands, and these sands will stay in the formation or perforation/well, causing productivity loss and well blockage. This pressure is determined by rock permeability;

7. Different from well A, in well B perforations parallel to Shmin show a better stability under in-situ stresses and allows for a larger drawdown. However, the advantage of perforation orientation optimization in this well is not that significant, as the difference in drawdown between various oriented perforations is relatively small, compared to well A.

Figs. 8.62 to 8.64 show a direct comparison of the critical drawdown for both sand failure and sand production with reservoir depletion for different rock strength and higher permeability. Results suggest that the sanding issue is more severe if there are more connected natural fractures in the rock. With low rock strength and high permeability resulting from natural fractures, smaller drawdown is required to avoid either sand failure (causing productivity loss) or massive sand production (causing facility damage), leaving difficulties for production operations. Therefore, if possible, reservoir regions with natural fractures should not be perforated to avoid sanding risks.

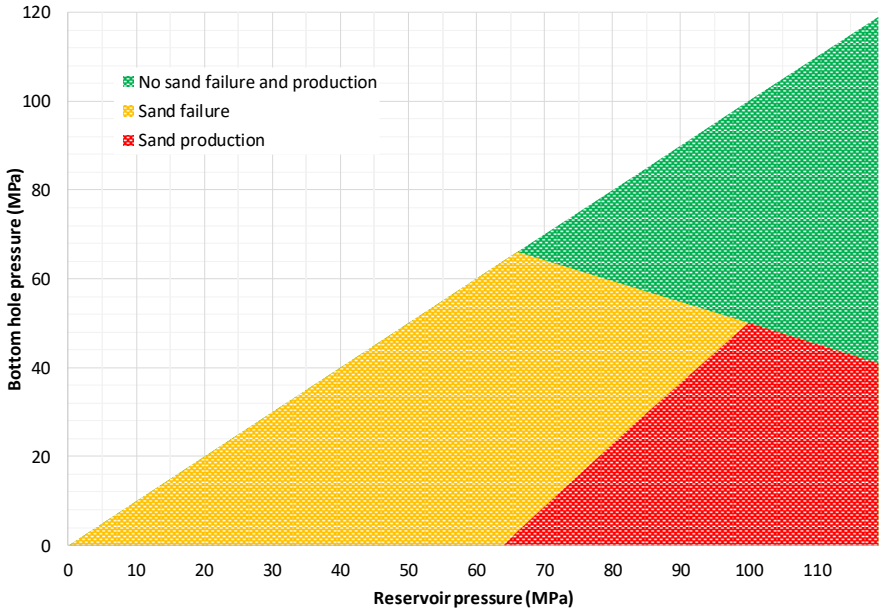

Fig. 8.50: Effect of natural fracture on critical drawdown in well B: perf // Shmin, coh = 4000psi, perm = 0.7mD

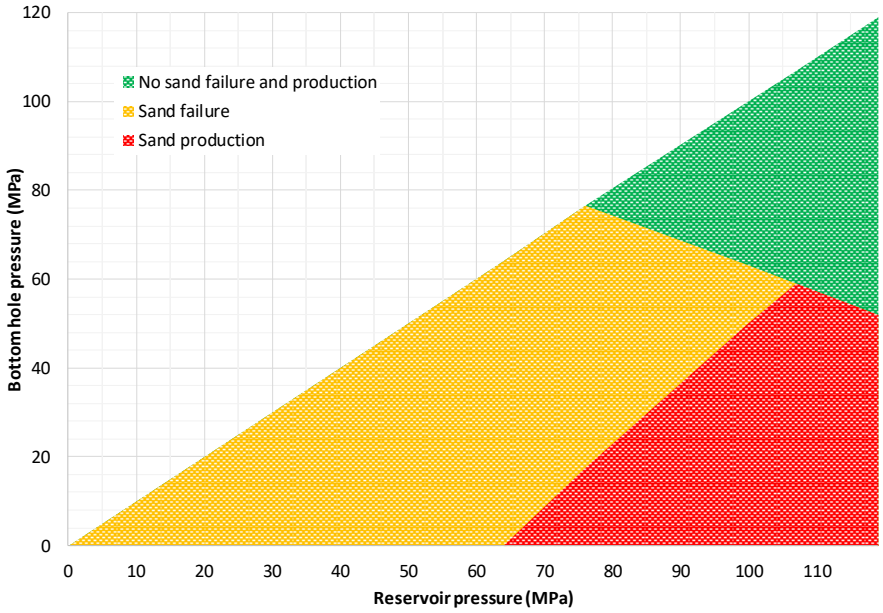

Fig. 8.51: Effect of natural fracture on critical drawdown in well B: perf // SHmax, coh = 4000psi, perm = 0.7mD

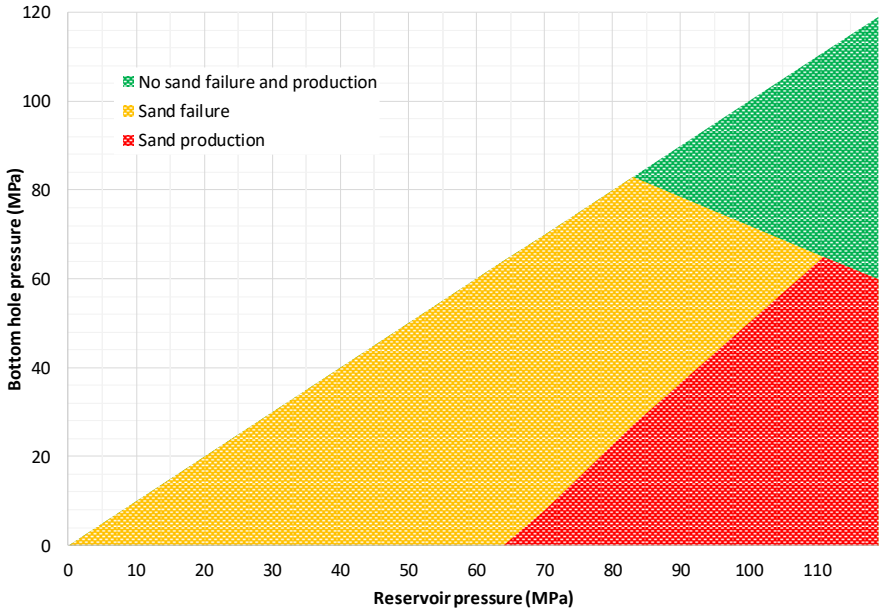

Fig. 8.52: Effect of natural fracture on critical drawdown in well B: perf // Shmin, coh = 3000psi, perm = 0.7mD

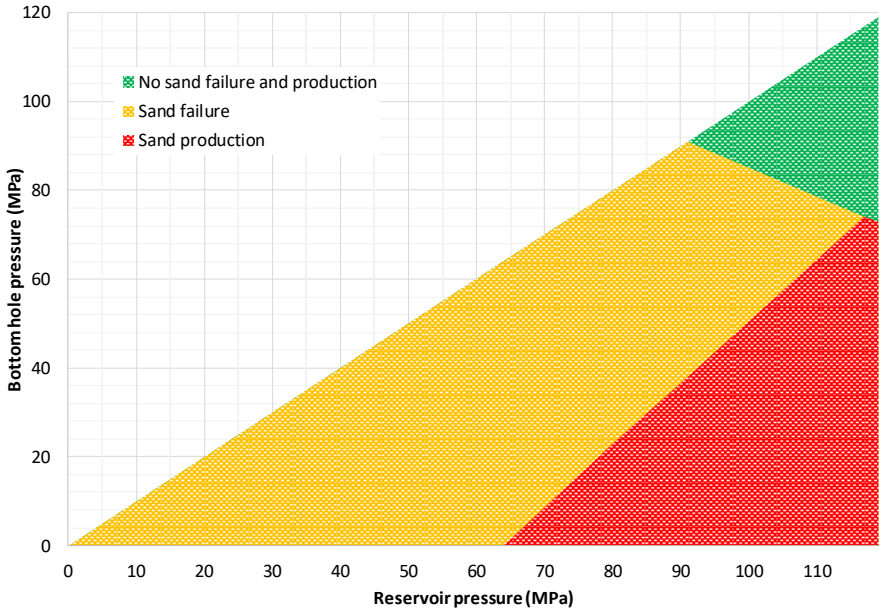

Fig. 8.53: Effect of natural fracture on critical drawdown in well B: perf // SHmax, coh = 3000psi, perm = 0.7mD

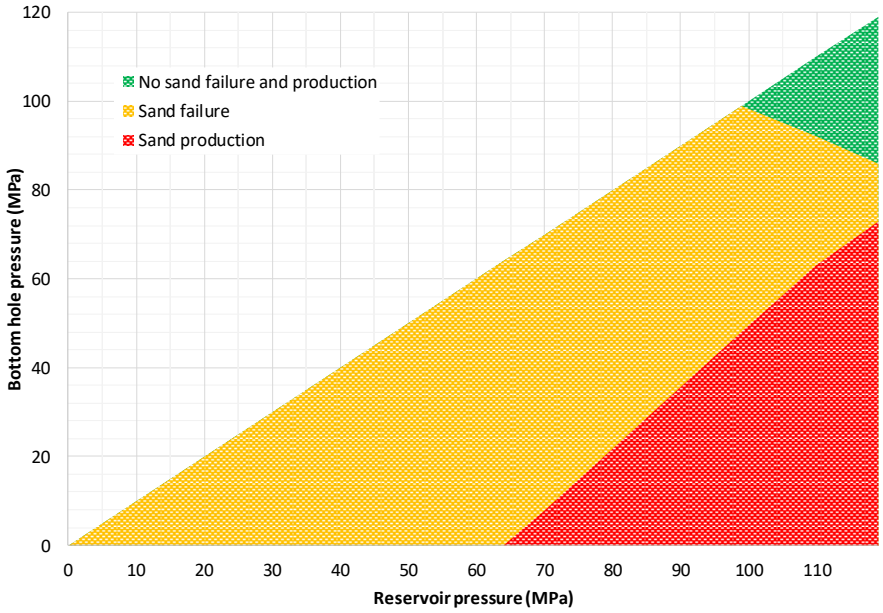

Fig. 8.54: Effect of natural fracture on critical drawdown in well B: perf // Shmin, coh = 2000psi, perm = 0.7mD

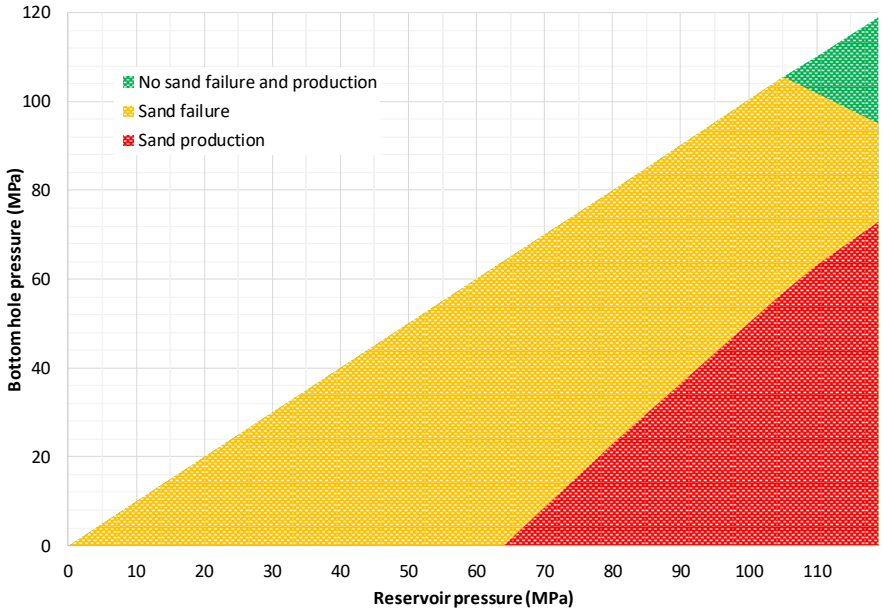

Fig. 8.55: Effect of natural fracture on critical drawdown in well B: perf // SHmax, coh = 2000psi, perm = 0.7mD

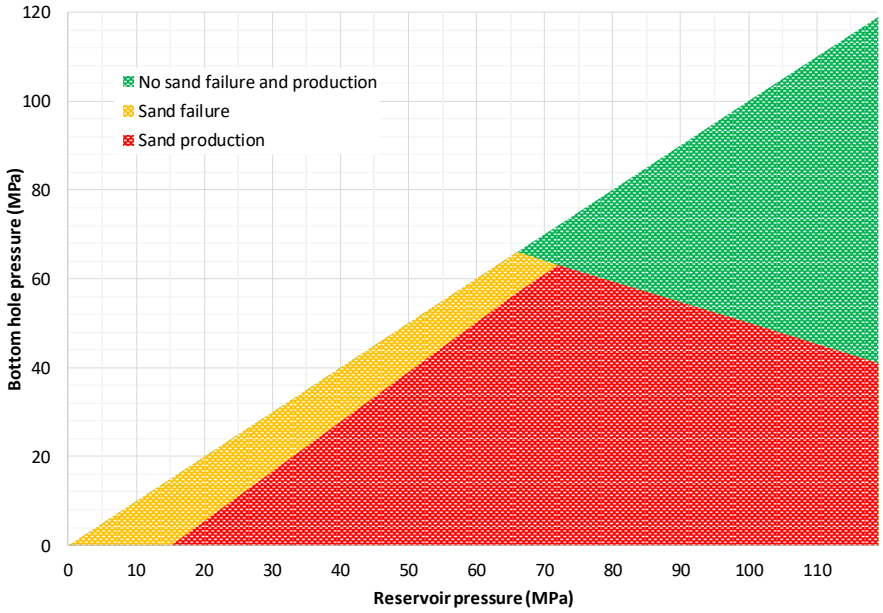

Fig. 8.56: Effect of natural fracture on critical drawdown in well B: perf // Shmin, coh = 4000psi, perm = 7mD

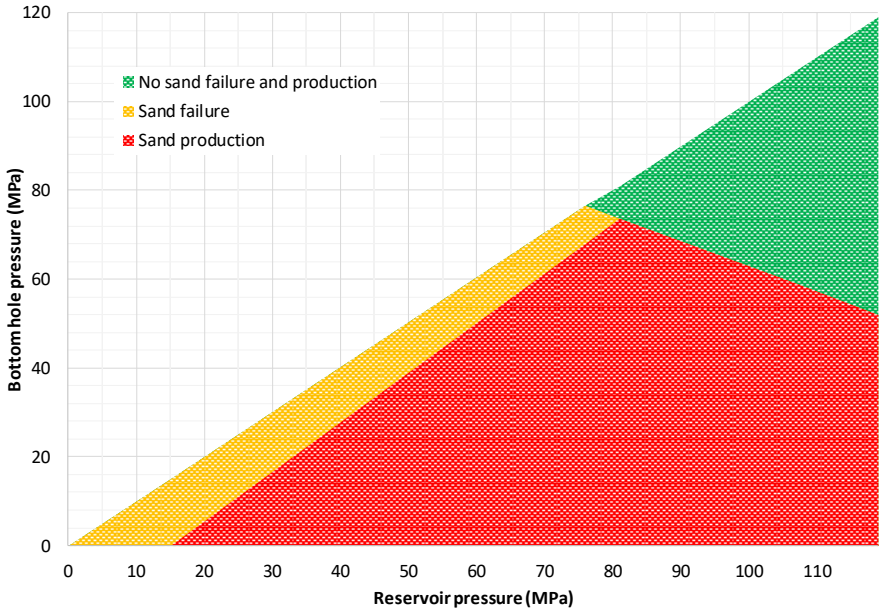

Fig. 8.57: Effect of natural fracture on critical drawdown in well B: perf // SHmax, coh = 4000psi, perm = 7mD

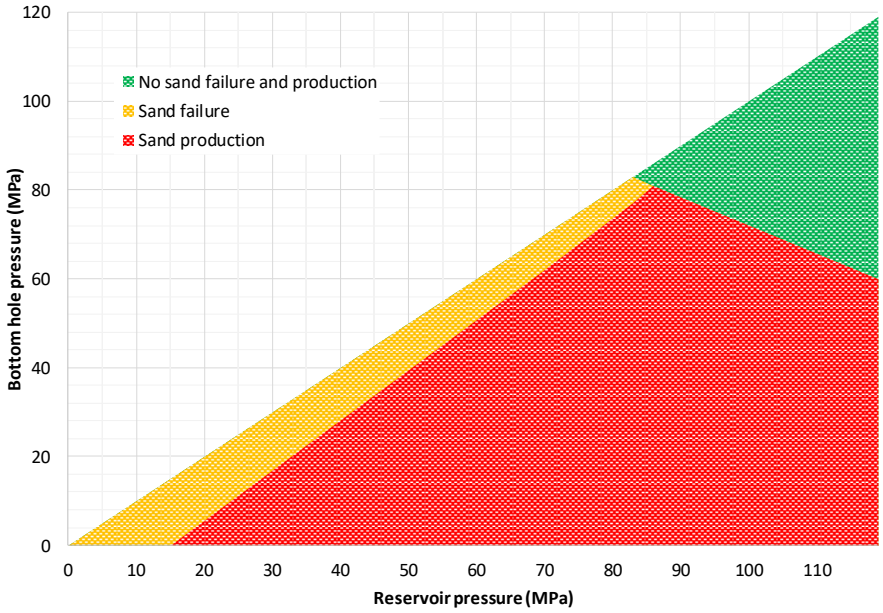

Fig. 8.58: Effect of natural fracture on critical drawdown in well B: perf // Shmin, coh = 3000psi, perm = 7mD

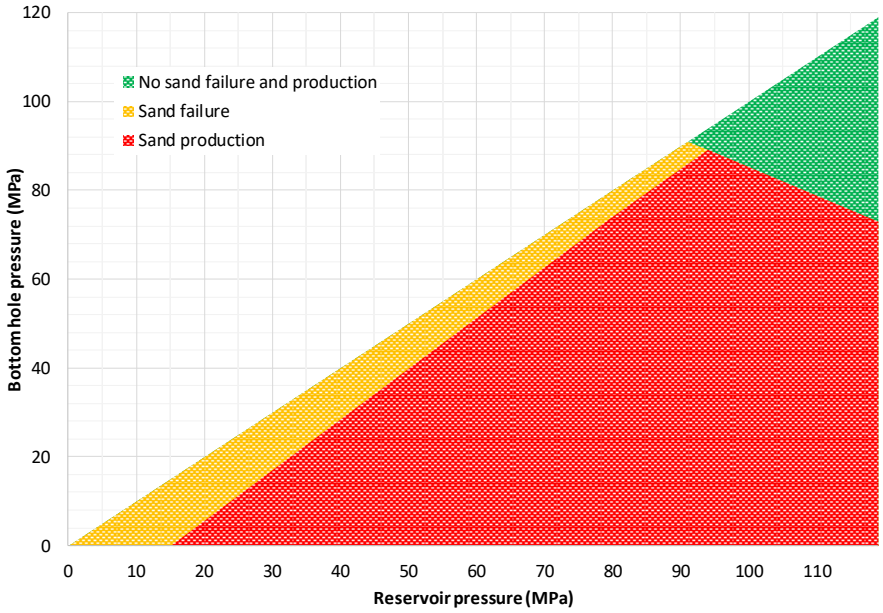

Fig. 8.59: Effect of natural fracture on critical drawdown in well B: perf // SHmax, coh = 3000psi, perm = 7mD

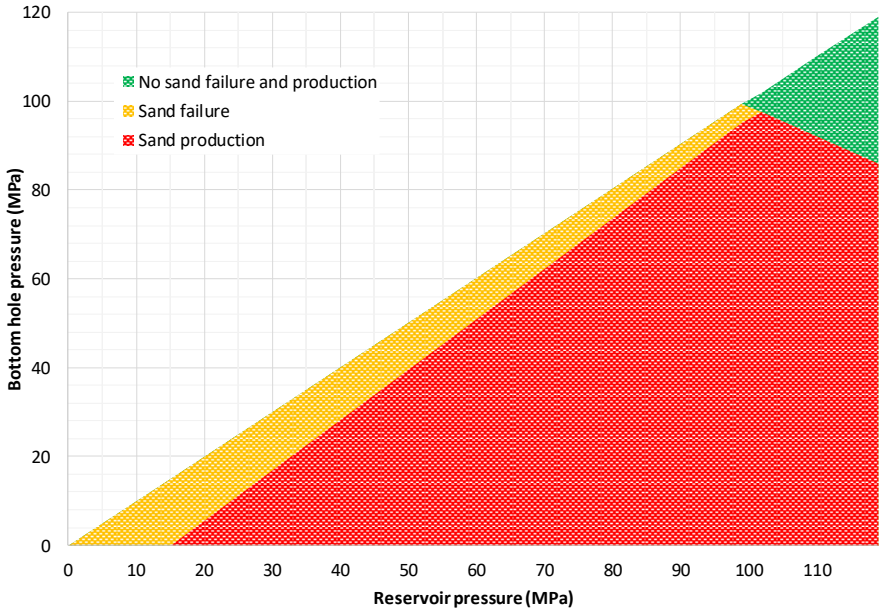

Fig. 8.60: Effect of natural fracture on critical drawdown in well B: perf // Shmin, coh = 2000psi, perm = 7mD

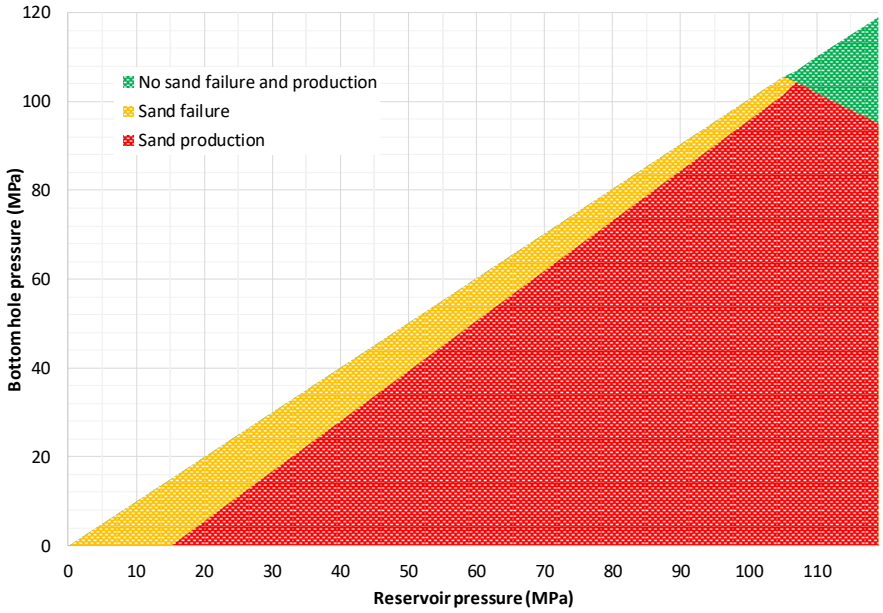

Fig. 8.61: Effect of natural fracture on critical drawdown in well B: perf // SHmax, coh = 2000psi, perm = 7mD

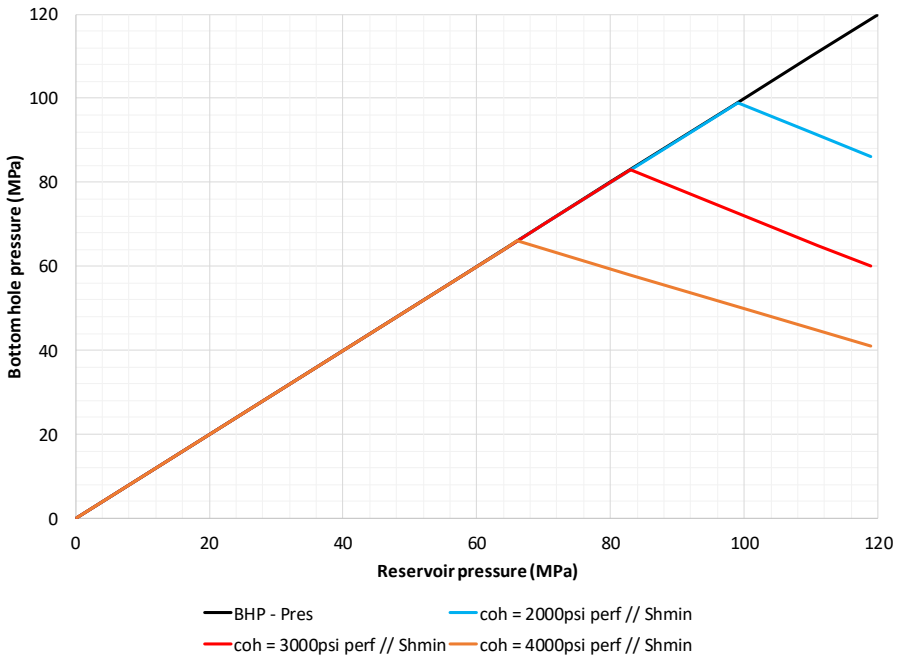

Fig. 8.62: Effect of cohesion on sand failure critical drawdown in well B: perf // Shmin

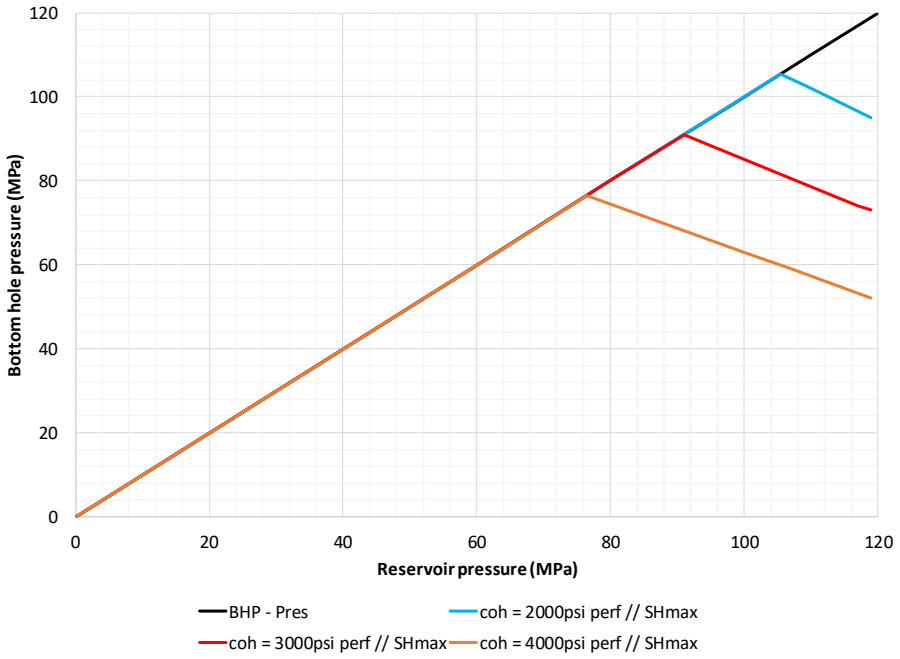

Fig. 8.63: Effect of cohesion on sand failure critical drawdown in well B: perf // SHmax

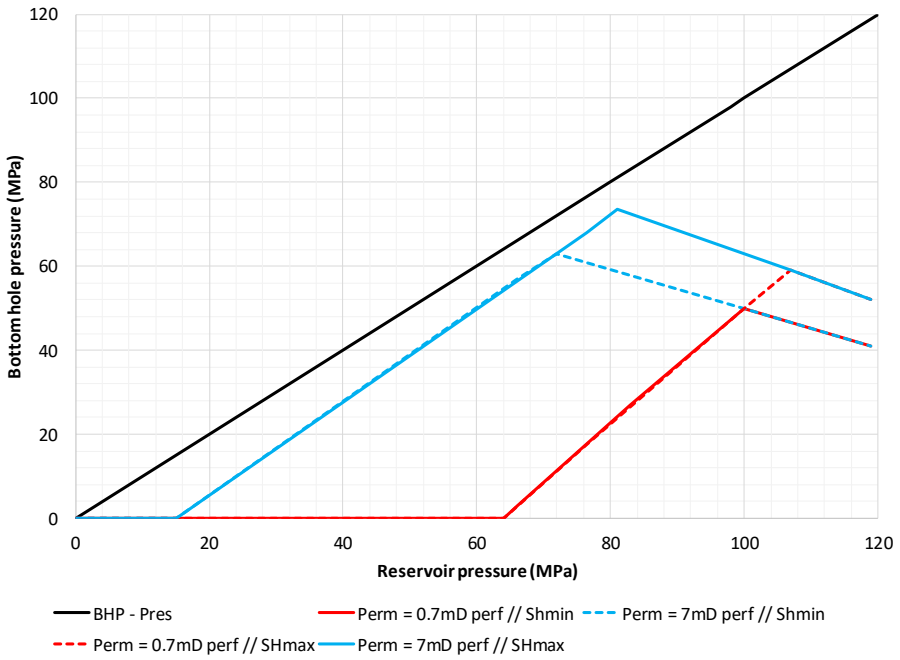

Fig. 8.64: Effect of permeability on sand production critical drawdown in well B

8.4.4 Open-Hole Completion for Two Wells

The previous results on sand failure and production for well A and well B mainly focused on cased and perforated well completions, which is the case in these two wells. In this section, we show the severity of sanding in other kinds of completions.

We did a preliminary study on open-hole completions by using all input data previously obtained. Wells are assumed to be vertical, and cohesion is 3000psi for both wells and the rock permeability is the same as in the earlier study. Results for critical drawdown on sand failure and production are shown in Figs. 8.65 and 8.66. In well A, the sand free production area is very small, initially with at most 1MPa drawdown. Most of the sanding issues in this completion type are related to sand failure, indicating productivity loss due to sand fill-up in the well. Compared to Figs. 8.24 and 8.25 for perforated wells, it clearly shows a smaller allowable drawdown for sand free condition in open-hole completions. However, the contact area between the reservoir and the wellbore is much

larger in this case compared to perforated wells, so the velocity induced drag force is much smaller and cannot exceed the resistance force. Thus, no sand production occurs at any drawdown condition during production. Similarly, in well B, the potential risk of sand failure is higher in open-hole completions (compared to Figs. 8.52 and 8.53 in perforated wells), while there is no sand production predicted at any drawdown during production. Based on these observations, sand failure and sand fill-up into wellbores are the most important concerns in open-hole wells. Therefore, it is recommended that a screen or gravel pack be used to prevent sand production into the wellbore and prevent wellbore blockage and productivity loss.

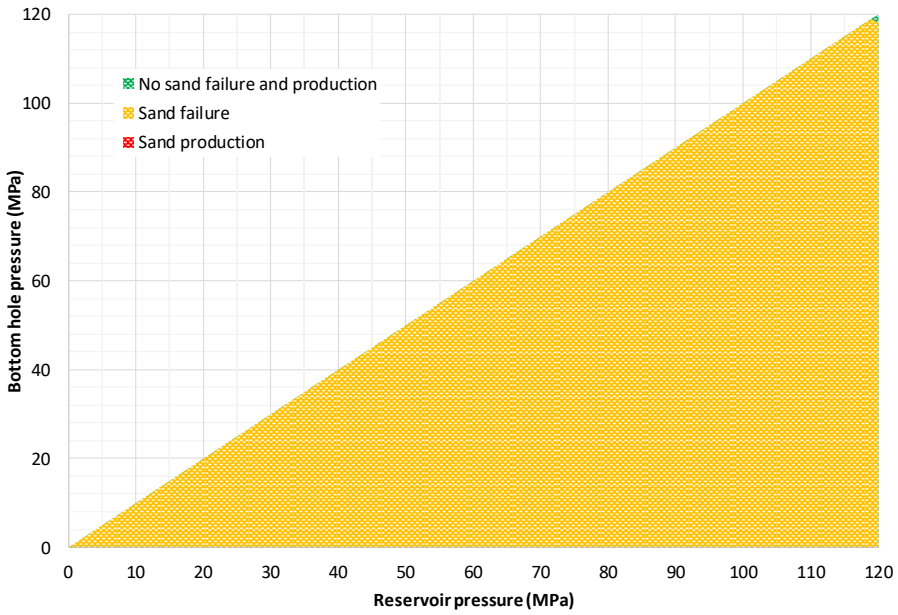

Fig. 8.65: OH completion - Critical drawdown vs. reservoir depletion in well A

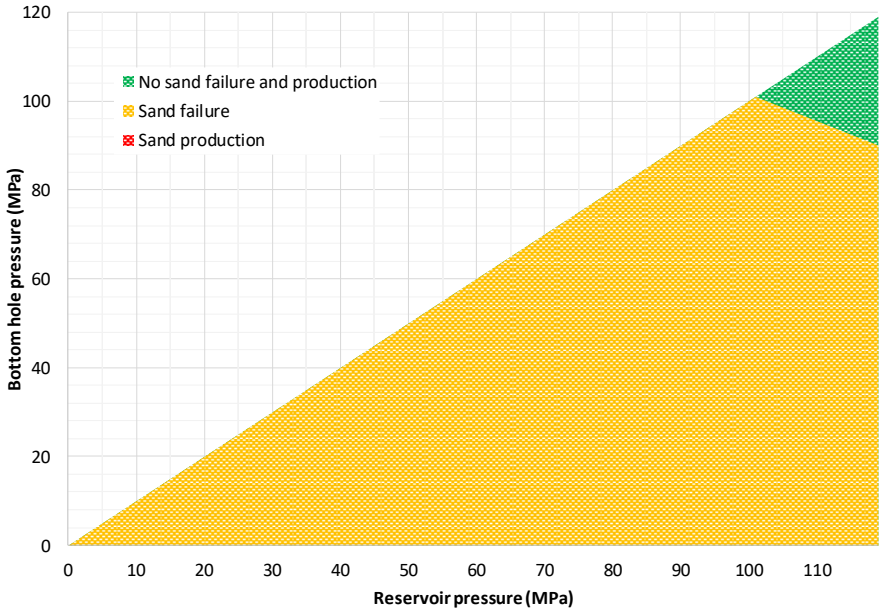

Fig. 8.66: OH completion - Critical drawdown vs. reservoir depletion in well B

8.5 CONCLUSIONS

Our numerical sand production model has been used to evaluate sand failure and production in Tarim HPHT wells and to study the sanding mechanisms behavior based on rock properties, in-situ stresses, bottom hole pressure, perforation operations, reservoir depletion, cement quality, and natural fractures.

Results reveal that rock strength tends to be the most important factor for sand production. Low rock strength in sanding area may result from rock heterogeneity and existence of natural fractures, where drilling and perforating should be avoided. In addition, high in-situ stresses, high stress contrast, and high pore pressure in the reservoir put another risk on sanding. It requires careful drawdown management (as shown in BHP vs reservoir charts) and completion design (such perf orientation, different well completions, etc.). Furthermore, pressure fluctuation has been frequently observed in these production wells, which accelerates rock yielding and failure. Therefore, well shut-in and liquid loading need

a controlled well to prevent large pressure pulse and high frequency of pressure fluctuations.

Finally, the workflow provided in Fig. 8.67 is proposed to ensure that sand free production can be achieved in every well in the field.

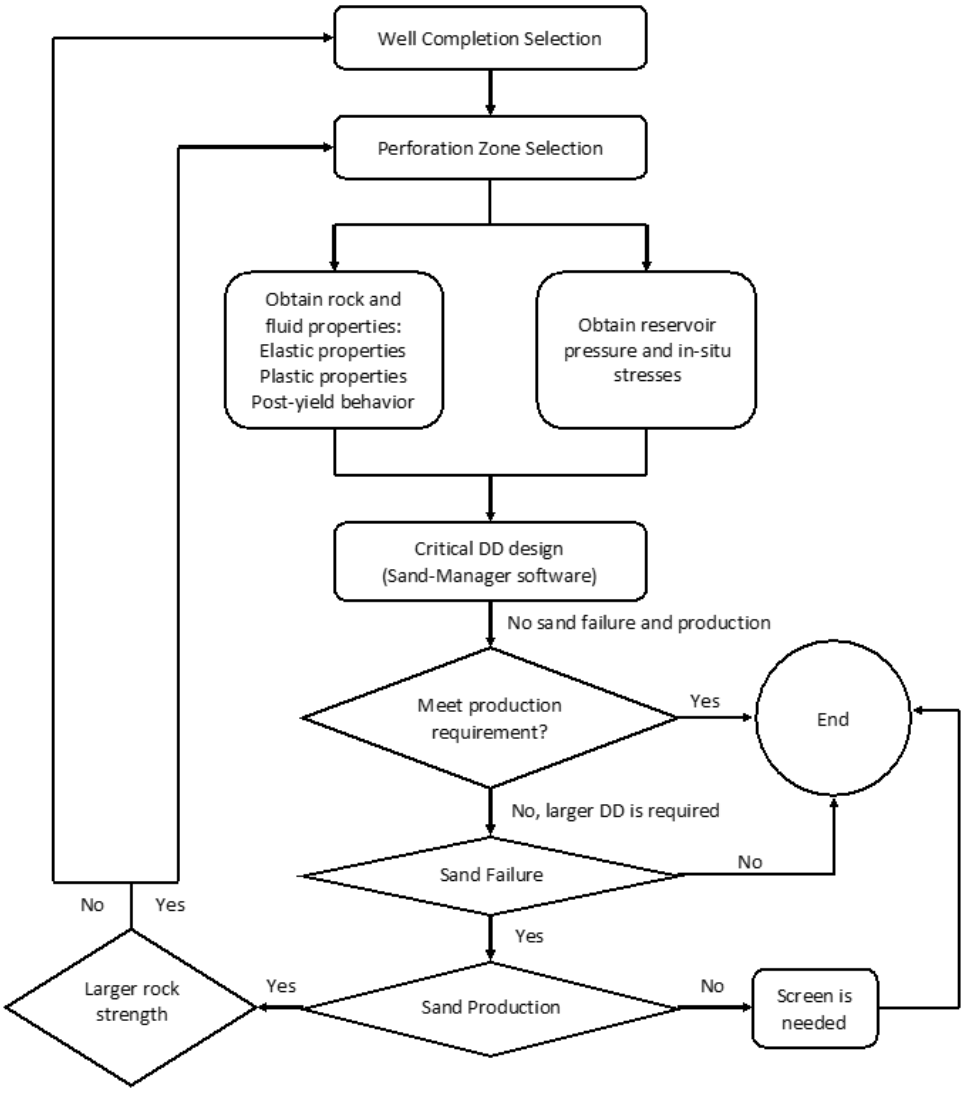

Fig. 8.67: Workflow for designing sand free operation

REFERENCES

Allen, R. F. and M. Walters. 1999. Erskine Field: Early Operating Experience. *Offshore Europe Oil and Gas Exhibition and Conference.*

Detournay, E. and A. H. D. Cheng. 1993. Fundamentals of poroelasticity. *In Comprehensive Rock Engineering: Principles, Practice & Projects, Vol. II, Analysis and Design Method: 113-171.* Pergamon Press.

Glass, A. W. 2005. High pressure, high temperature developments in the United Kingdom Continental Shelf. *Research report 409.*

Law, D., A. S. Dundas, and D. J. Reid. 2000. HPHT Horizontal Sand Control Completion. *In SPE/CIM International Conference on Horizontal Well Technology.*

Palmer, I. D., N. Higgs, I. Ispas, K. Baksh, and K. O. Krieger. 2006. Prediction of sanding using oriented perforations in a deviated well, and validation in the field. *In SPE International Symposium and Exhibition on Formation Damage Control.*

Salencon, J. 1969. Contraction quasi-statique d'une cavite a symetrie spherique ou cylindrique dans un milieu elastoplastique. *In Annales des ponts et chaussées, 4:* 231-236.

Tovar, J. J., L. Zerpa, and E. Guerra. 1999. Impact of formation damage on sand production in Deep Eocene Reservoirs, Lake Maracaibo, Venezuela: A case history. *European formation damage conference.*

Vaziri, H. 1986. Mechanics of fluid and sand production from oil sand reservoirs. *Annual Technical Meeting. Petroleum Society of Canada.*

Wang, H., X. Yang, W. Zhang, and M. M. Sharma. 2018. Predicting Sand Production in HPHT Wells in the Tarim Basin. *Presented at the SPE Annual Technical Conference and Exhibition held in Dallas, Texas, 24–26 September 2018. SPE-191406-MS.*

Chapter 9: Conclusions and Future Work

9.1 Summary and Conclusions

In this research, we have developed a 3D multi-phase poro-elasto-plastic numerical model, and applied it to quantitatively estimate sand failure, onset of sanding, and sand production under different conditions. With the model, the mechanisms for sanding issues in field operation, including sand failure caused by water hammer events, sand production being delayed in gas flow, sand production in water breakthrough, sanding behavior in different well completions, and distinguishing different cavity shapes caused by sand production, have been thoroughly explored. Finally, the model is used to evaluate sand production in the Tarim field, along with the recommendations for cementing, completion and production to avoid productivity loss and sand fill-up in gas production wells.

In this chapter, we summarize the conclusions for each aspect of the research and propose recommendations for future work.

9.1.1 Development of Poro-Elasto-Plastic Model

1. A 3D fully coupled poro-elasto-plastic model for single phase and multi-phase fluid flow has been developed to calculate dynamically evolving fluid pressure transients, and rock deformation and stresses.
2. Plastic deformation is calculated from the modified Mohr-Coulomb Cap model, which is capable of capturing complex post-yield behavior such as strain hardening/softening.
3. The model has been validated with analytical solutions for multiple cases, from pure fluid flow to rock deformation, and further to fully coupled poro-elastic problems.

9.1.2 Development of the Sand Production Model

1. A sand production model has been developed by adding sanding criteria in the poro-elasto-plastic model.
2. The novel sanding criteria for the entrainment of sands consist of both mechanical failure (shear/tensile/compressive failure) and fluid erosion.
3. A novel dynamic cell removal algorithm has been implemented to simulate cavity propagation during sand production.
4. Dynamic mesh refinement/un-refinement has been incorporated in the model to efficiently capture the plastic zone.
5. The model is verified by comparing its results with sand production experiments. Results show that, for the first time, a sand production model can match the onset of sanding, sand production, and cavity shape after sanding.

9.1.3 Sanding Mechanisms in Distinct Cavity Shapes

1. The sand production model can match all cavity shapes observed in sand production experiments, including spiral shear bands, V-shape breakouts, dog-ear breakouts, and slit mode cavities.
2. Shear failure dominates the first three failure patterns, while compressive failure is the main mechanism for slit mode cavity.
3. Strain localization plays an important role in the development of cavity shapes.
4. Cavity shapes are sensitive to stresses, drawdown, and rock properties and these effects are quantified by the model
5. Slit mode cavity is likely to happen in depleted reservoirs due to high mean effective stresses.

9.1.4 Sand Failure and Production in Different Well Completions

1. The linear fluid-flow pattern in frac-pack completions reduces the plastic strain and associated shear failures compared to the radial flow pattern in an open-hole completion. This clearly indicates the potential advantage of frac-packs from a sand control standpoint.
2. The frac-pack width is an important design factor as it changes the initial hoop stress and subsequent shear failure pattern. Large fracture width leads to shear-failure along the frac-pack and this failed sand needs to be kept away from the wellbore by packing the fracture and annulus with proppant.
3. The strain softening characteristics of the rock (rock post-yield behavior) can alter the pattern of shear failure from a V-shaped cavity to a more spiral-band pattern and increase the extent of overall failure.
4. The plasticity of the rock must be taken into account for accurately predicting sand failure and for well completion design.
5. Near-well shear failure can provide yielding planes for compressive failure which occurs further away from the well.
6. Reservoir pressure maintenance should be considered to minimize compressive failure (such as pore collapse) near frac-packs. This can be a critical failure mechanism when combined with V-shaped or spiral-band-shaped shear failure.
7. Strain localization is observed around the well where strain softening happens. This is crucial and controls the location of sanding and the sanding rate, as well as the sanding pattern. With strain localization, sanding starts along shear bands with sand being produced at a continuous rate, until a part of rock is detached, yielding a massive burst in sand production.

8. Mohr Coulomb parameters, post-yield parameters, permeability, grain size and stress contrast are shown to be important for both the onset of sanding and sand production rate. Mechanical properties play an important role in sand initiation, while fluid flow properties have a bigger effect on sand production rate.
9. For cased and perforated wells, different perforation orientations are simulated to study the effect of perforation orientation on sanding. For vertical wells in a normal faulting regime, results indicate that perforations parallel to the minimum horizontal stress tend to be more stable. After sand production has started, perforation orientation may not be a dominant factor.
10. Perforation dimensions, including perforation diameter and length, are shown to be important for both the onset of sanding and sand production rate. Perforations with smaller diameter and length tend to be more stable and help to decrease sand production.

9.1.5 Effect of Fluid Flow on Sand Failure and Production

1. Water evaporation caused by gas flow can lead to sand strengthening, which makes it more difficult to fail the sand and thus sustain larger stresses without sanding. However, this does not occur in oil wells since there is no evaporation of water in oil wells.
2. If sanding is dominated by fluid erosion, non-Darcy flow of gas requires a higher flow rate for sand production.
3. While studying the sanding issue in a gas well, neglecting non-Darcy effects will result in overestimating both the onset of sanding and the severity of sanding.

4. With water breakthrough, both mechanical failure and fluid erosion are triggered more easily, and this will result in more sand production.
5. The water cut (near wellbore water saturation) plays an important role in determining the onset of sanding and the sanding rate. This is primarily due to a reduction in the capillary cohesion between sand grains.
6. A large water hammer pressure pulse can be generated as a result of a quick shut-off of a valve in a water injector. The pressure variation at the sand-face has been simulated by a water hammer simulator and integrated with our geomechanical sand failure model.
7. For unconsolidated sands, the sand failure zone is much larger for cases with a water hammer event (compared to a smooth pressure decrease).
8. The simulations can be used to optimize the location of subsurface valves (to minimize sanding risks).
9. Rapid valve closures always result in more sand failure and should always be avoided to prevent massive sand production.
10. A permeability reduction caused by cross-flow and fines reinjection (driven by water hammer events) can dramatically influence near-wellbore pressure gradients and enlarge the impact of water hammer events on sand failure.
11. The sand failure zone grows with each shut-in (for multiple shut-ins). This effect is magnified in the presence of water hammer events.
12. Strain softening behavior of the rock can dramatically increase the sanding risks and severity. This is particularly true when water hammer events are accounted for.

13. The impact of water hammer events on sand failure is crucial for rocks with a low UCS. Thus, for low UCS, poorly consolidated sands, well shut-ins and restarts must be carefully controlled to avoid water hammer events.

9.1.6 Sand Production Prediction in the Tarim Field

1. Rock strength is shown to be the most important factor affecting sand production. From simulation results, a lower cohesion value (3000 psi) had to be used compared to the experimentally measured value (5800 psi) to match the onset of sanding observed in the field for two wells. It was concluded that the explanation of this discrepancy is likely that the core was taken from a competent and harder section of the rock while the weakest rock in the core was not sampled. It is, therefore, very likely that the part of the rock on which the experiments were conducted was not the weakest section of the formation (where sand production is likely to occur). This means that the core samples may not be representative of the entire wellbore section.
2. Lower cohesion values in the field (compared to the lab) can be caused by two factors: rock heterogeneity and natural fractures. Some perforations are likely to be in low cohesion zones and are at risk of sand production.
3. It is important to consider in-situ stresses when designing sand control methods. As studied above, in-situ stresses play an important role on hoop stresses and can dramatically change perforation performance.
4. A combination of large and sharp BHP decreases can lead to an increase in sanding rate, which we want to avoid. Thus, it is important to design proper drawdown management and install control valves carefully to prevent a sudden

decrease in BHP. This means that sudden and unanticipated shut-downs and restarts of the well should be avoided or properly managed.

5. Depletion is another important factor as it can increase sanding risk by not only increasing the shear stresses (induce shear failure) but also increasing the mean stress (induce volumetric failure). By studying critical drawdown vs. reservoir depletion, we observed that as the reservoir pressure depletes, the allowable drawdown for sand failure decreases, which increases the potential risk of sanding.
6. Perforation orientation needs to be considered carefully during well completion design, as it can change the stress distribution and the sanding behavior. The orientation of perforations can be optimized to significantly reduce sanding risks in some cases (shown in Well A). However, there is no universal rule for the best perforation orientation, as it may change as the in-situ stresses change.
7. Cement quality needs to be taken into account as a potential mechanism for sand failure. Low strength cements caused by poor cementing may lead to failure under high in-situ stress, even at the beginning of production.
8. Fluid velocity determines whether failed sands can be produced or not. Sand production will occur when the production rate exceeds the critical rate needed to entrain and produce the failed sand.
9. Pressure fluctuation is also crucial for sanding. More cycles of pressure fluctuation can increase the plastic strain leading to rock failure. Furthermore, larger pressure pulses and high frequency pressure fluctuations will result in more rock failure.
10. Achieving sand free production is more related to rock strength than permeability. As reservoir pressure depletes, the pressure drawdown over

which sand will be produced shrinks until sand production occurs at all drawdowns.

11. The range of drawdowns over which sand production occurs becomes larger when more natural fractures are present.
12. Larger drawdown is acceptable at higher reservoir pressure, due to smaller effective stresses around the perforation/well.
13. The critical drawdown for sand production increases with reservoir depletion. This makes the drag force sufficiently large for sand erosion.
14. In hydraulically fractured wells, or wells with natural fractures a smaller drawdown is sufficient for sand erosion. Below a certain reservoir pressure, the drag force may never exceed the resistance force and the failed sands will stay in the formation or perforation/well, causing productivity loss and well blockage. This pressure is determined by rock permeability and thus is related to the presence of natural fractures.
15. In naturally fractured wells, the sand may be produced in large pieces or chunks. This is due to failure occurring along the natural fractures (regions of low cohesion) and the failed rock fragments may remain intact.
16. The production of such large pieces of rock (much larger than the individual sand grains) into the well is much more likely to lead to well blockage if a large drawdown is applied. This is because these large pieces of rock are very difficult to transport up the well. The larger these pieces of rock are, the more difficult it is for them to flow out of the well.
17. The well completion type plays an important role in both sand failure and sand production, as it not only alters the stress distribution but also changes the fluid

pressure gradient. Thus, well completion design should be rethought to avoid sanding issues.

Based on the conclusions above, some recommendations for the Tarim field are provided here:

1. Avoid perforating the low rock strength zones (as detected by logs).
2. Fracturing treatments, such as SRV fracturing, need to be carefully designed to avoid intersecting and reactivating natural fractures.
3. Make full use of in-situ stresses to help select perforation orientation. In well A, perforations parallel to S_{Hmax} tend to be stable. In well B, before sand production, perforations parallel to S_{hmin} tend to be stable. There is no universal rule for the best perforation orientation, thus it is important to take in-situ stresses into account and rely on a sand production model for a better design.
4. BHP must be controlled carefully as we do not want quick and sharp changes in drawdown during production. The magnitude of the allowable drawdown can be obtained from the model for each well to help pick a safe window for the bottom-hole pressure at any given time during production.
5. It is recommended that the drawdown at the sand face be selected based on the sand free (green) area from the charts of BHP vs. reservoir pressure obtained from Sand Manager. If the BHP falls in the sand failure region, it is recommended to utilize proper sand control methods such as a screen and gravel/frac pack to ensure that sand does not flow into the wellbore. If the BHP falls in the sand production region, we should think about producing in other high strength regions, or change the completion type.
6. Depletion induces shear and volumetric failure. Thus, in mature wells, reservoir pressure may need to be maintained to a certain level to avoid failure. Pressure

maintenance through injection should be considered as an option in the reservoir. However, this may not be practical given the cost and limited availability of injection fluids.

7. Cementation quality needs to be improved through the application of centralizers and vibrating the casing during cementation to ensure a good cement job.
8. Fractured production wells have worse sanding than un-fractured wells. It is suggested that hydraulic fracturing be combined with other changes to the completion to ensure that it does not make the sanding situation worse.
9. Rapid pressure fluctuations should be avoided to reduce sanding risks. It is recommended that the chokes and valves be carefully controlled to ensure that the fluctuations in the drawdown are minimized.
10. Unplanned shut-downs and restarts should be avoided by installing back-up chokes, valves and electrical generators so that electrical outages do not result in such shut-downs.
11. Since it is clear that wellbore plugging and sand production is occurring in many of the wells and that this is resulting in early well shut-down, the well completion needs to be redesigned to ensure sand free production. Such a completion design study should be conducted for both fractured and unfractured well completions.

9.2 FUTURE WORK

9.2.1 Fluid and Sand Transport Model in Wells

In this sand production model, an assumption made is that once mechanical failure and fluid erosion criteria are met, the sand will be produced to the surface of the well.

However, this ignores the transportation of fluid and sands in the well. In reality, if the fluid velocity in the tubing is insufficient, sands may drop into well rat hole and even cover some section of perforations. Thus, an add-on model of fluid and sand transport in the well will help to better predict sand production to the surface and inside the wellbore, and help estimate the severity of well productivity loss.

9.2.2 Model Extension to Incorporate Sand Control Methods

Currently, the model predicts sand production without common sand control methods. This may overestimate sanding severity since in the field sand control methods usually applied. Typical sand control methods include gravel pack, frac pack, stand-alone screens, etc. Frac packs can redistribute stresses and fluid pressure and can help reduce sanding risk from both mechanical failure and fluid erosion. On the other hand, gravel pack and stand-alone screens help prevent sand production from the formation into the well by mechanically blocking the sand from flowing into the well. Extending the sand production model to incorporate typical sand control methods can not only make sand production prediction more practical, but also help evaluate and design sand control methods.

APPENDICES

APPENDIX A. STRESS RETURN REGIONS AND CONDITIONS

Assume

$$\sigma_1 \le \sigma_2 \le \sigma_3$$

$$f_{MC} = a_{MC}^T(\sigma - \sigma_c) = \sigma_1 - \sigma_3 N_\phi + 2c\sqrt{N_\phi}$$

$$g_{MC} = b_{MC}^T\sigma = \sigma_1 - \sigma_3 N_\psi$$

The Rankine part of the modified MC criterion is represented by

$$f_R = a_R^T(\sigma - \sigma_a) = \sigma_3 - \sigma_t$$

$$g_R = b_R^T\sigma = \sigma_3$$

The 11 boundary planes that separate the stress regions are listed as ($p_{12} = -p_{21}$)

$$p_{12} = \left(r_{MC}^p \times r_1^{MC}\right)^T(\sigma - \sigma_c)$$

$$p_{13} = \left(r_2^{MC} \times r_{MC}^p\right)^T(\sigma - \sigma_c)$$

$$p_{14} = \left(r_3^R \times r_{MC}^p\right)^T(\sigma - \sigma_1^R)$$

$$p_{25} = \left(r_{MC}^p \times r_{E\psi 1}\right)^T(\sigma - \sigma_1^R)$$

$$p_{36} = \left(r_{E\psi 2} \times r_{MC}^p\right)^T(\sigma - \sigma_2^R)$$

$$p_{45} = \left(r_R^p \times r_{MC}^p\right)^T(\sigma - \sigma_1^R)$$

$$p_{46} = \left(r_{MC}^p \times r_R^p\right)^T(\sigma - \sigma_2^R)$$

$$p_{47} = \left(r_R^p \times r_3^R\right)^T(\sigma - \sigma_1^R)$$

$$p_{58} = \left(r_{E1} \times r_R^p\right)^T(\sigma - \sigma_1^R)$$

$$p_{78} = \left(r_R^p \times r_1^R\right)^T(\sigma - \sigma_a)$$

$$p_{89} = \left(r_R^p \times r_{E1}\right)^T(\sigma - \sigma_a)$$

where

$$a_{MC} = \begin{bmatrix} 1 & 0 & -N_\phi \end{bmatrix}^T$$

$$b_{MC} = \begin{bmatrix} 1 & 0 & -N_\psi \end{bmatrix}^T$$

$$a_R = b_R = [0 \quad 0 \quad 1]^T$$

$$r_{MC}^p = \frac{Eb_{MC}}{a_{MC}^T Eb_{MC}}$$

$$r_R^p = \frac{Eb_R}{a_R^T Eb_R}$$

$$r_{E\psi 1} = E\begin{bmatrix} 2 & -N_\psi & -N_\psi \end{bmatrix}^T$$

$$r_{E\psi 2} = E\begin{bmatrix} 1 & 1 & -2N_\psi \end{bmatrix}^T$$

$$r_{E1} = E[0 \quad 1 \quad 1]^T$$

$$r_1^{MC} = \begin{bmatrix} N_\phi & 1 & 1 \end{bmatrix}^T$$

$$r_2^{MC} = \begin{bmatrix} N_\phi & N_\phi & 1 \end{bmatrix}^T$$

$$r_1^R = [1 \quad 0 \quad 0]^T$$

$$r_2^R = [1 \quad 1 \quad 0]^T$$

$$r_3^R = [0 \quad 1 \quad 0]^T$$

$$\sigma_c = \frac{2c\sqrt{N_\phi}}{N_\phi - 1}[1 \quad 1 \quad 1]^T$$

$$\sigma_a = \sigma_t[1 \quad 1 \quad 1]^T$$

$$\sigma_1^R = \begin{bmatrix} N_\phi\sigma_t - 2c\sqrt{N_\phi} & \sigma_t & \sigma_t \end{bmatrix}^T$$

$$\sigma_2^R = \begin{bmatrix} N_\phi\sigma_t - 2c\sqrt{N_\phi} & N_\phi\sigma_t - 2c\sqrt{N_\phi} & \sigma_t \end{bmatrix}^T$$

$p_{12} \geq 0$ and $p_{13} \geq 0$ and $p_{14} \geq 0$: Return to $f_{MC} = 0$

$$\Delta\sigma_p = f_{MC} r_{MC}^p$$

$p_{12} < 0$ and $p_{25} > 0$: Return to l_1^{MC}

$$\sigma_{correct} = t_1^{MC} r_1^{MC} + \sigma_c$$

where

$$t_1^{MC} = \frac{\left(r_1^{gMC}\right)^T E^{-1}(\sigma - \sigma_c)}{\left(r_1^{gMC}\right)^T E^{-1} r_1^{MC}}$$

$$r_1^{gMC} = \begin{bmatrix} N_\psi & 1 & 1 \end{bmatrix}^T$$

$p_{13} < 0$ and $p_{36} > 0$: Return to l_2^{MC}

$$\sigma_{correct} = t_2^{MC} r_2^{MC} + \sigma_c$$

where

$$t_2^{MC} = \frac{\left(r_2^{gMC}\right)^T E^{-1}(\sigma - \sigma_c)}{\left(r_2^{gMC}\right)^T E^{-1} r_2^{MC}}$$

$$r_2^{gMC} = \begin{bmatrix} N_\psi & N_\psi & 1 \end{bmatrix}^T$$

$p_{14} < 0$ and $p_{45} < 0$ and $p_{46} < 0$ and $p_{47} > 0$: Return to l_3^R

$$\sigma_{correct} = t_3^R r_3^R + \sigma_1^R$$

where

$$t_3^R = \frac{\left(r_R^p \times r_{MC}^p\right)^T (\sigma - \sigma_1^R)}{\left(r_R^p \times r_{MC}^p\right)^T r_3^R}$$

$p_{25} \leq 0$ and $p_{45} \geq 0$ and $p_{58} \leq 0$: Return to σ_1^R

$$\sigma_{correct} = \sigma_1^R$$

$p_{36} \leq 0$ and $p_{46} \geq 0$: Return to σ_2^R

$$\sigma_{correct} = \sigma_2^R$$

$p_{47} \leq 0$ and $p_{78} \leq 0$: Return to $f_R = 0$

$$\Delta\sigma_p = f_R r_R^p$$

$p_{58} > 0$ and $p_{78} > 0$ and $p_{89} > 0$: Return to l_1^R

$$\sigma_{correct} = t_1^R r_1^R + \sigma_a$$

where

$$t_1^R = \frac{\left(r_1^{gR}\right)^T E^{-1}(\sigma - \sigma_a)}{\left(r_1^{gR}\right)^T E^{-1} r_1^R}$$

$$r_1^{gR} = [1 \quad 0 \quad 0]^T$$

$p_{89} \leq 0$: Return to σ_a

$$\sigma_{correct} = \sigma_a$$

APPENDIX B. STRESS RETURN FOR NON-SMOOTH MULTI-SURFACE PLASTICITY

The calculation of the incremental plastic strain for multiple surfaces follows Koiter's generalized form:

$$d\varepsilon_p = \sum_{i=1}^{n} \Delta\lambda^i \frac{\partial g_i}{\partial \sigma}$$

Where n is the number of active yield surfaces, and $\Delta\lambda^i$ is the increment of plastic multiplier corresponding to yield surface i. g_i is the plastic flow rule of yield surface i.

To calculate $\Delta\lambda^i$, we first expand the yield surface using Taylor series,

$$f(\lambda + \Delta\lambda) = f(\lambda) + \frac{\partial f(\lambda)}{\partial \lambda}\Delta\lambda$$

By assuming that the plastic flow rule is independent of λ, $\partial f(\lambda)/\partial\lambda$ can be expressed as,

$$\frac{\partial f(\lambda)}{\partial \lambda} = \begin{bmatrix} -\left(\frac{\partial f_1}{\partial \sigma}\right)^T E \frac{\partial g_1}{\partial \sigma} & -\left(\frac{\partial f_1}{\partial \sigma}\right)^T E \frac{\partial g_2}{\partial \sigma} & \dots \\ -\left(\frac{\partial f_2}{\partial \sigma}\right)^T E \frac{\partial g_1}{\partial \sigma} & -\left(\frac{\partial f_2}{\partial \sigma}\right)^T E \frac{\partial g_2}{\partial \sigma} & \dots \\ \dots & \dots & \dots \end{bmatrix}$$

With the Karesh-Kuhn-Tucker conditions, we have

$$\Delta\lambda = -\left[\frac{\partial f(\lambda)}{\partial \lambda}\right]^{-1} f(\lambda)$$

For multi-surface plasticity, $\Delta\lambda^i$ is a vector, which can be solved by a Newton-Raphson Method.

One difficulty in this stress return algorithm is the selection of active yield surfaces. Let's recall the Karesh-Kuhn-Tucker conditions, which are defined as

$$f_i \leq 0$$

$$\Delta\lambda^i \geq 0$$

$$\Delta\lambda^i f_i = 0$$

For the initial set of active yield surfaces, it is possible to have the following two cases, which violate the above conditions:

Case 1: $f_j^{trial} < 0 \; and \; \Delta\lambda^j < 0$

Case 2: $f_j^{trial} < 0 \; and \; f_j^{update} > 0$

where j∈i. Thus, the set of active yield surfaces must be determined by an iterative procedure.

BIBLIOGRAPHY

Acock, A., T. ORourke, D. Shirmboh, J. Alexander, G. Andersen, T. Kaneko, A. Venkitaraman, J. López-de Cárdenas, M. Nishi, M. Numasawa. and K. Yoshioka. 2004. Practical approaches to sand management. *Oilfield Rev, 16(1),* pp.10-27.

Addis, M. A., N. R. Barton, S. C. Bandis, and J. P. Henry. 1990. Laboratory studies on the stability of vertical and deviated boreholes. *In SPE Annual Technical Conference and Exhibition. Society of Petroleum Engineers, 1990.*

Allen, R. F. and M. Walters. 1999. Erskine Field: Early Operating Experience. *Offshore Europe Oil and Gas Exhibition and Conference.*

Antheunis, D., P. Vriezen, B. Schipper, and A. Van der Vlis. 1976. Perforation collapse: failure of perforated friable sandstones. *Paper presented at the SPE European Spring Meeting.*

Azadbakht, S., M. Jafarpour, H. Rahmati, A. Nouri, H. Vaziri, and D. Chan. 2012. A numerical model for predicting the rate of sand production in injector wells. *Paper presented at the SPE Deepwater Drilling and Completions Conference.*

Barry, W. J., M. T. Jones, and P. E. Plassmann. 1998. Parallel adaptive mesh refinement techniques for plasticity problems. *Advances in Engineering Software, 29(3-6),* 217-225.

Bhardwaj, P., R. Manchanda, J. Hwang, P. Cardiff, and M. M. Sharma. 2016. A New Reservoir Scale Model for Fracture Propagation and Stress Reorientation in Injection Wells. *Paper presented at 50th US Rock Mechanics Symposium, Houston, Texas, USA, June 2016.*

Bianco, L. and P. Halleck. 2001. Mechanisms of arch instability and sand production in two-phase saturated poorly consolidated sandstones. *Paper presented at the SPE European Formation Damage Conference.*

Bird, R. B., W. E. Stewart, and E. N. Lightfoot. 2007. Transport phenomena. *John Wiley & Sons.*

Brooks, R. and A. Corey. 1964. Hydraulic Properties of Porous Media. *Colorado State University, Hydro Paper*.

Buck, A. L. 1981. New equations for computing vapor pressure and enhancement factor. *J. Appl. Meteorol., 20:* 1527–1532.

Burton, R. C., E. R. Davis, and N. Morita. 1998. Application of Reservoir Strength Characterization and Formation Failure Modeling to Analyze Sand Production Potential and Formulate Sand Control Strategies for a Series of North Sea Gas Reservoirs. *Society of Petroleum Engineers*. doi:10.2118/48979-MS.

Carey, M. A. 2014. Water Hammer Fracture Diagnostics. Thesis. *The University of Texas at Austin.*

Carey, M. A., S. Mondal, and M. M. Sharma. 2015. Analysis of Water Hammer Signatures for Fracture Diagnostics. *Paper SPE 174866. https://doi.org/10.2118/174866-MS.*

Carey, M. A., S. Mondal, M. M. Sharma, and D. B. Hebert. 2016. Correlating Water Hammer Signatures with Production Log and Microseismic Data in Fractured Horizontal Wells. *Paper SPE 179108. https://doi.org/10.2118/179108-MS.*

Cerasi, P., A. Berntsen, L. E. Walle, and E. Papamichos. 2015. Sand production delay in gas flow experiments. *Paper presented at the 49th US Rock Mechanics Symposium, San Francisco, CA, USA, June 2015.*

Chang, Y. -B. 1990. Development and Application of an Equation of State Compositional Simulator. *Ph.D. Dissertation, University of Texas at Austin, Austin, Texas.*

Chen, W. F. and G. Y., Baladi. 1985. Soil plasticity: theory and implementation. *Vol. 38. Elsevier.*

Choi, S.-K. and W. S. B. Huang. 2011. Impact of Water Hammer in Deep Sea Water Injection Wells. *Paper SPE 146300. https://doi.org/10.2118/146300-MS.*

Coates, G. R. and S. A. Denoo. 1981. Mechanical properties program using borehole analysis and mohr's circle. *In Proceedings of the 22nd Annual Logging Symposium.*

Crook, T., S. Willson, J. G. Yu, and R. Owen. 2003. Computational modelling of the localized deformation associated with borehole breakout in quasi-brittle materials. *Journal of Petroleum Science and Engineering, 38*(3-4), 177-186. doi: 10.1016/s0920-4105(03)00031-7.

Dake, L. P. 1978. Fundamentals of Reservoir Engineering. *Elsevier Scientific Publishing Co., NY.*

Deb, A., J. H. Prevost, and B. Loret. 1996. Adaptive meshing for dynamic strain localization. *Computer methods in applied mechanics and engineering, 137(3-4),* 285-306.

Detournay, C. 2009. Numerical modeling of the slit mode of cavity evolution associated with sand production. *SPE Journal,* 14(04), 797-804.

Detournay, E. and A. H. D. Cheng. 1993. Fundamentals of poroelasticity. *In Comprehensive Rock Engineering: Principles, Practice & Projects, Vol. II, Analysis and Design Method: 113-171.* Pergamon Press.

Edwards, D. P., Y. Sharma, and A. Charron. 1983. Zones of sand production identified by log-derived mechanical properties: a case study. *In Proceedings of the 8th European Formation Evaluation Symposium*.

Elliott, G. S., R. A. Brockman, and R. M. Shivers. 1995. HPHT drilling and completion design for the Erskine field. *Offshore Europe Conference.*

Feng, Y., C. Arlanoglu, E. Podnos, E. Becker, and K. E. Gray. 2015. Finite-element studies of hoop-stress enhancement for wellbore strengthening. *SPE Drilling & Completion, 30 (01): 38-51. https://doi.org/10.2118/168001-PA.*

Fjar, E., R. M. Holt, A. M. Raaen, R. Risnes, and P. Horsrud. 2008. *Petroleum related rock mechanics*. Vol. 53. Elsevier, 2008.

Glass, A. W. 2005. High pressure, high temperature developments in the United Kingdom Continental Shelf. *Research report 409.*

Gravanis, E., E. Sarris, and P. Papanastasiou. 2015. Hydro-mechanical erosion models for sand production. *International Journal for Numerical and Analytical Methods in Geomechanics* 39.18 (2015): 2017-2036.

Haimson, B. 2007. Micromechanisms of borehole instability leading to breakouts in rocks. *International Journal of Rock Mechanics and Mining Sciences, 44(2),* 157-173.

Haimson, B. and J. Kovacich. 2003. Borehole instability in high-porosity Berea sandstone and factors affecting dimensions and shape of fracture-like breakouts. *Engineering Geology,* 69(3), 219-231.

Hainey, B. W. and J. C. Troncoso. 1992. Frac-pack: an innovative stimulation and sand control technique. *In SPE Formation Damage Control Symposium. Society of Petroleum Engineers.*

Haustveit, K., K. Dahlgren, H. Greenwood, T. Peryam, B. Kennedy, and M. Dawson. 2017. New Age Fracture Mapping Diagnostic Tools-A STACK Case Study. *Paper SPE 184862. https://doi.org/10.2118/184862-MS.*

Hawkins, A. B. and B. J. McConnell. 1992. Sensitivity of sandstone strength and deformability to changes in moisture content. *Quarterly Journal of Engineering Geology and Hydrogeology25.2 (1992):* 115-130.

Hwang, J. and M. M. Sharma. 2013. A 3-Dimensional Fracture Propagation Model for Long-Term Water Injection. *ARMA 13-575. https://www.onepetro.org/conference-paper/ARMA-2013-575.*

Hwang, J., H. Wang, and M. M. Sharma. 2018. Wellbore Integrity and Sand Failure Mechanisms of Frac-Packed Wells in Unconsolidated Sand Formations. *In 52nd US Rock Mechanics/Geomechanics Symposium. American Rock Mechanics Association, 2018.*

Hwang, J., M. J. Szabian, and M. M. Sharma. 2017. Hydraulic Fracture Diagnostics and Stress Interference Analysis by Water Hammer Signatures in Multi-Stage Pumping Data. *Paper URTeC 2687423, SPE/AAPG/SEG Unconventional Resources Technology Conference. https://www.onepetro.org/conference-paper/URTEC-2687423-MS.*

Jafarpour, M., H. Rahmati, S. Azadbakht, A. Nouri, D. Chan, and H. Vaziri. 2012. Determination of mobilized strength properties of degrading sandstone. *Soils and Foundations, 52*(4), 658-667. doi: 10.1016/j.sandf.2012.07.007.

Jing, L. 2003. A review of techniques, advances and outstanding issues in numerical modelling for rock mechanics and rock engineering. *International Journal of Rock Mechanics and Mining Sciences, 40(3), 283-353.*

Khan, A. S. and S. Huang. 1995. Continuum theory of plasticity. *John Wiley & Sons.*

Kim, S. H., M. M. Sharma, and H. J. Fitzpatrick. 2011. A Predictive model for sand production in poorly consolidated sands. *Paper presented at the International Petroleum Technology Conference.*

Law, D., A. S. Dundas, and D.J. Reid. 2000. HPHT Horizontal Sand Control Completion. In *SPE/CIM International Conference on Horizontal Well Technology*.

Liang, Y., B. Wen, M. A. Hesse, and D. DiCarlo. 2018. Effect of Dispersion on Solutal Convection in Porous Media. *Geophysical Research Letters.*

Liang, Y., D. DiCarlo, and M. A. Hesse. 2013. Experimental Study of Convective Dissolution of Carbon Dioxide in Heterogeneous Media. *Presented at the AGU Fall Meeting Abstracts.*

Liang, Y., D. DiCarlo, and M. A. Hesse. 2015. Experiment and Simulation Study of Hydrodynamic Dispersion and Finger Dynamics for Convective Dissolution of Carbon Dioxide. *Presented at the AGU Fall Meeting Abstracts.*

Liang, Y., J. Sheng, J. Hildebrand. 2017. Dynamic permeability models in dual-porosity system for unconventional reservoirs: Case studies and sensitivity analysis. *Presented at the SPE Reservoir Characterisation and Simulation Conference and Exhibition, Society of Petroleum Engineers.*

Liang, Y., Y. Ning, L. Liao, B. Yuan. 2018. Special Focus on Produced Water in Oil and Gas Fields: Origin, Management, and Reinjection Practice, in: Formation Damage During Improved Oil Recovery. *Elsevier, pp. 515–586.*

Mahadevan, J., M. M. Sharma, and Y. C. Yortsos. 2006. Flow-through drying of porous media. *AIChE Journal, 52(7),* 2367-2380.

Masoumi, H., J. Horne, and W. Timms. 2017. Establishing empirical relationships for the effects of water content on the mechanical behavior of Gosford sandstone. *Rock Mech. Rock. Eng. 50,* 2235–2242.

Meier, T., E. Rybacki, A. Reinicke, and G. Dresen. 2013. Influence of borehole diameter on the formation of borehole breakouts in black shale. *International Journal of Rock Mechanics and Mining Sciences, 62,* 74-85.

Mondal, S. 2010. Pressure Transients in Wellbores: Water Hammer Effects and Implications for Fracture Diagnostics. *Thesis, The University of Texas at Austin.*

Mondal, S., C. H. Wu, M. M. Sharma, R. A. Chanpura, M. Parlar, and J. A. Ayoub. 2016. Characterizing, Designing, and Selecting Metal Mesh Screens for Standalone-Screen Applications. *SPE Drilling & Completion,* 31(02), 85-94.

Morita, N. and P. A. Boyd. 1991. Typical sand production problems case studies and strategies for sand control. *SPE Annual Technical Conference and Exhibition.*

Morita, N., D. Whitfill, I. Massie, and T. Knudsen. 1989. Realistic sand-production prediction: numerical approach. *SPE production engineering,* 4(01), 15-24.

Morita, N., E. Davis, and L. Whitebay. 1998. Guidelines for solving sand problems in water injection wells. *In SPE Formation Damage Control Conference. Society of Petroleum Engineers.*

Morita, N., D. L. Whitfill, O. P. Fedde, and T. H. Lovik. 1989. Parametric study of sand production prediction: Analytical approach. *SPE Prod. Eng., 4:* 25–33.

Nordgren, R. P. 1977. Strength of well completions. *In Proceedings of the 18th US Symposium on Rock Mechanics*.

Nouri, A., E. Kuru, and H. Vaziri. 2007. Enhanced modelling of sand production through improved deformation and stress analysis. *Paper presented at the Canadian International Petroleum Conference.*

Nouri, A., E. Kuru, and H. Vaziri. 2009. Elastoplastic modelling of sand production using fracture energy regularization method. *Journal of Canadian Petroleum Technology*, 48(4), 64-71.

Nouri, A., H. Vaziri, H. A. Belhaj, and M. R. Islam. 2006. Sand-production prediction: a new set of criteria for modeling based on large-scale transient experiments and numerical investigation. *SPE Journal, 11*(02), 227-237.

Palmer, I. D., N. Higgs, I. Ispas, K. Baksh, and K.O. Krieger. 2006. Prediction of sanding using oriented perforations in a deviated well, and validation in the field. *In SPE International Symposium and Exhibition on Formation Damage Control.*

Papamichos, E. and M. Stavropoulou. 1998. An erosion-mechanical model for sand production rate prediction. *International Journal of Rock Mechanics and Mining Sciences, 35*(4), 531-532.

Papamichos, E., A. Skjærstein, and J. Tronvoll. 2000. A volumetric sand production experiment. *Paper presented at the 4th North American Rock Mechanics Symposium. American Rock Mechanics Association, 2000.*

Papamichos, E., I. Vardoulakis, J. Tronvoll, and A. Skjaerstein. 2001. Volumetric sand production model and experiment. *International Journal for Numerical and Analytical Methods in Geomechanics,* 25(8), 789-808. doi: 10.1002/nag.154

Papamichos, E., J. Stenebraten, P. Cerasi, A. Lavrov, I. Vardoulakis, G.F. Fuh, M. Brignoli, Goncalves CJ de Castro, and O. Havmoller. 2008. Rock type and hole failure

pattern effects on sand production. *Paper presented at the 42th US Rock Mechanics Symposium and 2th US-Canada Rock Mechanics Symposium, San Francisco, CA, USA, June 2008.*

Papamichos, E., P. Liolios, and P. J. Van den Hoek. 2004. Breakout stability experiments and analysis. *Paper presented at the 6th North America Rock Mechanics Symposium (NARMS). American Rock Mechanics Association.*

Papanastasiou, P. and A. Zervos. 1998. Three-dimensional stress analysis of a wellbore with perforations and a fracture. *In SPE/ISRM Rock Mechanics in Petroleum Engineering.*

Peden, J., and A. Yassin. 1986. The determination of optimum completion and production conditions for sand-free oil production. *Paper presented at the SPE Annual Technical Conference and Exhibition.*

Peiró, J. and S. Sherwin. 2005. Finite difference, finite element and finite volume methods for partial differential equations. *Handbook of materials modeling: 2415-2446.*

Rahmati, H., A. Nouri, H. Vaziri, and D. Chan. 2012. Validation of predicted cumulative sand and sand rate against physical-model test. *Journal of Canadian Petroleum Technology,* 51(5), 403-410.

Rahmati, H., M. Jafarpour, S. Azadbakht, A. Nouri, H. Vaziri, D. Chan, and Y. Xiao. 2013. Review of Sand Production Prediction Models. *Journal of Petroleum Engineering*, 2013, 1-16. doi: 10.1155/2013/864981.

Ray, P., M. Rijken, J. Cameron, C. Jones, and A. EI-Fayoumi. 2014. Estimating sand production volume in Oil and Gas Reservoir. *Paper presented at the SPE Annual Technical Conference and Exhibition, Amsterdam, The Netherlands, October 2014.*

Risnes, R., R. K. Bratili, and P. Horsrud. 1982. Sand stresses around a wellbore. *SPE Journal*, vol. 22, no. 6, pp. 883–898, 1982.

Saksala, T. 2009. Geometric return algorithm for non-associated plasticity with multiple yield planes extended to linear softening/hardening models. *Rakenteiden Mekaniikka (Journal of Structural Mechanics)*, *42*(2), pp.83-98.

Salencon, J. 1969. Contraction quasi-statique d'une cavite a symetrie spherique ou cylindrique dans un milieu elastoplastique. *In Annales des ponts et chaussées*, 4: 231-236.

Santarelli, F. J., E. Skomedal, P. Markestad, H. I. Berge, and H. Nasvig. 2000. Sand Production on Water Injectors: How Bad Can It Get? *SPE Drilling & Completion, 15(2), 132–139. https://doi.org/10.2118/64297-PA.*

Saucier, R. 1974. Considerations in gravel pack design. *Journal of Petroleum Technology, 26*(02), 205-212.

Servant, G., P. Marchina, Y. Peysson, E. Bemer, and J. F. Nauroy. 2006. Sand erosion in weakly consolidated reservoirs: experiments and numerical modeling. *Paper presented at the SPE/DOE Symposium on Improved Oil Recovery.*

Sinaki, A. R. Y. 2012. Sand production simulation under true-triaxial stress conditions.

Skjaerstein, A., J. Tronvoll, F. J. Santarelli, and H. Joranson. 1997. Effect of water breakthrough on sand production: experimental and field evidence. *Paper presented at the SPE annual technical conference and exhibition.*

Skjaerstein, A., M. Stavropoulou, I. Vardoulakis, and J. Tronvoll. 1997. Hydrodynamic erosion: A potential mechanism of sand production in weak sandstones. *International journal of Rock Mechanics and Mining Sciences*, vol. 34, no. 3-4, pp 292.el-292.e18.

Tovar, J. J., L. Zerpa, and E. Guerra. 1999. Impact of formation damage on sand production in Deep Eocene Reservoirs, Lake Maracaibo, Venezuela: A case history. *European formation damage conference.*

Tronvoll, J., M. Dusseault, F. Sanfilippo, and F. Santarelli. 2001. The tools of sand management. *Paper presented at the SPE Annual Technical Conference and Exhibition.*

Vardoulakis, I., M. Stavropoulou, and P. Papanastasiou. 1996. Hydro-mechanical aspects of the sand production problem. *Transport in porous media*, *22*(2), 225-244.

Vasarhelyi, B. and P. Van. 2006. Influence of water content on the strength of rock. *Engineering Geology 84:* 70-74.

Vaziri, H. 1986. Mechanics of fluid and sand production from oil sand reservoirs. *Annual Technical Meeting. Petroleum Society of Canada.*

Vaziri, H., A. Nouri, K. A. Hovem, and X. Wang. 2008. Computation of sand production in water injectors. *SPE Production & Operations, 23*(04), 518-524.

Vaziri, H., B. Barree, Y. Xiao, I. Palmer, and M. Kutas. 2002. What is the magic of water in producing sand? *Paper presented at the SPE Annual Technical Conference and Exhibition.*

Vaziri, H., Y. Xiao, and I. Palmer. 2002. Assessment of several sand prediction models with particular reference to HPHT wells. *Paper presented at the SPE ISRM Rock Mechanics Conference, Irving, TX.*

Vaziri., H, A. Nouri, K. Hovem, and X. Wang. 2007. Computation of Sand Production in Water Injectors. *Presented at the European Formation Damage Conference held in Scheveningen, The Netherlands, 2007.*

Veeken, C. A. M., D. R. Davies, C. J. Kenter, and A. P. Kooijman. 1991. Sand production prediction review: developing an integrated approach. *In SPE annual technical conference and exhibition.*

Vermeer, P. A. and R. De Borst. 1984. Non-associated plasticity for soils, concrete and rock. *Heron, 29(3): 3-64.*

Wan, R. and J. Wang. 2004a. Analysis of sand production in unconsolidated oil sand using a coupled erosional-stress-deformation model. *Journal of Canadian Petroleum Technology,* 43(2), 47-53.

Wan, R. and J. Wang. 2004b. Modelling of sand production and wormhole propagation in an oil saturated sand pack using stabilized finite element methods. *Journal of Canadian Petroleum Technology,* 43(4), 45-52.

Wang, H. and M. M. Sharma. 2016. A fully 3-D, multi-phase, poro-elasto-plastic model for sand production. *In SPE Annual Technical Conference and Exhibition. Society of Petroleum Engineers, 2016.*

Wang, H. and M. M. Sharma. 2017. The Role of Elasto-Plasticity in Cavity Shape and Sand Production in Oil and Gas Wells. *In SPE Annual Technical Conference and Exhibition. Society of Petroleum Engineers, 2017.*

Wang, H., D. P. Gala, and M. M. Sharma. 2017. Effect of Fluid Type and Multi-Phase Flow on Sand Production in Oil and Gas Wells. *In SPE Annual Technical Conference and Exhibition. Society of Petroleum Engineers, 2017.*

Wang, H., J. Hwang, and M. M. Sharma. 2018. Sand Production Caused by Water Hammer Events: Implications for Shut-In Protocols and Design of Water Injection Wells. *In SPE International Conference and Exhibition on Formation Damage Control. Society of Petroleum Engineers.*

Wang, H., P. Cardiff, and M. M. Sharma. 2016. A 3-D poro-elasto-plastic model for sand production around open-hole and cased & perforated wellbores. *Paper presented at 50th US Rock Mechanics Symposium, Houston, Texas, USA, June 2016.*

Wang, H., X. Yang, W. Zhang, and M. M. Sharma. 2018. Predicting Sand Production in HPHT Wells in the Tarim Basin. *Presented at the SPE Annual Technical Conference and Exhibition held in Dallas, Texas, 24–26 September 2018. SPE-191406-MS.*

Wang, J., D. Walters, A. Settari, and R. Wan. 2006. An integrated modular approach to modeling sand production and cavity growth with emphasis on the multiphase flow and 3D effects. *Paper presented at the Proceedings of the 41st US Symposium on Rock Mechanics Symposium.*

Wang, J., R. Wan, A. Settari, and D. Walters. 2005. Prediction of volumetric sand production and wellbore stability analysis of a well at different completion schemes. *Paper presented at the Alaska Rocks 2005 Proceedings of the 40th US Symposium on Rock Mechanics.*

Wang, X., K. A. Hovem, D. Moos, and Y. Quan. 2008. Water Hammer Effects on Water Injection Well Performance and Longevity. *Paper SPE 112282.*

Wang, Y. and M. B. Dusseault. 1996. Sand production potential near inclined, perforate wellbores. *CIM 47th Annual Technical Meeting. June10–12, Calgary, Alberta, Canada. Paper No. 96–27.*

Weingarten, J. and T. Perkins. 1995. Prediction of sand production in gas wells: methods and Gulf of Mexico case studies. *Journal of Petroleum Technology,* 47(07), 596-600.

Weingarten, J. S. and T. K. Perkins. 1992. Prediction of sand production in gas wells: Methods and Gulf of Mexico case studies. *J. Pet. Tech., 47:* 596–600.

Willson, S. M, Z. A. Moschovidis, J. R. Cameron, and I. D. Palmer. 2002. New model for predicting the rate of sand production. *Paper presented at the SPE/ISRM Rock Mechanics Conference, Irving, Texas, 20-23 October 2002.*

Wu, C.H., M. M. Sharma, M. J. Fuller and S. Mathis. 2018, February. Estimating Sand Production Through Gravel Packs. *In SPE International Conference and Exhibition on Formation Damage Control.*

Wu, C.H., M. M. Sharma, R. Chanpura, M. Parlar and J. Ayoub. 2016. Factors Governing the Performance of Multi-Layered Metal-Mesh Screens. *In SPE International Conference and Exhibition on Formation Damage Control. Society of Petroleum Engineers.*

Wu, Y.-S., J. Li, D. Ding, C. Wang, and Y. Di. 2014. A Generalized Framework Model for the Simulation of Gas Production in Unconventional Gas Reservoirs. *SPE Journal, 19(05): 845-857.*

Wu, Y.-S., J. Li, D. Ding, C. Wang, and Y. Di. 2014. A Generalized Framework Model for the Simulation of Gas Production in Unconventional Gas Reservoirs. *SPE Journal, 19(05):* 845-857.

Ye, Z., M. Janis, and A. Ghassemi. 2017. Injection-driven Shear Slip and The Coupled Permeability Evolution of Granite Fractures for EGS Stimulation. *In 51st US Rock Mechanics/Geomechanics Symposium. American Rock Mechanics Association.*

Yue, K., J. E. Olson, and R. A. Schultz. 2016. Calibration of stiffness and strength for layered rocks. *Presented at the 50th US Rock Mechanics/Geomechanics Symposium, Houston, Texas, June 26–29, 2016.*

Yue, K., J. E. Olson, and R. A. Schultz. 2018. Layered modulus effect on fracture modeling and height containment. *Presented at the Unconventional Resources Technology Conference, Houston, Texas, July 23–25, 2018.*

Zhou, Z., X. Cai, W. Cao, X. Li, and C. Xiong. 2016. Influence of water content on mechanical properties of rock in both saturation and drying processes. *Rock Mech Rock Eng 49:*3009–3025.